

CONTENTS

Chapter 1 Introduction	11
1.1 Multiphoton Processes	14
1.2 General Description Atom-Field Interaction	23
1.3 Floquet Theory	30
1.4 Perturbation Theory in the Floquet Picture	33
1.5 High-Frequency Floquet Theory	39
1.6 This Thesis	45
Chapter 2 Numerical Methods	49
2.1 Bound State Calculation	49
2.2 Solving an Inhomogeneous System; Lifetimes	56
Chapter 3 The Induction of H^{2-}	65
3.1 Introduction	65
3.2 Theoretical Basis	66
3.3 The Linearly Polarized Field, a Candidate?	67
3.4 The Appearance of H^{2-}	68
A The End-Point Potential	71
Chapter 4 Circularly Polarized Laser Fields as a Magic Potion for AMCNI	75
4.1 Introduction	75
4.2 Atomic Structure in Circularly Polarized Fields	76
4.3 AMCNI in a Bichromatic Radiation Field	88
4.4 Realizability and Stability	91
A Bichromatic Radiation and the End-Point Potential	92
Chapter 5 Dressage of AMCNI by Linearly Polarized Laser Fields	95
5.1 Introduction	95
5.2 AMCNI in a Linearly Polarized Laser Field	97
5.3 The Appearance and Structure of AMCNI	105
5.4 Applicability of HFFT	110
5.5 Conclusions	113
A Applicability of Scaling Laws of End-point Potential in AMCNI	114
Chapter 6 Calculation of AC-Quasienergy of H^- using Interparticle Coordinates	117
6.1 Introduction	117
6.2 Decomposition in Euler Angles and Interparticle Coordinates	120
6.3 AC Shifts and Widths of H^-	125
6.4 Remarks about Method	137
Chapter 7 Detachment Rates of H^{2-} in an Intense Linearly Polarized Laser Field	139

7.1	The Complex Quasienergy Beyond the High-Frequency Limit	140
7.2	Calculation of the Detachment Rate	143
7.3	Stabilization and Angular Dependence of the Electron Detachment	148
7.4	Applicability of the Calculation	153
A	Quadrature Formulas for a Logarithmic Singularity	157
	Bibliography	159
	Samenvatting voor iedereen	167

1

INTRODUCTION

The simplest system in atomic physics, used extensively in the evolution of quantum mechanics, is the hydrogen atom, consisting of one proton and one electron. Despite the repulsive Coulombic interaction between electrons, being of equal magnitude to their attraction to a proton, it is possible to attach an electron to the hydrogen atom. Although very weakly bound, the two electrons and the proton together form the singly charged negative hydrogen ion, H^- . However, attaching an additional electron to H^- leads to an unstable configuration which will decay quickly by auto-detachment. Nature does not allow the existence of atomic multiply charged negative ions. The attractive interaction between the nucleus and the electrons is too weak to compensate the repulsive electron-electron interaction.

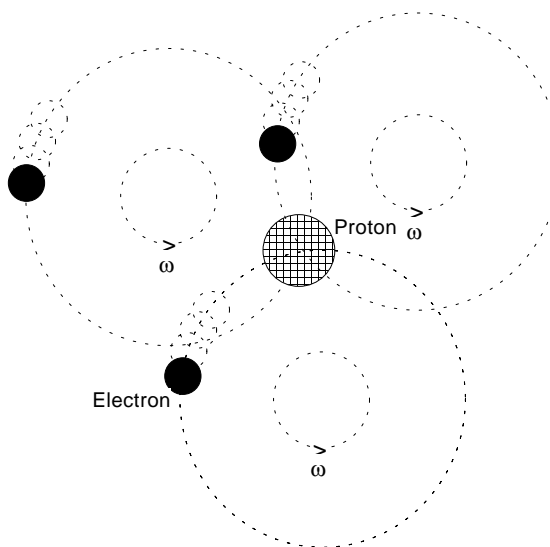


Figure 1.1: Schematic picture of the doubly charged negative hydrogen ion H^{2-} in a circularly polarized high-frequency laser field. The interaction between the electrons (black dots) and the intense laser field forces each electron to move with constant speed along a circle. The electrons have arranged themselves into a configuration minimizing their total repulsive energy. While the electrons move along the circles, their inter-electronic distances are constant. The angular speed of the electrons is equal to the frequency ω of the laser field. Due to the attractive interaction between the proton (shaded dot) and the electrons, the circles the electrons move on intersect with the fixed position of the proton.

In the presence of intense radiation fields, the character of nature changes dramatically and exotic phenomena start to play a role. One of these phenomena is a major topic in this Thesis: stable configurations of atomic multiply charged negative ions of hydrogen can exist in radiation fields. Driven by the field, the electrons arrange themselves into a configuration in which they share the attraction with the proton while minimizing their repulsive interaction. In Figure 1.1 the configuration of H^{2-} in a circularly polarized field is reflected schematically.

In order to understand and to gain insight in the influence of radiation fields on the atomic structure, it is relevant to know how the field and the atom interact. This Chapter introduces the reader to the field where this interaction plays a central role, the field of intense laser-atom physics. The purpose of this Introduction is twofold, and therefore it is divided into two parts.

Firstly, in Part I, consisting of Sections 1.1 and 1.2, we comment on some important intense-field phenomena and describe the way these have been handled theoretically. An impression is given of the history and present status of the field of laser-atom physics. In particular, we will concentrate on new phenomena in laser-atom physics that showed up when the highest achievable intensity increased further and further. In these phenomena, multiphoton processes, i.e. processes in which the number of photons exchanged between the atom and the laser field exceeds one, play an important role.

Secondly, the purpose of Part II, which consists of Sections 1.3 through 1.5, is to explain the theory that is relevant throughout this Thesis and which is used extensively in theoretical laser-atom physics, namely Floquet theory. It has been shown before that in intense high-frequency fields counterintuitive phenomena show up, which are supported by Floquet theory. In addition, high-frequency Floquet theory is explored in more detail, because of its relevance for the existence of bound configurations of multiply charged negative ions of hydrogen.

Part I

In the beginning of the 20-th century, the theory of quantum mechanics developed with an unprecedented speed into a mature formalism describing the physics of processes on the atomic scale. Although quantum mechanics was theoretically well formulated, at that time technology did not undergo this tremendous change needed to support experimentally most quantum mechanical predictions. Some of these predictions could be tested by measuring the absorption- and emission-spectra of atoms exposed to a radiation field. Due to relatively low maximum intensities and poorly defined frequencies of radiation sources in those days, the information about the internal structure that could be obtained from this spectroscopy was rather limited. However, roughly half a century later in the 1960's, the invention of the laser, a coherent monochromatic radiation source, opened a wide range of possibilities to investigate in more detail quantum mechanical processes. From the interaction between the radiation from the laser and an atom (or molecule), information can be extracted about the atom and in particular about the electrons it contains. Since the laser-atom interaction depends critically on the temporal and spatial dependence of the laser light, the experimental study is strongly linked to the evolution of laser technology. During this evolution experimental results acted as a stimulation for theoreticians to perform calculations on atomic systems interacting with electromagnetic radiation.

In the last two decades, laser technology has experienced a huge evolution in both the intensity- and frequency-domain. From the infra-red to the ultra-violet it has become possible to generate intensities far beyond the atomic unit (the intensity of 1 a.u. = $3.51 \cdot 10^{16} \text{ W/cm}^2$ corresponds to an AC-field amplitude equal to the static field generated by a proton measured at a distance of one Bohr radius; i.e. the field strength at the average distance between the electron and the proton in the ground state of hydrogen). This radiation regime was entered for the first time in 1985 by Rhodes [1], who constructed a laser with intensities in the $10^{15} - 10^{17} \text{ W/cm}^2$ regime. Although lowest-order (non-vanishing) perturbation theory (LOPT) has proven to be a good tool to calculate AC-Stark shifts and multiphoton transition probabilities (see e.g. Refs.[2] and [3]), at these higher intensities the perturbation series do not converge and, as a consequence, LOPT loses its applicability [4]. Due to this breakdown of LOPT, the description of the interaction between the atom and these fields required a new type of approach. The interaction between a *free* classical electron and a superintense field was treated by incorporating relativistic theories by Kibble in 1966 [5]. However, to find an appropriate method to describe the atom-field interaction at high intensities, i.e. beyond the perturbative regime, appeared to be a difficult task challenging physicists. Since the evolution of non-perturbative theories proceeded rather slowly, trying to solve the problem by integrating the time-dependent Schrödinger equation (TDSE) numerically became popular. By using simplified one-dimensional model potentials theoreticians started to gain more and more insight in the interaction with intense fields.

In Section 1.2 a general theoretical description of the atom-field interaction will be given. But we will consider first some of the main phenomena that showed up during both the experimental and theoretical study of laser-atom physics. In particular, the phenomena connected to the interaction with intense fields will be discussed.

1.1 Multiphoton Processes

One of the most important fields that opened up when higher intensities became available is the field of multiphoton processes. Since the probability of interaction between the field and the atom increases with the intensity of the radiation field, processes involving more than one photon become relevant at higher intensities. As pointed out by Bunkin and Prokhorov in 1964 (see Ref.[6]), at higher intensities or, similarly, at higher field amplitudes, the role of these so-called multiphoton processes in the interaction between the atom and the field becomes dominant. The relevance of the study of multiphoton physics lies in the fact that due to the dominant role in the non-perturbative regime, the evolution of the study of multiphoton physics contributes to the knowledge of strongly perturbed quantum systems.

When the field amplitude increases further, it will exceed the atomic unit, entering the non-perturbative regime. For these and higher field amplitudes the Rayleigh-Schrödinger perturbation series do not converge. The detailed convergence properties of the perturbation series have been investigated by Pont and Shakeshaft [7] and Manakov and Fainshtein [8]. Another cause for the breakdown of perturbation theory is the presence of resonant states in the multiphoton process. A resonant state is an eigenstate of the atom *in the field* that is degenerate with the initial state modulo an integer multiple of the photon energy. In case resonant states are present, the resolvent operator in the expression of the perturbation series diverges, which, as a consequence, implies the breakdown of LOPT. Therefore, even for intensities far below the atomic unit, the presence of resonant states can destroy the applicability of LOPT.

Apart from the theoretical description there is another important difference between resonant and non-resonant multiphoton processes, as can be illustrated with the following hand-waving argument. In a multiphoton process with n photons, the atom has to transit $n - 1$ intermediate states. Now two cases are to be distinguished: on one hand, if such an intermediate state is not an eigenstate of the atom in the field, this state is called a "*virtual state*". On the other hand, if it is, we are dealing with a resonant state. The time Δt the electron can spend in a virtual state is determined by Heisenberg's uncertainty relation. If the energy difference between the virtual state and the nearest eigenstate is denoted as ΔE , we have $\Delta t \approx \hbar/\Delta E$, which is generally very short, in the order of the period of an optical cycle ($\simeq 10^{-15}$ s). This short lifetime implies that a high-intensity field is needed to create a sufficiently high interaction probability between atom and field in order to "pump" the atom from initial to final state. Except when within the small time interval Δt another photon passes the atom and is absorbed, the atom will return to the initial state and stimulated emit the photon in its original direction. In case the intermediate state is resonant, the time the atom can spend in the intermediate state is only limited by the natural line width of this particular resonant state. In general this time is orders of magnitude larger than in case of the virtual intermediate state. Therefore, at the same intensity, the amplitude of resonant multiphoton processes is much larger than that of non-resonant processes. If q resonant states are involved in the multiphoton process, it is illustrative to imagine the process as $q + 1$ independent subsequent processes.

A similar reasoning also holds in case a continuum state is resonantly coupled to one of the intermediate states. There is, however, an important difference with a bound state on one hand and a continuum state on the other as intermediate state. An electron can absorb a photon only if it is close to the core (see below). In case the intermediate state

is a continuum state, the time the electron has for absorbing an excess photon is limited by the speed it leaves the core with. The difference with the case in which a bound state is the resonance state lies in the fact that in the latter case the electron has the chance to absorb an additional photon during each evolution of the atomic orbit, whereas in case of a continuum state the electron passes the core only once. This means that the amplitude for absorption of an excess photon after the atom is ionized (a process referred to as excess-photon ionization) depends on the photon energy, i.e. on the frequency of the radiation field. For a review on resonant enhanced multiphoton processes, see for example Georges and Lambropoulos, Ref.[9].

1.1.1 Multiphoton Ionization

An important multiphoton processes is multiphoton ionization (MPI). A MPI process differs from the conventional ionization process in the fact that a number of photons is required in order to couple the initial bound state with the continuum. Processes involving multiphoton ionization have been explored in great detail in the last two decades. In Figure 1.2 a typical example of a MPI process is depicted in which 7 photons are required to couple the initial state with the continuum. As a matter of fact, the photons can be "piled up" to bridge the energy gap between the initial state and the continuum. If one of the intermediate states involved is degenerate with an eigenstate of the atom in the field (i.e. it is resonantly coupled), the ionization process is strongly enhanced. This process is often referred to as resonant enhanced multiphoton ionization, or REMPI (see e.g. Faisal, Ref.[10] p.114). The phenomenon of multiphoton ionization has been discussed extensively in literature, both experimentally and theoretically. For non-resonant MPI processes see for example Morrelec *et al* [11], or for general MPI processes Manakov *et al* [12]. There are several books that describe different parts of the field, of which I want to mention here the following: Mittleman 1982 [13], Delone and Krainov 1984 [14], Chin and Lambropoulos 1984 [2], Faisal 1987 [10], Evans and Chin 1994 [15].

Where on one hand experimentalists were weighed down by limitations of optical equipment, on the other hand the evolution of computer capacities determined the speed for theoreticians on their way to give a detailed description of MPI processes. Since the number of photons involved in these processes equals two or more, Fermi's Golden Rule (a result from first order perturbation theory) is not applicable. However, the order of perturbation theory can be increased to the number of photons involved. The complexity of the calculations increases with the order of the perturbation series, and therefore perturbation theory is not unlimitedly applicable to describe the electron response to an intense field, even if it would converge.

The first theoretical treatments of MPI were given in the 1960s by Geltman [16] and later by Bunkin and Fedorov [17] and by Keldysh [18, 19]. The absence of systematic non-perturbative approaches to strong-field multiphoton theory forced the development of purely numerical methods in those days [20]. Keldysh was actually the first who came up with a non-perturbative theory [18, 19], describing the MPI process as a transition from an unperturbed initial state to a "Volkov state" [21], the latter being an exact solution of the Schrödinger equation of a free electron in a radiation field. Later, the idea of Keldysh was extended by Faisal [22] and Reiss [23]. The resulting Keldysh-Faisal-Reiss theory (KFR-theory) has proven to be a good tool for describing non-perturbative effects in multiphoton ionization processes in the low-frequency regime. As is shown by Dörr *et al* [24], the Keldysh theory yields remarkably good results as long as the system under

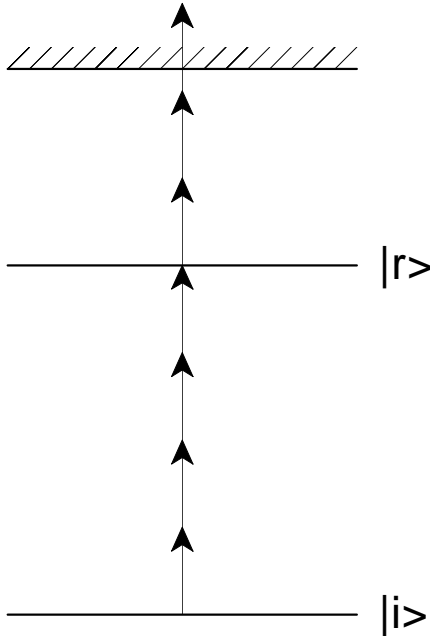


Figure 1.2: An illustration of a multiphoton ionization process where the energy axis is drawn vertically and where the length of the arrows is a measure for the photon energy. For this particular process 7 photons are required to bridge the energy gap between the initial state $|i\rangle$ and the continuum (shaded area). In this example, the initial state is resonantly coupled with an eigenstate $|r\rangle$ of the atom in the field. Due to this resonant coupling with an intermediate state, the multiphoton ionization yield is strongly enhanced, a process referred to as Resonance Enhanced MultiPhoton Ionization (REMPI).

consideration does not contain more than one active electron and no resonant states are involved. However, in multielectron systems where electron-electron correlation starts to play a role, the KFR theory starts to fail and correlation has to be included (see Dörr *et al* [24] for the case of the negative hydrogen ion, H^-). The approach to use a Volkov state for describing the final state has been used by Mittleman [25], and also by Pert [26], in order to calculate ionization rates in fields in which the electron-field interaction is asymptotically large compared to the electron-core interaction. Especially at high intensities the perturbation of the initial state, although tightly bound by the electrostatic field, starts to play a non-negligible role. In 1982 Mittleman initiated a method in which the initial state in the ionization process is not unperturbed [13]. Janjusevic and Mittleman [27] applied this method to calculate ionization rates of atomic hydrogen by first neglecting the electron-core interaction and then treating the electrostatic interaction as a corrective term. However, neglecting initially the electron-core interaction gives rise to a poorly described distorted initial state. By including this interaction from the beginning, Pont [28] calculated ionization rates of atomic hydrogen that are in disagreement with those obtained by Janjusevic and Mittleman.

Experimentally MPI was demonstrated for the first time in 1965 in Moscow by Voronov and Delone [29, 30] who measured 7-photon ionization of Xe, and by Agostini *et al* in 1968 in Saclay [31]. In the early days of the experimental study of MPI processes, only the remaining ions could be detected. This means that only total ionization rates

could be obtained from the experiment, leaving angular distributions and partial rates unknown. The role of resonant states in the MPI process was nicely shown by Petite *et al* [32], who demonstrated that the total ionization yield decreases dramatically when, due to the AC-Stark shift, an intermediate state shifts out of resonance.

Parallel to the evolution of laser technology, new unexpected phenomena were shown experimentally. Before these will be discussed below, the concept of ponderomotive potential energy and its effects, playing an important role in these new phenomena, will be clarified next.

1.1.2 Ponderomotive Potential

In order to get a better understanding of MPI processes in laser foci, it is important to know more about the interaction between the ionized electron and the laser field. Despite the fact that due to energy and momentum conservation the electron can not absorb photons (the wavelength is such that the photons hardly carry momentum), it can scatter from them. Treating the field classically, the resulting motion of a free electron in a homogeneous monochromatic field with (possibly complex) polarization axis $\hat{\varepsilon}$, $\mathbf{E}(t) = \text{Re}(F_0\hat{\varepsilon}\exp(-i\omega t))$, can be found by solving Newton's equation of motion

$$\mu \frac{d}{dt} \mathbf{v}(t) = -e \mathbf{E}(t). \quad (1.1)$$

Here μ and e are the mass and charge resp. of the electron. With $\hat{\mathbf{e}}_1, \hat{\mathbf{e}}_2$ and $\hat{\mathbf{e}}_3$ a right-handed orthogonal coordinate system with $\hat{\mathbf{e}}_3$ the propagation direction of the light, the case $\hat{\varepsilon} = \hat{\mathbf{e}}_1$ corresponds to a linearly polarized field, whereas $\hat{\varepsilon} = (\hat{\mathbf{e}}_1 \pm i\hat{\mathbf{e}}_2)/\sqrt{2}$ corresponds to a left- or right-handed circularly polarized field. By integrating Eq.(1.1) the velocity of a free electron is expressed as

$$\mathbf{v}(t) = \mathbf{v}_0 + \frac{e}{\mu\omega} \text{Im}(F_0\hat{\varepsilon}\sin\omega t) \quad (1.2)$$

equal to a sum of a constant drift velocity and a velocity oscillating with the frequency of the field. The latter is often referred to as the "quiver motion", an harmonic motion along the trajectory

$$\alpha(t) = -\frac{eF_0}{\mu\omega^2} \text{Re}(\hat{\varepsilon}\exp(-i\omega t)) \equiv -\alpha_0 \text{Re}(\hat{\varepsilon}\exp(-i\omega t)) \quad (1.3)$$

Here α_0 is the quiver amplitude, a parameter that will play a central role throughout this Thesis. In case of zero drift velocity, the time-averaged kinetic energy of the electron in the field is equal to

$$U_P = \frac{e^2 F_0^2}{4\mu\omega^2}. \quad (1.4)$$

In other words, the minimum amount of energy required for a free electron to enter the laser focus equals U_P , the *ponderomotive energy*. Since U_P is a positive quantity, the laser focus can be treated as a repulsive barrier for the electron to enter the field. The potential corresponding to this barrier is called the ponderomotive potential, which, as can be seen from Eq.(1.4), is proportional to the intensity of the field.

In practice, the intensity in a laser focus is never homogeneous. In an inhomogeneous part of the focus, the number of scattering events between electron and photons in a region of higher intensity is larger than where the intensity is lower. As a result, as elaborated in detail by Kibble in 1966 [5], forces act on the electron. These so-called

ponderomotive forces, push the electron towards regions of lower intensity, i.e. out of the focus, in the direction of the intensity gradient. This has been verified experimentally by Bucksbaum *et al*, see Ref.[33]. An important effect of the ponderomotive force is that electrons gain an amount of kinetic energy equal to the ponderomotive energy while they are, after ionization, leaving the focus on their way to the detector. In the following subsections the importance of the role played by the ponderomotive forces will be illustrated.

1.1.3 Excess-Photon Ionization

Roughly a decade after the appearance of multiphoton processes, it became technically possible to detect not only the ions, but also the ionized electrons. This gave the opportunity to measure the angular distribution of the ionized electrons in addition to the total rate. More importantly, the resulting photoelectron spectra showed that in intense fields the atom can absorb even more photons than required to reach the continuum. These results could not be obtained by previous measurements since the excess energy from the additional photons is absorbed by the electrons and not by the remaining ions. This new type of multiphoton process, referred to as excess-photon ionization (EPI, or above-threshold ionization, ATI), opened up a new field in laser-atom physics that was studied intensively both experimentally and theoretically in the years after. The effect of EPI was discovered experimentally by Agostini *et al* in 1979 [34], who presented the first well-resolved photoelectron spectrum. This showed that there exists a set of ionization channels in which the electron can leave the atom, each channel labelled by the number of excess photons absorbed by the electron. Evidently, these channels are energetically separated by the photon energy and it is interesting to calculate and measure the branching ratio's between the different channels. Although in principle the phenomenon of EPI can be observed in any type of atom or molecule in an intense field of any frequency, almost all experiments on EPI in the years after its discovery were performed using xenon (see e.g. Refs.[35] and [36]), although a complex atom, a simple gas to handle experimentally.

In the early 1980s numerous people carried out calculations on EPI using LOPT methods. Gontier *et al* [37] for example, in 1980 calculated transition probabilities of EPI processes. This group from Saclay introduced the acronym ATI for the EPI process. On the other hand, numerical methods were applied to perform calculations beyond LOPT (see for example Aymar and Crance [38] and Potvliege and Shakeshaft [39]). The latter methods were especially useful to gain more insight into the physics behind EPI spectra obtained from measurements where resonant states were involved, i.e. REMPI spectra. Most non-perturbative theories assume a purely monochromatic field for which quasistationary states can be defined, so-called Floquet states with associated quasienergy (see below). However, in case of hydrogen, exact expressions exist for the Greens' function [40]. Therefore, as long as there are no resonant intermediate states involved, LOPT proved to be successful especially for hydrogen, see e.g. Klarsfeld [41], Karule [42] and the book by Faisal [10]. Moreover, LOPT was also applied to make direct comparison with experimental results by Fabre *et al* in 1982 [43].

1.1.3.1 Channel Closure

Using higher intensities, still in the perturbative regime however (i.e. for intensities < 1 a.u.), experiments showed results that could not be interpreted by perturbation theory. By varying the intensity of the laser, Kruit *et al* [44] showed that the relative height of the

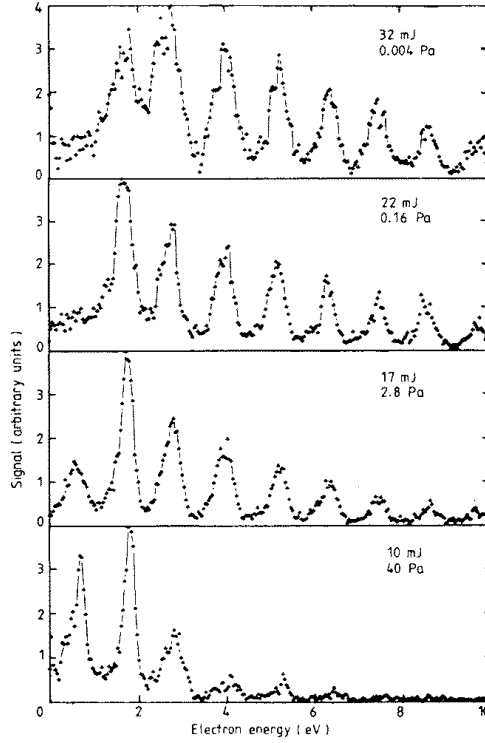


Figure 1.3: Photoelectron spectra for various intensities (of the order of 10^{13} W/cm^2) from xenon irradiated by a 1064 nm (Nd-Yag) laser. At this wavelength 11 photons are required to couple the initial state with the continuum. Up to 8 excess-photon ionization peaks are observed. As the intensity increases the amplitude of the lowest order peak decreases whereas those of higher orders increase. (Reproduced from Kruit *et al*, Ref.[44])

lowest order peak in the photoelectron spectrum decreases very abruptly as the intensity increases, in contrast to predictions from LOPT, see Figure 1.3. Moreover, the heights of the higher-order peaks increase. The explanation for this so-called *peak-suppression*, given by Muller *et al* (see Refs.[45] and [46]), lies in the fact that the ionization threshold increases with increasing intensity. This can be understood as follows. In the final state in the EPI process the electron is free. Since a free electron requires a minimum amount of energy equal to the ponderomotive energy, as explained above, the continuum threshold shifts by an amount equal to the ponderomotive energy. On the other hand, in the initial state the electron is hardly affected by the external field, since the initial state is a tightly bound state (it is shifted by the AC-Stark shift Δ_i , but this shift is negligible compared to the ponderomotive shift in an intense low-frequency field). As a result, the kinetic energy the electron arrives with at the detector after absorption of n photons from the initial state with energy E_i is given by

$$E_{kin} = E_i + n\hbar\omega + \Delta_i - U_P. \quad (1.5)$$

The minimum number N_0 of photons needed to couple the initial state with the continuum is the smallest integer for which

$$N_0 = \frac{E_i + U_P - \Delta_i}{\hbar\omega}, \quad (1.6)$$

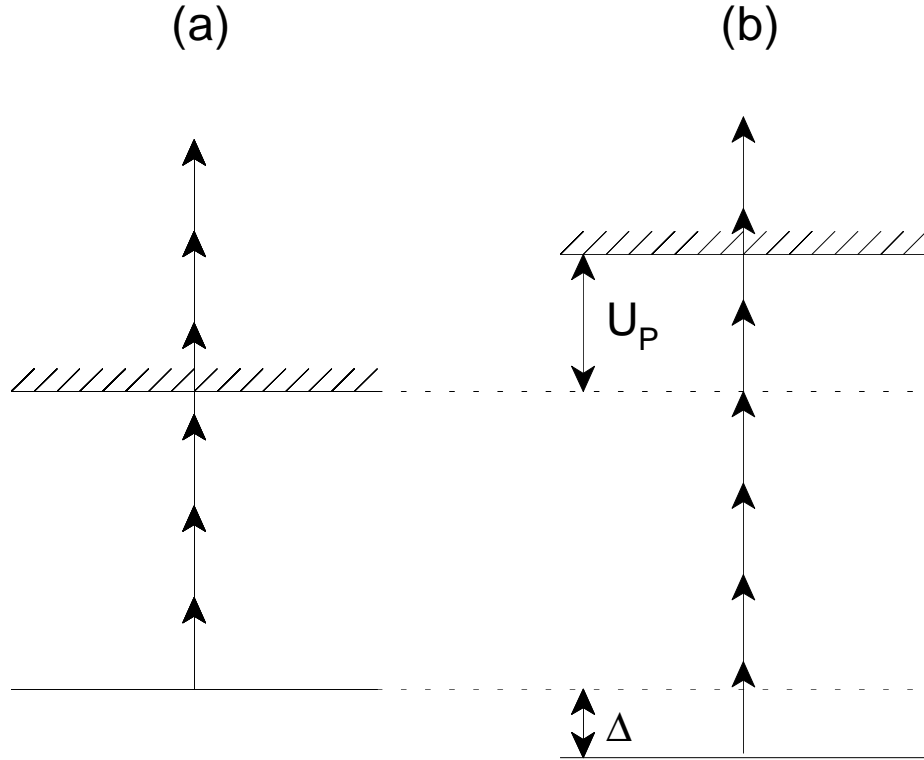


Figure 1.4: Schematic picture of an excess-photon ionization process in a low-frequency field at low intensity (a) and at high intensity (b). In Figure (a), the minimum number of photons N_0 to ionize the atom is $N_0 = 4$. For higher intensities, see (b), the ionization threshold is shifted upwards by the ponderomotive energy, and the real part of the energy of the initial state is shifted downwards by the AC-Stark shift Δ . As a result $N_0 = 6$ and the $n = 4$ and $n = 5$ ionization channels are closed, whereas at this intensity the ionization signal (not depicted) from the $n = 7$ channel is increased. (The energy scheme as depicted here is not gauge-invariant (see below); this picture is according the description of the atom-field interaction in the length gauge. In the velocity gauge the continuum threshold does not shift and the ground state shifts downwards over $P + \Delta$, so that the effect of channel closure is gauge independent.)

which is a function of the intensity through Δ_i and U_P . Since U_P increases linearly with the intensity and $P \gg \Delta_i$, the lowest order non-vanishing ionization channel will close as the intensity increases, see Figure 1.4. In literature, this effect is referred to as *channel-closure*. At the same time, as the intensity increases, new higher-order peaks appear. In Figure 1.5 the partial rates and total rate are given as a function of the intensity. Note that the total rate seems to follow the power law predicted by perturbation theory, whereas the partial rates do not. This illustrates the importance of measuring the photoelectron spectra (i.e. individual ionization channels) instead of the ion yield in order to obtain a correct physical picture of atoms in intense fields.

1.1.4 Short Pulse Effects

One of the major causes behind the increase in achievable laser intensities is the generation of short pulses. Whereas in the beginning of the laser evolution, pulse durations

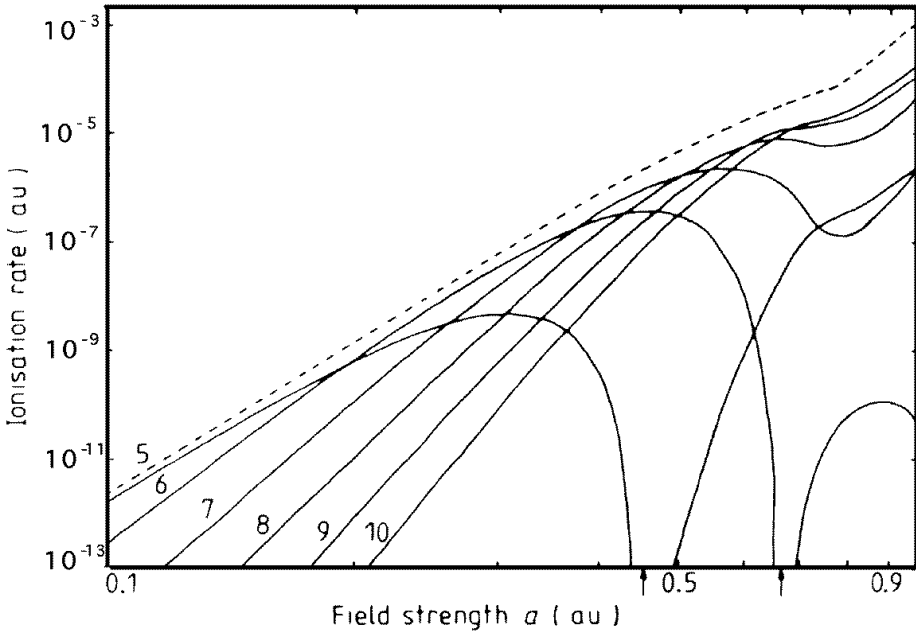


Figure 1.5: Partial rates for the absorption of various number of photons (indicated along curves) as a function of the field amplitude. The sum of the partial rates is represented by the dotted curve. Whereas the total rate suggests that perturbation theory is applicable, the curves of the partial rates illustrate a non-perturbative effect: the channel closure of the energetically lowest channels, occurring at a field amplitude indicated by the arrows (Results obtained from Muller *et al*, Ref.[45]).

were of the order of nanoseconds ($1\text{ns} = 10^{-9}$ sec), the shortest pulses today are of the order of 10 femtoseconds ($1\text{fs} = 10^{-15}$ sec). Since the number of photons in the pulse can be kept constant, the power in the pulse increases when the pulse duration gets shorter. The generation of short laser pulses is still one of the most challenging topics in laser physics. In addition to the effect of higher intensities, the generation of short laser pulses has revealed another interesting experimental field of interest. If an electron is ionized by a short pulse, it will not be accelerated by the ponderomotive force because the laser field has vanished before the photoelectron can escape the focal region. Due to the absence of the ponderomotive acceleration in a process involving short pulses, the photoelectron spectrum demonstrates the intensity dependence of the MPI process. This can be understood by considering the following (see also Figure 1.6). Due to the intensity dependence of the continuum threshold (see Eq.(1.5)), the photoelectron entering the continuum has a different kinetic energy at different intensities. Since in practice the intensity profile of a laser pulse is inhomogeneous in space and time, the kinetic energy of a photoelectron directly after ionization depends on where and when the atom was ionized. The AC-Stark shift of a loosely bound state (e.g. a Rydberg state) is roughly equal to U_P , because these states almost quiver as a free electron would do. This means that, if the initial state is tightly bound, a whole set of such loosely bound states shift in and out of resonance with the initial state as the intensity varies (see Freeman *et al*, Ref.[47]). Due to resonance enhanced multiphoton ionization, in case of short pulse durations, peaks appear in the photoelectron spectra at different positions corresponding to different resonant states. Since the frequency of the field is a known

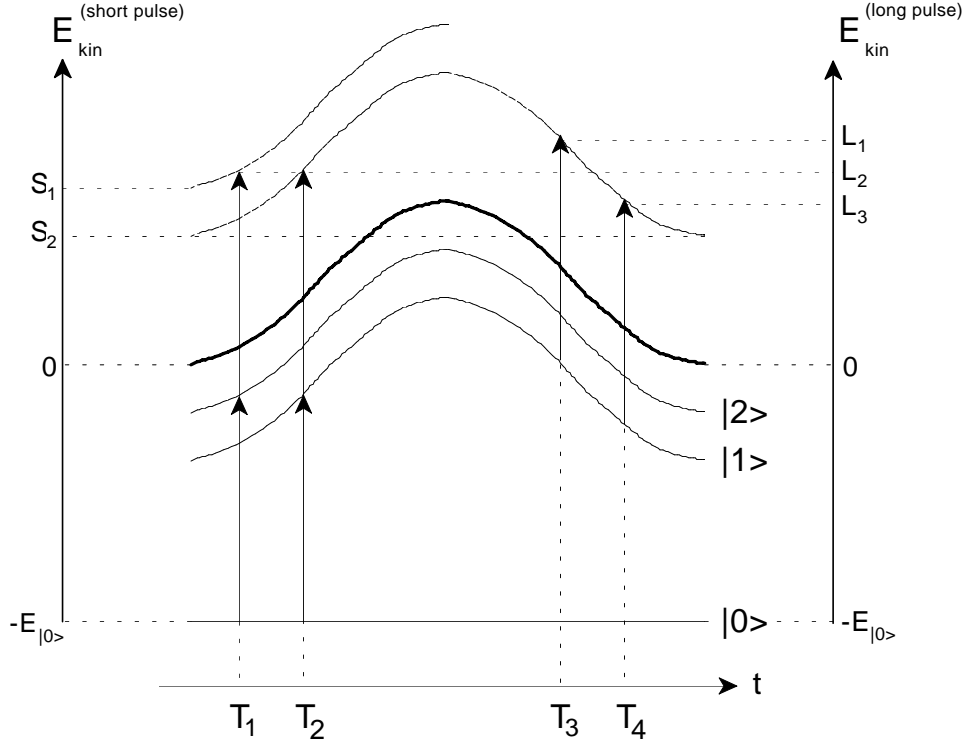


Figure 1.6: An illustration of the mechanism leading to photoelectron energy spectra corresponding to short laser pulses (left energy axis) and long laser pulses (right energy axis). The dark curve represents the continuum threshold during the laser pulse as a function of time. The states $|0\rangle$, $|1\rangle$ and $|2\rangle$ denote a tightly bound state (e.g. ground state) and two loosely bound states resp. Since the ponderomotive energy U_P is proportional to the intensity, the energy U_P a photoelectron can gain depends on the moment the ionization takes place and is therefore a function of time, $P(t)$. The loosely bound states have roughly the same ponderomotive shift as the continuum threshold. If state $|0\rangle$ is the initial state, the states $|1\rangle$ and $|2\rangle$ shift into resonance at time T_1 resp. T_2 . Due to the resonant enhancement, the photoelectron spectrum has peaks corresponding to these REMPI processes. The position of these peaks in the spectrum depends on the pulse duration. In case of long pulses, the peaks are located at the same position L_2 due to the different ponderomotive acceleration. Since in case of short pulses there is no time for the photoelectrons to be accelerated by the ponderomotive force, the positions of the peaks corresponding to the enhancement by different resonant states differ by $|P(T_1) - P(T_2)|$ and are located at S_1 and S_2 resp. In case the initial state is a loosely bound state the situation is the contrary since the binding energy now is time-independent (compare the ionization at time T_3 and T_4). For a short pulse, therefore, the peaks in the photoelectron spectrum are located at the same position, i.e. at S_2 . Since for long pulses the photoelectrons gain a different amount of ponderomotive energy, the positions of the peaks originating from ionization at T_3 and T_4 are separated by $|P(T_3) - P(T_4)|$ and are located at L_1 and L_3 respectively.

quantity, the position of a peak in the photoelectron spectrum determines the intensity at which the resonance yielding this peak was populated. If the pulse duration were long, however, these peaks would appear all at the same position in the energy spectrum. The reason for this is that the difference in kinetic energy immediately after the

ionization is balanced by the kinetic energy obtained by the ponderomotive acceleration while leaving the focus after the ionization. Compared to a tightly bound initial state, the situation with respect to the position of the peaks is the reverse if the initial state is loosely bound. Theoretically, Gontier [48] made predictions on this intensity dependence far before it was verified experimentally by Freeman *et al* [47] (see also Bucksbaum et al., Ref.[33]).

An advantage of the short pulse experiments is that the peaks are very narrow because the energy detected is simply an integer multiple of the photon energy minus the binding energy of the resonant state which is *intensity-independent*. For long pulses however, peaks resulting from ionization via these states are shifted towards higher energies due to the ponderomotive acceleration, which is *intensity-dependent*. Since the intensity varies slowly with time, the photoelectron does not gain exactly the ponderomotive energy corresponding to the intensity at which it was ionized. As a result, the peaks in the photoelectron spectrum are broadened.

1.2 General Description Atom-Field Interaction

The theoretical formalism treating the interaction between the atomic system and the radiation field can be set up in two ways. The first method is to describe both the field and the atom fully quantized. Using a quantized description for the field is useful as long as the number of photons in the field small, i.e. the field strength is weak. However, if the field strength increases, so does the number of photons in the field, and the commutator of the creation and annihilation operators of the radiation field can be approximated by zero. In that case, the field operators can be replaced by scalars, corresponding to a classical description of the radiation field. Since the atomic system requires a quantum mechanical treatment at any time, the method in which the field is described classically is often referred to as the semi-classical approach. The radiation fields related to the processes described in this Thesis are so strong that this semi-classical approach is applicable.

So for our purposes we can describe the field with a classical vector potential $\mathbf{A}(\mathbf{r}, t)$ and an electrostatic potential $\Phi(\mathbf{r})$. Considering the radiation source to be at infinite distance, one can set $\Phi(\mathbf{r}) = 0$ and from the Lorentz condition this leads to $\nabla \cdot \mathbf{A}(\mathbf{r}, t) = 0$. For a monochromatic classical radiation field with frequency ω , the vector potential $\mathbf{A}(\mathbf{r}, t)$ and corresponding electric field vector $\mathbf{E}(\mathbf{r}, t)$ are given by

$$\begin{aligned}\mathbf{A}(\mathbf{r}, t) &= \frac{c}{\omega} \text{Im}(A_0 \hat{\varepsilon} \exp(-i\omega t)) \\ \mathbf{E}(\mathbf{r}, t) &= \text{Re}(F_0 \hat{\varepsilon} \exp(-i\omega t)).\end{aligned}\quad (1.7)$$

Here F_0 is the electric field amplitude and c is the speed of light. Moreover, the unit vector $\hat{\varepsilon}$ is the complex polarization vector. Within this picture, the Schrödinger equation for a N -electron system in a monochromatic field reads

$$\left[\sum_{j=1}^N \frac{1}{2\mu} (\mathbf{p}_j - \mathbf{A}(\mathbf{r}, t))^2 + V_{at}(\mathbf{r}_1, \dots, \mathbf{r}_N) \right] \Psi(\mathbf{r}_1, \dots, \mathbf{r}_N; t) = i\hbar \partial_t \Psi(\mathbf{r}_1, \dots, \mathbf{r}_N; t). \quad (1.8)$$

Here the potential $V_{at}(\mathbf{R})$, with \mathbf{R} an abbreviation for $\mathbf{r}_1, \dots, \mathbf{r}_N$, contains the electron-electron interaction and the attraction between the electrons and the core.

In case the wavelength of the radiation is large compared to the spatial extension of the initial atomic state, the vector potential can be considered as space-independent. This approximation, better known as the *dipole approximation*, is similar to the assumption that on the scale of the size of the atomic system the phase of the radiation is constant in space, which implies that retardation effects can be neglected. However, it has been shown that for high-frequency fields with intensities in the non-perturbative regime the validity of the dipole approximation breaks down; different results for the ionization yield are obtained from calculations with and without a correction to the dipole approximation (see Bugacov *et al*, Ref.[49]). Moreover, at high intensities the velocity of the electrons in the fields can become so high that relativistic effects start to play a role. Including these effects leads to a completely different character of the states in the field, as pointed out by Krstic and Mittleman (see Refs.[50] and [51]).

In case the dipole approximation is applicable and an electron has left the volume of constant $\mathbf{A}(t)$, for example by ionization, spatial variation of the vector potential start to play a role in terms of ponderomotive forces. The effects of these forces on the energy spectrum and angular distribution are easily accounted for since the electron can be treated classically in that regime.

In the dipole approximation, the $\mathbf{A}^2(t)$ term in Eq.(1.8) can be eliminated by a simple unitary transformation

$$\Psi(\mathbf{R}; t) \longrightarrow \Psi^{(v)}(\mathbf{R}; t) = \Psi(\mathbf{R}; t) \exp \left[\frac{i}{\hbar} \frac{e^2}{2\mu c^2} \int_{-\infty}^t \mathbf{A}^2(t') dt' \right] \quad (1.9)$$

The Schrödinger equation for $\Psi^{(v)}$ is given by

$$\left[\sum_{j=1}^N \left(\frac{1}{2\mu} \mathbf{p}_j^2 - \frac{e}{\mu c} \mathbf{A}(t) \cdot \mathbf{p}_j \right) + V_{at}(\mathbf{R}) \right] \Psi^{(v)}(\mathbf{R}; t) = i\hbar \partial_t \Psi^{(v)}(\mathbf{R}; t). \quad (1.10)$$

The way the interaction between the field and the atom is described in Eq.(1.10) is according the so-called *velocity-* or *momentum gauge*. This nomenclature stems from the fact that the potential describing the coupling with the field, represented by the vector potential $\mathbf{A}(t)$, involves the momentum operator.

Let us return to Eq.(1.8) and multiply the electron wavefunction with the following phase factor

$$\Psi(\mathbf{R}; t) \rightarrow \Psi^{(l)}(\mathbf{R}; t) = \exp \left[i \frac{e}{\hbar c} \sum_{j=1}^N \mathbf{r}_j \cdot \mathbf{A}(t) \right] \Psi(\mathbf{R}; t) \quad (1.11)$$

Transforming the Hamiltonian according this unitary operator, the Schrödinger equation reads

$$\left[\sum_{j=1}^N \left(\frac{1}{2\mu} \mathbf{p}_j^2 - e \mathbf{E}(t) \cdot \mathbf{r}_j \right) + V_{at}(\mathbf{R}) \right] \Psi^{(l)}(\mathbf{R}; t) = i\hbar \partial_t \Psi^{(l)}(\mathbf{R}; t) \quad (1.12)$$

In contrast to Eq.(1.10), in Eq.(1.12) the coupling between the field and the electron involves the position operator \mathbf{r}_j instead of the momentum operator. Therefore, the representation of the coupling between the electron and field in the Schrödinger equation as in Eq.(1.12) is referred to as the *length gauge*. Combining Eqs.(1.9) and (1.11), it is clear that the wave vector in the length gauge is related to the corresponding wave

vector in the velocity gauge by

$$\Psi^{(l)}(\mathbf{R}; t) = \exp \left[i \frac{e}{\hbar c} \sum_{j=1}^N \mathbf{r}_j \cdot \mathbf{A}(t) - \frac{i}{\hbar} \frac{e^2}{2\mu c^2} \int_{-\infty}^t \mathbf{A}^2(t') dt' \right] \Psi^{(v)}(\mathbf{R}; t) \quad (1.13)$$

From Eqs.(1.8) through (1.13) we see that the term proportional to $\mathbf{A}^2(t)$ is included in the length gauge whereas it is not in the velocity gauge. In other words, the *cycle averaged energy* of a free electron in the length gauge is shifted upwards by the ponderomotive energy U_P (compare with Eq.(1.4))

$$U_P = \frac{e^2}{2\mu c^2} \int_0^{2\pi} \mathbf{A}^2(t') dt' = \frac{e^2 F_0^2}{4\mu\omega^2}. \quad (1.14)$$

Let us denote the energy shift of the initial state, i.e. its AC-Stark shift, as $\Delta_i^{(l)}$, where the superscript denotes the gauge in which the AC-Stark shift is evaluated. As long as the frequency is small compared to the energy spacing between the initial state and the lowest resonant state, $\Delta_i^{(l)} \ll P$. For higher frequencies and high intensities, cases of interest in this Thesis, the magnitude of the AC-Stark shift can become similar to that of U_P .

Despite the fact that the two gauges are theoretically equivalent because they stem from the same Schrödinger equation Eq.(1.8), in the numerical evaluation there can be differences between the two gauges. In principle, the result of a calculation of *any observable* should be independent of the gauge that is used in the calculation, i.e. the result should be *gauge-invariant*. For example, the energy difference between two atomic levels is an observable. As a consequence of Eq.(1.14) and the remark above it, the shift of each individual state is not gauge-invariant, and we have

$$\Delta_i^{(v)} = \Delta_i^{(l)} - U_P. \quad (1.15)$$

For the same reason the imaginary part of the energy parameter, $-\Gamma/2$, is a gauge-invariant quantity, since Γ/\hbar equals the inverse of the lifetime of the atomic state.

In highly non-perturbative situations, the advantage of the velocity gauge is that, compared to the length gauge, fewer angular momenta are involved. This can be understood with the following hand-waving argument. Due to the interaction with the intense field, the ionized electron quivers with a high velocity along a straight line with quiver momentum $\mathbf{A}(t)$. The number of l -states needed to represent the variation in angular momentum is proportional to $\Delta l \sim |r \times \Delta p| + |\Delta r \times p|$. In contrast to the velocity gauge, in the length gauge U_P varies with the quiver momentum $\mathbf{A}(t)$, inducing a variation in l which asymptotically diverges with r due to the $|r \times \Delta p|$ -term. In the velocity gauge this quiver momentum $\mathbf{A}(t)$ is eliminated (see Eq.(1.11)), thereby reducing the first term in Δl to zero. In addition, in both the length gauge and the velocity gauge the second term in Δl yields a finite contribution proportional to $\alpha_0 p$ due to the quiver motion. As a result, in the velocity gauge the number of l -states needed is smaller than in the length gauge, making the velocity gauge computationally favorable. As a matter of fact, gauge-invariance is frequently used by theoreticians to test the reliability of their calculation by solving the Schrödinger equation in both gauges and comparing the two results.

In the following, two different approaches will be discussed that are commonly used in order to obtain information about the evolution of an atom in an intense laser field. In particular these methods are used to calculate (multi)photon ionization rates. One

method is the Floquet method, a method in which the Schrödinger equation is solved in the frequency domain. Especially for potentials with temporal periodicity, like the potential describing the atom-field interaction, the Floquet method is very suitable. Another method is to solve the Schrödinger equation in the time domain. In this time-dependent picture, the Schrödinger equation is integrated using numerical methods.

1.2.1 Time-Dependent Calculations

From the start of the study of multiphoton processes in the 1960s time-dependent methods were developed to calculate the dynamics of an atom exposed to an intense laser field. One of the most important reasons for the initialization of these numerical studies is the fact that there was not a complete non-perturbative theory yet. One of the major advantages of these numerical methods is that for the numerical integration of the Schrödinger equation no assumptions need to be made about the relative strength of laser-atom and intra-atom interactions. Moreover, since the calculations involve the time-dependence of the laser field, the influence of the shape of the laser pulse can be investigated. In the time-dependent picture, the Schrödinger equation is solved by evaluating the wavefunction on a spatial grid and propagating the wavefunction in time in discrete time-steps. In principle, the accuracy of these calculations is limited by the spatial grid size and the temporal step size. Because of finite computer sizes (i.e. computer time and memory), these spatial and temporal steps can not be made arbitrary small. One of the major arts in this work is therefore to create numerical procedures that achieve the required accuracy with as large as possible step sizes.

In order to reduce the amount of memory space required by the calculation, numerous calculations have been performed on one-dimensional models. These so-called "numerical experiments" were employed in order to gain more insight in (multiphoton) ionization processes and proved to be very successful. The numerical experiments contain a model potential for a one-electron system, usually a simplification of the real potential: the electron is treated as spinless, relativistic effects are neglected and the binding potential is asymptotically treated as Coulombic. As one of the first, in 1978 Goldberg [52] studied single photon ionization from a square well containing one single bound state (see also Geltman (1977), Ref.[53] and Austin (1979), Ref.[54]). Later, many more one-dimensional calculations have been performed, the majority on atomic hydrogen (see for example Javanainen and Eberly [55], Eberly *et al* [56, 57], Collins and Merts [58], Bardsley and Comella [59], Reed and Burnett [60]). For a detailed overview on numerical experiments, see Eberly *et al* [61].

Results from a time-dependent calculation on a higher dimensional model were presented for the first time by Kulander [62], treating atomic hydrogen in a linearly polarized field. Due to symmetry properties (axial symmetry) this three-dimensional calculation, performed in the velocity gauge using cylindrical coordinates, reduces to a two-dimensional one. Low-order multiphoton ionization rates are calculated and compared with LOPT and experiment, with which excellent agreement is found. Later Kulander treated helium as well, integrating the time-dependent Hartree-Fock equations [63]. Even calculations on xenon were performed by Kulander, where he found excellent agreement with experimental rates [64]. However, in these calculations the grid size was too small to obtain information about partial rates for ionization into different continuum channels. A large grid is required in order to analyze the photoelectrons, since on a small grid the photoelectrons arrive at an absorbing wall, placed at the edge of the grid,

before the end of the laser pulse. This problem was solved by changing to spherical coordinates (see e.g. Refs.[65],[66],[67] and [68]). This change allowed for fewer grid points and therefore increased the maximum grid size. Moreover, using these coordinates it became possible to calculate angular distributions and probability amplitudes of excited states during or after the laser pulse.

Time-dependent calculations are also used to calculate the phenomenon of stabilization against photoionization in intense laser fields, a highly non-perturbative effect (for more details about stabilization, see below). It has been shown by numerical integration that the ionization rate of hydrogen excited states starts to *decrease* with *increasing intensity* as soon as the ponderomotive energy is roughly equal to the photon energy, see Pont and Shakeshaft, Ref.[69] (the results were confirmed by a high-frequency Floquet calculation, see below, by Vos and Gavrila, Ref.[70]). Pont and Shakeshaft performed this time-dependent calculation for various durations of the laser pulse. They showed that to see stabilization, a long pulse corresponding to a small bandwidth (small compared to the binding energy) is required in order to prevent ionization out of the excited states by Raman transitions to the continuum¹. In addition, Kulander [74] performed a similar type of time-dependent calculation for an atom in a short pulse high-frequency laser field and he observed adiabatic stabilization as well.

As a final remark concerning time-dependent calculations, I want to mention another reason, of importance in time-dependent calculations, namely why the length gauge is less favorable than the velocity gauge. This additional reason is related to the discrete time-propagation. In the time-propagation with time step τ , the propagation operator $\exp[-iH\tau/\hbar] = \exp[-i(H_{at} + V_{int})\tau/\hbar]$ is evaluated, where H_{at} and V_{int} are the atomic Hamiltonian and interaction potential resp.. For small time steps τ , the exponent in the time evolution can be approximated by its first order expansion, introducing an error of order $O([H\tau]^2)$ (This error however can be reduced to order τ^3 by applying the so-called "split operator" method, see for example Hermann and Fleck [75], Feit *et al* [76] and De Vries [77]). In the length gauge the interaction $V_{int}^{(l)} = e\mathbf{E}(t) \cdot \mathbf{r}$ increases linearly in r . Therefore $V_{int}^{(l)}$ gets large while the electron is ionized and drifts away out of the laser focus. In the velocity gauge $V_{int}^{(v)} = -\frac{e}{\mu c}\mathbf{A}(t) \cdot \mathbf{p}$ diverges in momentum space for large \mathbf{p} , but not as quick as the $\mathbf{p}^2/2\mu$ term in H_{at} does. As a consequence, in the ionization process the expectation value of the total Hamiltonian H increases more rapidly in the length gauge than in the velocity gauge. Since a large H forces the step size τ to be small in order not to induce large errors, the time needed for the computation is larger when it is performed in the length gauge.

¹In case the bandwidth is small, energy conservation prevents resonant transition from an excited state to an energetically lower lying state (i.e. low l and n). The probability density of the latter state is more pronounced close to the nucleus because of a lower centrifugal barrier and a smaller atomic orbit size. Since the momentum transfer required for ionization takes place near the nucleus, coupling with lower lying states would increase the ionization rate of the atom. Note that for states with high magnetic quantum number $m = l$, the excited state can not couple to low l -states since m is conserved in a radiation field (for a demonstration of this effect, see Pont and Shakeshaft, Ref.[69]). The stability of high- l states has another effect. If the initial state is tightly bound, the multiphoton-ionization rate is hardly enhanced if the initial state is coupled resonantly with a high- l state. This effect was found experimentally in the "Bielefeld experiment" by Rottke *et al*, Refs.[71],[72] and confirmed theoretically by Dörr *et al*, Ref.[73].

1.2.2 Time-Independent Calculations

The calculations presented in this Thesis are performed in the time-independent picture. Time-independent here means that the atom is exposed to a radiation field with *constant intensity* and stationary frequency. A method to transform the time-dependent Schrödinger equation into a time-independent problem is the Floquet method, described in more detail in the next Section². Radiation fields with time-independent intensities do not exist in practice, since they simply have to be switched on and off at a certain moment in time. It is therefore important to know about the assumptions made when applying Floquet theory in order to be able to compare its results with experiment. The present paragraph is devoted to this point.

As employed by Floquet theory, mathematically the transformation from a time-dependent problem to a time-independent one, can be performed if and only if the field is strictly monochromatic with time-independent frequency. This is equivalent to a field of which the intensity is constant in time. Under the assumption that the population of the initial state is not depleted completely in the field, the probability to find an electron in the initial state follows the law of exponential decay, i.e. it decays with a *constant rate*.

As mentioned above, in practice laser fields are pulsed fields, and therefore are not monochromatic but have a finite bandwidth. As long as the field is turned on and off sufficiently slowly, the band-width is small and the electron effectively interacts with a monochromatic field. Sufficiently slowly here means that the variation in intensity should be slow on the time scale set by the inverse of the electronic level spacing. In addition, the intensity should vary little during one light period, so that the notion of frequency is meaningful. In fields that vary slowly in time, the atomic states can adjust adiabatically to the applied field; the field is turned on and off adiabatically. Finally, in order to obtain results for a definite intensity, it is important that the spatial change in intensity is small on the scale of the De Broglie wavelength of the atom.

Even in case of fields that are switched on and off adiabatically, Floquet theory can lose self-consistency. Namely, if the lifetime of the atom calculated with Floquet theory is of the order of the period of the field, the frequency is not well defined. Especially in low-frequency fields this might cause a breakdown of the applicability of Floquet theory, as is shown by Shakeshaft *et al* [82].

An appropriate parameter determining the dynamics of the ionization process is the Keldysh parameter [18]. A low frequency field can be approximated by a static field if the period of the light field τ_{cyc} is very large compared to the characteristic atomic orbit time τ_{at} . In the static-field limit, a potential barrier is generated by the atomic potential and the instantaneous field. For tunneling to occur, the time τ_{tun} it takes to penetrate the barrier should be small compared to the cycle time. The Keldysh parameter γ is proportional to the ratio of the tunneling time and the cycle time, $\gamma \sim \tau_{tun}/\tau_{cyc}$ (see Shakeshaft, Ref.[83]). In case the Keldysh parameter is smaller than unity, the electron effectively feels a static field and will escape by tunneling through the barrier. The multiphoton ionization amplitude is very small in the low-frequency regime since the ionization process is a high-order process for these frequencies. Using

²Although this Thesis concentrates on Floquet theory applied to atomic systems, molecules have been studied as well using Floquet theory (see e.g. Bandrauk and McCann, Ref.[78], Giusti-Suzor *et al*, Ref.[79] and Bucksbaum *et al*, Ref. [80]). For an extended overview of time-independent calculations based on the Floquet ansatz I would like to refer to Potvliege and Shakeshaft in Ref.[81].

Floquet theory, Dörr *et al* [24] have calculated the ionization yield for an atom in an intense low-frequency field and their results were in agreement with the Keldysh theory (experimentally tunneling ionization has been studied by Augst et. al., Ref.[84]).

Floquet calculations are in good agreement with time-dependent calculations as long as these involve pulses that are switched on and off adiabatically. In practice this condition is fulfilled if the pulse contains about 10 optical cycles or more. See for example Pindzola and Dörr [85] and Schafer and Kulander [86]. In the static field limit, i.e. in low-frequency fields, calculations on the MPI process using Floquet theory (Shakeshaft, [82]) yield similar results as those obtained by numerical integration of the Schrödinger equation (Kulander, [64]).

If the field intensity is varied diabatically, the initial state, which is an eigenstate of the bare atomic Hamiltonian, is projected on the eigen states of the atom *in the field*. This may lead to population of highly excited states (and states of lower energy if the initial state was an excited state). This process is referred to as sudden shake-up or shake-down. Since in case of shake-up the initial state can be ionized suddenly, the atom does not survive enough optical cycles needed for the applicability of the Floquet ansatz.

The results from Floquet calculations can be compared with experimental data in two steps. In the first step, ionization rates are calculated for various intensities. Secondly, with knowledge about the temporal and spatial character of the laser pulse, these rates can be integrated over the pulse duration and spatial profile. In case of an adiabatically evolving field, this procedure reproduces a macroscopic ionization yield which can be compared with the experimental result. It should be noted that on their way to the detector, the electrons are accelerated by the ponderomotive force. In this region, the electrons are far away from the parent core moving in a slowly varying potential, and therefore can be treated classically. In case of short pulses, this effect will hardly influence the energy spectrum and angular distribution. In case of long pulses however, accurate knowledge about the pulse shape is required in order to reproduce the change in angular distribution due to the ponderomotive acceleration.

Part II

In the following three Sections we explore the theory on which the calculations presented in this Thesis are based, Floquet theory. We will start presenting the general concept of Floquet theory in Section 1.3.

In Section 1.4 it is illustrated how to apply Floquet theory in the calculation of the ionization rate and shift of the energy of an atom in a perturbative field using Rayleigh Schrödinger perturbation theory. With the expressions for the rate and shift obtained in both length and velocity gauge, we show the gauge-invariance for the observables. In addition, a method is described to use the terms of the perturbation series in order to calculate the energy in the non-perturbative regime, the *effective Hamiltonian* method.

Section 1.5 concludes Part II, describing high-frequency Floquet theory, applicable for fields intensities that lie beyond the perturbative regime. The Kramers-Henneberger frame is introduced, the frame of reference in high-frequency Floquet theory.

1.3 Floquet Theory

1.3.1 Floquet Ansatz

More than a century ago G. Floquet [87] developed a method to solve differential equations with *periodic properties*. Since the Schrödinger equation for any system exposed to an oscillating field is such a differential equation, Shirley [88] reformulated this Floquet method to describe the interaction between an atom or molecule and a radiation field (see also Ritus [89, 90], Zel'dovich [91, 92], Cohen-Tannoudji and Haroche [93]). The Floquet method transforms the *time-dependent Schrödinger equation* of an atom in a monochromatic radiation field with frequency ω and constant intensity I to an *infinite set of time-independent coupled differential equations*.

The time-dependent Schrödinger equation for a one-electron system reads

$$\left[\frac{1}{2\mu} \mathbf{p}^2 + V_{at}(\mathbf{r}) + V_{int}^{(g)}(\mathbf{r}, t) \right] \Psi(\mathbf{r}, t) = i\hbar \partial_t \Psi(\mathbf{r}, t) \quad (1.16)$$

where $\mathbf{p}^2/2\mu + V_{at}(\mathbf{r}) \equiv H_{at}$ is the atomic unperturbed Hamiltonian. $V_{int}^{(g)}$ is the gauge-dependent interaction Hamiltonian, which, in the dipole approximation, is given by

$$\begin{aligned} V_{int}^{(v)} &= -\frac{e}{\mu c} \mathbf{p} \cdot \mathbf{A}(t) \\ V_{int}^{(l)} &= -e \mathbf{r} \cdot \mathbf{E}(t) \end{aligned} \quad (1.17)$$

The Floquet ansatz consists of seeking solutions of Eq.(1.16) of the form

$$\Psi(\mathbf{r}, t) = e^{-iE(I)t/\hbar} \phi(\mathbf{r}, t), \quad (1.18)$$

where $\phi(\mathbf{r}, t)$ is a periodic function in t with period $2\pi/\omega$. Moreover, $E(I)$ is the complex cycle-averaged quasienergy of the ionizing state which can be written as³

$$E(I) = E_{at} + \Delta(I) - i \frac{\Gamma(I)}{2}. \quad (1.19)$$

³In principle the energy is a function of the field strength or vector potential. However, by shifting the origin of time by half a laser period, the field strength changes sign. Since the energy is independent of the origin of time, its expression can only contain even powers of the field strength, i.e. powers of the intensity.

In Eq.(1.19), $\Delta(I)$ is the real shift from the energy E_{at} of the unperturbed atom. From Eqs.(1.18) and (1.19) we see that the probability density is given by

$$e^{-\Gamma(I)t/\hbar} \langle \phi(\mathbf{r}, t) | \phi(\mathbf{r}, t) \rangle. \quad (1.20)$$

Therefore, apart from oscillatory behavior of frequency ω , the probability density decreases exponentially in time. The characteristic lifetime τ of the atom is given by \hbar/Γ . Since for physically meaningful solutions of the Schrödinger equation lifetimes can not be negative, Γ is a positive quantity.

Since both the interaction potential V_{int} and ϕ are periodic in time, they can be expanded in their time-independent Fourier components (with $\chi \equiv \omega t$)

$$\begin{aligned} \phi_n(\mathbf{r}) &= \frac{1}{2\pi} \int_0^{2\pi} e^{in\chi} \phi(\mathbf{r}, \chi/\omega) d\chi \\ V_n^{(g)}(\mathbf{r}) &= \frac{1}{2\pi} \int_0^{2\pi} e^{in\chi} V_{int}^{(g)}(\mathbf{r}, \chi/\omega) d\chi. \end{aligned} \quad (1.21)$$

Substituting Eqs.(1.18) and (1.21) into the time-dependent equation Eq.(1.16), the following set of time-independent coupled differential equations is obtained for the Floquet components ϕ_n ,

$$(E + n\hbar\omega - H_{at}(\mathbf{r})) \phi_n(\mathbf{r}) = \sum_{m=-\infty}^{+\infty} V_{n-m}(\mathbf{r}) \phi_m(\mathbf{r}), \quad (1.22)$$

where the superscript for the gauge is omitted in V_{n-m} .

1.3.2 Boundary Conditions

In order to define a solution of Eq.(1.22) boundary conditions for the harmonic components $\phi_n(\mathbf{r})$ in position space must be specified. With N_0 the minimum number of photons for which $\text{Re}(E) + N_0\hbar\omega > 0$, we expect the function ϕ_n for $n \geq N_0$ to obey the Siegert [94] boundary condition

$$\phi_n(\mathbf{r}) \rightarrow \frac{1}{r} f_n(\hat{\mathbf{r}}) \exp[i(k_n |\mathbf{r} - \alpha(t)| - \nu_n \ln 2k_n |\mathbf{r} - \alpha(t)|)] \text{ for } |\mathbf{r}| \rightarrow \infty. \quad (1.23)$$

The factor $\nu_n = Ze^2\mu/\hbar^2 k_n$ provides for the logarithmic distortion of the phase in case the potential has a Coulombic tail due to a remaining charge Z (for short range potentials, $Z = 0$). The angular asymptotic behavior is described by the ionization amplitude $f_n(\hat{\mathbf{r}})$.

The momenta $\hbar k_n$ in the boundary condition for the Floquet components can be expressed in terms of the quasienergy $E(I)$ of the initial state (see Eq.(1.19)), using the generalized Einstein equation

$$\frac{\hbar^2 k_n^2}{2\mu} = E + n\hbar\omega \equiv E_n. \quad (1.24)$$

Since the energy of those channels for which $n < N_0$ does not lie in the continuum, the corresponding ϕ_n does not contribute to the asymptotic current and therefore should vanish for $r \rightarrow \infty$. This can be accomplished with the boundary condition given in Eq.(1.23) by taking k_n complex, $k_n \equiv k'_n - ik''_n$. In terms of k'_n and k''_n we have for the

real and imaginary part of the energy $E_n = W_n - i\Gamma/2$,

$$\begin{aligned} W_n &= \frac{\hbar^2}{2\mu} (k_n'^2 - k_n''^2) \\ \Gamma &= \frac{2\hbar^2}{\mu} k_n' k_n''. \end{aligned} \quad (1.25)$$

The signs of k_n' and k_n'' now can be chosen such that ϕ_n decays exponentially as $r \rightarrow \infty$ for $n < N_0$. Let us define channels with $W_n > 0$ as *open channels* and those with $W_n < 0$ as *closed channels*. Open channels should obey outgoing wave behavior and therefore (see Eq.(1.23)) have $k_n' > 0$. Closed channels should decay exponentially as $r \rightarrow \infty$ and therefore have $k_n'' < 0$. Since Γ is a positive quantity the real and imaginary part of the momentum in the open and closed channels obey

$$\begin{aligned} k_n' &> k_n'' > 0 & \text{open channels} \\ k_n'' &< k_n' < 0 & \text{closed channels} \end{aligned} \quad (1.26)$$

This complex k_n , a result of obeying natural boundary conditions for *both* open and closed channels, is actually the reason for the energy to be complex in the Floquet picture, see Eq.(1.19). The complex energy is the price to be paid if one is looking for a stationary ionization solution of the Schrödinger equation Eq.(1.16).

For the open channels, the time-independent solution has some unphysical properties. As can be seen from Eq.(1.23), the quasienergy solution for $n \geq N_0$ is non-normalizable, since for the open channels $k_n'' > 0$. For an electron that is initially localized in a bound state, i.e. a square integrable state, this is an unphysical situation. Since the Hamiltonian describing the electron is Hermitian, the normalization integral should be constant. As the electron ionizes, the total probability to find the electron within a sphere of radius R decreases exponentially. This decrease has to be compensated by an increase in probability outside the sphere, expressed by the outgoing spherical waves represented by Eq.(1.23). The essential point here is the causality principle, saying that the outgoing wave is bounded by a wavefront at a distance $r_{\max} = \hbar k_n' t / \mu$. If restricted to a radius r_{\max} , the outgoing wave solution is a good representation of the decaying state, keeping the probability integral conserved.

1.3.3 Light-Induced States

If the sign of the momentum of the quasienergy solution obeys Eq.(1.26), its boundary condition is physically natural. However, by changing from k_n to $-k_n$ we still are dealing with a solution with quasienergy E_n , but with different boundary conditions. Since the energy E_n has a square root branch, see Eq.(1.24), the complex k -plane has to be divided into two halves in order to identify the solution uniquely. The way this division is made is fully arbitrary (see e.g. Ref.[95]). The solution with the boundary condition determined by k_n obeying Eq.(1.26) is called the "dominant" solution, all other states are referred to as "shadow" states or even "ghost" states (see Eden and Taylor, Ref.[96]). Due to the square-root singularity, for each channel the Riemann energy surface consists of two sheets. Since there infinitely many channels, there are infinitely many sheets. The sheet of which the negative real axis contains the poles of the bound states in the zero field limit is called the *physical sheet*, all other sheets are referred to as *unphysical sheets*. These sheets are coupled to each other by branch cuts. For each channel there is a branch cut, for channel m the branch cut starts at $E = m\omega$ in the complex energy plane

($m \in (-\infty, +\infty)$). The orientation of the branch cut in the energy plane is determined by the way the complex k -plane is divided into two.

The shadow- and dominant states correspond to poles of the multichannel scattering S-matrix (see the book by Taylor, [97], Chap.13, Sect. a and b). When the laser field is switched off, one would expect that all dominant and shadow states reduce to the states of the bare system. Indeed, it has been shown by Dörr and Potvliege [98] that at least one of the light-induced states in a one-dimensional Gaussian potential, found by Bardsley, Szöke and Comella [99], could be traced back to a true excited bound state in the zero field limit. In fact, in 1977 Ostrovskii [100] was the first who treated the shadow poles in connection with multiphoton processes, considering a one-dimensional zero-range potential that is periodic in time.

In zero field, the positions of the dominant pole and the shadow poles coincide, namely on the negative real energy axis in case of a bound state and just below the positive real energy axis in case of an autoionizing state. When the field is switched on, the poles start to move through the energy plane (along the real axis due to the ponderomotive shift and Stark shift, along the imaginary axis due to the finite decay probability in the field). If during this move induced by the field one of the shadow poles crosses a branch cut, this shadow pole becomes the dominant pole and might interchange role with the dominant pole (see Potvliege and Shakeshaft, Ref.[95]). In other words, states that have no physical boundary condition when the field is switched off (and therefore are practically undetectable), can become physical when the field is on. When a shadow pole becomes dominant in the field without replacing an existing dominant pole, a *light induced state* appears. The appearance of light-induced states plays an important role in this Thesis. The dynamics behind the appearance, however, i.e. the movement and interplay of the poles in the complex energy Riemann surface, is not part of the research described here. The role of the light-induced states has been investigated in the last few years and at the end of this Chapter we will come back to this issue.

1.4 Perturbation Theory in the Floquet Picture

For field strengths below the atomic unit it is natural to use perturbation theory in order to describe the interaction between the atom and the field. For a monochromatic field with constant intensity, the time-independent shift and width can be calculated in the Floquet picture. These can be extracted from the quasienergy that is found by solving Eq.(1.22). For such a field defined by Eq.(1.7), the Fourier expansion of the interaction potential $V_{int}^{(g)}$ (see Eq.(1.21)) consists of two terms $V_{n=\pm 1}^{(g)}$ only that are gauge-dependent,

$$\begin{aligned} V_{n=+1}^{(v)} &= -\frac{eF_0}{2i\mu\omega}\hat{\varepsilon} \cdot \mathbf{p} \\ V_{n=+1}^{(l)} &= -\frac{eF_0}{2}\hat{\varepsilon} \cdot \mathbf{r}, \end{aligned} \quad (1.27)$$

and with $V_{n=-1}^{(g)} = [V_{n=+1}^{(g)}]^\dagger$. Abbreviating these terms as V_\pm , the Schrödinger equation for the Floquet components ϕ_n , Eq.(1.22), can be rewritten as

$$(E_n - H_{at}(\mathbf{r}))\phi_n(\mathbf{r}) = V_-(\mathbf{r})\phi_{n+1}(\mathbf{r}) + V_+(\mathbf{r})\phi_{n-1}(\mathbf{r}). \quad (1.28)$$

Writing the ϕ_n as components of a vector Φ , this equation reduces to a matrix equation

$$\bar{\mathbf{H}}\Phi = E\Phi \quad (1.29)$$

where $\bar{\mathbf{H}}$ is a tridiagonal matrix with elements

$$\bar{\mathbf{H}}_{mn} = (H_{at} - m\hbar\omega)\delta_{mn} + V_+\delta_{m,n+1} + V_-\delta_{m,n-1}. \quad (1.30)$$

The problem of finding the quasienergy E , from which widths and shifts can be extracted, is now cast into the eigenvalue problem Eq.(1.29) involving the Floquet matrix $\bar{\mathbf{H}}$. In most of the Floquet calculations the elements ϕ_n of the Floquet wave vector Φ is spanned by a discrete basis set consisting of square integrable functions (Chu and Reinhardt (1977), Ref.[101]). A very successful type of basis functions to calculate the properties of multiphoton ionization processes with are products of spherical harmonics and complex Sturmians, introduced by Shakeshaft in 1986 (see Refs.[102] and [103]). Complex Sturmians are modified from the hydrogenic wavefunctions by replacing Z by the current charge of the nucleus and by allowing the wavenumber to be complex, the latter in order to describe both closed and open channels. Complex Sturmians are used for multiphoton processes in both the perturbative and the non-perturbative regime (for the latter, see e.g. Potvliege and Shakeshaft, Ref.[39]). With the basis set representation for the Floquet components, Eq.(1.29) can be solved using the so-called method of inverse iteration, see Maquet et al., Ref.[104].

1.4.1 Calculation of Widths and Shifts using Rayleigh-Schrödinger Perturbation Theory

For intensities in the non-perturbative regime, i.e. for small V_\pm , an adequate solution of Eq.(1.28) can be found by expanding the quasienergy and the harmonic components ϕ_n in powers of the field amplitude F_0 ,

$$\begin{aligned} E &= \sum_{k=0}^{\infty} F_0^{2k} E^{(2k)}, \\ \phi_n &= \sum_{k=0}^{\infty} F_0^k \phi_n^{(k)} \text{ or } \Phi = \sum_{k=0}^{\infty} F_0^k \Phi^{(k)} \end{aligned} \quad (1.31)$$

Since by definition the component ϕ_n describes a state that has exchanged n photons with the field, $\phi_n^{(k)} = 0$ for $n > k$. Let us define the field-independent quantities $v_\pm^{(g)} \equiv V_\pm^{(g)}/F_0$. By collecting powers of F_0 Eq.(1.28) reduces to the general perturbation equation (leaving both the superscript for the gauge and the \mathbf{r} -dependence)

$$(E + n\hbar\omega - H_{at}) \phi_n^{(k)} = v_+ \phi_{n-1}^{(k-1)} + v_- \phi_{n+1}^{(k-1)} - \sum_{l=1}^k E^{(k)} \phi_n^{(l-k)}. \quad (1.32)$$

Considering the zeroth-order term only ($k = 0$, and therefore $n = 0$) this equation reduces to

$$(E^{(0)} - H_{at}) \phi_0^{(0)} = 0. \quad (1.33)$$

The solution of this equation yields the unperturbed eigenstate $\phi_0^{(0)}$ of H_{at} with energy $E^{(0)}$. Increasing the perturbation order by one, we get (remember that $E^{(k)} = 0$ for k

odd, this is generally true for the dipole interaction)

$$(E^{(0)} \pm \hbar\omega - H_{at}) \phi_{\pm 1}^{(1)} = v_{\pm} \phi_0^{(0)}, \quad (1.34)$$

$$(E^{(0)} - H_{at}) \phi_0^{(1)} = 0. \quad (1.35)$$

The solution Eq.(1.35) is $\phi_0^{(1)} = 0$, because according to the boundary condition of perturbation theory the total wavefunction should converge to the unperturbed solution $\phi_0^{(0)}$ in zero field. This is in fact another way of saying that the ϕ_0 is normalized according $\langle \phi_0 | \phi_0^{(0)} \rangle = 1$ with $\phi_0^{(0)}$ a properly normalized eigenstate of H_{at} . To second order in F we get

$$(E^{(0)} + m\hbar\omega - H_{at}) \phi_m^{(2)} = v_+ \phi_{m-1}^{(1)} + v_- \phi_{m+1}^{(1)} - E^{(2)} \phi_m^{(0)}, \quad (1.36)$$

which yields five different equations for $m \in [-2, +2]$. An expression for the second order energy correction $E^{(2)}$ can be found from the equation for $m = 0$. Premultiplying both sides of Eq.(1.36) with the bra $\langle \phi_0^{(0)} |$ and using Eq.(1.33), the following expression for $E^{(2)}$ is found,

$$E^{(2)} = \sum_{s=\pm 1} \langle \phi_0^{(0)} | v_s | \phi_{-s}^{(1)} \rangle, \quad (1.37)$$

which is a standard result from Rayleigh Schrödinger perturbation theory.

This perturbation series can be extended to any order in F_0 . Results of calculations of $E^{(4)}$ for the negative hydrogen ion H^- are presented in Chapter 6 of this Thesis. Knowing $E^{(k)}$, the shift and width of the state in the field can be extracted from the real and imaginary part of $E^{(k)}$, which will be illustrated for the case of $E^{(2)}$ below.

1.4.2 Gauge Invariance

With the gauge dependence of $v_{\pm}^{(g)}$, the gauge invariance of the width and the gauge variance of the shift can be illustrated. To calculate $E^{(2)}$ we need an expression for $\phi_{\pm 1}^{(1)}$. The function $\phi_{\pm 1}^{(1)}$, obeying Eq.(1.34), can be expressed in term of the Greens' function $G(\mathbf{r}, \mathbf{r}', E \pm \hbar\omega)$, which is a solution of

$$(E^{(0)} \pm \hbar\omega - H_{at}) G(\mathbf{r}, \mathbf{r}', E^{(0)} \pm \hbar\omega) = \delta(\mathbf{r} - \mathbf{r}'). \quad (1.38)$$

Using Eq.(1.38), the solution of Eq.(1.34) can be written as (see Messiah, *Quantum Mechanics*, Ref.[105], Chap. XIX, § 5)

$$\phi_{\pm 1}^{(1)}(\mathbf{r}) = \int G(\mathbf{r}, \mathbf{r}', E^{(0)} \pm \hbar\omega) v_{\pm}(\mathbf{r}') \phi_0^{(0)}(\mathbf{r}') d\mathbf{r}' \quad (1.39)$$

This equation is similar to the operator equation (Messiah, Quantum Mechanics [105], Chap. XIX, § 10)

$$\left| \phi_{\pm 1}^{(1)} \right\rangle = \lim_{\varepsilon \downarrow 0} \frac{1}{E^{(0)} \pm \hbar\omega - H_{at} \pm i\varepsilon} v_{\pm} \left| \phi_0^{(0)} \right\rangle \quad (1.40)$$

Combining Eqs.(1.37) and (1.40) $E^{(2)}$ can be written as

$$E^{(2,g)} = \sum_{s=\pm 1} \left\langle \phi_0^{(0)} \left| v_s^{(g)} (E^{(0)} - s(\hbar\omega + i\varepsilon) - H_{at})^{-1} v_{-s}^{(g)} \right| \phi_0^{(0)} \right\rangle. \quad (1.41)$$

With the polarization axis along the z -axis, $\hat{\varepsilon} = \hat{\mathbf{z}}$, in the *velocity gauge* the expression for $E^{(2,v)}$ reads

$$E^{(2,v)} = \frac{e^2}{4\mu^2\omega^2} \sum_{s=\pm 1} \left\langle \phi_0^{(0)} \left| p_z (E^{(0)} - s(\hbar\omega + i\varepsilon) - H_{at})^{-1} p_z \right| \phi_0^{(0)} \right\rangle. \quad (1.42)$$

Introducing a complete set of eigenstates $|k\rangle$ of H_{at} with energy E_k and using the commutation relation $[H_{at}, z] = \frac{i\hbar}{\mu} p_z$, Eq.(1.42) can be re-expressed as

$$E^{(2,v)} = \frac{e^2}{4} \sum_k \frac{(E^{(0)} - E_k)^2}{\hbar^2\omega^2} \sum_{s=\pm 1} \left\langle \phi_0^{(0)} \left| z \frac{|k\rangle\langle k|}{E^{(0)} - s(\hbar\omega + i\varepsilon) - E_k} z \right| \phi_0^{(0)} \right\rangle. \quad (1.43)$$

In the *length gauge* $E^{(2,l)}$ is given by

$$E^{(2,l)} = \frac{e^2}{4} \sum_k \sum_{s=\pm 1} \left\langle \phi_0^{(0)} \left| z \frac{|k\rangle\langle k|}{E^{(0)} - s(\hbar\omega + i\varepsilon) - E_k} z \right| \phi_0^{(0)} \right\rangle. \quad (1.44)$$

The shift and width to second order in F_0 can now be calculated in both gauges by taking the real resp. imaginary part of Eqs.(1.43) and (1.44). For the evaluation of the real and imaginary parts of $E^{(2,g)}$ the following identities can be used,

$$\text{Re} \left[\frac{1}{E^{(0)} - s(\hbar\omega + i\varepsilon) - E_k} \right] = PV \left(\frac{1}{E^{(0)} - s(\hbar\omega + i\varepsilon) - E_k} \right) \quad (1.45)$$

$$\begin{aligned} \text{Im} \left[\frac{1}{E^{(0)} - s(\hbar\omega + i\varepsilon) - E_k} \right] &= -\frac{\varepsilon}{(E^{(0)} - s\hbar\omega - E_k)^2 + \varepsilon^2} \\ &= -\pi\delta(E^{(0)} - s\hbar\omega - E_k), \end{aligned} \quad (1.46)$$

where PV denotes the principal value part. Due to the $\delta(E^{(0)} - s\hbar\omega - E_k)$, the sum over k in Eqs.(1.43) and (1.44) reduces to $k = s$.

Since for $s = \pm 1$ the factor $(E^{(0)} - E_k)^2 / \hbar^2\omega^2 = 1$, the width $\Gamma^{(2)} = -2\text{Im } E^{(2)}$ is the same in both gauges, as already mentioned above. For the real part however, the shift $\Delta^{(2)}$ is not gauge invariant, but differs by the ponderomotive energy U_P (see the remark above Eq.(1.14)). Since the difference in shift between length and velocity gauge equals U_P for all energy levels, the energy spacing between two levels, an observable, is gauge-invariant, as it should be.

1.4.3 Resonant Ionization

In the beginning, perturbation theory using the Floquet ansatz was applied to calculate total ionization rates (Maquet [104]), but later as well for calculating ionization rates into different ionization channels (Crance *et al* [106]). With more effort even angular distributions of the detached electrons and partial rates have been calculated by Potvliege and Shakeshaft (see Refs.[107] and [108]). If compared to experimental results, partial rates and angular distributions obtained from calculations of MPI processes in intense fields for atomic hydrogen are very accurate except in regions where resonances play a role, i.e. near threshold (see Potvliege and Shakeshaft, Ref.[108]; for experimental comparison see Freeman *et al*, Ref.[47]). From Eqs.(1.43) and (1.44) we see that if the initial state is coupled resonantly with another eigenstate of H_{at} , such that $E^{(0)} - n\hbar\omega$ is very small, the convergence of the perturbation series is very weak (or it even diverges).

The Floquet ansatz remains applicable when resonant states play a role. However, it is important to keep track of the time scale on which these resonances are passed. At fixed frequency, the shift of the resonances changes roughly linearly with the intensity. Therefore, whether or not a state is resonant is determined by the instantaneous intensity which varies in time. The resonance is passed quickly if the intensity sweeps fast on the time scale set by the inverse of the Rabi coupling frequency Ω . In this case, the state follows the diabatic curve and it can be represented by a single "diabatic" Floquet wavefunction. As a result the ionization can be described by a single width obtained from the quasienergy of the diabatic state. For this situation, Breuer *et al* showed that close to resonances the ionization yield has non-monotonic structure (see Ref.[109]; the calculation was performed in the low-frequency regime with excited states of atomic hydrogen as the initial state). As mentioned before, the presence of resonant states leads to an enhanced ionization amplitude (a process referred to as REMPI). By varying the intensity, the initial state couples with various resonant states leading to strong peaks in the ionization signal, as shown by Dörr *et al* [73]).

In case the resonance is passed slowly on the scale Ω^{-1} , the avoided crossing is passed adiabatically and population transfer takes place between the different states. In this case, the atom has to be described by two Floquet states with time-dependent coefficients (see Ho and Chu, Ref.[110] and Potvliege and Shakeshaft, Ref.[111]). The ionization process can not be described with a single width anymore. To calculate the evolution of the wavefunction of the electron as the avoided crossing is passed, Landau Zener type formulas can be applied (see e.g. Szöke, Ref.[112] and Crance, Ref.[106]). The cases we will be interested in in the remainder of this Thesis involve photon energies that exceed the binding energy of the atom in the field. This implies that we are not dealing with the influence of resonances in the determination of the quasienergy.

1.4.4 Beyond Perturbation Theory; The Effective Hamiltonian

The Rayleigh Schrödinger perturbation theory as described above is successful for the description of atoms in perturbative fields. In the presence of resonances or for field strengths in the non-perturbative regime, the Rayleigh Schrödinger perturbation series, an expansion in powers of field strength F_0 , diverges. In order to describe the behavior of an atom in a field where perturbation theory breaks down, it is interesting to know the reason for the divergence of the series and how to circumvent this.

In general, a uniformly convergent series converges independent of its argument, i.e. everywhere in the complex plane. Moreover, a uniformly convergent series of analytic functions is differentiable everywhere, it has no singularities of any type. As a result, an analytical function without singularities can be represented by a uniformly convergent power series. A branch point is a point in the complex F -plane where two quasienergies coincide modulo an integer multiple of the photon energy $\hbar\omega$. This means that at a branch point the quasienergy $E(F)$ is not differentiable. In other words, when branch points are present, the quasienergy is not analytic everywhere. This means that its expansion in powers of F (which are analytic functions) has a finite radius of convergence.

Applying these results to Rayleigh Schrödinger perturbation theory, the radius of convergence of the perturbation series is determined by the branch point lying closest to the origin in the complex F -plane. Let us illustrate this with the following example. Consider a two level system with states $|1\rangle$ and $|2\rangle$. Let the energy of the unperturbed states be E_1 and $E_2 > E_1$ and consider a coupling potential V_{int} with strength F_0 . By

diagonalizing the Hamiltonian, the following eigenvalues E'_1 and E'_2 for the perturbed states $|1'\rangle$ and $|2'\rangle$ are found

$$E'_{1,2}(F_0) = \frac{E_1 + E_2}{2} \pm \left| \frac{E_1 - E_2}{2} \right| \sqrt{1 + \left(\frac{2F_0 V_{12}}{E_1 - E_2} \right)^2}. \quad (1.47)$$

Here the minus (plus) sign refers to state $|1\rangle$ ($|2\rangle$) and $V_{12} \equiv \langle 1 | V_{int} | 2 \rangle$. At the value of F_0 for which these eigen values coincide the quasienergy has a branch point. For this example, the branch points are located at

$$F_0^{(b)} = \pm i \frac{E_1 - E_2}{2V_{12}}. \quad (1.48)$$

As described above, the radius of convergence of the Rayleigh Schrödinger perturbation series is now equal to $|F_0^{(b)}|$. From Eq.(1.48) we see that if the energy spacing $E_1 - E_2$ of the unperturbed levels is large compared to the coupling V_{12} , the radius of convergence goes to infinity. On the other hand, if the perturbation is of the order of this energy spacing, the radius of convergence is very small and perturbation theory will yield poor results, a standard result from Rayleigh Schrödinger perturbation theory.

In order to check the result for the radius of convergence based on the position of the branch points, let us expand the square root in Eq.(1.47) in powers of the coupling strength F_0 ,

$$E'_{1,2}(F_0) = \frac{E_1 + E_2}{2} \pm \left| \frac{E_1 - E_2}{2} \right| \left[1 + \frac{1}{2} \frac{4F_0^2 V_{12}^2}{(E_1 - E_2)^2} - \frac{1}{4} \frac{16F_0^4 V_{12}^4}{(E_1 - E_2)^4} + \dots \right]. \quad (1.49)$$

We see that the series converges for $|F_0| < |(E_1 - E_2)/2V_{12}|$, in correspondence with the value given in Eq.(1.48).

In order to calculate quasienergies of an atom in non-perturbative fields, we have to increase the maximum field amplitude for which perturbation theory yields reliable results beyond $F_0^{(b)}$. There are several ways to achieve this. One of these is to invert the perturbation series using the coefficients from the Rayleigh Schrödinger perturbation series, yielding the field amplitude expressed in terms of the quasienergy (see M.G. Baik *et al*, Ref.[113]). The resulting equation for a particular field amplitude can be solved using the Padé summation method. Quasienergies at field amplitudes far into the non-perturbative regime can be calculated with this method, reproducing for example stabilization curves of atomic hydrogen.

Another method to calculate properties of the atom in a non-perturbative field, applied in Chapter 6 of this Thesis, is the so-called "effective Hamiltonian" method, explored by Shakeshaft *et al* (for an application, see M.G. Baik *et al*, Ref.[114]). Although the functions $\phi_n^{(k)}$ in the expansion of ϕ_n (see Eq.(1.31)) are part of a diverging series in the non-perturbative regime, they still carry information about the function ϕ_n and therefore can be used in order to obtain information about the atom in a non-perturbative field. Instead of using the Rayleigh Schrödinger perturbation expansion as in Eq.(1.31), one can expand ϕ_n on a finite basis spanned by the $\phi_n^{(k)}$, with $k \leq k_{\max}$, as

$$\phi_n = \sum_{k=0}^{k_{\max}} c_k(F_0) \phi_n^{(k)}. \quad (1.50)$$

Since $\phi_n^{(k)} = 0$ for $|n| < k$, the vector Φ reduces to a $(2n + 1)$ -dimensional vector and the Floquet Hamiltonian $\bar{\mathbf{H}}$ to a $(2n + 1)$ -dimensional matrix, cf. Eq.(1.29). Expanding the components of Φ on a discrete basis set (in general a set of products of Sturmians and spherical harmonics), this results in a generalized eigen value problem, which can be solved by using the inverse iteration method (see Maquet *et al*, Ref.[104]). The effective Hamiltonian method is applicable in non-perturbative regime as long as there are not too many resonances involved, since these can not be represented by the few states (k_{\max}) that are used in the expansion. By choosing the frequency such that it is large compared to the binding energy of the initial state this drawback is avoided. The method yields widths and shifts that are accurate in the high-frequency high-intensity regime, the accuracy being of the same order as for the inverted perturbation series.

1.5 High-Frequency Floquet Theory

1.5.1 The Kramers-Henneberger Frame

Apart from Rayleigh Schrödinger perturbation theory, in the previous Section methods are mentioned to calculate quasienergies in non-perturbative fields using results from the perturbation expansion. High-frequency Floquet theory (HFFT), developed by Gavrila and Kaminski in 1984 [115], is a theory that can be applied in the high-intensity regime which is independent of results from perturbation theory. For an overview on HFFT, see for example Gavrila in Ref.[116]. Before we proceed, let us turn back to the one-electron version of Eq.(1.10)

$$\left[\left(\frac{1}{2\mu} \mathbf{p}^2 - \frac{e}{\mu c} \mathbf{A}(t) \cdot \mathbf{p} \right) + V_{at}(\mathbf{r}) \right] \Psi^{(v)}(\mathbf{r}; t) = i\hbar \partial_t \Psi^{(v)}(\mathbf{r}; t). \quad (1.51)$$

HFFT proceeds from a space-translated version of Eq.(1.51)⁴, translated over $-\alpha(t)$,

$$\Psi^{(v)}(\mathbf{r}; t) = \exp \left[\frac{ie}{\hbar \mu c} \int_{-\infty}^t \mathbf{A}(\tau) \cdot \mathbf{p} d\tau \right] \Psi^{(KH)}(\mathbf{r}; t) = \exp \left[-\frac{i}{\hbar} \alpha(t) \cdot \mathbf{p} \right] \Psi^{(KH)}(\mathbf{r}; t). \quad (1.52)$$

This unitary transformation connects the laboratory frame with the so-called *Kramers-Henneberger frame*, the rest frame of a free electron, quivering along the trajectory $\alpha(t) = -\alpha_0 \operatorname{Re}(\hat{\varepsilon} \exp(-i\omega t))$ with the frequency of the radiation field. In other words

$$\Psi^{(v)}(\mathbf{r}; t) = \Psi^{(KH)}(\mathbf{r} - \alpha(t); t). \quad (1.53)$$

Since Eq.(1.52) is a unitary transformation, all observables in the lab-frame are equal to those in the Kramers-Henneberger frame. Defining $\mathbf{r}' \equiv \mathbf{r} - \alpha(t)$, the space-translated Schrödinger equation, i.e. the one in the Kramers-Henneberger frame, is of the form

$$\left[\frac{1}{2\mu} \mathbf{p}^2 + V_{at}(\mathbf{r}' + \alpha(t)) \right] \Psi^{(KH)}(\mathbf{r}'; t) = i\hbar \partial_t \Psi^{(KH)}(\mathbf{r}'; t). \quad (1.54)$$

⁴The idea of a space-translated Schrödinger equation was first proposed by Pauli and Fierz in 1938 [117]. Later it was applied in the renormalization of quantum electrodynamics by Kramers in 1956 [118] and finally, in 1968, in the context of laser-atoms interactions by Henneberger [119].

Similar to the velocity and length gauge, we expand $V_{at}(\mathbf{r}' + \alpha(t))$ in its Fourier components V_n ,

$$V_n(\alpha_0; \mathbf{r}') = \frac{1}{2\pi} \int_0^{2\pi} e^{in\chi} V_{at}(\mathbf{r}' + \alpha(\chi/\omega)) d\chi. \quad (1.55)$$

A special term that will be of great importance in this Thesis is the $n = 0$ term, which will be referred to as the "dressed potential". The dressed potential V_0 , given by

$$V_0(\alpha_0; \mathbf{r}') = \frac{1}{2\pi} \int_0^{2\pi} V_{at}(\mathbf{r}' + \alpha(\chi/\omega)) d\chi. \quad (1.56)$$

is the time-averaged of the space-translated Coulomb potential, averaged over one period of the radiation. In connection with laser-atom interactions, the dressed potential V_0 was used for the first time by Henneberger [119]. With this Fourier expansion the Schrödinger equation can be cast into an infinite set of coupled differential equations for the Floquet components $\phi_n^{(KH)}$,

$$[E + n\hbar\omega - H_0] \phi_n^{(KH)} = \sum_{m \neq n} V_{n-m} \phi_m^{(KH)}. \quad (1.57)$$

Here H_0 is the *dressed-potential Hamiltonian* $H_0(\alpha_0; \mathbf{r}) \equiv \mathbf{p}^2/2\mu + V_0(\alpha_0; \mathbf{r})$. Note that H_0 depends on the field only via the quiver amplitude α_0 . In the high-frequency limit it plays a dominant role as will be shown below.

In order to represent an atom that decays after photoionization, the Floquet components in the open channels should have outgoing wave behavior. The boundary condition for the $\phi_n^{(KH)}$ for $n \geq N_0$ (where N_0 is the minimum amount of photons needed to couple the initial state with the continuum) is given by

$$\phi_{n \geq N_0}^{(KH)}(\mathbf{r}) \rightarrow \frac{1}{r} f_n(\hat{\mathbf{r}}) \exp[i(k_n r - \nu_n \ln 2k_n r)] \text{ for } r \rightarrow \infty, \quad (1.58)$$

and for the closed channels the Floquet components decrease exponentially for large r ,

$$\phi_{n < N_0}^{(KH)} \rightarrow 0 \text{ for } r \rightarrow \infty. \quad (1.59)$$

Compared with the boundary condition in the laboratory frame, see Eq.(1.23), we see that the asymptotic behavior is simplified in the Kramers–Henneberger frame since the oscillatory behavior, proportional to $\alpha(t)$, does not need to be included.

1.5.2 High-Frequency Limit

1.5.2.1 Iteration Scheme

The transformation to the Kramers-Henneberger frame is useful in particular in the case of high frequencies. Because of rapid oscillations of the integrand in Eq.(1.55) in the limit $\omega \rightarrow \infty$, all Fourier components V_n are zero, except the dressed potential V_0 . As a consequence, in the high-frequency limit the Schrödinger equation Eq.(1.57) reduces to a homogeneous equation

$$[E + n\hbar\omega - H_0] \phi_n = 0 \quad (1.60)$$

The superscript (KH) is omitted for notational convenience. If the photon energy is large compared to the binding energy of the electron *in the field*, i.e. one-photon ionization is possible, the boundary condition for ϕ_n consists of an outgoing wave. In general we are interested in a state in the field that adiabatically evolves from a bound state

supported by the bare atomic Hamiltonian $H_{at} = \mathbf{p}^2/2\mu + V_{at}(\mathbf{r})$. If, at constant high frequency, the intensity decreases, the quiver amplitude goes to zero. In other words, in the high frequency limit the dressed-potential Hamiltonian H_0 converges to the atomic Hamiltonian as the intensity goes to zero. In the high-frequency limit the $n = 0$ channel is the only channel of which the Floquet component energetically can evolve adiabatically from an unperturbed atomic state and of which the Floquet component has a bound-state boundary condition. Therefore, for $\omega \rightarrow \infty$ and provided there are no avoided crossings between the initial bound state and the other Floquet components, ϕ_0 is the function to which a bound state of H_{at} evolves adiabatically when the field is switched on. As a result, in the high-frequency limit we have

$$\lim_{\omega \rightarrow \infty} \left\{ [E + n\hbar\omega - H_0] \phi_n = \sum_{m \neq n} V_{n-m} \phi_m \right\} \Leftrightarrow \begin{cases} [E - H_0] \phi_0 = 0 \\ \phi_{n \neq 0} = 0. \end{cases} \quad (1.61)$$

Using the Greens' function formalism, Eq.(1.57) can be cast into the form

$$\phi_n = \phi_0 \delta_{n0} + (1 - \delta_{n0}) G^{(+)}(E + n\hbar\omega) \sum_{m \neq n} V_{n-m} \phi_m, \quad (1.62)$$

where $G^{(+)}(E_n)$ is the resolvent operator of the dressed potential Hamiltonian. For *finite frequencies* the $V_{n \neq 0}$ are non-zero and the Floquet components $\phi_{n \neq 0}$ do get populated as they couple with ϕ_0 through Eq.(1.62). Moreover, for finite frequencies the zeroth order Floquet component obeys

$$[E - H_0] \phi_0 = \sum_{m \neq 0} V_{-m} \phi_m. \quad (1.63)$$

Equation (1.62) can be solved by iteration. Such an iteration procedure is useful only if it converges (rapidly). Iterating zero times, the Floquet components of channel $n \neq 0$ equal $\phi_{n \neq 0}^{(0)} = 0$. As a result the component from channel zero obeys

$$[E^{(0)} - H_0(\alpha_0; \mathbf{r})] \phi_0^{(0)} = 0, \quad (1.64)$$

where the superscript denotes the iteration number. Note that the equations obtained after zero iteration correspond to the limit for infinite frequencies, cf. Eq.(1.61). Since H_0 is Hermitian, its eigen value $E^{(0)}$ is real and will be denoted as W . We see that this equation is independent of the frequency and intensity explicitly and depends on the field only via the quiver amplitude $\alpha_0 = eF_0/\mu\omega^2$, included in the dressed potential. Therefore, W is a function of α_0 only, $W = W(\alpha_0)$. Moreover, the dressed potential Hamiltonian H_0 supports bound states that are attracted to a time-independent potential, V_0 . These bound states, denoted as $\Phi_0 \equiv \phi_0^{(0)} \in L^2$, can be properly normalized according

$$\langle \Phi_0 | \phi_0 \rangle = 1. \quad (1.65)$$

The eigenvalue equation for an atom in an intense radiation field involving the dressed potential, Eq.(1.64), was considered before by Gersten and Mittleman in 1976 [120] for bound states in the high-frequency regime.

After one iteration the Floquet component $\phi_{n \neq 0}$ is given by

$$\phi_n^{(1)} = G^{(+)}(W + n\hbar\omega) V_n \Phi_0 \equiv G_n^{(+)} V_n \Phi_0. \quad (1.66)$$

This equation can be cast into the following form

$$\phi_n^{(1)} = \sum_k \lim_{\varepsilon \rightarrow 0} \frac{|k\rangle}{W + n\hbar\omega - E_k + i\varepsilon} \langle k | V_n \Phi_0 \rangle, \quad (1.67)$$

where $|k\rangle$ denotes a complete set of eigenstates of H_0 with eigenvalues E_k . Now an important feature of HFFT becomes transparent: if $|k\rangle$ is a continuum state such that $W + n\hbar\omega - E_k$ is small for large frequencies, the matrix element on the right-hand side of Eq.(1.67) is extremely small due to the rapid oscillatory behavior of the continuum state. If on the other hand $|k\rangle$ is a bound state, the matrix element is roughly of order $O(1)$, but now the denominator is very large *for ω large compared to the energy spacing of the eigenstates of H_0* . Since for high frequencies the denominator is dominated by $n\hbar\omega$, the Greens' function scales as ω^{-1} in the high-frequency limit. As a result, $\phi_n^{(1)}$ is roughly a factor ω smaller than the zeroth order term $\phi_0^{(0)}$. Moreover, we see from Eq.(1.62) that by increasing the number of iterations, the number of Greens' functions increases, thereby picking up an additional factor $1/\omega$ after each iteration. Therefore, the higher the frequency the more rapid the convergence of the iteration procedure. The convergence of this iteration scheme has been tested with one-dimensional model calculations by Bardsley and Comella [59] and Bhatt et al. [121]. The convergence-test was performed in one dimension since these simplified models allow for an exact numerical solution.

The first order iteration formula for $\phi_0^{(1)}$ with help of Eq.(1.63) by collecting terms of the same order,

$$\begin{aligned} \phi_0^{(1)} &= \Phi_0 + G_0(W) \sum_{m \neq 0} V_{-m} \phi_m^{(1)} \\ &\equiv \Phi_0 + \Delta\phi_0^{(1)}. \end{aligned} \quad (1.68)$$

Writing the quasienergy as $E = W + \sum_{i=1}^{\infty} \Delta E^{(i)}$ the energy correction $\Delta E^{(1)}$, the lowest order correction in ω^{-1} , can be extracted from Eq.(1.63) using Eq.(1.67),

$$[W - H_0] \Delta\phi_0^{(1)} = \left[\sum_{m \neq 0} V_{-m} G_m^{(+)} V_m - \Delta E^{(1)} \right] \Phi_0. \quad (1.69)$$

Premultiplying both sides with the bra $\langle \Phi_0 |$, the right-hand side reduces to zero and the following expression is found for the lowest order energy correction,

$$\Delta E^{(1)} = \sum_{m \neq 0} \langle \Phi_0 | V_{-m} G_m^{(+)} V_m | \Phi_0 \rangle. \quad (1.70)$$

Note that $\Delta E^{(1)}$ has a non-zero imaginary part due to the presence of the resolvent operator $G_m^{(+)}$. So after one iteration the quasienergy becomes complex, in other words ionization sets in. From the real and imaginary part of $\Delta E^{(1)} = \Delta W^{(1)} - i\Gamma^{(1)}/2$, the real shift $\Delta W^{(1)}$ and the width $\Gamma^{(1)}$ can be calculated,

$$\begin{aligned} \Delta W^{(1)} &= \sum_{m \neq 0} \left\langle \Phi_0 \left| V_{-m} PV \left(\frac{1}{W + m\hbar\omega - H_0} \right) V_m \right| \Phi_0 \right\rangle \\ \Gamma^{(1)} &= 2\pi \sum_{m \neq 0} \langle \Phi_0 | V_{-m} \delta(W + m\hbar\omega - H_0) V_m | \Phi_0 \rangle. \end{aligned} \quad (1.71)$$

Let $\chi_{k_m}^{(-)}$ be a scattering solution of H_0 with energy $W_m = W + m\hbar\omega = \hbar^2 k_m^2 / 2\mu$ with k_m real (k_m is real, since W is the energy after zero iterations, i.e. $E^{(0)}$, which is real). If $\chi_{k_m}^{(-)}$ is normalized per unit solid angle with asymptotic amplitude 1, $\Gamma^{(1)}$ can be expressed in terms of $\chi_{k_m}^{(-)}$ as

$$\Gamma^{(1)} = \frac{\mu}{4\pi^2 \hbar^3} \sum_{m \neq 0} k_m \left| \left\langle \chi_{k_m}^{(-)} | V_m | \Phi_0 \right\rangle \right|^2. \quad (1.72)$$

Naturally the $m = 0$ channel is not included in this sum since in that channel the initial bound state Φ_0 is not coupled to the continuum. The choice of a natural boundary condition, i.e. an outgoing wave for the open channels, implies that k_m has a positive real part. Eq.(1.72) then shows that $\Gamma^{(1)}$ is positive and that the quasienergy E is complex as anticipated in Eq.(1.19).

Let us examine if the boundary condition of the Floquet components, obtained after one iteration, is obeyed (Note that since the solution after zero iterations is a L^2 function in the closed channel $n = 0$, it does obey the boundary condition Eq.(1.58)). Since in the high-frequency limit all channels $n \neq 0$ are open, the $\phi_n^{(1)}(\mathbf{r})$ should follow the asymptotic behavior described in Eq.(1.23). In order to check this, let us express Eq.(1.67) in coordinate space

$$\phi_n^{(1)}(\mathbf{r}) = \int G_n(\mathbf{r}, \mathbf{r}'; W_n) V_n(\mathbf{r}') \Phi_0(\mathbf{r}') d\mathbf{r}'. \quad (1.73)$$

From the asymptotic behavior of the Greens' function (see for example Messiah [105], Chap. XIX, § 13)

$$\lim_{|\mathbf{r}| \rightarrow \infty} G_n(\mathbf{r}, \mathbf{r}'; W_n) = -\frac{\mu}{2\pi\hbar^2} \frac{\exp[i(k_n r - \nu_n \ln 2k_n r)]}{r} \left[\chi_{k_n}^{(-)}(\mathbf{r}') \right]^*, \quad (1.74)$$

we obtain the following asymptotic behavior of $\phi_n^{(1)}(\mathbf{r})$,

$$\lim_{|\mathbf{r}| \rightarrow \infty} \phi_n^{(1)}(\mathbf{r}) = -\frac{\mu}{2\pi\hbar^2} \frac{\exp[i(k_n r - \nu_n \ln 2k_n r)]}{r} \left\langle \chi_{k_n}^{(-)} | V_n | \Phi_0 \right\rangle. \quad (1.75)$$

where $\chi_{k_n}^{(-)}$ is a scattering solution of H_0 as above. Comparison of Eqs.(1.58) and (1.75) indicates that Eq.(1.73) has the right asymptotic behavior. Moreover, combining Eqs.(1.58),(1.73) and (1.75) yields an expression for the n -photon ionization amplitude in channel n after one iteration,

$$f_n^{(1)}(\hat{\mathbf{r}}) = -\frac{\mu}{2\pi\hbar^2} \left\langle \chi_{k_n}^{(-)} | V_n | \Phi_0 \right\rangle. \quad (1.76)$$

The angle-integrated partial ionization rate in channel n is defined as

$$\Gamma_n^{(1)} \equiv \hbar k_n / \mu \left| f_n^{(1)}(\hat{\mathbf{r}}) \right|^2. \quad (1.77)$$

Inserting Eq.(1.76) into this expression for the $\Gamma_n^{(1)}$ we get

$$\Gamma_n^{(1)} = \frac{\mu}{4\pi^2 \hbar^3} k_n \left| \left\langle \chi_{k_n}^{(-)} | V_n | \Phi_0 \right\rangle \right|^2 \quad (1.78)$$

Comparing Eq.(1.72) with (1.78) we see that the width obtained from the ionization amplitude is equal to that obtained from the imaginary part of the energy parameter as it should be. Moreover these equations imply that the width can be expressed as a sum of partial widths of each channel, $\Gamma^{(1)} = \sum_{n \neq 0} \Gamma_n^{(1)}$. It should be mentioned here

that the sum over n only includes those n that correspond to open channels. However, in the high-frequency limit, $\hbar\omega$ is larger than the binding energy W of the initial state and therefore all channels $n \neq 0$ are open.

1.5.2.2 Limitations and Applications of HFFT

As mentioned above, for infinite frequencies the solution of the time-independent problem consists of an eigenstate of the dressed potential Hamiltonian with *real eigenvalue* $W(\alpha_0)$, obtained after zero iterations. In Floquet language this means that the Floquet state of the electron is described by the zeroth Floquet component $\phi_0^{(0)} = \Phi_0(\alpha_0)$. Moreover, its quasienergy E is real which implies that the atom does not decay. In this frequency domain, calculations are performed on the structure of atomic hydrogen. Although Φ_0 represents a non-decaying state, it is severely distorted, as is shown by Pont [122]. He also showed that this distortion depends strongly on the polarization of the field. For linearly polarized fields, the electronic wavefunction splits into two non-overlapping parts as the quiver amplitude α_0 increases. This phenomenon is referred to in the literature as *dichotomy* [123]. For circular polarization, the electronic wavefunction is smeared out along a torus with radius α_0 , referred to as *toroidal shaping* of the wavefunction [124]. In the high frequency regime people also treated more electron systems (for a treatment on the negative hydrogen ion H^- in a linearly polarized field, see for example Schertzer and Gavrila [125]).

In practice, however, the frequency is finite. It follows from the iteration procedure that for finite frequencies the iteration scheme is not converged after zero iterations and more iterations are required for an accurate description of the Floquet state and quasienergy. Whereas after zero iterations the Floquet state is dominated by Φ_0 , the Floquet components $\phi_{n \neq 0}$ start to play a role for finite frequencies. In addition, in higher order iteration the quasienergy becomes complex: in other words, ionization sets in. Although the importance of the Floquet components $\phi_{n \neq 0}$ compared to the Φ_0 increases as the frequency decreases from infinity to finite values, the iteration procedure shows that the zeroth order term is a good approximation as long as

$$\hbar\omega \gg |W(\alpha_0)|. \quad (1.79)$$

To test this high-frequency condition Marinescu *et al* [126] performed a one-dimensional model calculation at different frequencies. They calculated the quasienergy after zero and one iterations, i.e. $W(\alpha_0)$ and $W(\alpha_0) + \Delta E^{(1)}$ resp., and compared the results with a full Floquet calculation (i.e. solving Eq.(1.57) involving many channels n). For frequencies larger than roughly twice the binding energy the quasienergies obtained from the different approaches converge to the same value. For fixed frequency, the quasienergy converges to the high-frequency limit as α_0 increases. This can be understood considering the fact that the binding energy decreases rapidly as α_0 increases. Since at fixed frequency α_0 increases with the intensity, the high-frequency condition Eq.(1.79) is obeyed more easily at higher intensities.

While the intensity increases at fixed frequency, the iteration scheme converges more rapidly. Therefore, provided Eq.(1.79) is obeyed, the quasienergy is dominated more and more by the zeroth order term W_0 at higher intensities. Since W_0 is real, this implies that *the ionization rate decreases while the intensity increases*; the atom stabilizes against photoionization. This highly non-perturbative phenomenon is referred to as *adiabatic stabilization*. It demonstrates the opposite effect as predicted by Fermi's Golden Rule, an expression applicable for perturbative fields only. Stabilization was shown for

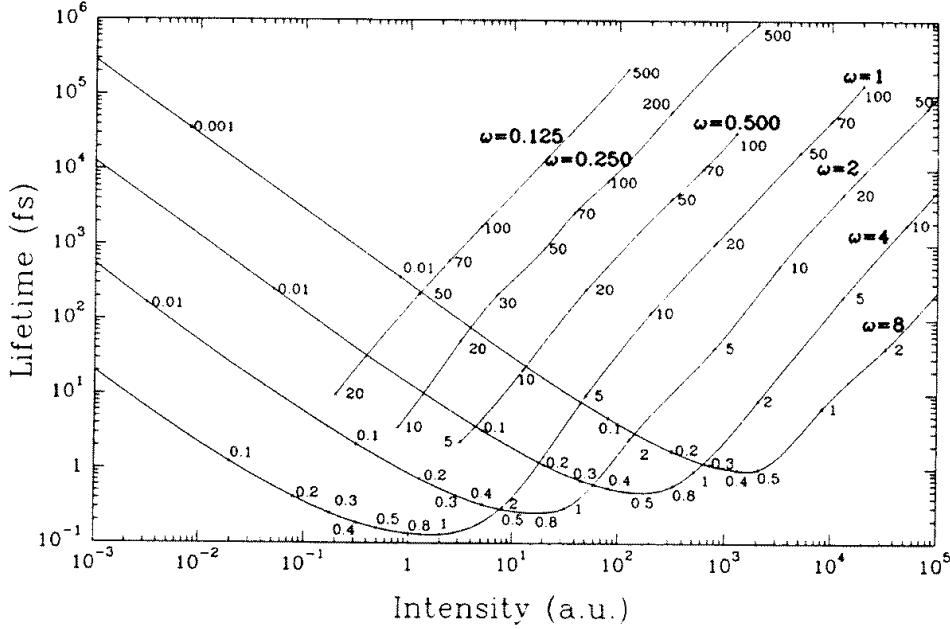


Figure 1.7: Lifetime of hydrogen in the ground state in a circularly polarized laser field for various frequencies as a function of the intensity. The numbers along the curves denote the corresponding value of α_0 . At a particular intensity the lifetime of the atom starts to increase with increasing intensity, entering the stabilization regime. Since the binding energy decreases rapidly with increasing α_0 , for lower frequencies the stabilization sets in at lower intensity, in correspondence with high-frequency theory. (Reproduced from Pont and Gavrila, Ref.[28])

the first time by calculations on the ground state of atomic hydrogen in a circularly polarized field by Pont and Gavrila [28], see Figure 1.7. Later, calculations were performed on Rydberg states of atomic hydrogen (see e.g. Vos and Gavrila, Ref.[70], Potvliege and Shakeshaft, Ref.[127]). Stabilization is also demonstrated using the inverted perturbation series method and the effective Hamiltonian method described above. The onset of stabilization has been confirmed experimentally in 1994 using Rydberg states of neon exposed to an intense circularly polarized laser field (see De Boer *et al* [128] and Van Druten *et al* [129]).

1.6 This Thesis

Before this Introduction is concluded with the outline of the Thesis, it is important to realize what gave the impulse for the work presented here. For this purpose we briefly recall the appearance of light-induced states, a phenomenon playing a role in highly non-perturbative fields.

1.6.1 High-Intensity Phenomena; Light-Induced States

In the last decade, several calculations have been performed indicating that, if exposed to a radiation field, an atom or ion does exhibit additional states. Additional in the sense that the number of states with physical boundary conditions (outgoing wave behavior for open channels and exponentially decaying functions for closed channels) in a situation in

which the field is switched on is larger than when it is switched off. In all cases analyzed so far, at their appearance the quasienergy of these new states is an integer multiple of the photon energy. This indicates that the appearance of these states corresponds to a shadow state that becomes dominant after passing an ionization threshold, without replacing an existing dominant pole. Since the appearance of these states is supported by the interaction between the atom and the field they are referred to as light-induced states.

The appearance of light-induced states has been studied with full Floquet calculations on one dimensional short range potentials (see Yao and Chu [130], Bardsley, Szöke and Comella [99], Bhatt, Pireaux and Burnett [121] and Fearnside, Potvliege and Shakeshaft [131]). In addition to these full Floquet calculations, they performed calculations in the high-frequency regime involving the dressed-potential Hamiltonian H_0 , see Eq.(1.64). Comparison between the full Floquet calculation and a high-frequency calculation shows that the real part of the quasienergy obtained from the full Floquet calculation lies very close to the real energy W of a new bound state supported by H_0 . The appearance of a bound state in the dressed potential coincides with that of a light-induced state in the full Floquet calculation. For example, Fearnside *et al* [131] showed that a shadow pole of the ground state of atomic hydrogen becomes dominant and converges to the ground state of the dressed potential as the frequency increases⁵. In general, new bound states of H_0 are the high-frequency limit of light-induced states that have a complex quasienergy. Conversely this is not always true. Therefore, the appearance of new bound states based on a high-frequency calculation predict the appearance of a light-induced state with a complex quasienergy. It should be noted that the existence of light-induced states is yet to be confirmed by experiment.

With a calculation including electron correlation, Muller and Gavrila [133] demonstrated the appearance of excited states of the negative hydrogen ion H^- in the high-frequency limit. In Figure 1.8 the appearance of the excited states is illustrated, more and more bound states coming in as the quiver amplitude α_0 increases. Although H^- supports one loosely bound state only, an intense radiation field apparently can change the structure of nature such that new electronic configurations become possible. For higher intensities the original structure of the ion is distorted so dramatically that more states shift onto the sheet with the right physical boundary conditions.

The appearance of light-induced states in the high-frequency limit is one of the main motives for the research presented in this Thesis. We investigate the possibility of the appearance of bound states of the dressed-potential Hamiltonian for *a system that does not support bound states in the absence of the radiation field*. An example of such a system is an atomic multiply charged negative ion (AMCNI) of hydrogen.

1.6.2 Outline

To be able to perform the numerical calculations involving the dressed-potential Hamiltonian described in Chapters 3 and 7, we developed a new computer program. The methods in this code that are used to perform these calculations is described in Chapter 2.

In the first part of the Thesis, consisting of the Chapters 3 through 5, we describe the appearance of bound states of atomic multiply charged negative ions (AMCNI) of

⁵In literature this state is referred to as the $1s'$ state. For full Floquet calculations on hydrogen in the high-frequency limit, see also Dörr *et al*, Ref.[132].

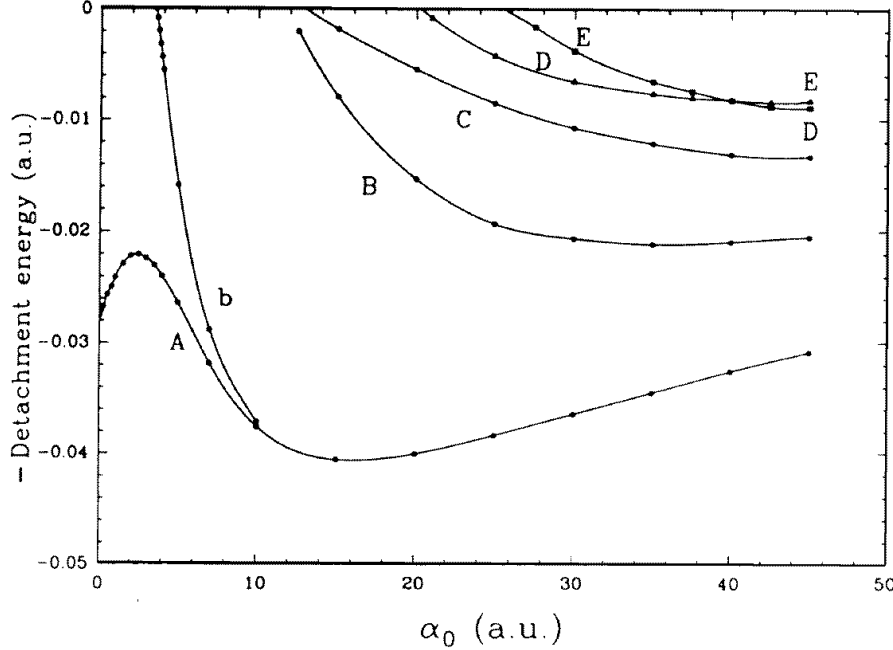


Figure 1.8: Negative of the detachment energy of the ground state (A) and new bound states (B-E) of the negative ion of hydrogen H^- , calculated in the high-frequency limit as a function of α_0 . These new bound states are the high-frequency limits of light-induced states. (Reproduced from Muller and Gavrila, Ref.[133])

hydrogen. The calculations presented in these Chapters are performed in the high-frequency limit, using the dressed-potential Hamiltonian. They therefore yield bound states that are the high-frequency limit of light-induced states. In the high-frequency limit, the underlying physics is described completely by the quiver amplitude α_0 . The laser conditions for the appearance of bound states of AMCNI therefore are determined by this parameter. As we will see, above a certain value of α_0 , called the *appearance value* for reference, bound states appear in the spectrum of the AMCNI.

In Chapter 3 the appearance of the simplest AMCNI of hydrogen, H^{2-} , induced by a linearly polarized monochromatic laser field is presented⁶. This appearance is founded with a Hartree calculation. The structure and spectrum of the ion is discussed.

In Chapter 4 we present an analytical treatment of AMCNI of hydrogen induced by circularly polarized fields. We show that, based on HFFT, bound states of AMCNI of hydrogen appear with up to 4 electrons. The laser parameters required for the appearance are listed, indicating that the creation of AMCNI of hydrogen might be realized experimentally at moderate laser intensities and in a frequency domain that lies within physical reach.

The case of linear polarization, treated numerically in Chapter 3, is extended with an analytical description in Chapter 5. In this Chapter, similar to the circular case, the appearance values are determined as well as the binding energy as a function of α_0 .

In the second part of this Thesis, consisting of the Chapters 6 and 7, we go one step further in determining the energy of hydrogen ions exposed to a laser field. This Part

⁶Evidence for a resonance state of H^{2-} is presented (1997) by Sommerfeld *et al*, see Ref.[134]). This evidence is contradicted recently by Morishita *et al* [135]. Besides, earlier calculations performed by Robicheaux *et al* [136] also show evidence of the nonexistence of H^{2-} resonances.

differs from the first one in the fact that we do not concentrate only on the real part of the energy but calculate the complex quasienergy of the ion from which ionization or detachment rates can be extracted.

In Chapter 6 multiphoton multiple ionization rates of H^- are calculated using a formalism including electron correlation in both the initial and the final state⁷. In both the perturbative and the non-perturbative regime rates are obtained. In the perturbative regime, Rayleigh Schrödinger perturbation theory is applied. We obtain accurate results for the quasienergy in second and fourth order perturbation theory. For the non-perturbative calculations, we used the effective Hamiltonian method as described in Section 1.4. Using this method, calculations far into the non-perturbative regime can be performed, yielding adiabatic stabilization curves.

In Chapter 7 we go beyond the high-frequency limit. We present a method to calculate to lowest order in ω^{-1} the energy correction to the high-frequency result. This correction yields a complex quasienergy from which detachment rates are extracted. The method is tested by applying it to atomic hydrogen for which ionization rates are known in the high-intensity high-frequency regime. As an application, detachment rates of H^{2-} in a linearly polarized laser field are calculated.

As a final remark we mention that we use atomic units throughout this Thesis, unless stated otherwise.

⁷The work described in this Chapter is performed in collaboration with the group of Robin Shakespeare at the University of Southern California in Los Angeles.

2

NUMERICAL METHODS

This Chapter comments on the routines and methods used in order to calculate the wavefunction and quasienergy of the simplest AMCNI of hydrogen, H^{2-} . These calculations, based on a *basis set method*, are applicable for calculations on H^{2-} induced by *linearly polarized* laser fields. Firstly, in Section 2.1, the code for calculating the zeroth order Floquet component of the wavefunction and the corresponding real quasienergy (see Chapter 1) is described. The application and its results of this routine are presented in Chapter 3. In Section 2.2 the method for calculating the complex quasienergy, from which the lifetime of H^{2-} is extracted, is evaluated. The results from the latter calculation are presented in Chapter 7.

2.1 Bound State Calculation

In this Section the method applied to find the solution of the structure equation for the zeroth order Floquet component $\phi_0^{(0)}$ of the N -electron wavefunction, obtained after zero iterations (for the iteration procedure in the high-frequency limit, see Chapter 1, Eq.(1.33)). This equation, which mathematically coincides with the structure equation obtained in the limit $\omega \rightarrow \infty$, reads

$$(E^{(0)} - H^{(N)})\phi_0^{(0)} = 0. \quad (2.1)$$

Here the N -electron Hamiltonian $H^{(N)}$ is given by

$$H^{(N)} = \sum_{i=1}^N \left[\frac{1}{2} \mathbf{p}_i^2 + V_0(\alpha_0; \mathbf{r}_i) + \sum_{j=1}^{i-1} \frac{1}{r_{ij}} \right], \quad (2.2)$$

where $r_{ij} = |\mathbf{r}_i - \mathbf{r}_j|$. Before explicit calculations involving the Hamiltonian will be discussed below, the method of finding the optimal basis-set representation for $\phi_0^{(0)}$ is described. In what follows, N is taken to be 3 and will be omitted for notational convenience.

2.1.1 The Generalized Eigenvalue Problem

Since the Hamiltonian is Hermitian, Eq.(2.1) supports real eigenvalues. This implies that the solution $\phi_0^{(0)}$ is a square-integrable function and can be represented by a basis set consisting of L^2 functions. Specifying basis function j as χ_j , the basis-set representation for $\phi_0^{(0)}$ constructed by N basis functions is: $\phi_0^{(0)} = \sum_{j=1}^N c_j \chi_j$, where c_j are real coefficients. With this notation for $\phi_0^{(0)}$, Eq.(2.1) can be written as an equation for the

N -dimensional vector $\mathbf{c} = (c_1, \dots, c_N)$,

$$\underline{\mathbf{H}} \mathbf{c} = E^{(0)} \underline{\mathbf{S}} \mathbf{c}. \quad (2.3)$$

Here $\underline{\mathbf{H}}$ and $\underline{\mathbf{S}}$ are $N \times N$ matrices, whose elements H_{ij} and S_{ij} are given by

$$\begin{aligned} H_{ij} &= \langle \chi_i | H | \chi_j \rangle \\ S_{ij} &= \langle \chi_i | \chi_j \rangle. \end{aligned} \quad (2.4)$$

Eq.(2.3) is the generalized eigenvalue problem for the function $\phi_0^{(0)}$ and the eigenvalue $E^{(0)}$ belonging to it. After transforming the basis set to an orthonormal one, the generalized eigenvalue problem can be solved by diagonalizing the matrix $\underline{\mathbf{H}}$, yielding the coefficients c_j and eigenvalue $E^{(0)}$.

In general, in solving the generalized eigenvalue problem one encounters numerical problems while calculating a basis-set representation in case there exist no orthogonality relations for the basis functions. In absence of such relations the basis functions can become linearly dependent, in particular for larger basis-set representations. As a result the overlap matrix tends to become singular leading to loss of accuracy. This problem can be circumvented by incorporating a procedure that avoids the choice of a basis function that is almost linearly dependent on the basis functions already chosen. A way to do this is to add a small fraction of the diagonal of the overlap matrix to the Hamiltonian,

$$\underline{\mathbf{H}} \rightarrow \underline{\mathbf{H}}' = \underline{\mathbf{H}} + \varepsilon \text{Diag}\{\underline{\mathbf{S}}\}. \quad (2.5)$$

The eigenvalue one obtains this way is equal to $E^{(0)} + \delta E^{(0)}$. If the basis set is diagonalized by the matrix $\underline{\mathbf{D}}$ and subsequently normalized with a diagonal matrix $\underline{\mathbf{N}}$ (such that $\underline{\mathbf{N}} \underline{\mathbf{D}} \underline{\mathbf{S}} \underline{\mathbf{D}}^\dagger \underline{\mathbf{N}}^\dagger = I$), the energy correction $\delta E^{(0)}$ is given by

$$\delta E^{(0)} = \varepsilon \underline{\mathbf{N}} \underline{\mathbf{D}} \text{Diag}\{\underline{\mathbf{S}}\} \underline{\mathbf{D}}^\dagger \underline{\mathbf{N}}^\dagger. \quad (2.6)$$

Since ε is a small number, typically of the order of $O(10^{-10})$, in general the energy correction induced by solving the eigenvalue problem for $\underline{\mathbf{H}}'$ is negligible. However, if one adds a basis function that is almost linearly dependent with the other functions in the representation, the normalization matrix contains a very large element. As a result, by adding this function, the energy correction $\Delta E^{(0)}$ will, even after multiplication with ε , yield a large positive contribution to the energy. Since a basis-set calculation in general determines an upper-limit for the energy of the state one is interested in, using this procedure it is not favorable to add a function that is linearly dependent. In the next paragraph the procedure that determines which linear combination of basis functions represents $\phi_0^{(0)}$ the best is explained.

2.1.2 Optimization Procedure

Since the Hamiltonian H supports more than one bound state, all with a different spatial character, the choice of basis functions for the representation for $\phi_0^{(0)}$ depends strongly on which bound state one is interested in. In general, let us write state $k \leq M$ represented by M basis functions as $\Psi_M^{(k)}$. Optimizing the representation for state k , the best function from the basis set to add as the $(M+1)$ -st one is that function that minimizes the k -th lowest energy.

Suppose that we want to calculate the energy and wavefunction of state k with N basis functions, i.e. $E_N^{(k)}$ resp. $\Psi_N^{(k)} \equiv \mathbf{c}_N^{(k)} \cdot \chi^{(k)}$. Moreover, suppose that at a certain

stage in the calculation, the wavefunction is represented by $M < N$ basis functions and coefficients. Since H is Hermitian, its eigenfunctions are orthogonal, giving

$$\left\langle \Psi_M^{(k)} | \underline{\mathbf{S}} | \Psi_M^{(l)} \right\rangle = \delta_{kl}. \quad (2.7)$$

For the Hamiltonian one has

$$\left\langle \Psi_M^{(k)} | \underline{\mathbf{H}} | \Psi_M^{(l)} \right\rangle = E_M^{(k)} \delta_{kl}. \quad (2.8)$$

For the optimal representation of $\Psi^{(k)}$ by $M + 1$ basis functions, one can add χ_{M+1} as an arbitrary trial function. On the basis spanned by the eigenvectors of the M -dimensional problem and the basis function χ_{M+1} , i.e. $\{\Psi_M^{(1)}, \dots, \Psi_M^{(M)}, \chi_{M+1}\}$, the generalized eigenvalue problem Eq.(2.3) is given by

$$\begin{pmatrix} E_M^{(1)} & & a_M^{(1)} \\ & \ddots & \vdots \\ & & E_M^{(M)} & a_M^{(M)} \\ a_M^{(1)} & \dots & a_M^{(M)} & H_{M+1,M+1} \end{pmatrix} \mathbf{q}_{M+1} = E_{M+1}^{(k)} \begin{pmatrix} 1 & & b_M^{(1)} \\ & \ddots & \vdots \\ & & 1 & b_M^{(M)} \\ b_M^{(1)} & \dots & b_M^{(M)} & S_{M+1,M+1} \end{pmatrix} \mathbf{q}_{M+1}, \quad (2.9)$$

where

$$\begin{aligned} a_M^{(l)} &\equiv \left\langle \Psi_M^{(l)} | \underline{\mathbf{H}} | \chi_{M+1} \right\rangle \\ b_M^{(l)} &\equiv \left\langle \Psi_M^{(l)} | \underline{\mathbf{S}} | \chi_{M+1} \right\rangle, \end{aligned} \quad (2.10)$$

and

$$\begin{aligned} H_{M+1,M+1} &\equiv \left\langle \chi_{M+1} | \underline{\mathbf{H}} | \chi_{M+1} \right\rangle \\ S_{M+1,M+1} &\equiv \left\langle \chi_{M+1} | \underline{\mathbf{S}} | \chi_{M+1} \right\rangle. \end{aligned} \quad (2.11)$$

The vector \mathbf{q}_{M+1} now contains the coefficients of the M eigen vectors of the M -dimensional problem and the coefficient of χ_{M+1} , $\mathbf{q}_{M+1} \equiv (q_M^{(1)}, \dots, q_M^{(M)}, q_{M+1})$. Eq.(2.9) leads to the following equations for the coefficients $q_M^{(l)}$ and q_{M+1} ,

$$\begin{aligned} (E_M^{(l)} - E_{M+1}^{(k)}) q_M^{(l)} + (a_M^{(l)} - E_{M+1}^{(k)} b_M^{(l)}) q_{M+1} &= 0 \\ \sum_{l=1}^M (a_M^{(l)} - E_{M+1}^{(k)} b_M^{(l)}) q_M^{(l)} + (H_{M+1,M+1} - E_{M+1}^{(k)} S_{M+1,M+1}) q_{M+1} &= 0. \end{aligned} \quad (2.12)$$

Eliminating the $q_M^{(l)}$ from Eq.(2.12), an equation is obtained for the coefficient of χ_{M+1} ,

$$-\sum_{l=1}^M \frac{(a_M^{(l)} - E_{M+1}^{(k)} b_M^{(l)})^2}{(E_M^{(l)} - E_{M+1}^{(k)})} q_{M+1} + (H_{M+1,M+1} - E_{M+1}^{(k)} S_{M+1,M+1}) q_{M+1} = 0. \quad (2.13)$$

Since this equation is still general, it has to hold for all q_{M+1} , and therefore we can eliminate q_{M+1} from Eq.(2.13) for all $q_{M+1} \neq 0$. At this stage we make the assumption that *the change in level spacing by increasing the number of basis functions by one is negligible compared to the level spacing itself*: $E_M^{(l)} - E_{M+1}^{(k)} \simeq E_M^{(l)} - E_M^{(k)} \forall l \neq k$.

Isolating the $k = l$ -term from the sum in Eq.(2.13), the following expression, exact to order $O\left(\left[E_{M+1}^{(k)} - E_M^{(k)}\right]^2\right)$, can be extracted for the energy of level k ,

$$E_{M+1}^{(k)} = E_M^{(k)} - (a_M^{(k)} - E_M^{(k)} b_M^{(k)})^2 \times F_M^{-1}, \quad (2.14)$$

where

$$F_M = 2b_M^{(k)} \left[a_M^{(k)} - E_M^{(k)} b_M^{(k)} \right] + \sum_{l \neq k}^M \frac{(a_M^{(l)} - E_{M+1}^{(k)} b_M^{(l)})^2}{(E_M^{(l)} - E_{M+1}^{(k)})} - \left(H_{M+1,M+1} - E_{M+1}^{(k)} S_{M+1,M+1} \right). \quad (2.15)$$

For every function in the basis set, $E_{M+1}^{(k)}$ is calculated according Eq.(2.14). The routine adds that basis function χ_{M+1} as the $(M+1)$ -st basis function to the representation of $\Psi_{M+1}^{(k)}$ for which $E_{M+1}^{(k)}$ is minimized.

In order to evaluate Eq.(2.14) one needs to know the matrix elements defined in Eqs.(2.10) and (2.11). Note that the eigen functions $\Psi_M^{(l)}$ of the M -dimensional problem are represented by the basis function from the same basis set as where the χ_{M+1} is taken from. Therefore, all that needs to be calculated are matrix elements of the form defined in Eq.(2.4).

2.1.3 Matrix Elements

In case of linearly polarized laser fields, the dressed Coulomb potential V_0 , entering the Hamiltonian in Eq.(2.2), is axially symmetric around the polarization axis. In the following, the polarization axis is taken to be the z -axis. As will be described in more detail in Chapter 3, V_0 is generated by a charge line with inhomogeneous charge density extending from $z = -\alpha_0$ to $z = +\alpha_0$. Since in the regime where bound states of H^{2-} do exist correlation effects play a minor role, its wavefunction is assumed to have no azimuthal dependence. This assumption reduces the calculation to a 2-dimensional problem. The coordinates used for this 2-dimensional calculation are prolate spheroidal coordinates¹ ξ and η , centered at the end-points of the charge line, i.e. at $z = \pm\alpha_0$,

$$\begin{aligned} \xi &= \frac{r_+ + r_-}{2\alpha_0} \\ \eta &= \frac{r_+ - r_-}{2\alpha_0}, \end{aligned} \quad (2.16)$$

where $r_{\pm} \equiv |\mathbf{r} \pm \alpha_0 \hat{\mathbf{z}}|$. The volume element in these coordinates reads $dV = \alpha_0^3 (\xi^2 - \eta^2) d\xi d\eta d\varphi$. In Figure 2.1 a schematic picture is given of the prolate spheroidal coordinates. Curves of constant ξ and constant η are depicted, giving a system of confocal ellipses resp. hyperbolas. The domain of these coordinates is $\xi \in [1, \infty)$ and $\eta \in [-1, +1]$: On the line of charge, $\xi = 1$ and ξ increases to ∞ as $|\mathbf{r}|$ does. Coordinate $\eta = -1$ at $z = -\alpha_0$ and increases towards $\eta = +1$ as z reaches the other end-point at $z = +\alpha_0$. Since in case of H^- the electrons have negligible overlap for $\alpha_0 > 20$, the individual electronic orbitals in H^{2-} are not expected to have any overlap, since H^{2-} has bound states for $\alpha_0 > 155$ only (see Chapter 3). Therefore, exchange terms are negligible, and a Hartree calculation is suitable. The calculation shows that there is indeed no overlap between the one-electron orbitals in the regime $\alpha_0 > 155$, demonstrating the self-consistency.

¹See for example Abramowitz and Stegun, Ref.[137] p.752.

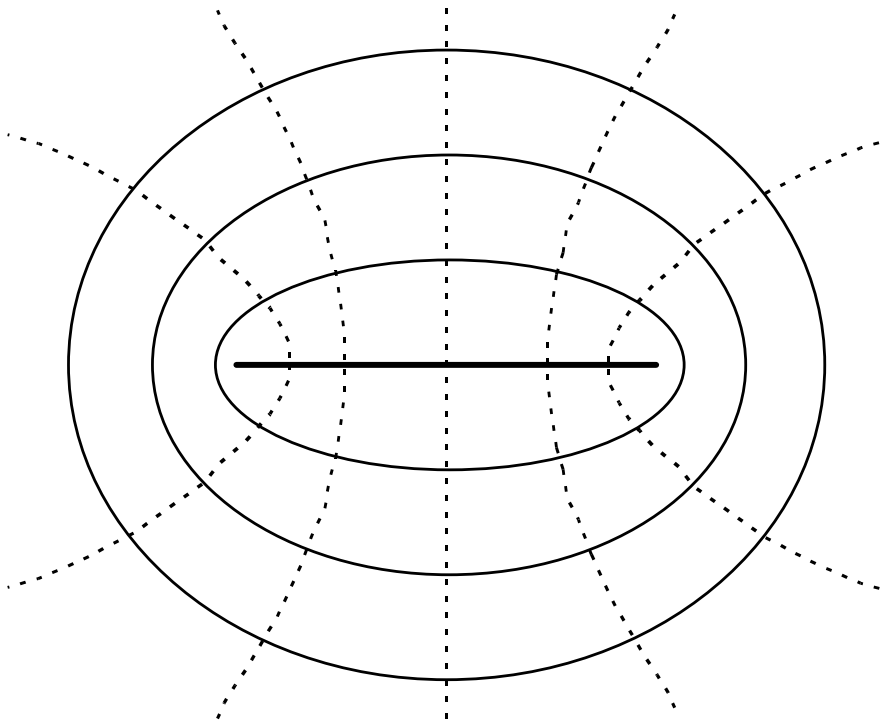


Figure 2.1: Schematic picture of prolate spheroidal coordinates centered at the end-points of the line of charge (fat line). The hyperbolas (dashed lines) are lines of constant η , whereas the confocal ellipses are lines of constant ξ . Note that the lines of constant η and ξ are orthogonal. At large distances from the line of charge, the coordinates ξ and η are asymptotically equal to the cylindrical coordinates r resp. ϕ .

This implies that the basis set should consist of one-electron basis functions. In order to be able to construct one-electron orbitals that are centered around the end-points or around $z = 0$ (which is essential for the calculation on H^{2-} , see Chapter 3), the L^2 basis functions χ_j are defined as

$$\chi_j^{(M_j, N_j, \gamma_j)}(\xi, \eta) \equiv \eta^{M_j} (\xi - 1)^{N_j} e^{-\gamma_j(\xi-1)}. \quad (2.17)$$

The exponential decay in the ξ -direction locates the wavefunction around the line of charge whereas (high) powers of η force the wavefunction to be concentrated around the end-points. Moreover, linear combinations of basis functions with coefficients of opposite sign and with different powers of η can generate a wavefunction that is centered around the origin at $z = 0$.

In the next paragraphs the different integrals needed to evaluate Eq.(2.4) are discussed. In case the integrals involve the basis functions χ_i and χ_j , we use the abbreviated notation $N \equiv N_i + N_j$, $M = M_i + M_j$ and $\gamma \equiv \gamma_i + \gamma_j$. For more notational convenience,

we define the following integrals,

$$\begin{aligned} I_\xi(N) &\equiv \int_1^\infty (\xi - 1)^N e^{-\gamma(\xi-1)} d\xi = \frac{N!}{\gamma^{N+1}}, \\ I_\eta(M) &\equiv \int_{-1}^{+1} \eta^M d\eta = \frac{2}{M+1}. \end{aligned} \quad (2.18)$$

2.1.3.1 Overlap Integral

In prolate spheroidal coordinates the overlap integral between two basis function, defined in Eq.(2.17), is given by

$$S_{ij} = 2\pi\alpha_0^3 \langle \chi_i | \chi_j \rangle = \int_1^\infty d\xi \int_{-1}^{+1} d\eta (\xi^2 - \eta^2) \eta^M (\xi - 1)^N e^{-\gamma(\xi-1)}. \quad (2.19)$$

The overlap integral and can be solved analytically and gives

$$S_{ij} = 2\pi\alpha_0^3 \{ I_\eta(M) [I_\xi(N+2) + 2I_\xi(N+1) + I_\xi(N)] - I_\eta(M+2)I_\xi(N) \}. \quad (2.20)$$

2.1.3.2 Kinetic Energy

In prolate spheroidal coordinates the Laplacian is given by

$$\frac{1}{2}\mathbf{p}^2 = -\frac{1}{2\alpha_0^2(\xi^2 - \eta^2)} [\partial_\xi (\xi^2 - 1) \partial_\xi + \partial_\eta (1 - \eta^2) \partial_\eta]. \quad (2.21)$$

One of the major advantages of prolate spheroidal coordinates is that, due to the multiplication with volume element, the integral involving the kinetic energy is separable,

$$\begin{aligned} \left\langle \chi_i \left| \frac{1}{2}\mathbf{p}^2 \right| \chi_j \right\rangle &= \left[I_\eta(M) \int_1^\infty d\xi (\xi - 1)^{N_i} e^{-\gamma_i(\xi-1)} \partial_\xi (\xi^2 - 1) \partial_\xi (\xi - 1)^{N_j} e^{-\gamma_j(\xi-1)} + \right. \\ &\quad \left. I_\xi(N) \int_{-1}^{+1} d\eta \eta^{M_i} \partial_\eta (1 - \eta^2) \partial_\eta \eta^{M_j} \right] \times (-\pi\alpha_0). \end{aligned} \quad (2.22)$$

Again, both integrals can be evaluated analytically, yielding

$$\begin{aligned} \left\langle \chi_i \left| \frac{1}{2}\mathbf{p}^2 \right| \chi_j \right\rangle &= \pi\alpha_0 \left\{ I_\eta(M) \left[\sum_{m=0}^2 C_m \{ I_\xi(N+m) + 2I_\xi(N+m-1) \} \right] + \right. \\ &\quad \left. I_\xi(N) M_i M_j [I_\eta(M-2) - I_\eta(M)] \right\}, \end{aligned} \quad (2.23)$$

where the coefficients C_m are given by

$$\begin{aligned} C_0 &= N_i N_j \\ C_1 &= -(N_i \gamma_j + N_j \gamma_i) \\ C_2 &= \gamma_i \gamma_j. \end{aligned} \quad (2.24)$$

2.1.3.3 Dressed Potential

The matrix element involving the dressed Coulomb potential reads $\langle \chi_i | V_0(\alpha_0; \mathbf{r}) | \chi_j \rangle$, where for linearly polarized laser fields $V_0(\alpha_0; \mathbf{r})$ is given by

$$V_0(\alpha_0; \mathbf{r}) = \frac{\omega}{2\pi} \int_0^{2\pi/\omega} \frac{dt}{|\mathbf{r} - \alpha_0 \hat{\mathbf{z}} \cos \omega t|}. \quad (2.25)$$

For the matrix element, an expression for $V_0(\alpha_0; \mathbf{r})$ in terms of prolate spheroidal coordinates is required. This expression can be found by solving the Laplace equation in

prolate spheroidal coordinates

$$\nabla^2 \frac{1}{r_{12}} (\xi_1, \eta_1, \varphi_1; \xi_2, \eta_2, \varphi_2) = -4\pi\delta(\xi_1 - \xi_2)\delta(\eta_1 - \eta_2)\delta(\varphi_1 - \varphi_2). \quad (2.26)$$

The solution of Eq.(2.26) is given by

$$\frac{1}{r_{12}} = \frac{1}{\alpha_0} \sum_{l=0}^{\infty} (2l+1) \sum_{m=-l}^{+l} P_l^m(\eta_1) P_l^m(\eta_2) P_l^m(\xi_<) Q_l^m(\xi_>) e^{im(\varphi_1 - \varphi_2)}, \quad (2.27)$$

where $\xi_<$ resp. $\xi_>$ is the smaller resp. larger one of the ξ_1 and ξ_2 , and were P_l^m and Q_l^m are the associated Legendre polynomials (see for example Abramowitz and Stegun, Ref.[137], p.332). The expansion in Eq.(2.27) for $1/r_{12}$ in Legendre polynomials is referred to as the Von Neumann expansion. Note that due to the azimuth-independent basis functions χ and the periodic dependence of r_{12}^{-1} on the azimuthal angles, the integrals over the azimuthal angles φ_1 and φ_2 in the matrix element for the $V_0(\alpha_0; \mathbf{r})$ vanish for $m \neq 0$. Another simplification arises because in the case of the dressed Coulomb potential the proton moves along the line of charge, and therefore $\xi_{proton} = \xi_< = 1$ and its η -coordinate can be replaced by $\eta_{proton} = \cos t$. This results in the following expression for the matrix element of V_0 , expressed in terms of η_{el} and ξ_{el} ,

$$\begin{aligned} \langle \chi_i | V_0(\alpha_0; \eta_{el}, \xi_{el}) | \chi_j \rangle &= \alpha_0^2 \sum_{l=0}^{\infty} (2l+1) \int_0^{2\pi} P_l(\cos t) dt \times \int_{-1}^{+1} d\eta_{el} \int_1^{\infty} d\xi_{el} \\ &\quad \left\{ \eta_{el}^M P_l(\eta_{el}) (\xi_{el} - 1)^N e^{-\gamma(\xi_{el}-1)} Q_l(\xi_{el}) (\xi_{el}^2 - \eta_{el}^2) \right\}. \end{aligned} \quad (2.28)$$

The integration over the η -coordinate of both the electron and the proton can be evaluated analytically using the relations (see also Ref. [138])

$$C_{core}(l) \equiv \frac{2l+1}{2\pi} \int_0^{2\pi} P_l(\cos t) dt = \begin{cases} (2l+1) \left[\frac{\Gamma(\frac{1}{2})}{\Gamma(1+\frac{l}{2})\Gamma(\frac{1-l}{2})} \right]^2 & \text{for } l \text{ even} \\ 0 & \text{for } l \text{ odd} \end{cases} \quad (2.29)$$

$$C_{el}(l, M) \equiv \int_{-1}^{+1} \eta_{el}^M P_l(\eta_{el}) d\eta_{el} = \begin{cases} \frac{\Gamma(\frac{1+M}{2})\Gamma(\frac{1-M}{2})}{\Gamma(1+\frac{M-l}{2})\Gamma(\frac{3+M+l}{2})} & \text{for } M+l \text{ even and } l \leq M \\ 0 & \text{otherwise} \end{cases} \quad (2.30)$$

The matrix element in Eq.(2.28) is now of the form

$$\begin{aligned} \langle \chi_i | V_0 | \chi_j \rangle &= 2\pi\alpha_0^2 \sum_{l=0}^{M+2} C_{core}(l) \times \\ &\quad \int_1^{\infty} d\xi_{el} (C_{el}(l, M) \xi_{el}^2 - C_{el}(l, M+2)) (\xi_{el} - 1)^N e^{-\gamma(\xi_{el}-1)} Q_l(\xi_{el}). \end{aligned} \quad (2.31)$$

At this stage it is convenient for analytical solution of the integral to write the associated Legendre polynomial $Q_l(\xi_{el})$ as

$$Q_l(\xi_{el}) = \frac{1}{2} P_l(\xi_{el}) \ln \frac{\xi_{el} - 1}{\xi_{el} + 1} - W_{l-1}(\xi_{el}), \quad (2.32)$$

where the polynomial W_{l-1} is determined by (see Abramowitz and Stegun, Ref.[137], p.334 Eq.8.6.19)

$$W_{l-1}(\xi_{el}) = \frac{2l-1}{1 \cdot l} P_{l-1}(\xi_{el}) + \frac{2l-5}{3 \cdot (l-1)} P_{l-3}(\xi_{el}) + \frac{2l-9}{5 \cdot (l-2)} P_{l-5}(\xi_{el}) + \dots \quad (2.33)$$

The integral in Eq.(2.31) now consists of two parts, one with a sum of polynomials in ξ_{el} (proportional to the W_{l-1} -part) and one with a sum of Legendre polynomials times the logarithm, given in Eq.(2.32). The former can be solved straightforwardly, extracting the coefficients of the polynomials from Eq.(2.33). Moreover, the latter, containing the logarithmic dependence, can be solved analytically by integration by parts, thereby solving the matrix element for the dressed Coulomb potential.

2.1.3.4 Electron-Electron Repulsion

As mentioned before, in the calculation of the bound states of H^{2-} , both correlation energy and exchange energy can be neglected due to the high values of α_0 at which H^{2-} supports bound states. Therefore, the matrix elements describing the electron-electron interaction are calculated with a Hartree Hamiltonian. Treating the electrons as a smooth distribution of negative charge with charge density ρ , the potential energy of the electron under consideration, say electron q , in their field is given by

$$V_{e-e}(\mathbf{r}_q) = \int \frac{\rho(\mathbf{r}')}{|\mathbf{r}_q - \mathbf{r}'|} d\mathbf{r}'. \quad (2.34)$$

The charge density ρ is generated by the remaining electrons,

$$\rho(\mathbf{r}') = \sum_{p \neq q} |\Psi(\mathbf{r}_p)|^2. \quad (2.35)$$

Suppose that the one-electron orbitals Ψ are constructed of N basis functions, i.e. $\Psi = \sum_{n=1}^N c_n \chi_n$. In order to evaluate the matrix element $\langle \chi_i | V_{e-e} | \chi_j \rangle_{pq}$, which equals the potential energy of electron p due to its repulsive interaction with electron q , there are N^2 integrals to be solved,

$$\langle \chi_i | V_{e-e} | \chi_j \rangle = \sum_{n,m=1}^N c_n^* c_m \int d\eta_p d\eta_q \int d\xi_p d\xi_q \chi_i^*(\xi_q, \eta_q) \frac{\chi_n^*(\xi_p, \eta_p) \chi_m(\xi_p, \eta_p)}{r_{pq}} \chi_j(\xi_q, \eta_q). \quad (2.36)$$

Similar to the case of the dressed Coulomb potential V_0 , the Von Neumann expansion is used for the operator $1/r_{pq}$ in the expression for the e-e repulsion (see Eq.(2.27)). In the latter case the coordinates of the particles are not fixed, in contrast to the former case, where the ξ -coordinate of the proton is fixed, nl. $\xi = 1$. Therefore, the ξ integration has to be split up into two parts, one containing the interval $\xi_p < \xi_q$ and one with $\xi_p > \xi_q$. Apart from this split up, the ξ integration goes fully analogous to that in case of V_0 . The η integration can be performed exactly the same way as for the η coordinate of the electron in the V_0 case.

2.2 Solving an Inhomogeneous System; Lifetimes

For finite frequencies, the Hamiltonian is not Hermitian and therefore the eigenvalues E become complex; electron detachment from the ion after absorption of $m > M$ photons sets in, where M is the minimum number of photons needed to couple the initial state with the continuum, $E_M \equiv E + M\omega > 0$. In order to calculate lifetimes (to lowest order

in $1/\omega$) of the N -electron system, consider first the structure equation obtained after one iteration,

$$\left[E^{(1)} - H - \sum_{m \neq 0} V_{-m} G_m (E_m^{(1)}) V_m \right] \phi_0^{(1)} = 0, \quad (2.37)$$

where V_m is the m -th Fourier component of the space-translated Coulomb potential,

$$V_m (\alpha_0; \mathbf{r}) = \frac{1}{2\pi} \int_0^{2\pi} \frac{e^{-imt}}{|\mathbf{r} - \alpha_0 \hat{\mathbf{z}} \cos t|} dt. \quad (2.38)$$

In the high-frequency limit, the term $\sum_{m \neq 0} V_{-m} G_m (E_m^{(1)}) V_m$ can be treated perturbatively, since in this limit $G_m (E_m^{(1)})$ is proportional to $1/\omega$. The energy correction $\Delta E^{(1)} = E^{(1)} - E^{(0)}$ can be obtained applying first order perturbation theory,

$$\Delta E^{(1)} = \sum_{m \neq 0} \left\langle \phi_0^{(0)} | V_{-m} G_m (E_m^{(1)}) V_m | \phi_0^{(0)} \right\rangle. \quad (2.39)$$

From the imaginary and real part of this expression one can extract the photodetachment rate resp. the correction to the real high-frequency binding energy $E^{(0)}$. It can be seen from Eq.(2.39) that to get the lowest order correction, one can replace $E_m^{(1)}$ by the *real* $E_m^{(0)} = E^{(0)} + m\omega$. Since in lowest order perturbation theory

$$\phi_m^{(1)} = G_m (E_m^{(0)}) V_m \phi_0^{(0)}, \quad (2.40)$$

the energy correction can be written as

$$\Delta E^{(1)} = \sum_{m \neq 0} \left\langle \phi_0^{(0)} | V_{-m} | \phi_m^{(1)} \right\rangle. \quad (2.41)$$

Since we are interested in the detachment rate of the ground state of H^{2-} , the sum over m in Eq.(2.41) runs over positive m only. The method applied to calculate the photodetachment rates consists of first solving Eq.(2.40), after which $\Delta E^{(1)}$ is calculated by evaluating the matrix elements in Eq.(2.41).

2.2.1 Basis Set Representation

We are looking for a basis-set representation of the $\phi_m^{(1)}$ obeying Eq.(2.40), where $m > 0$. Those channels m for which $E_m^{(0)} > 0$ (i.e. $m \geq M$) are called open, since in these channels an electron can be detached after absorption of m photons. Logically, the other channels are called the closed channels. Since we are primarily interested in high-frequency fields, i.e. fields for which ω is larger than the binding energy, we have $M = 1$. To find the unique solution of the equation determining $\phi_m^{(1)}$, a boundary condition is required. In the open channels the Floquet component $\phi_{m>M}^{(1)}$, obeying the boundary condition described in Chapter 1 in Eq.(1.58), asymptotically consists of an outgoing wave with momentum $k_m = \sqrt{2E_m^{(0)}}$. Moreover, the phase of the outgoing wave contains a logarithmic phase factor because of the long range character of the Coulomb potential. It is clear that the basis functions contained in the L^2 basis set, used to represent the $\phi_0^{(0)}$, can not obey this boundary condition. Therefore, the basis set used for the $\phi_0^{(0)}$ needs to be extended with functions $\notin L^2$. Next we will show what type of basis function

is appropriate to extend the L^2 basis set with in order to create a physical representation of $\phi_m^{(1)}$.

For computational convenience, we look for a continuum basis function that is separable in the coordinates ξ and η . The applicability of such a basis function to describe a detached electron is determined by the separability of the matrix elements containing the one-electron Hamiltonian generated by the remaining H^- ion. The matrix elements containing the kinetic energy are separable (see Eq.(2.22)). Therefore, the separability of the Hamiltonian is determined by the separability of the dressed Coulomb potential V_0 in combination with the repulsive potential generated by the two remaining electrons of H^- .

The repulsive potential generated by these electrons can be approximated by that generated by two electrons located at $z = \pm\alpha_0$, each on one end-point. This can be understood considering the following. Numerical calculations on H^- show that for $\alpha_0 > 20$, the electronic wavefunction consists of two non-overlapping parts, each part representing an electron centered around an end-point. At increasing α_0 , the wavefunction even contracts more and more towards these end-points². Since the calculations are performed in the regime where $\phi_0^{(0)}$ represents a bound state, i.e. in the regime $\alpha_0 > 155$, the electronic wavefunctions of H^- peak strongly around the end-points.

On the other hand, writing down the multipole expansion of the dressed Coulomb potential using Eq.(2.28), it can be seen that only matrix elements containing the monopole of V_0 are separable in ξ and η ,

$$\begin{aligned} V_0(\xi, \eta) dV/(2\pi\alpha_0^3) &= V_0(\xi, \eta) (\xi^2 - \eta^2) d\xi d\eta \\ &= \left[-\xi - \frac{1}{4\xi} \left(\frac{55}{3} + 51\eta^2 \right) + O(\xi^{-3}) \right] d\xi d\eta. \end{aligned} \quad (2.42)$$

The second term in Eq.(2.42) destroys the separability of the quadrupole moment of V_0 . The same monopole as for V_0 , defined as V_0^{mono} , is generated by two charges with $q = +1/2$, one located at each end-points.

Therefore, the combination of V_0^{mono} together with the repulsive potential generated by the two electrons can, for large α_0 , be treated as separable. This combination, referred to as the effective potential V^{eff} , can be generated by two charges with $q = -1/2$, fixed at the end-points, and can be written as

$$V^{eff}(\xi, \eta) = -\frac{\xi}{\alpha_0(\xi^2 - \eta^2)}. \quad (2.43)$$

The effective potential determines the separable ‘‘continuum’’ basis function χ_c for the detached electron of H^{2-} . For this purpose, an eigen function of the Hamiltonian containing the effective potential has to be constructed. This function appears to be of the following form

$$\chi_c^{M, k_m}(\xi, \eta) = \eta^M \exp \left[ik_m \alpha_0 \xi - \left(1 + \frac{i}{k_m} \right) \ln \xi \right]. \quad (2.44)$$

Note that the logarithmic tail due to the long range character of the Coulomb potential is included in χ_c . It has in fact the same exponential character as the continuum wavefunction of atomic hydrogen, the differences arise from the different expressions for the

²The distance of the centre of electronic charge to the end-point scales as $2.3 \times \alpha_0^{1/3}$, see Pont, Ref.[122]. For more details, see Chapter 5.

Laplacian in radial and prolate spheroidal coordinates. Asymptotically for large ξ , the function χ_c obeys

$$\left[E_m - \frac{1}{2} \mathbf{p}^2 - V^{eff} \right] \chi_c^{M,k_m} (\xi, \eta) = 0 + O\left(\frac{1}{\xi^3}\right). \quad (2.45)$$

Together with the L^2 basis functions defined in Eq.(2.17), this function forms the basis set with which the Floquet components $\phi_m^{(1)}$ will be represented³. The construction of this basis set representation is discussed in the following Section.

2.2.2 Determination of the Floquet Components

The Floquet component $\phi_m^{(1)}$, obeying Eq.(2.40), is to be represented by a linear combination of basis functions. This Section deals with the procedure that determines the optimal linear combination of basis functions to represent $\phi_m^{(1)}$. Optimal here means that the norm of the function

$$|\Theta\rangle \equiv |(E + m\omega - H) \phi_m^{(1)}\rangle - |V_m \phi_0^{(0)}\rangle \quad (2.46)$$

is minimized using a basis-set representation for $\phi_m^{(1)}$. In order to ensure that the basis set representation of $\phi_m^{(1)}$ describes the unique solution of Eq.(2.40), it is essential that the basis set is complete in the sense that any extension of the basis set applied does not induce a change in the representation.

The representation is obtained by minimizing the norm of the vector defined in Eq.(2.46), defined as ε . Since matrix elements involving terms proportional to V_0^2 and V_m^2 cannot be calculated analytically, a complete set can be inserted to get around calculating matrix elements containing H^2 . The expression for ε then reads

$$\varepsilon = \sum_k \langle (E_m - H) \phi_m^{(1)} - V_m \phi_0^{(0)} | k \rangle \langle k | (E_m - H) \phi_m^{(1)} - V_n \phi_0^{(0)} \rangle. \quad (2.47)$$

Suppose that the Floquet component is represented by a total of $N \geq 0$ basis functions, of which C are continuum basis functions as defined in Eq.(2.44),

$$\phi_m^{(1)} = \sum_{j=1}^{N-C} b_j \chi_j + \sum_{j=1}^C d_j \chi_{c,j} \equiv \sum_{j=1}^N c_j \varphi_j. \quad (2.48)$$

In case $C \neq 0$, the coefficients c_j, b_j and d_j are complex. The parameter $\varepsilon \geq 0$, obtained with N basis functions, can be written as

$$\varepsilon(N) = \sum_{j,j'=1}^N c_j^* M_{j,j'} c_{j'} - \sum_{j=1}^N (c_j^* q_j^* + c_j q_j) + \varepsilon_0, \quad (2.49)$$

³In addition to the two types of basis functions, we used a mixture of these. For details, see Chapter 7 of this Thesis, Sec.7.2.2.

where

$$\begin{aligned} M_{j,j'} &\equiv \sum_k \langle (E_m - H) \varphi_j | k \rangle \langle k | (E_m - H) \varphi_{j'} \rangle, \\ q_j &\equiv \sum_k \langle V_m \phi_0^{(0)} | k \rangle \langle k | (E_m - H) \varphi_j \rangle, \\ \varepsilon_0 &\equiv \sum_k \langle V_m \phi_0^{(0)} | k \rangle \langle k | V_m \phi_0^{(0)} \rangle. \end{aligned} \quad (2.50)$$

The coefficients c_j are optimally chosen if the change $\delta\varepsilon(N)$ in $\varepsilon(N)$ induced by *any* infinitesimally change $c_j \rightarrow c_j + \delta c_j$ is zero, i.e.

$$\delta\varepsilon(N) = \left[\sum_{j,j'=1}^N \delta c_j^* M_{j,j'} c_{j'} - \sum_{j=1}^N \delta c_j^* q_j^* \right] + c.c. = 0 \quad \forall \delta c_j. \quad (2.51)$$

This yields the following equation for the coefficients c_j ,

$$\sum_{j=1}^N M_{j,j'} c_{j'} = q_j^* \quad (2.52)$$

The coefficients c_j can now be found by inverting the matrix $M_{j,j'}$. With these coefficients the value of $\varepsilon(N)$ determined by this optimal representation with N basis functions can be calculated, combining Eq.(2.49) and Eq.(2.52),

$$\varepsilon(N) = - \sum_{j=1}^N \delta c_j q_j + \varepsilon_0. \quad (2.53)$$

Next, the basis set representation of $\phi_m^{(1)}$ is extended to $N + 1$ basis functions with the function that minimizes $\varepsilon(N + 1)$. The $\varepsilon(N + 1)$ is calculated for each remaining basis functions in the set. Note that the procedure used to calculate $\varepsilon(N + 1)$ allows the coefficients of all N basis functions used in the previous N iterations to vary during the addition of the $(N + 1)$ -st basis function. This ensures that the representation for the $\phi_m^{(1)}$ is the optimal representation with $N + 1$ basis functions.

The complete set as introduced in Eq.(2.47) is in fact an idealization and can not be represented by a finite set of functions. Although finite, it can be treated as complete as long as none of the functions in the basis set for $\phi_m^{(1)}$ is orthogonal to it. We use a set of δ -functions for the "complete" set. The distribution of the δ -functions is inhomogeneous in space, i.e. more centered at positions where $V_m \phi_0^{(0)}$ strongly varies, and less where it is almost constant. The total number of δ -functions is roughly 2000, whereas the number of basis functions for the representation of $\phi_m^{(1)}$ is 1000.

With the set of δ -functions as a representation for the complete set, the calculation of the matrix elements $M_{j,j'}$, the vector q_j and ε_0 , see Eq.(2.51), consists of evaluating $(E_m - H) \varphi_j$ and $V_m \phi_0^{(0)}$ at the positions of the δ functions. The latter is obtained by numerical integration of the integral defined in Eq.(2.38), and evaluation of the known function $\phi_0^{(0)}$ at these positions. For the evaluation of $(E_m - H) \varphi_j$ at the position of the δ functions, an analytical expression in terms of prolate spheroidal coordinates is needed for the Hamiltonian H acting on φ_j . The term proportional to the kinetic energy can be obtained using Eq.(2.21) for the Laplacian. The dressed Coulomb potential can be

evaluated to order $O(10^{-8})$: In contrast to the V_m with $m \neq 0$, there exists an analytical expression (see also Refs.[137] and [122]) for the integral defining the V_0 , see Eq.(2.25),

$$V_0(\alpha_0; \mathbf{r}) = -\frac{2}{\pi} \frac{1}{\sqrt{r_+ r_-}} K \left[\left(\frac{1 - \hat{\mathbf{r}}_+ \cdot \hat{\mathbf{r}}_-}{2} \right)^{1/2} \right]. \quad (2.54)$$

(For definition \mathbf{r}_+ and \mathbf{r}_- , see Section 2.1.3). In Eq.(2.54), K is the complete elliptic integral of the first kind, see Ref.[137],

$$K(k) = \int_0^1 \frac{dx}{\sqrt{1-x^2}\sqrt{1-k^2x^2}}. \quad (2.55)$$

In terms of prolate spheroidal coordinates, the argument of K in Eq.(2.54) can be written as

$$k = \left(\frac{1 - \hat{\mathbf{r}}_+ \cdot \hat{\mathbf{r}}_-}{2} \right)^{1/2} = \left(1 - \frac{\xi^2 - 1}{\xi^2 - \eta^2} \right)^{1/2} \equiv \sqrt{1-p}. \quad (2.56)$$

The elliptic integral can be evaluated at a certain position (ξ, η) using

$$K(k) = \sum_{i=0}^4 a_i p^i - \ln p \sum_{i=0}^4 b_i p^i + O(10^{-8}), \quad (2.57)$$

where a_i and b_i are constants, see Abramowitz and Stegun, Ref.[137] p.591. Moreover, in prolate spheroidal coordinates the prefactor $1/\sqrt{r_+ r_-}$ is given by

$$\frac{1}{\sqrt{r_+ r_-}} = \frac{1}{\alpha_0} \frac{1}{\sqrt{\xi^2 - \eta^2}}. \quad (2.58)$$

Combining Eqs.(2.54) through (2.58), the following expression for V_0 in prolate spheroidal coordinates can be extracted

$$V_0(\alpha_0; \mathbf{r}) = -\frac{2}{\pi \alpha_0 \sqrt{\xi^2 - \eta^2}} K \left[\left(1 - \frac{\xi^2 - 1}{\xi^2 - \eta^2} \right)^{1/2} \right], \quad (2.59)$$

where the K integral is to be evaluated according Eq.(2.57). From Eqs.(2.57) and (2.59) it can be seen that the dressed Coulomb potential V_0 has a square-root singularity at the end-point $z = \pm \alpha_0$ and a logarithmic singularity at the line connecting the end-points. Together with the expression of the basis functions, Eq.(2.17) and Eq.(2.44), this explicit expression for V_0 in terms of ξ and η enables us to evaluate the Hamiltonian H at any position.

2.2.3 Calculation Decay Rates

Once the basis-set representation for the Floquet components $\phi_m^{(1)}$ is found, it is possible, together with the representation for the $\phi_0^{(0)}$, to calculate the partial photodetachment rates $\Gamma_m^{(1)}$ in each channel m . The total photodetachment rate is obtained by summing the partial rates from the open channels

$$\Gamma^{(1)} = \sum_{m \geq M} \Gamma_m^{(1)} \quad (2.60)$$

The matrix elements to be evaluated read

$$\Gamma_m^{(1)} = -2 \operatorname{Im} \Delta E^{(1)} = -2 \operatorname{Im} \left\langle \phi_0^{(0)} | V_m | \phi_m^{(1)} \right\rangle. \quad (2.61)$$

The $\phi_0^{(0)}$ consists of L^2 basis functions, whereas the $\phi_m^{(1)}$ may consist of non-square integrable functions of the type defined in Eq.(2.44) as well. The evaluation of the matrix elements is different for these type of basis functions. Whereas for the L^2 basis functions the matrix elements can be evaluated analytically, numerical integration procedures are needed for the case of non-square-integrable basis functions. Firstly, an expression will be given for the V_m in terms of prolate spheroidal coordinates, which is needed to calculate the matrix elements. Subsequently, the calculation of these elements is described.

As for the dressed Coulomb potential V_0 , the Von Neumann expansion for $1/r_{ij}$ is used, see Eq.(2.27). With this expansion, V_m can be written in prolate spheroidal coordinates as

$$V_m(\alpha_0; \xi, \eta) = 2\pi\alpha_0^2 \sum_{l=0}^{\infty} \left\{ \frac{2l+1}{2\pi} \int_0^{2\pi} e^{imt} P_l(\cos t) dt \right\} P_l(\eta) Q_l(\xi). \quad (2.62)$$

The integral between parentheses can be rewritten as

$$\begin{aligned} \frac{2l+1}{2\pi} \int_0^{2\pi} e^{imt} P_l(\cos t) dt &= (-1)^{m+l} \times \frac{2l+1}{\pi} \int_0^\pi \cos(mt) P_l(\cos t) dt \\ &= (-1)^{m+l} \times \frac{2l+1}{\pi} \sum_{k=m \bmod 2}^m b_k^{(m)} \int_0^\pi \cos^k t P_l(\cos t) dt, \end{aligned} \quad (2.63)$$

where the summation variable k increases by 2 in each step. The coefficients $b_k^{(m)}$ are given by

$$b_k^{(m)} = \begin{cases} 2^{k-1} \left(\frac{m+k}{2} - 1 \right) \frac{2m}{m-k} (-1)^{\frac{m-k}{2}} & k < m \\ 2^{m-1} & k = m \end{cases} \quad (2.64)$$

Since the integral in Eq.(2.63) yields zero for $l+k$ odd, $l+m$ should be even. Changing the integration variable to $y = \cos t$, this integral is given by

$$\begin{aligned} \int_0^{2\pi} e^{imt} P_l(\cos t) dt &= \frac{2(2l+1)}{\pi} \sum_{k=m \bmod 2}^m b_k \int_0^1 \frac{y^k}{\sqrt{1-y^2}} P_l(y) dy \\ &= \frac{(2l+1)}{\sqrt{\pi}} \sum_{k=m \bmod 2}^m b_k \frac{\Gamma(\frac{1+k}{2})}{\Gamma(1+\frac{k}{2})} {}_3F_2 \left(\frac{l+1}{2}, -\frac{l}{2}, \frac{1}{2}; 1, \frac{3+k}{2}; 1 \right) \\ &\equiv V_{m,l} \end{aligned} \quad (2.65)$$

where ${}_3F_2$ is the confluent hypergeometric function; for this and the Γ function, see Abramowitz and Stegun, Ref.[137]. The m -th Fourier component V_m can now be written as

$$V_m(\alpha_0; \xi, \eta) = 2\pi\alpha_0^2 \sum_{l=0}^{\infty} V_{m,l} P_l(\eta) Q_l(\xi). \quad (2.66)$$

With this expression for V_m , it is possible to calculate the matrix elements as in Eq.(2.61). This matrix element can be split into two parts, one containing the L^2 basis functions

and another containing the continuum basis functions (see Eq.(2.48))

$$\left\langle \phi_0^{(0)} | V_m | \phi_m^{(1)} \right\rangle = \sum_{j=1}^{N-C} b_j \left\langle \phi_0^{(0)} | V_m | \chi_j \right\rangle + \sum_{j=1}^C d_j \left\langle \phi_0^{(0)} | V_m | \chi_{c,j} \right\rangle. \quad (2.67)$$

Since the $\phi_0^{(0)}$ consists of the same type of L^2 basis functions, the first term on the right-hand side of Eq.(2.67) is evaluated analogously to the calculation of the matrix elements containing the V_0 , see Section 2.1.3.3. The matrix element containing the continuum basis functions, however, can not be evaluated analytically due to the complex exponential behavior of $\chi_{c,j}$. Whereas the η -integration can be performed analytically and similar to the V_0 case, the ξ -integration can not. The matrix element for the V_m is of the following form

$$\begin{aligned} \langle \chi_i | V_m | \chi_{c,j} \rangle &= 2\pi\alpha_0^2 \sum_{l=0}^{M+2} V_{m,l} \int_1^\infty d\xi \left\{ (C_{el}(l, M)\xi^2 - C_{el}(l, M+2)) \times \right. \\ &\quad \left. (\xi - 1)^N e^{-\gamma(\xi-1)} e^{ik_m \alpha_0 \xi - (1+i/k_m) \ln \xi} Q_l(\xi) \right\}, \end{aligned} \quad (2.68)$$

where the coefficient $C_{el}(l, M)$ is defined in Eq.(2.30). Using the expansion Eq.(2.32) for the polynomial Q_l , the integral in Eq.(2.68) can be written in terms of integrals of the type

$$\sum_{k=0}^{l+M+N+2} \int_0^\infty dx e^{i(k_m \alpha_0 x - 1/k_m \ln[x+1])} \frac{e^{-\gamma x} x^k}{(x+1)} \left[p_k \ln \frac{x}{x+2} + q_k \right]. \quad (2.69)$$

The coefficients p_k and q_k are built up by the coefficients of the Legendre polynomials P_l resp. W_{l-1} in combination with the C_{el} . These integrals are evaluated numerically.

With these methods we are now able to calculate the matrix elements in Eq.(2.61), and therefore the lifetimes of the multiply charged negative ion H^{2-} in a linearly polarized laser field.

3

THE INDUCTION OF H^{2-}

3.1 Introduction

Nature does not allow stable atomic multiply charged negative ions in vacuo. It has been proven theoretically that a proton cannot bind more than two electrons, i.e., that the doubly charged negative ion of hydrogen does not have bound states (see Lieb, Ref.[139]). Moreover, there is no experimental evidence for the existence of atomic multiply charged negative ions (AMCNI) [140]. However, in the last decade it has been shown, both theoretically and experimentally, that the character of atomic systems changes drastically in a radiation field. For example, whereas distribution of the ground-state wavefunction of an electron in a Coulombic potential is spherically symmetric around the nucleus, in a superintense high-frequency laser field this wavefunction is extremely distorted. In case of linear polarization, the wavefunction splits up into two non-overlapping parts, an effect also referred to as dichotomy of the electronic wavefunction, see Pont *et al*, Refs.[122] and [123]. As shown by Pont in Ref.[124], for circular polarization, the distortion of the wavefunction leads to toroidal shaping.

Another striking feature, resulting from the interaction between the atom and the radiation field, is the existence of states that do not exist outside this radiation field. These so-called light-induced states were shown to exist for example in H^- , in the presence of a superintense high-frequency laser field (see for example Dörr *et al*, Ref.[132] and Fearnside *et al*, Ref.[131]). In vacuo, H^- exhibits only one loosely bound state in the symmetry manifold 1S_g ($L = 0, S = 0$, even parity), for which the detachment energy is small, $D = 0.751$ eV. As shown by Muller and Gavrila, Ref.[133], in a superintense high-frequency laser field, however, H^- does have excited states as well. Apparently it is possible, with the help of a radiation field, to create stable atomic states that do not exist outside this field. If a radiation field is the appropriate environment in which the character of an AMCNI of hydrogen changes such that it does exhibit bound states is the question we will answer positively in this Chapter.

The *classical picture* of how an AMCNI might exist, consists of a set of N ($N > 2$) electrons oscillating in the radiation field with field frequency ω . The nucleus is assumed to be infinitely heavy, and therefore does not follow this so-called quiver motion. If the quiver motion, which is the same for all N electrons, has a large amplitude $\alpha_0 = E_0/\omega^2$, where E_0 is the field amplitude, it is possible for each of the N electrons to be near the nucleus for part of the quiver period and to be far away from the other electrons during whole the period. This sharing of the attractive interaction with the nucleus could eventually create the possibility for N electrons to be bound to one single proton. By increasing the amplitude of the quiver motion, an extra electron can share the attraction

to the proton, since the total repulsive energy decreases more rapidly than the attractive energy with increasing amplitude (see below).

The numerical calculation presented in this Chapter is quantum-mechanically and is based on previous results obtained in the high-frequency limit. It is this limit in which it has been shown that there exist light induced excited states of H^- . Therefore, we are interested in high frequencies when we are looking for a radiation field in which an AMCNI might exhibit bound states.

In the remaining part of this Chapter we will first briefly describe the theory that is used as a basis for our calculations. Next we will concentrate on the case of a linearly polarized laser field, for which we use a self-consistent-field procedure to calculate the energy and wavefunction of the ground state of the simplest type of an AMCNI, H^{2-} .

3.2 Theoretical Basis

We are interested primarily in a monochromatic field, for arbitrary polarization labelled by the ellipticity parameter δ , with electric field vector

$$\mathbf{E}(t) = -E_0 (\mathbf{e}_1 \cos \omega t + \tan \delta \mathbf{e}_2 \sin \omega t), \quad (3.1)$$

where \mathbf{e}_j ($j = 1, 2$) are unit vectors orthogonal to each other and to the propagation direction ($\delta = 0$ corresponds to linear polarization, and $\delta = \pm\pi/4$ to circular polarization). We make the dipole approximation, neglecting retardation effects ($\vec{A}(\vec{r}, t) = \vec{A}(t)$) and magnetic terms ($\vec{B} = \nabla \times \vec{A}$).

If the frequency of the radiation field is large compared to the spacing of the electronic levels, the wavefunctions of all electronic levels, bound as well as continuum, are forced to oscillate in the field. Therefore, it is appropriate to use the rest frame of a freely oscillating electron as reference frame. This frame, also referred to as the Kramers-Henneberger frame (K-H-frame) (see Refs.[118] and [119]) is connected to the lab-frame via a space translation over $\alpha(t) = \alpha_0 [\hat{\mathbf{e}}_1 \cos \omega t + \tan \delta \hat{\mathbf{e}}_2 \sin \omega t]$. In the K-H-frame, the proton oscillates with the frequency of the radiation field and with amplitude α_0 .

We use high-frequency Floquet theory (HFFT) for describing the interaction between the ion and the laser field. The HFFT proceeds from the "space-translated" version of the Schrödinger equation (discovered by Pauli and Fierz, see Ref.[117]), i.e. the Schrödinger equation in the K-H-frame, which, for a system of one proton and N ($N \geq 2$) electrons reads

$$\sum_{i=1}^N \left[\frac{1}{2} \mathbf{p}_i^2 - \frac{1}{|\mathbf{r}_i + \alpha(t)|} + \sum_{j=1}^{i-1} \frac{1}{|\mathbf{r}_i - \mathbf{r}_j|} \right] \Psi = i \frac{\partial \Psi}{\partial t}, \quad (3.2)$$

where $\alpha(t) = (\alpha_0/E_0)\mathbf{E}(t)$. By making the Floquet ansatz one seeks to determine solutions of Eq.(3.2) characterizing a regime of steady ionization, with constant rates. At photon energies ω sufficiently high with respect to the average excitation energy of the atomic system in the field, the HFFT gives the following structure equation¹ [116],

$$\sum_{i=0}^N \left\{ \frac{1}{2} \mathbf{p}_i^2 + V_0(\mathbf{r}_i, \alpha_0) + \sum_{j=1}^{i-1} \frac{1}{|\mathbf{r}_i - \mathbf{r}_j|} \right\} \Phi_0 = W(\alpha_0) \Phi_0, \quad (3.3)$$

¹For a one-electron atom, Eq.(3.3) was obtained heuristically in the high-frequency context by I.J. Gersten and M. Mittleman, see Ref.[120].

where Φ_0 is now the zeroth order Floquet component of the N -electron wavefunction (cf with $\phi_0^{(0)}$ in Chapter 1, Sec.1.5.2, Eq.1.64). In Eq.(3.3) V_0 , the "dressed" Coulomb potential, is the time-average of $-1/|\mathbf{r} + \alpha(t)|$ entering Eq.(3.2):

$$V_0(\alpha_0; \mathbf{r}) = -\frac{1}{2\pi} \int_0^{2\pi} \frac{1}{|\mathbf{r} + \alpha(\chi/\omega)|} d\chi. \quad (3.4)$$

The occurrence of V_0 appears classically quite naturally if one notes that at high laser frequency (large with respect to that of the orbital motion) the electron explores the vicinity of \mathbf{r} along the curve $\alpha(t)$, so that the effective potential, $V_0(\alpha_0, \mathbf{r})$, governing the orbital motion will be the average of $V(\mathbf{r}) = -1/r$ along this curve. Referring to Eq.(3.4), V_0 appears as the electrostatic potential generated by the unit charge of the nucleus smeared out along the trajectory $\alpha(t)$; this we shall call the "line of charge", see Ref.[116], Sec.IV C. Since the Hamiltonian in Eq.(3.3) is Hermitian, the eigenvalues $W(\alpha_0)$ are real, showing the stability with respect to photodetachment of the ion in the high-frequency limit. Moreover, it should be mentioned that the eigenvalues only depend on the field strength and frequency via the parameter α_0 .

3.3 The Linearly Polarized Field, a Candidate?

A linearly polarized monochromatic laser field induces a V_0 that is generated by a line charge with an inhomogeneous charge density. If the polarization axis is defined as z -axis, the charge of the proton is smeared out along the line segment $z = [-\alpha_0, +\alpha_0]$, with a non-uniform charge density σ ,

$$\sigma = \frac{1}{\pi \sqrt{\alpha_0^2 - z^2}}. \quad (3.5)$$

The charge density has an integrable singularity at $z = \pm\alpha_0$, since the proton has zero velocity at these points, whereas at $z = 0$, the point the proton passes at highest velocity, the charge density is smallest². Parity and total angular momentum projected on the z -axis are good quantum numbers.

At large α_0 -values a two-electron atom is in a dichotomous state, because of the accumulation of the smeared proton charge towards the end-points of the line of charge (see Ref.[125]; also [116] Sec.V.A.3). To dominant order in α_0^{-1} , the electrons are independent of each other, and their motion is governed by the limiting form of the potential $V_0(\alpha_0, \mathbf{r})$ in the vicinity of the end points; the limiting form will be denoted as "end-point potential", $\tilde{V}_0(\alpha_0, \mathbf{r})$; In Appendix A the connection between the dressed Coulomb potential V_0 and the end-point potential is explored in more detail. This means that the electrons are localized around the two end points at $z \pm \alpha_0$, and there is practically no electronic charge at the origin. Together with the fact that the attractive potential has a logarithmic singularity in the direction perpendicular to the polarization axis, this suggests that it is in the vicinity of the origin that a third electron could be bound to form H^{2-} . From symmetry considerations, the one-electron wavefunction (of the ground state) of the third electron is confined to be symmetric in the plane $z = 0$. Although the electron located around the point $z = 0$ would be repelled by the two electrons

²In case of circular polarization, the line of charge is a circle with radius α_0 , traced out by the proton once per period. Although the charge density is smallest at $z = 0$ in the linear case, it still is twice as large as that for circular polarization, since the proton passes the interval $z = [-\alpha_0, +\alpha_0]$ twice per period of the field. For details about the circular case, see Chapter 4 and references therein.

located around the end points, it would also be attracted by the exposed line of charge, which could lead to binding³. In fact, it can be shown that to dominant order in α_0^{-1} , the binding energy to the end-point potential scales as $\alpha_0^{-2/3}$ (see Refs.[123] and [122]), whereas the binding energy of an electron located in the interval around $z = 0$ scales as $\alpha_0^{-1} \ln \alpha_0$ (see Chapter 5, Sec.5.2.1). Since the repulsive energy due to the e-e interaction scales as α_0^{-1} , one would expect, based on these scaling laws, that by increasing α_0 the total energy of H^{2-} becomes negative, thereby inducing a bound state. Therefore, a linearly polarized laser source is a good candidate as an external radiation source to change the character of the ion such that three electrons can be bound to one proton ($N = 3$), resulting in a light stabilized AMCNI, H^{2-} .

3.4 The Appearance of H^{2-}

3.4.1 Self-Consistent Field Calculation

With this in mind we have started a *self-consistent field calculation* in order to prove the possibility of attachment of an extra electron to H^- as described above. As a start-up choice for the wavefunctions of the three electrons we have taken delta functions located at⁴ $z = \pm\alpha_0$ and $z = 0$. Each iteration in the self-consistent field calculation actually consists of three steps; Step 1: an electronic wavefunction is calculated in the field generated by the dressed Coulomb potential $V_0(\alpha_0; \mathbf{r})$ and the electrons near $z = 0$ and $z = -\alpha_0$. This wavefunction appears to be located around $z = +\alpha_0$. Step 2: calculation of an electronic wavefunction in the field generated by $V_0(\alpha_0; \mathbf{r})$, the electron around $z = 0$ and the wavefunction calculated in Step 1. This results in a one-electron wavefunction around $z = -\alpha_0$. Step 3: Calculation of the wavefunction in the field generated by $V_0(\alpha_0; \mathbf{r})$ and the wavefunctions obtained in Step 1 and Step 2. This final wavefunction, as expected, is located around $z = 0$. During the iterations, the one-electron orbitals turn out to be non-overlapping and this property does not change at any later stage in the iterations. Hence, the exchange terms of the Hartree-Fock equations vanish, and we have had to solve in fact only Hartree equations (see for example Messiah, Ref.[105], Chap XVII, Sec.II, p.773); besides, since the Hamiltonian is spin-independent, the eigenvalues are degenerate with respect to spin.

The solution of the Hartree equations was carried out in elliptical coordinates ξ, η (see Chapter 2 or Refs.[142] and [137]) centered at $z = \pm\alpha_0$ (for the ground state the azimuthal coordinate does not appear), by representing the orbitals in a basis set of the form

$$\chi_{p,q,\gamma}(\xi, \eta) = (\xi - 1)^p \eta^q e^{-\gamma(\xi-1)}, \quad (3.6)$$

with p, q positive integers; the eigenvalues were obtained by diagonalization (see also Ref.[133]). The number of basis functions is increased at each iteration cycle. Self-consistency is achieved rapidly: about three iterations are needed for an accuracy of better than 0.1% on the energy of the three-electron system. The number of basis functions used for the last iteration was 50.

³For the case of Lithium, in contrast to H^{2-} bound in vacuum, this three-electron configuration has been suggested by Mittleman, Ref.[141].

⁴We do not expect the one-electron orbitals to have any overlap, since simple point-charge calculations show that H^{2-} becomes bound only for values of $\alpha_0 > 100$, i.e. far in the regime where H^- is dichotomized (H^- dichotomizes for $\alpha_0 > 20$).

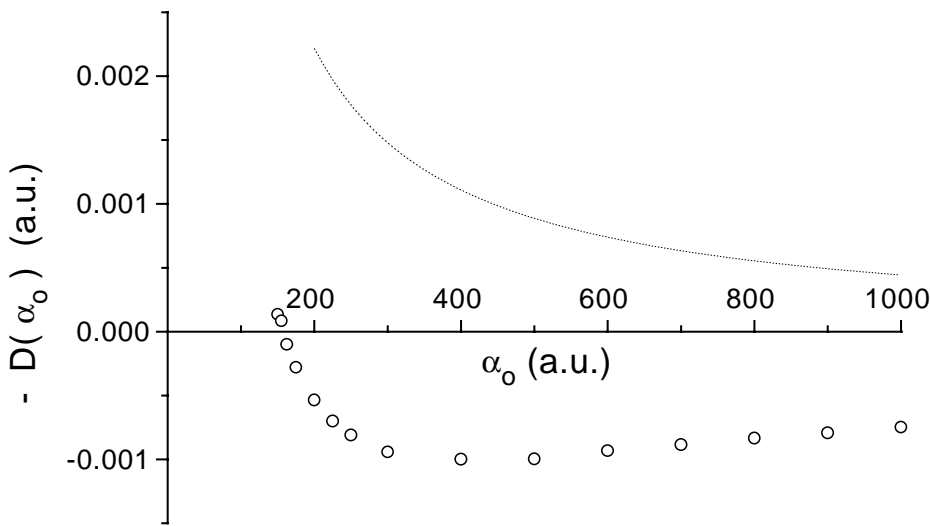


Figure 3.1: Negative of the detachment energy for the ground state of H^{2-} (open dots) in the Σ_g -manifold as a function of α_0 . For values of $\alpha_0 > 155$ (a.u.), H^{2-} exhibits a bound state. For $\alpha_0 \approx 400$, the maximum detachment energy is reached, $D_{max} = 0.0272$ eV. For α_0 slightly smaller than 155, states with negative detachment energy lie far below the top of the potential barrier (dashed line), giving rise to shape resonances.

3.4.2 The Appearance Value $\alpha_0^{(N)}$

In order to determine the "appearance value $\alpha_0^{(N)}$ of the N -electron ion (in our case, $N = 3$), one has to take into account the relaxation energy: After detachment of the electron with smallest binding energy from the N -electron ion, the remaining $N - 1$ electrons in general will rearrange themselves into a new equilibrium configuration, i.e. the configuration of lowest energy for the $(N - 1)$ -electron system. The relaxation energy is the energy difference between the energy of $N - 1$ electrons in the $(N - 1)$ -electron system and the energy of $N - 1$ electrons in the N -electron system. To take this relaxation energy into account, we shall define in general the *detachment energy* of an electron from a N -electron ion by

$$D^{(N)}(\alpha_0) \equiv W^{(N-1)}(\alpha_0) - W^{(N)}(\alpha_0) \geq 0 \quad (3.7)$$

where $W^{(N)}$ and $W^{(N-1)}$ are the total energies of the $(N - 1)$ - and N -electron ions resp., obtained with the self-consistent field calculation. Assuming that the $(N - 1)$ -electron ion exists ($W^{(N-1)} < 0$), the appearance value $\alpha_0^{(N)}$ for the N -electron ion is given by the equation $D^{(N)} = 0$. The α_0 -dependence of $D^{(3)}$ is shown in Figure 3.1: $D^{(3)}$ increases from 0 at $\alpha_0 = 155$, to a maximum value of 1.005×10^{-3} (27.3 meV), at $\alpha_0 = 445$, to decrease thereafter slowly to zero⁵. The appearance value for $N = 3$ is well within the range of lasers now under construction⁶. In Figure 3.2 we superimpose

⁵Note that $\alpha_0 = 445$ the value of the binding energy of the H atom is only 0.01.

⁶For example, a short wavelength free-electron laser is now under construction at NSLS, Brookhaven National Laboratory, designed to operate at higher than Rydberg frequencies ($\omega > 0.5$ a.u.) and intensities of about 100 a.u.

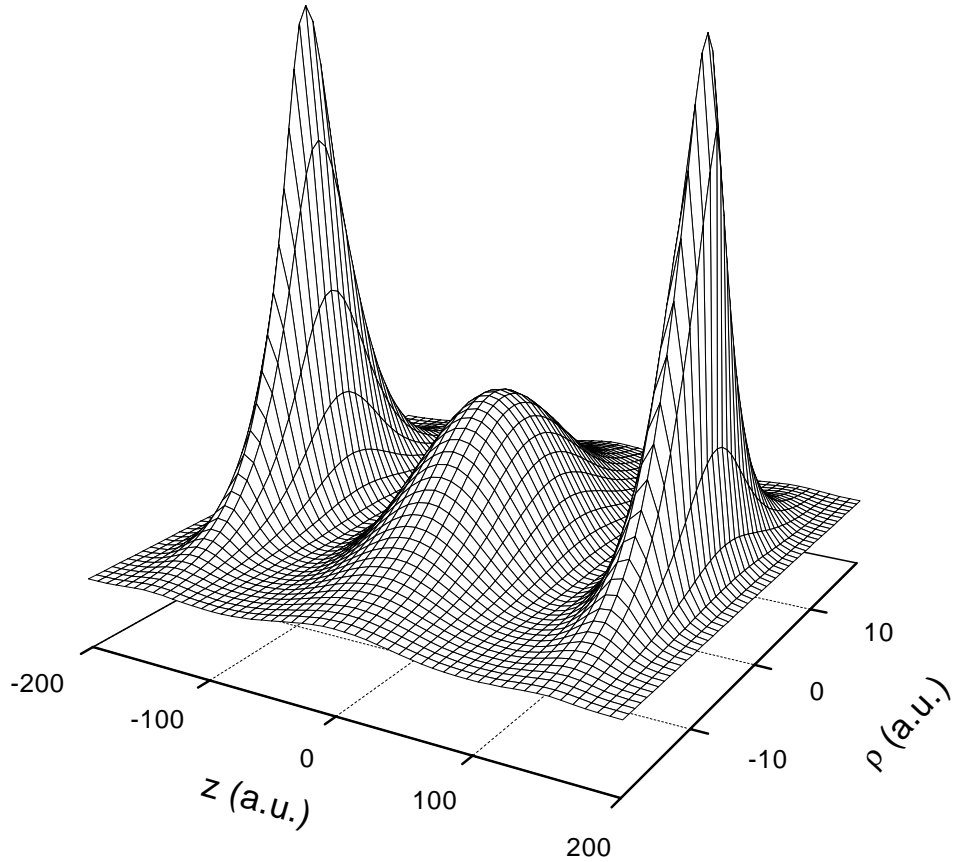


Figure 3.2: The three-electron wavefunction of H^{2-} in a linearly polarized (along z -axis) laser field at $\alpha_0 = 155$. Note there is no spatial overlap between the one-electron orbitals. The orbital of the electron centered around $z = 0$ is more diffuse in the z -direction than the orbitals at $z \pm \alpha_0$, since the potential along the polarization axis near $z = 0$ is harmonic with a small force constant. Despite the repulsive interaction with the electron around $z = 0$, the wavefunctions of the electrons at $z \pm \alpha_0$ are slightly polarized towards $|z| < \alpha_0$ due to the attraction those electrons feel with the positive line charge.

in the same plot the normalized electronic orbitals for $\alpha_0 = 155$ (appearance value). Note the non-overlap of the orbitals from their very appearance, and the more diffuse character of the orbital of the middle electron. As α_0 increases, the one-electron orbitals become more and more spatially separated. Above the appearance value, i.e. $\alpha_0 > 155$, the one-electron orbitals of the electrons around $z \pm \alpha_0$ behave according to the scaling laws for the "end-point" potential to within a few percent. Below the appearance value, $\alpha_0 < 155$, the ground state of H^{2-} has the character of a shape resonance: At long range, the (repulsive) potential due to the outer two electrons at $z = \pm\alpha_0$ dominates the (attractive) potential generated by the positive line charge, causing a potential barrier the middle electron has to penetrate in order to detach. For α_0 large enough, however smaller than the appearance value, this barrier is wide enough to support a metastable state. As α_0 increases even more, the barrier becomes wider and the metastable state turns into a bound state when α_0 has reached the appearance value $\alpha_0^{(N=3)}$.

3.4.3 On the Stability of H^{2-}

We shall now briefly address the issue of stabilization of the negative ions, explored in detail in Chapter 7. In all cases considered, the electrons are in fact independent of each other to lowest order in α_0^{-1} , so that the total decay rate $\Gamma^{(N)}$ of the N -electron ion can be expressed as the sum of the decay rates for the individual electrons.

There are two reasons, based on the applicability of the high-frequency approximation *for the middle electron only*, why the middle electron is expected to be more stable against photoionization than the two electrons around the end-points of the line charge. Firstly, since the binding energy of the middle electron is much smaller than that of the outer two electrons, it might happen that for a certain fixed frequency the high-frequency approximation holds for the electron around $z = 0$, whereas it does not for the outer two electrons. In that case, the quasienergy of the outer two electrons has a much larger imaginary part than the electron in the middle. Secondly, since the proton passes the origin $z = 0$ twice per period of the laser, the electron at $z = 0$ effectively "sees" a frequency that is twice the frequency "seen" by the outer two electrons. This is also illustrated by the expression for the total decay rate, which is (to lowest order in ω^{-1}) given by

$$\Gamma = 2\pi \sum_{m \neq 0} \sum_k |\langle \Phi_0 | V_m | k \rangle|^2 \delta(W + m\omega - E_k). \quad (3.8)$$

Since the V_m have parity m , all $V_m(z = 0) = 0$ for m odd. Therefore, the first contribution to the decay rate in the sum in Eq.(3.8) for the middle electron comes from the $m = 2$ -term. This also reflects the fact that the electron around $z = 0$ "sees" frequency twice the frequency seen by the outer two electrons.

For these reasons we expect that the lifetime of H^{2-} is mainly determined by the lifetime of the electrons near the end-points, i.e. the underlying H^- ion. This expectation will be confirmed in Chapter 7. It has been shown that the lifetime of H^- equals half the lifetime of hydrogen in the same field, see Ref.[125]. Since atomic hydrogen is fully dichotomized at those values of α_0 for which H^{2-} exists, we can apply this result to find an expression for the lifetime of H^{2-} . So the n -photon ionization rate of H^{2-} is slightly larger than twice the ionization rate of hydrogen in the same field:

$$\Gamma_n^{(H^{2-})} \simeq 2\Gamma_n^{(H)}, \quad (3.9)$$

Since we know that atomic hydrogen adiabatically stabilizes against ionization, we see from Eq.(3.9) that the AMCNI H^{2-} also adiabatically stabilizes.

A The End-Point Potential

For linear polarization, the dressed Coulomb potential $V_0(\alpha_0; \mathbf{r})$ from Eq.(3.4) can be cast into an expression containing the complete elliptic integral of the first kind⁷ K (see

⁷For details on elliptic integrals, see for example: Stegun and Abramowitz, Ref.[137], Chap. 17 p.587, or Gradshteyn and Ryzhik, Ref.[138], Chap.8, Sec.8.1 p.907.

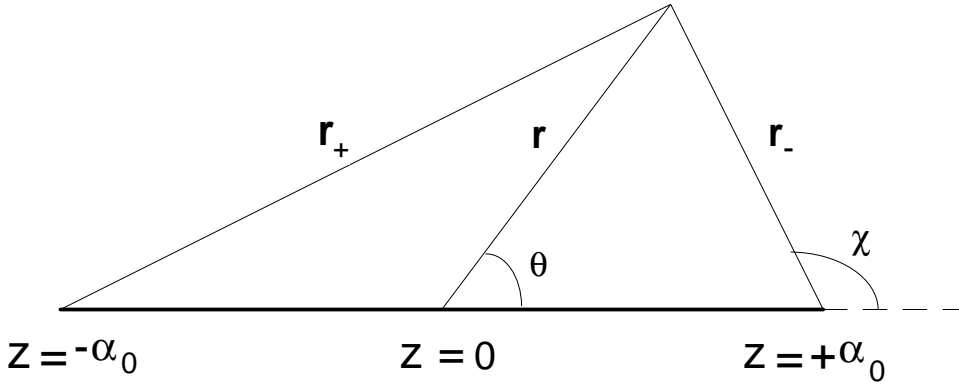


Figure 3.3: Definition of the coordinates r and θ , r_+ and r_- , and χ used to express the dressed Coulomb potential and the end-point potential, where the polarization axis is chosen to be along the z -axis.

Gavrila and Kaminski, Ref.[115]),

$$V_0(\alpha_0; \mathbf{r}) = -\frac{1}{2\pi} \int_0^{2\pi} \frac{1}{|\mathbf{r} + \alpha(\chi/\omega)|} d\chi \quad (\text{A.1})$$

$$= -\frac{2}{\pi} \frac{1}{\sqrt{r_+ r_-}} K \left[\left(\frac{1 - \hat{\mathbf{r}}_+ \cdot \hat{\mathbf{r}}_-}{2} \right)^{1/2} \right]. \quad (\text{A.2})$$

Here the vectors \mathbf{r}_+ and \mathbf{r}_- are defined as $\mathbf{r}_\pm \equiv \mathbf{r} \pm \alpha_0 \hat{\mathbf{e}}_\parallel$, with $\hat{\mathbf{e}}_\parallel$ a unit vector parallel to the polarization axis. The angle between the vectors \mathbf{r}_- and \mathbf{r} and the polarization axis are denoted as χ resp. θ ; see Figure 3.3 for the definition of the coordinates r_+ , r_- , θ and χ . Since bound states of H^{2-} (and of other AMCNI of hydrogen as well, as we shall see in the next two Chapters) appear at relatively large values of α_0 , we are preliminary interested in the asymptotic form of the dressed Coulomb potential for large α_0 . In this Appendix, the asymptotic expressions of Eqs.(A.1) and (A.2) for $V_0(\alpha_0; \mathbf{r})$ are derived, and they are shown to be equal.

Let us consider first the elliptic integral of the first kind in Eq.(A.2),

$$-\frac{2}{\pi} \frac{1}{\sqrt{r_+ r_-}} K \left[\left(\frac{1 - \hat{\mathbf{r}}_+ \cdot \hat{\mathbf{r}}_-}{2} \right)^{1/2} \right] = -\frac{2}{\pi} \frac{1}{\sqrt{r_+ r_-}} \int_0^1 \frac{dt}{\sqrt{1-t^2} \sqrt{1 - (\hat{\mathbf{r}}_+ \cdot \hat{\mathbf{r}}_- - 1)/2 t^2}}, \quad (\text{A.3})$$

and find an expression for the right-hand side of Eq.(A.3) for large α_0 in the vicinity of the end-point $z = +\alpha_0$. Denoting the unit vector perpendicular or parallel to the polarization axis as $\hat{\mathbf{e}}_\perp$ resp. $\hat{\mathbf{e}}_\parallel$, the vector \mathbf{r} can be written as

$$\mathbf{r} = \alpha_0 (1 + \frac{r_- \cos \chi}{\alpha_0}) \hat{\mathbf{e}}_\parallel + r_- \sin \chi \hat{\mathbf{e}}_\perp. \quad (\text{A.4})$$

Assuming that r_- scales as α_0^n with $n < 1$, for large α_0 Eq.(A.4) implies that

$$\lim_{\alpha_0 \rightarrow \infty} r = \alpha_0 + O(\alpha_0^0). \quad (\text{A.5})$$

From Eq.(A.4) it follows that, to lowest order in α_0^{-1} , the unit vector $\hat{\mathbf{r}}_+$ is given by

$$\hat{\mathbf{r}}_+ = \hat{\mathbf{e}}_\parallel + O(\alpha_0^{-1}). \quad (\text{A.6})$$

Moreover, $r_+ = \sqrt{r^2 + \alpha_0^2 + 2\alpha_0 r \cos \theta}$. Since for large α_0 , $\theta \ll 1$, one can make the approximation $\theta \simeq (r_- \sin \chi)/\alpha_0$. Therefore, using Eq.(A.5), asymptotically r_+ can be written as

$$\lim_{\alpha_0 \rightarrow \infty} r_+ = 2\alpha_0 + O(\alpha_0^0). \quad (\text{A.7})$$

Inserting Eqs.(A.6) and (A.7) into Eq.(A.3), the asymptotic expression for the dressed Coulomb potential reads

$$\begin{aligned} \lim_{\alpha_0 \rightarrow \infty} V_0(\alpha_0; \mathbf{r}) &= -\frac{2}{\pi} \frac{1}{\sqrt{2\alpha_0 r_-}} \int_0^1 \frac{dt}{\sqrt{1-t^2} \sqrt{1-\sin^2(\frac{\chi}{2}) t^2}} \\ &= -\frac{2}{\pi} \frac{1}{\sqrt{2\alpha_0 r_-}} K\left(\sin\left(\frac{\chi}{2}\right)\right) \\ &\equiv \tilde{V}_0(\alpha_0; \mathbf{r}), \end{aligned} \quad (\text{A.8})$$

where $\tilde{V}_0(\alpha_0; \mathbf{r})$ denotes the "end-point potential" around $z = +\alpha_0$. A similar expression holds for the potential around the end-point $z = -\alpha_0$, in which case r_- is to be replaced by r_+ . Note the square-root singularity of \tilde{V}_0 at the end-point and the angular dependence, forestalling spherical symmetry. It is known that this potential supports bound states for which the spatial extension typically scales as $r_- = O(\alpha_0^{1/3})$, which is self-consistent with the assumption made above, since $n = 1/3$. As a result of this scaling behavior, the wavefunction of the eigenstates in the dressed potential dichotomizes for large α_0 , see Refs.[123] and [122].

Starting from Eq.(A.1), one can derive the asymptotic expression for the dressed Coulomb potential by taking $\alpha(t) = \alpha_0 \hat{\mathbf{e}}_\parallel \cos \omega t$, such that at $t = 0$ the proton is at the end-point. Taking the origin in the end-point, the expression for V_0 , expanding the integrand in powers of t , reads

$$V_0(\alpha_0; \mathbf{r}') = -\frac{1}{2\pi} \int_{-\pi}^{+\pi} \frac{dt}{|\mathbf{r}' - \alpha_0 \hat{\mathbf{e}}_\parallel(-\frac{1}{2}t^2 + \frac{1}{24}t^4 + \dots)|}. \quad (\text{A.9})$$

Changing to integration variable $u = \sqrt{\alpha_0}t$ one gets after taking the limit $\alpha_0 \rightarrow \infty$,

$$\begin{aligned} \lim_{\alpha_0 \rightarrow \infty} V_0(\alpha_0; \mathbf{r}') &= -\frac{1}{2\pi \sqrt{\alpha_0}} \int_{-\infty}^{+\infty} \frac{du}{|\mathbf{r}' - \frac{1}{2}\hat{\mathbf{e}}_\parallel u^2|} \\ &= -\frac{1}{2\pi} \int_{-\infty}^{+\infty} \frac{dt}{|\mathbf{r}' - \frac{1}{2}\alpha_0 \hat{\mathbf{e}}_\parallel t^2|}. \end{aligned} \quad (\text{A.10})$$

The lowest order correction to Eq.(A.10) is of order $O(\alpha_0^{-3/2})$. From Eq.(A.10) we see that the asymptotic form of V_0 is generated by an uniformly accelerated proton moving along the polarization axis with its turning point at an end-point. Next it will be shown that the asymptotic form in Eq.(A.10) is equal to that in Eq.(A.8).

Changing to the new variable $x = \frac{1}{2}\alpha_0 t^2$, Eq.(A.10) can be written as

$$\begin{aligned} -\frac{1}{2\pi} \int_{-\infty}^{+\infty} \frac{dt}{|\mathbf{r}' - \frac{1}{2}\alpha_0 \hat{\mathbf{e}}_\parallel t^2|} &= -\frac{1}{\pi \sqrt{\alpha_0}} \int_0^{+\infty} \frac{dx}{\sqrt{2x} |\mathbf{r}' - x \hat{\mathbf{e}}_\parallel|} \\ &= -\frac{1}{\pi \sqrt{2\alpha_0}} \int_0^\infty \frac{dx}{\sqrt{x^3 + 2rx^2 \cos \chi + r^2 x}} \end{aligned} \quad (\text{A.11})$$

Since the denominator has one real root $x = 0$, the integral in Eq.(A.11) can be solved analytically (see Abramowitz and Stegun, Ref.[137] p.597 Eq.17.4.70 and p.589 Eq.17.2.6), yielding for the right-hand side of Eq.(A.11)

$$-\frac{1}{\pi\sqrt{2\alpha_0 r}} \int_0^\pi \frac{d\gamma}{\sqrt{1 - \sin^2 \frac{\chi}{2} \sin^2 \gamma}}. \quad (\text{A.12})$$

Changing to the new variable $t = \sin \gamma$, one finally finds for Eq.(A.10)

$$\begin{aligned} \lim_{\alpha_0 \rightarrow \infty} V_0(\alpha_0; \mathbf{r}') &= -\frac{2}{\pi} \frac{1}{\sqrt{2\alpha_0 r}} \int_0^1 \frac{dt}{\sqrt{1-t^2} \sqrt{1 - \sin^2 \frac{\chi}{2} t^2}} \\ &= -\frac{2}{\pi} \frac{1}{\sqrt{2\alpha_0 r}} K\left(\sin \frac{\chi}{2}\right), \end{aligned} \quad (\text{A.13})$$

which equals Eq.(A.8), QED.

4

CIRCULARLY POLARIZED LASER FIELDS AS A MAGIC POTION FOR AMCNI

4.1 Introduction

Superintense laser fields can change the nature of atoms and ions drastically, and can give rise to paradoxical effects. In order to get a better understanding of these effects, non-perturbative methods are required to describe the interaction between the field and the atom or ion. One of the drastic changes is the distortion of the electronic wavefunction in the field, the distortion being polarization dependent: for both linear and circular polarization, the atomic distortion of hydrogen is studied by Pont (see Pont *et al.*, Ref.[122] and Pont, Ref.[124] respectively). Another, rather counter intuitive, effect arising in superintense laser-atom physics is adiabatic stabilization against photoionization, i.e., the ionization rate starts to decrease at increasing intensity, in contrast to the prediction of Fermi's Golden Rule. For one-electron atoms, stabilization has been predicted theoretically for the ground state of hydrogen in a circularly polarized field by M. Pont and M. Gavrila [28] and for Rydberg states by R.J. Vos and M. Gavrila [70]. Moreover, stabilization is confirmed experimentally, see Refs.[128] and [129]. Besides the effects mentioned above, revealed by both theoretical and experimental research on superintense laser-atom physics in the last decade, it is the exotic phenomenon of light-induced states (see also Chapter 1 in this Thesis, Sec.1.3.3) which forms the motive behind the investigation presented in this Chapter. Light-induced excited states are closely related to shadow states, that were first introduced by R.J. Eden and J.R. Taylor [96]. For the connection between shadow states and light-induced (excited) states, see for example Dörr *et al.*, Ref.[132] and Muller *et al.*, Ref.[133]. Light induced (excited) states are states that exist only in the field. For a clear explanation about their appearance we refer to Potvliege and Shakeshaft in Ref.[95]. Using high-frequency Floquet theory (HFFT), in Chapter 3 we have shown numerically that the simplest atomic multiply charged negative ion (AMCNI) of hydrogen, H^{2-} , can have bound states in a superintense high-frequency laser field, while, as shown by Lieb in Ref.[139], no bound states exist in vacuo. The main parameter determining the existence of the AMCNI appears to be $\alpha_0 = E_0/\omega^2$, where E_0 and ω are the amplitude resp. frequency of the field. Here we will found the existence of multiply charged negative ions analytically, extended to an arbitrary number of electrons N . In particular, we are interested in the scaling behavior of the electronic wavefunctions and total energy of the AMCNI as a function of α_0 . In the high-frequency limit, the polarization of the field determines the symmetry of the potential generated by the positive nucleus. In this Chapter we focus on the case of circular polarization. Besides, the case of a bichromatic radiation field, obtained by superposing two circularly polarized fields, is discussed.

The non-perturbative theory we apply for the laser-ion interaction is high-frequency Floquet theory (see Chapter 1, Sec.1.5 of this Thesis or for example Gavrila, Ref.[116]). Preceded by a review of the one-electron case, the appearance and structure of AMCNI in a circularly polarized field is described in Section 4.2, where we will comment the conditions for the applicability of HFFT for predicting the appearance of AMCNI as well. In Section 4.3 the bichromatic case is treated, and this Chapter will be concluded in Section 4.4, where experimental realizability and stability is commented.

4.2 Atomic Structure in Circularly Polarized Fields

4.2.1 Atomic Hydrogen

To gain insight in the structure of an AMCNI induced by a circularly polarized laser field, we start to look at the one-electron case (atomic hydrogen). For details of the distortion of atomic hydrogen in an intense high-frequency circularly polarized laser field, see M. Pont, Ref.[124]. Due to the cylindrical symmetry of the dressed potential, it is appropriate to adopt circular cylindrical coordinates (ρ, z, φ) [143], centered around the propagation axis of the light. The one-electron HFFT Hamiltonian is given by

$$H^{(1)}(\rho, z, \varphi) = H_0(\rho, z) - \frac{1}{2\rho^2} \frac{\partial^2}{\partial \varphi^2}, \quad (4.1)$$

where

$$H_0(\rho, z) = -\frac{1}{2} \left[\frac{\partial^2}{\partial \rho^2} + \frac{1}{\rho} \frac{\partial}{\partial \rho} + \frac{\partial^2}{\partial z^2} \right] + V_0^c(\alpha_0; \rho, z). \quad (4.2)$$

In Eq.(4.2), $V_0^c(\alpha_0; \rho, z)$ is the dressed potential for the circular case. It has been shown [124] that at large α_0 the Hamiltonian H_0 supports eigenfunctions $\tilde{\Phi}_{\nu|\lambda|}(\rho, z)$ that have an azimuth-independent amplitude. Moreover, $\tilde{\Phi}_{\nu|\lambda|}(\rho, z)$ is negligible small at distances from the circle of charge larger than $O_1(\alpha_0^{1/2})$; this phenomenon is called toroidal shaping (for details about the quantum numbers ν and λ , see Ref.[124]: ν can be compared to the principal quantum number in a spherically symmetric problem, and λ to the azimuthal quantum number with the line of charge as quantization axis). Moreover, the leading term in the binding energy $E_{\nu|\lambda|}$ scales as $\alpha_0^{-1} \ln \alpha_0$. For the ground state, $\nu = 1$ and $\lambda = 0$, we have

$$E_{1,0} = -\frac{1}{2\pi\alpha_0} \left[\ln \frac{64\alpha_0}{\pi} - 0.360 \right], \quad (4.3)$$

which is correct up to order $O_0(\alpha_0^{-2} \ln^2 \alpha_0)$. This higher-order correction comes from the motion not tangential to the circle of charge, i.e. in the (ρ, z) -plane. This motion or polarization of the electronic wavefunction perpendicular to the circle of charge vanishes for $\alpha_0 \rightarrow \infty$, since in that case the electron locally sees a potential that does not differ from a potential generated by a straight line. For finite α_0 however, the one-electron wavefunction around a certain angle φ is polarized towards the origin of the circle by that part of the nuclear charge around angle $\varphi + \pi$. Separating the φ -dependent part of the full wavefunction Ψ ,

$$\Psi_{\nu|\lambda|m}(\rho, z, \varphi) = \tilde{\Phi}_{\nu|\lambda|}(\rho, z) \frac{e^{im\varphi}}{\sqrt{2\pi}}, \quad (4.4)$$

it can be seen from Eq.(4.1) that the eigenvalue of $H^{(1)}$ contains, in addition to the eigenvalue of H_0 , a contribution from the azimuthal motion equal to m^2/ρ^2 . This contribution is of order α_0^{-2} , which, for the ground state, reduces to zero ($m = 0$).

4.2.2 The Multiply Charged Negative Ion

Let us now turn to the N -electron ($N > 2$) Hamiltonian,

$$H^{(N)} = \sum_{i=1}^N \left[H^{(1)}(\rho_i, z_i, \varphi_i) + \sum_{j=1}^{i-1} \frac{1}{r_{ij}} \right], \quad (4.5)$$

with $r_{ij} \equiv |\mathbf{r}_i - \mathbf{r}_j|$ and where $H^{(1)}(\rho_i, z_i, \varphi_i)$ is the one-electron Hamiltonian as in Eq.(4.1) for electron i . In the presence of other electrons, the toroidal wavefunction is expected to polarize towards the outside of the charge ring, due to the component of the e-e repulsion perpendicular to the charge circle. Using the scaling laws for the size and excitation energies of the atomic case, this polarization can be calculated perturbatively. In dominant (second) order, the polarizability is given by the square of the size of the system divided by its energy level spacing. This leads to a polarizability of order $O(\alpha_0^2)$. Since the interelectronic distance scales linearly with α_0 , the polarization due to the monopole interaction (in the plane of the circle of charge) scales as α_0^0 , and thus becomes negligible compared to the size of the wavefunction¹. For determining the structure of AMCNI we thus suppose that all electrons have the same toroidal shape as in the case of atomic hydrogen, i.e. they reside very close to the charge ring.

Since the attraction to the charge ring is rotational symmetric, the azimuthal structure of the AMCNI is purely determined by the repulsive interaction between the electrons. In order to investigate this, we decompose the N -electron Hamiltonian as follows:

$$\begin{aligned} H^{(N)} &= H' + H'' \\ H' &= \sum_{i=1}^N H_0(\rho_i, z_i) \\ H'' &= \sum_{i=1}^N \left[-\frac{1}{2\rho_i^2} \frac{\partial^2}{\partial \varphi_i^2} + \sum_{j=1}^{i-1} \frac{1}{r_{ij}} \right]. \end{aligned} \quad (4.6)$$

¹Spontaneous symmetry breaking *perpendicular* to the plane of the charge circle could in principle occur if the electrons would be able to polarize each other sufficiently strong in this direction. More precisely, such "puckering" would occur if a symmetry perturbation of one of the electrons would polarize the others so much that the electric field generated by this polarization would be able to sustain or enhance the original symmetry perturbation. This does not happen in our case: consider two of the N electrons on the circle of charge, labelled i and j , separated by a distance r_{ij} which is $O(\alpha_0)$. Suppose that electron i is puckering, thereby inducing a dipole moment \mathbf{P}_i perpendicular to the circle of charge. This dipole moment induces a field $\varepsilon_i(\mathbf{r}_j)$ which equals $\varepsilon_i(\mathbf{r}_j) = -\mathbf{P}_i/r_{ij}^3$. This field gives rise to a polarization (puckering) of electron j , inducing dipole moment $\mathbf{P}_j = \chi \varepsilon_i(r_j)$, where χ is the polarizability which scales as α_0^2 (see text). Dipole moment \mathbf{P}_j generates a field at \mathbf{r}_i which is equal to $\varepsilon_j(\mathbf{r}_i) = -\mathbf{P}_j/r_{ij}^3$. This latter field induces a dipole $\mathbf{P}'_i = \chi^2/r_{ij}^6 \mathbf{P}_i = O(\alpha_0^{-2})\mathbf{P}_i$. For the ground state of the AMCNI, one gets $\mathbf{P}'_i \leq 144/\alpha_0^2 \mathbf{P}_i$. This result implies that, for $\alpha_0 \leq 12$ a finite dipole moment perpendicular to the circle of charge does induce a spontaneous symmetry braking of the ring symmetry. However, since the appearance values of the AMCNI are much larger than 12, see below, this will not happen in our case.

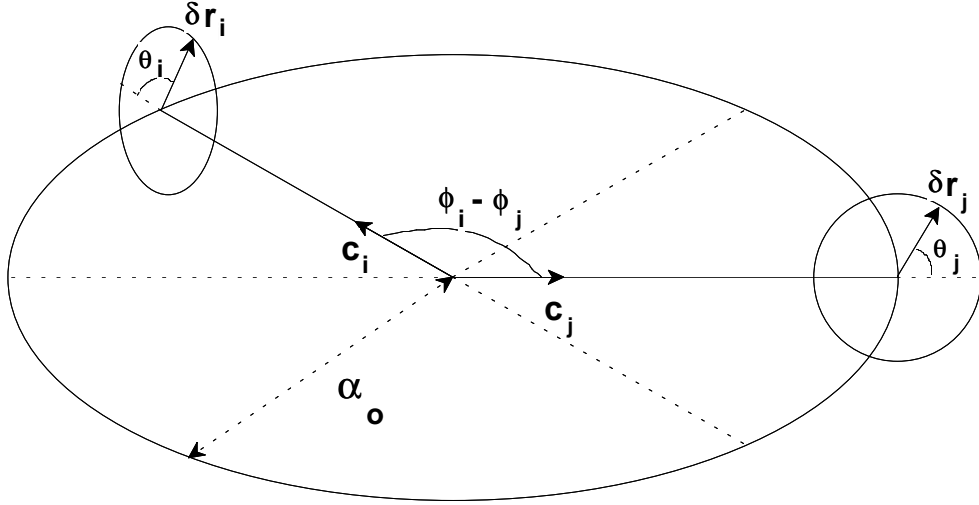


Figure 4.1: Illustration of the definition of the coordinates determining the position of the electrons in an AMCNI for circular polarization. The repulsive interaction between the electrons, which are labelled by i,j , can be expressed in terms of the azimuthal angles φ_i , the angles θ_i and the distance from the circle of charge δr_i , see Eq.4.7.

For large α_0 , H' is that part of the Hamiltonian that supports a toroidally shaped eigenfunction, $\prod_{i=1}^N \tilde{\Phi}_{\nu_i, |\lambda_i|}(\rho_i, z_i)$. H'' describes, to lowest order in α_0 , the azimuthal motion only. In order to prove this, consider the electron-electron (e-e) interaction in H'' . We denote the N -electron wavefunction as $\Psi^{(N)}(\mathbf{r}_1, \dots, \mathbf{r}_N)$. Due to the splitting of the total Hamiltonian into H' and H'' and the toroidal shape of the eigenfunctions of H' , the contribution to the energy $W^{(N)}(\alpha_0) = \langle \Psi^{(N)} | H^{(N)} | \Psi^{(N)} \rangle$ comes from those \mathbf{r}_i lying within the torus. The \mathbf{r}_i can be written as $\mathbf{r}_i = \alpha_0 \hat{\mathbf{c}}_i + \delta \mathbf{r}_i$, where $\hat{\mathbf{c}}_i$ is a unit radial vector pointing towards the circle of charge, see Figure 4.1, and $\delta \mathbf{r}_i$ a vector perpendicular to the circle with $\langle \delta \mathbf{r}_i \rangle = O_1(\alpha_0^{1/2})$, see Ref.[124]. In terms of $\delta \mathbf{r}$ we get the following expression for the e-e interaction,

$$\frac{1}{r_{ij}} = \frac{1}{\sqrt{2}\alpha_0} (1 - \cos(\varphi_i - \varphi_j))^{-1/2} (1 + (|\delta \mathbf{r}_i| \cos \theta_i + |\delta \mathbf{r}_j| \cos \theta_j) O_2(\alpha_0^{-1})). \quad (4.7)$$

It is clear from Eq.(4.7) that the dominant term in the e-e interaction comes from the angular distribution of the electrons and is of order α_0^{-1} . The corrective term in the e-e interaction, of order $\alpha_0^{-3/2}$, comes from the extension $\delta \mathbf{r}$ of the electronic wavefunctions perpendicular to the circle. This proves that to lowest order in α_0 the Hamiltonian H'' is a function of the azimuthal angles only. Let us therefore split the N -electron wavefunction into a product of normalized eigenfunctions of H' times an arbitrary normalized function A of the angles $\varphi_1, \dots, \varphi_N$,

$$\Psi_{\nu, \lambda}^{(N)} = \prod_{i=1}^N \tilde{\Phi}_{\nu_i, |\lambda_i|}(\rho_i, z_i) \times A(\varphi_1, \dots, \varphi_N), \quad (4.8)$$

normalized as

$$\begin{aligned}\left\langle \widetilde{\Phi}_{\nu_i,|\lambda_i|}(\rho_i, z_i) | \widetilde{\Phi}_{\nu_i,|\lambda_i|}(\rho_i, z_i) \right\rangle &= 1 \quad \forall i = 1, \dots, N, \\ \langle A(\varphi_1, \dots, \varphi_N) | A(\varphi_1, \dots, \varphi_N) \rangle &= 1.\end{aligned}\quad (4.9)$$

In Eq.(4.8), ν, λ abbreviates the set $\nu_i, \lambda_i \forall i$. Using Eqs.(4.5) through (4.8) we get for the Schrödinger equation

$$\begin{aligned}H^{(N)} \Psi_{\nu, \lambda}^{(N)} &= \left[\sum_{i=1}^N E_{\nu_i, |\lambda_i|} + O_0(\ln^2 \alpha_0 / \alpha_0^2) \right] \Psi_{\nu, \lambda}^{(N)} + \\ &\quad \{H'' A(\varphi_1, \dots, \varphi_N)\} \prod_{i=1}^N \widetilde{\Phi}_{\nu_i, |\lambda_i|}(\rho_i, z_i) \quad (4.10)\end{aligned}$$

$$= W_{\nu, \lambda}^{(N)}(\alpha_0) \Psi_{\nu, \lambda}^{(N)}, \quad (4.11)$$

where we can rewrite H'' in the second term in Eq.(4.10), using $\langle \rho_i \rangle = \langle \alpha_0 + \cos \theta_i |\delta \mathbf{r}_i| \rangle = \alpha_0(1 + O_1(\alpha_0^{-1/2}))$, as

$$\begin{aligned}H'' &= -\frac{1}{2\alpha_0^2} \sum_{i=1}^N \left(1 - 2 \frac{|\delta \mathbf{r}_i| \cos \theta_i}{\alpha_0} + |\delta \mathbf{r}_i|^2 O_1(\alpha_0^{-2}) \right) \frac{\partial^2}{\partial \varphi_i^2} + \\ &\quad \sum_{i=1}^N \sum_{j=1}^{i-1} \frac{1}{\sqrt{2}\alpha_0} \frac{(1 + (|\delta \mathbf{r}_i| \cos \theta_i + |\delta \mathbf{r}_j| \cos \theta_j) O_2(\alpha_0^{-1}))}{\sqrt{1 - \cos(\varphi_i - \varphi_j)}} \\ &\equiv \frac{1}{\alpha_0^2} \sum_{i=1}^N \left\{ -\frac{1}{2} \frac{\partial^2}{\partial \varphi_i^2} + \sum_{j=1}^{i-1} \frac{\alpha_0}{\sqrt{2}} V(\varphi_i - \varphi_j) \right\}. \quad (4.12)\end{aligned}$$

Treating the term in the kinetic energy proportional to $|\delta \mathbf{r}_i| \cos \theta_i$ perturbatively, results in a correction to H'' of order $O(\alpha_0^{-4})$, which we neglect (note that due to parity this correction comes in through second order only). Moreover, we have included the corrective term $O_2(\alpha_0^{-1})$ into the definition of the potential V . Since we are interested in the appearance values $\alpha_0^{(N)}$, we will from now on concentrate on the ground state only. This means that $\lambda_i = 0$, $\nu_i = 1 \forall i$, and we will omit the subscripts λ and ν for simplicity.

4.2.3 Transition to Real Normal Coordinates

Because of the cylindrical symmetry of the system, the configuration with the N electrons on the corners of a regular N sided polygon is an equilibrium configuration. For the moment we assume that this equilibrium is stable, and that this configuration produces the absolute minimum of the repulsive energy (and thus of $W^{(N)}(\alpha_0)$). The consistency of this assumption will be shown later. The differences in the azimuthal angles then obey

$$\varphi_{k+1} - \varphi_k = \frac{2\pi}{N}; \quad k = 1, \dots, N-1. \quad (4.13)$$

Let us denote the values of φ_k minimizing the total energy as φ_k^0 , and write φ_k as

$$\begin{aligned}\varphi_k &= \varphi_k^0 + \Delta \varphi_k \\ &\equiv (k-1) \frac{2\pi}{N} + \Delta \varphi_k,\end{aligned}\quad (4.14)$$

where $\Delta\varphi_k$ is a deviation from the equilibrium value φ_k^0 and where $\varphi_1^0 \equiv 0$. We introduce the variable $\beta_k \equiv \varphi_j^0 - \varphi_{j+k}^0 = \frac{2\pi k}{N}$, which, due to the equilibrium configuration of the N electrons on the corners of a regular N -sided polygon, is j -independent. By expanding the total potential up to second order in the $\Delta\varphi_j - \Delta\varphi_{j+k}$, the corrective term is of order $(\Delta\varphi_j - \Delta\varphi_{j+k})^3$. The harmonic approximation of the total repulsive potential in Eq.(4.12) can be written as

$$\begin{aligned}
V_{rep} &= \frac{1}{\alpha_0^2} \sum_{i=1}^N \left\{ \frac{\alpha_0}{\sqrt{2}} \sum_{j=1}^{i-1} V(\varphi_i - \varphi_j) \right\} \\
&= \frac{1}{2\sqrt{2}\alpha_0} \sum_{k=1}^{N-1} \left[\sum_{j=1}^N V(\beta_k + \Delta\varphi_j - \Delta\varphi_{j+k}) \right] \\
&= \frac{1}{2\sqrt{2}\alpha_0} \sum_{k=1}^{N-1} \sum_{j=1}^N \left[V(\beta_k) + \frac{1}{2} V''(\beta_k) (\Delta\varphi_j - \Delta\varphi_{j+k})^2 + O(\Delta\varphi_j - \Delta\varphi_{j+k})^3 \right] \\
&= \frac{N}{2\sqrt{2}\alpha_0} \sum_{k=1}^{N-1} V(\beta_k) + \sum_{j=1}^N \left[\frac{1}{2\sqrt{2}\alpha_0} \sum_{k=1}^{N-1} V''(\beta_k) \right] \Delta\varphi_j^2 - \\
&\quad \frac{1}{2\sqrt{2}\alpha_0} \sum_{j=2}^N \sum_{i=1}^{j-1} [V''(\beta_{j-i}) + V''(\beta_{N-j+i})] \Delta\varphi_i \Delta\varphi_j + O(\Delta\varphi_j - \Delta\varphi_{j+k})^3 \\
&\equiv \frac{N}{2\sqrt{2}\alpha_0} \sum_{k=1}^{N-1} V(\beta_k) + \frac{1}{2} (\Delta\varphi_1, \dots, \Delta\varphi_N) \mathbf{V} \begin{pmatrix} \Delta\varphi_1 \\ \vdots \\ \Delta\varphi_N \end{pmatrix} + \\
&\quad O(\Delta\varphi_j - \Delta\varphi_{j+k})^3. \tag{4.15}
\end{aligned}$$

In Eq.(4.15), we have defined a matrix \mathbf{V} , representing the second order term of the expansion of the total repulsive potential. The diagonal terms of the matrix \mathbf{V} are identical and equal to

$$\mathbf{V}_{ii} = \frac{1}{2\sqrt{2}\alpha_0} \sum_{k=1}^{N-1} V''(\beta_k). \tag{4.16}$$

After symmetrization of \mathbf{V} , the off diagonal elements \mathbf{V}_{ij} ($j > i$) can be written as

$$\mathbf{V}_{ij} = \frac{-1}{4\sqrt{2}\alpha_0} [V''(\beta_{j-i}) + V''(\beta_{N-j+i})] = \mathbf{V}_{ji}. \tag{4.17}$$

From Eq.(4.17) we see that $\mathbf{V}_{ij} = \mathbf{V}_{i+1,j+1}$. Therefore, all elements in an off-diagonal are the same as well. Moreover, \mathbf{V} can always be written as a symmetric matrix. These properties of \mathbf{V} imply that we can find the eigenmodes by introducing normal coordinates u_m of the form

$$u_m = \frac{1}{\sqrt{N}} \sum_{j=1}^N \exp(-imj\frac{2\pi}{N}) \Delta\varphi_j. \tag{4.18}$$

On the basis spanned by the normal coordinates, \mathbf{V} is diagonal, the diagonal elements \mathbf{V}_{mm} being the force constants of eigenmode m . Moreover, from Eq.(4.18) we see that $u_m^* = u_{-m}$, where, due to rotational symmetry, $u_{-m} = u_{N-m}$. For later convenience

it is useful to change to *real* normal coordinates. Since $u_m = u_{N-m}^*$, the real normal coordinates u'_m are defined as ($m < N/2$)

$$\begin{aligned} u'_m &\equiv \frac{1}{\sqrt{2}}(u_m + u_{N-m}) = \sqrt{\frac{2}{N}} \sum_{j=1}^N \cos(mj\frac{2\pi}{N}) \Delta\varphi_j, \\ u'_{N-m} &\equiv \frac{i}{\sqrt{2}}(u_m - u_{N-m}) = \sqrt{\frac{2}{N}} \sum_{j=1}^N \sin(mj\frac{2\pi}{N}) \Delta\varphi_j, \\ u'_{N/2} &\equiv u_{N/2} = \frac{1}{\sqrt{N}} \sum_{j=1}^N (-1)^j \Delta\varphi_j ; \quad (N \text{ even}), \\ u'_N &\equiv u_N = \frac{1}{\sqrt{N}} \sum_{j=1}^N \Delta\varphi_j. \end{aligned} \quad (4.19)$$

If we express the quadratic term in Eq.(4.15) in terms of u'_m , we get for the total repulsive potential,

$$V_{rep} = \frac{N}{2\sqrt{2}\alpha_0} \sum_{k=1}^{N-1} V(\beta_k) + \frac{1}{2} \sum_{m=1}^N \frac{(u'_m)^2 + (u'_{N-m})^2}{2} \sum_{k=1}^{N-1} \frac{V''(\beta_k)}{2\sqrt{2}\alpha_0} \left(2 - 2 \cos \frac{2\pi mk}{N} \right). \quad (4.20)$$

In terms of the real normal coordinates, we see that the total repulsive potential is generated by the sum of the repulsive potential of N point charges with unit charge, located at the N corners of the N -sided polygon, and the potential of N uncoupled harmonic oscillators. With Eqs.(4.15) and (4.20) we can rewrite Eq.(4.12) as

$$H''A = \frac{1}{\alpha_0^2} \sum_{m=1}^N \left\{ -\frac{1}{2} \frac{\partial^2}{\partial(u'_m)^2} + \frac{1}{2} \alpha_0 C_m^{(N)} (u'_m)^2 \right\} A + \frac{N}{2\sqrt{2}\alpha_0} \sum_{k=1}^{N-1} V(\beta_k) A. \quad (4.21)$$

The coefficient $C_m^{(N)}$ in the force constant $\alpha_0 C_m^{(N)}$ of the m -th oscillator \mathbf{V}_{mm} has magnitude

$$C_m^{(N)} \equiv \frac{1}{2\sqrt{2}} \sum_{k=1}^{N-1} V''(\beta_k) \left(2 - 2 \cos \frac{2\pi mk}{N} \right). \quad (4.22)$$

We see that $C_m^{(N)} = C_{N-m}^{(N)}$, which proves that the matrix \mathbf{V} is invariant under the coordinate transformation described in Eq.(4.19). Moreover, for $m = N$, we see from Eq.(4.22) that $C_N^{(N)} = 0$, i.e. normal mode N describes a free rotation. This can also be understood in terms of coordinates $\Delta\varphi_j$, since $C_N^{(N)}$ is the force constant for the motion along coordinate u_N , which lies, in the N -dimensional space, along the line $\Delta\varphi_1 = \Delta\varphi_2 = \dots = \Delta\varphi_N$. So, in Eq.(4.21), for $m = N$, the Schrödinger equation reduces to a Schrödinger equation for a free particle moving along coordinate u_N . We therefore separate the function A , which we write now as a function of the normal coordinates u'_1, \dots, u'_N , as follows,

$$A(u'_1, \dots, u'_N) \equiv A'(u'_1, \dots, u'_{N-1}) \exp(-iqu'_N). \quad (4.23)$$

Now Eq.(4.21) can be rewritten as

$$\begin{aligned} H'' A'(u'_1, \dots, u'_N) &= \frac{1}{\alpha_0^2} \sum_{m=1}^{N-1} \left\{ -\frac{1}{2} \frac{\partial^2}{\partial(u'_m)^2} + \frac{1}{2} \alpha_0 C_m^{(N)} (u'_m)^2 \right\} A'(u'_1, \dots, u'_{N-1}) + \\ &\quad \left\{ \frac{q^2}{\alpha_0^2} + \frac{N}{2\sqrt{2}\alpha_0} \sum_{k=1}^{N-1} V(\beta_k) \right\} A'(u'_1, \dots, u'_N). \end{aligned} \quad (4.24)$$

For the ground state however, the free rotor does not rotate, i.e. $q = 0$, and we are left with the following Schrödinger equation for the azimuthal coordinates,

$$H'' A' = \frac{1}{\alpha_0^2} \sum_{m=1}^{N-1} \left\{ -\frac{1}{2} \frac{\partial^2}{\partial(u'_m)^2} + \frac{1}{2} \alpha_0 C_m^{(N)} (u'_m)^2 + \frac{N\alpha_0}{2\sqrt{2}} V(\beta_m) \right\} A'. \quad (4.25)$$

Since the AMCNI in a circularly polarized field is invariant under azimuthal rotations over 2π , the total potential in Eq.(4.25) should be invariant under these rotations as well. With Eq.(4.19), this implies that the potential in Eq.(4.25) has to be invariant under the following transformation ($m < N/2$)

$$\begin{aligned} u'_m &\longrightarrow u'_m + k2\pi q_m \\ u'_{N-m} &\longrightarrow u'_{N-m} + k2\pi q_{N-m} \\ u'_{N/2} &\longrightarrow u'_{N/2} + k2\pi q_N \\ u'_N &\longrightarrow u'_N + k2\pi q_N \end{aligned} \quad (4.26)$$

where k is an integer and the q 's are given by

$$\begin{aligned} q_m &= \sqrt{\frac{2}{N}} \min_{j=1}^N \left\{ \cos mj \frac{2\pi}{N} \right\} \\ q_{N-m} &= \sqrt{\frac{2}{N}} \min_{j=1}^N \left\{ \sin mj \frac{2\pi}{N} \right\} \\ q_N &= \frac{1}{\sqrt{N}}. \end{aligned} \quad (4.27)$$

The harmonic expansion of the repulsive potential, expressed in terms of the normal coordinates, is exact within order $O((u'_m)^2)$. In order to realize the L^1 rotational invariance of the potential in Eq.(4.25), while maintaining the same order of accuracy, we can substitute

$$u'_m \longrightarrow x_m \equiv q_m \sin \frac{u'_m}{q_m} = u'_m + O((u'_m)^3). \quad (4.28)$$

Since the coordinate x_m is invariant under rotations over 2π of any of the N azimuthal angles φ_j , the Hamiltonian is if expressed in terms of the coordinate x_m .

4.2.4 Expansion of Binding Energy in α_0^{-1}

Let us now return to Eq.(4.10). Since we have an expression for the second term in Eq.(4.10), namely Eq.(4.21), we can give an expression for the energy of the N -electron ion

$$\begin{aligned} W^{(N)}(\alpha_0) &= \langle \Psi^{(N)} | H^{(N)} | \Psi^{(N)} \rangle \\ &= \langle \Psi^{(N)} | H' | \Psi^{(N)} \rangle + \langle \Psi^{(N)} | H'' | \Psi^{(N)} \rangle, \end{aligned} \quad (4.29)$$

where the last term can be evaluated using Eq.(4.25) together with the known expressions for the energy of the harmonic oscillator. The scaling behavior of the energy $W^{(N)}(\alpha_0)$ of an AMCNI can be extracted from the scaling laws for both energy and wavefunction of the one-electron problem, as mentioned above, together with the scaling behavior of the eigenvalues and eigenfunctions of Eq.(4.25). It is important to note that, in determining this scaling behavior, the operator V , and thus also the $C_m^{(N)}$, depend on the distance to the circle of charge, see Eq.(4.12). In order to facilitate the expression for the α_0 -dependence of the total energy, let us define the potential \tilde{V} as

$$\begin{aligned} V(\beta_m) &\equiv \tilde{V}(\beta_m) (1 + (|\delta\mathbf{r}_j| \cos \theta_j + |\delta\mathbf{r}_{j+m}| \cos \theta_{j+m}) O_2(\alpha_0^{-1})) \\ &\equiv \tilde{V}(\beta_m) + \tilde{V}_p(\beta_m). \end{aligned} \quad (4.30)$$

Similarly, through the definition of the force constants in Eq.(4.22), we can define a $\tilde{C}_m^{(N)}$ and $\tilde{C}_{p_m}^{(N)}$,

$$C_m^{(N)} \equiv \tilde{C}_m^{(N)} + \tilde{C}_{p_m}^{(N)}. \quad (4.31)$$

Note that $\tilde{V}(\beta_m)$ and $\tilde{C}_m^{(N)}$ do *not* depend on α_0 and are \mathbf{r} -independent. Moreover, the α_0 dependence of $\tilde{V}_p(\beta_m)$ and $\tilde{C}_{p_m}^{(N)}$ is the same, i.e. $(|\delta\mathbf{r}_j| \cos \theta_j + |\delta\mathbf{r}_{j+m}| \cos \theta_{j+m}) O_2(\alpha_0^{-1})$. Inserting Eqs.(4.30) and (4.31) into Eq.(4.25), we can decompose H'' into

$$H'' = \tilde{H}'' + \frac{1}{\alpha_0} \tilde{H}_p'' \quad (4.32)$$

where

$$\begin{aligned} \tilde{H}'' &= \frac{1}{\alpha_0^2} \sum_{m=1}^{N-1} \left\{ -\frac{1}{2} \frac{\partial^2}{\partial x_m^2} + \frac{1}{2} \alpha_0 \tilde{C}_m^{(N)} x_m^2 \right\} + \sum_{m=1}^{N-1} \frac{N \tilde{V}(\beta_m)}{2\sqrt{2}} \frac{1}{\alpha_0} \\ \tilde{H}_p'' &= \sum_{m=1}^{N-1} \left\{ \frac{1}{2} \tilde{C}_{p_m}^{(N)} x_m^2 + \frac{N \tilde{V}_p(\beta_m)}{2\sqrt{2}} \right\} \end{aligned} \quad (4.33)$$

From Eqs.(4.30) and (4.31) we see that, for α_0 large, $\tilde{V}_p(\beta_m)$ and $\tilde{C}_{p_m}^{(N)}$ can be treated perturbatively. Consequently, for α_0 large, $\frac{1}{\alpha_0} \tilde{H}_p''$ is a perturbation to $H' + \tilde{H}''$. Therefore, applying Rayleigh-Schrödinger perturbation theory, we write the total N -electron wavefunction as $\Psi^{(N)} = \sum_{i=0}^{\infty} \left(\frac{1}{\alpha_0} \right)^i \Psi_i^{(N)}$ and the eigenvalue as $W^{(N)}(\alpha_0) = \sum_{i=0}^{\infty} \left(\frac{1}{\alpha_0} \right)^i W_i^{(N)}$.

The eigenfunction of the unperturbed Hamiltonian $H' + \tilde{H}''$ can, using the expression for the harmonic oscillator, be written as

$$\begin{aligned} \Psi_{0 \{n_m\}}^{(N)}(\rho, \mathbf{z}, \mathbf{x}) &= \prod_{i=1}^N \tilde{\Phi}_{1,0}(\rho_i, z_i) \times A'(x_1, \dots, x_{N-1}) \\ &= \prod_{i=1}^N \tilde{\Phi}_{1,0}(\rho_i, z_i) \prod_{m=1}^{N-1} \left[N_{n_m} \exp \left(-\frac{1}{2} \left(\alpha_0 \tilde{C}_m^{(N)} \right)^{1/2} x_m^2 \right) \times \right. \\ &\quad \left. H_{n_m} \left(\left[\alpha_0 \tilde{C}_m^{(N)} \right]^{1/4} x_m \right) \right]. \end{aligned} \quad (4.34)$$

In Eq.(4.34) n_m denotes the quantum number of the m^{th} harmonic oscillator. The function A' is a product of eigen functions of $N - 1$ harmonic oscillators along the real normal coordinates. The vectors ρ, \mathbf{z} and \mathbf{x} denote the sets (ρ_1, \dots, ρ_N) , (z_1, \dots, z_N) and (x_1, \dots, x_{N-1}) respectively. H_{n_m} is a Hermite polynomial of order n_m , and N_{n_m} is a normalization constant for the eigenfunction of each harmonic oscillator,

$$N_{n_m} = \left\{ \frac{\left(\alpha_0 \tilde{C}_m^{(N)}\right)^{1/4}}{\sqrt{\pi} 2^{n_m} n_m!} \right\}^{1/2}. \quad (4.35)$$

The zeroth order eigenfunction $\Psi_{0 \{n_m\}}^{(N)}$ can be written as an azimuth-dependent function, $\Psi_{0 \{n_m\}}^{(N)}(\rho, \mathbf{z}; \varphi_1, \dots, \varphi_N)$, using the inverse transformation of Eqs.(4.18),(4.19),(4.14) and (4.28). Besides, it can be seen, using Eq.(4.28), that the eigenfunction obeys the right boundary condition, i.e. $\Psi_{0 \{n_m\}}^{(N)}$ is invariant under the transformation $\varphi_i \rightarrow \varphi_i + 2\pi \forall i = 1, \dots, N$. The zeroth order term in the expansion for the total energy now becomes a function of both the quantum numbers of the harmonic oscillators, i.e. the set $\{n_m\}$, and α_0 ,

$$\begin{aligned} W_0^{(N)}(\alpha_0; \{n_m\}) &= \sum_{m=1}^{N-1} \left[\frac{N \tilde{V}(\beta_m)}{2\sqrt{2}} \alpha_0^{-1} + \left(n_m + \frac{1}{2}\right) \sqrt{\tilde{C}_m^{(N)}} \alpha_0^{-3/2} \right] + \\ &\quad N E_{1,0} + O_0(\ln^2 \alpha_0 / \alpha_0^2). \end{aligned} \quad (4.36)$$

$W_0^{(N)}$ is built up by the binding energy to the line of charge plus the repulsion energy of the N point-like electrons at the corners of the N -sided regular polygon and the energy of the $N - 1$ harmonic oscillators. From Eqs.(4.30) and (4.31) we see that $\tilde{V}_p(\beta_m)$ and $\tilde{C}_{pm}^{(N)}$, and consequently the perturbation \tilde{H}_p'' , are odd functions due to the $\cos \theta$ dependence. Since $\Psi_{0 \{n_m\}}^{(N)}$ is toroidally shaped, the first-order energy correction $W_1^{(N)}(\alpha_0) = 0$ due to parity. The first non-zero term in the perturbation series comes in through second order,

$$\begin{aligned} \frac{1}{\alpha_0^2} W_2^{(N)}(\alpha_0) &= \left\langle \Psi_{0 \{n_m\}}^{(N)} \left| \frac{1}{\alpha_0} \tilde{H}_p'' G_0 \frac{1}{\alpha_0} \tilde{H}_p'' \right| \Psi_{0 \{n_m\}}^{(N)} \right\rangle \\ &\sim \frac{1}{\alpha_0^2} \sum_{m=1}^{N-1} \left\langle \Psi_{0 \{n_m\}}^{(N)} \left| (|\delta \mathbf{r}_j| \cos \theta_j + |\delta \mathbf{r}_{j+m}| \cos \theta_{j+m}) O_2(\alpha_0^{-1}) G_0 \right. \times \right. \\ &\quad \left. \left. (|\delta \mathbf{r}_j| \cos \theta_j + |\delta \mathbf{r}_{j+m}| \cos \theta_{j+m}) O_2(\alpha_0^{-1}) \right| \Psi_{0 \{n_m\}}^{(N)} \right\rangle, \end{aligned} \quad (4.37)$$

where G_0 is the resolvent operator of the unperturbed Hamiltonian $H' + \tilde{H}''$. From Eqs.(4.3) and (4.36) we see that, to dominant order in $1/\alpha_0$, $W_0^{(N)}(\alpha_0; \{n_m\})$ scales as $\ln \alpha_0 / \alpha_0$. Therefore, G_0 is of order $\alpha_0 / \ln \alpha_0$. Consequently, using Eqs.(4.30),(4.31) and (4.33) and the scaling behavior for the extension from the circle of charge $\langle \delta \mathbf{r}_m \rangle = O_1(\alpha_0^{1/2})$, the second order energy correction $\alpha_0^{-2} W_2^{(N)}(\alpha_0)$ is of order $O_2(1/(\alpha_0^2 \ln \alpha_0))$.

The total energy $W^{(N)}$ can now be written as

$$\begin{aligned} W^{(N)}(\alpha_0; \{n_m\}) &= W_0^{(N)}(\alpha_0; \{n_m\}) + O_2(1/(\alpha_0^2 \ln \alpha_0)) \\ &= N E_{1,0} + \sum_{m=1}^{N-1} \left[\frac{N \tilde{V}(\beta_m)}{2\sqrt{2}} \alpha_0^{-1} + (n_m + \frac{1}{2}) \sqrt{\tilde{C}_m^{(N)}} \alpha_0^{-3/2} \right] + \\ &\quad O_0(\ln^2 \alpha_0 / \alpha_0^2) + O_2(1/(\alpha_0^2 \ln \alpha_0)). \end{aligned} \quad (4.38)$$

Up to order $\alpha_0^{-3/2}$, we have solved the Schrödinger equation of the N -electronic negative ion of hydrogen in a circularly polarized laser field. With the expression for the energy of the AMCNI, Eq.(4.38), we can find the appearance values $\alpha_0^{(N)}$. Before we do this, we will concentrate on the structure of the AMCNI considering the Pauli exclusion principle.

4.2.5 The Pauli Exclusion Principle

Due to the Pauli exclusion principle, the N -electron wavefunction has to be antisymmetric with respect to the interchange of any pair of electrons. Therefore, the eigenfunction in Eq.(4.34), although a solution of the Schrödinger equation, is not physically admissible. Physically, the interchange of two electrons also implies the interchange of their spin-coordinates. However, since the Hamiltonian is spin-independent, different spin-states are non-degenerate only if the exchange energy is non-zero (Hund's first rule). In case of the AMCNI, it follows from Eq.(4.34) that the overlap of the electronic orbitals is negligible, and therefore *all spin-states are degenerate*. The total wavefunction, including the spin coordinates, can, for each spin state, be anti-symmetrized using the ground state wavefunction of the Hamiltonian only, i.e. $\Psi_0^{(N)} \{n_m\}$ with $n_m = 0 \forall m$. With this in mind we have, with Eq.(4.38), an expression for the total energy of the N -electronic ion from which we will now derive the appearance values $\alpha_0^{(N)}$.

4.2.6 The Appearance Values

With the expression for the ground state energy of the multiply charged negative ion of hydrogen, Eq.(4.38), we can, similar to the linear case in Chapter 5, find the appearance value $\alpha_0^{(N)}$ by solving

$$D^{(N)} = W^{(N-1)}(\alpha_0) - W^{(N)}(\alpha_0) = 0. \quad (4.39)$$

For values of α_0 smaller than the appearance value $\alpha_0^{(N)}$, at least one of the N electrons of the N -electron negative ion of hydrogen auto-detaches, as is depicted in Figure 4.2 for $N = 5$. For solving Eq.(4.39) we need to know the coefficients in the force constants $\tilde{C}_m^{(N)}$, which can be extracted from Eq.(4.22),

$$\tilde{C}_m^{(N)} = \sum_{k=1}^{N-1} \frac{1 + \cos^2 \beta_k / 2}{8 \sin^3 \beta_k / 2} \left(1 - \cos \frac{2\pi m k}{N} \right) \quad (4.40)$$

The values of the force constants are listed in Table 4.1². With these values we finally get the appearance values listed in Table 4.2.

²All force constants are non-negative, implying that we are indeed dealing with a configuration of minimum energy. In fact, the second derivative matrix of a sum of Coulomb potentials is non-negative in any configuration, indicating that this minimum must be a global one.

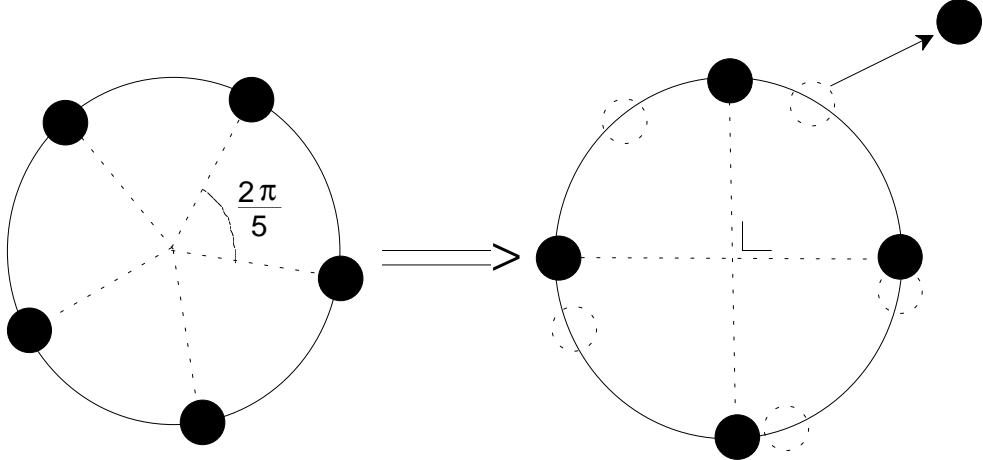


Figure 4.2: Schematic picture of the detachment of an electron at $\alpha_0^{(N=4)} < \alpha_0 < \alpha_0^{(N=5)}$ for circular polarization. For simplicity, the electronic wavefunctions are depicted as dots, whereas they are spread out along and perpendicular to the line of charge. After detachment, the remaining 4 electrons rearrange themselves into a configuration minimizing the total repulsive potential due to the e-e interaction.

We compare these values with those, obtained if one would neglect the azimuthal motion of the electron, which are listed in brackets. In other words, the values in brackets are the appearance values one would obtain neglecting the extension of the electronic wavefunction along and perpendicular to the line of charge. Note that the difference between the two methods can be neglected for $N > 4$. This can be understood considering the expression for the total energy $W^{(N)}(\alpha_0)$, i.e. Eq.(4.38). From this equation we see that the error in the energy, while treating the electronic wavefunctions as δ -functions, is of order $\alpha_0^{-3/2}$, which vanishes for large α_0 . Moreover, we can understand it from another point of view, by considering the shape of the azimuthal part of the eigenfunction. From Eq.(4.34), we see that the relative size of the wavefunction, in the azimuthal direction, decreases as $\alpha_0^{-1/4}$. So, as α_0 increases, the charge distribution of electron k , ($k = 1, \dots, N$), starts to resemble more and more a δ -function, centered at φ_k^0 . We see however, that the appearance value for $N = 3$ changes significantly by considering the electronic motion along the circle. At its appearance value, the three one-electron wavefunctions of H^{2-} have considerable spread along the circle of charge. Moreover, the

N	$\tilde{C}_1^{(N)}$	$\tilde{C}_2^{(N)}$	$\tilde{C}_3^{(N)}$	$\tilde{C}_4^{(N)}$	$\tilde{C}_5^{(N)}$	$\tilde{C}_6^{(N)}$
2	$\frac{1}{4}$	0	-	-	-	-
3	$\frac{1}{2}\sqrt{3}$	$\frac{1}{2}\sqrt{3}$	0	-	-	-
4	$\frac{1}{4} + \frac{3}{2\sqrt{2}}$	$\frac{3}{2\sqrt{2}}$	$\frac{1}{4} + \frac{3}{2\sqrt{2}}$	0	-	-
5	1.98	3.90	3.90	1.98	0	-
6	$2 + \frac{5}{4\sqrt{3}}$	$\frac{21}{4} + \frac{5}{4\sqrt{3}}$	$7\frac{1}{4}$	$\frac{21}{4} + \frac{5}{4\sqrt{3}}$	$2 + \frac{5}{4\sqrt{3}}$	0

Table 4.1: Values of the parameter $\tilde{C}_m^{(N)}$ determining force constants for different values of N , see Eqs.(4.22) and (4.31).

N	$\alpha_0^{(N)}$ monochromatic	$ W^{(N)}(\alpha_0^{(N)}) $	$137/\alpha_0^{(N)}$
3	2.2×10^2 (1.6×10^2)	9.4×10^{-3}	6.3×10^{-1}
4	3.8×10^4 (3.7×10^4)	1.2×10^{-4}	3.6×10^{-3}
5	1.5×10^7 (1.5×10^7)	5.6×10^{-7}	9.1×10^{-6}
6	9.7×10^9 (9.7×10^9)	2.5×10^{-9}	1.4×10^{-8}

Table 4.2: Left column, the appearance values $\alpha_0^{(N)}$ for different N . The appearance values are calculated taking into account the spread of the N -electron wavefunction in the azimuthal direction. This spread is calculated using a harmonic approximation for the electron repulsion around that angular distribution that minimizes the total repulsive interaction. The influence of the extension of the wavefunction perpendicular to the circle of charge on the appearance value $\alpha_0^{(N)}$ is of lower order in α_0 (see text) and is neglected. Between parentheses, the values obtained treating the N electrons as point particles. The lower and upper limit on ω defining the validity criterion for the applicability of HFFT are listed in the right two columns, evaluated at the appearance value. It can be seen that for $N > 4$ these limits are too close for a frequency to exist that allows application of the theory used.

oscillator quantum energy, $\alpha_0^{-3/2} \tilde{C}_m^{1/2}$, is comparable to the repulsion energy between the point charges.

The validity criterion for the application of non-relativistic HFFT yields a restriction on the field frequency, which is the same as for the case of linear polarization described in Chapter 5:

$$|W^{(N)}(\alpha_0)| \ll \omega \ll 137/\alpha_0. \quad (4.41)$$

From Eq.(4.38) we see that, for α_0 large, the dominant term in the energy $W^{(N)}(\alpha_0)$ is of order $\ln \alpha_0/\alpha_0$. Therefore, $|W^{(N)}(\alpha_0)|$ is a monotonically decreasing function, which, for α_0 large, falls off less rapidly than $137/\alpha_0$. This implies that there is a critical value for α_0 , denoted as $\alpha_0^c(N)$ and obeying $|W^{(N)}(\alpha_0^c(N))| = 137/\alpha_0^c(N)$, above which the theory, according Eq.(4.41), loses self-consistency. In other words, for a certain fixed N , the existence of a bound state of an N -electron ion in the field can be predicted by this theory, if, in addition to Eq.(4.41), the following relation holds,

$$\alpha_0^{(N)} < \alpha_0^c(N). \quad (4.42)$$

However, due to the logarithmic scaling behavior of $W^{(N)}(\alpha_0)$ in case of a circularly polarized field, this critical value takes extremely large values ($\alpha_0^c > e^{137}$) for any N . Therefore, the criterion in Eq.(4.42) can be fulfilled. Despite the fact that α_0^c is large, the range in which ω may vary according Eq.(4.41) decreases rapidly as N increases. In Table 4.2 the upper and lower limit of the validity criterion Eq.(4.41), $|W^{(N)}(\alpha_0)|$ resp. $137/\alpha_0$, are listed, evaluated at the appearance value. From this list and Eq.(4.41), we can conclude that the appearance of bound states of H^{2-} and H^{3-} in a circularly polarized laser field can be founded by HFFT, whereas more highly-charged negative ions, should they exist, require a relativistic description or low-frequency theory.

4.3 AMCNI in a Bichromatic Radiation Field

4.3.1 The Bichromatic Field

The appearance value of the ions can be substantially reduced if the monochromatic laser source is replaced by a *bichromatic* source, obtained by superposing two circularly polarized fields of opposite sense. For the N -electron ion the superposition should be chosen as: $\mathbf{E} = \mathbf{E}^{(1)} + (N - 1)\mathbf{E}^{(2)}$, where

$$\begin{aligned}\mathbf{E}^{(1)} &= E_0(\mathbf{e}_1 \cos \omega t \pm \mathbf{e}_2 \sin \omega t), \\ \mathbf{E}^{(2)} &= E_0(\mathbf{e}_1 \cos(N - 1)\omega t \mp \mathbf{e}_2 \sin(N - 1)\omega t),\end{aligned}\quad (4.43)$$

where \mathbf{e}_1 and \mathbf{e}_2 are unit vectors perpendicular to each other and to the propagation direction. The trajectory $-\alpha(t)$ of a classical electron in this bichromatic field has a starred shape, contained between two circles with radii $\frac{N-2}{N}\alpha_0^{bi}$ and α_0^{bi} , where α_0^{bi} is defined as $\frac{N}{N-1}\frac{E_0}{\omega^2} = \frac{N}{N-1}\alpha_0^{mono}$. For $N = 3$ the trajectory is shown in Figure 4.3 (the creation of Lissajous-like trajectories in bichromatic radiation fields was mentioned before by Lewenstein, see Ref.[144]). The N spikes of the star are on the circle of radius α_0^{bi} , and the velocity of the electron at the tip of each spike is zero at $t_k = \frac{2k\pi}{N\omega} = \frac{\beta_k}{\omega}$, where $k = 1, \dots, N$. Consequently, in the K-H-frame the line of charge generating the dressed potential $V_0(\alpha_0, \mathbf{r})$ has enhanced charge density at the spikes of the star. Moreover, since the spikes are equally spaced, the N electrons, if bound in the ground state, will be located near these spikes. The expansion of the trajectory $\alpha(t)$ in powers of t around spike k reads

$$\alpha(t) = \begin{pmatrix} \alpha_1(t) \mathbf{e}_1 \\ \alpha_2(t) \mathbf{e}_2 \end{pmatrix} = \alpha_0^{bi} \begin{pmatrix} 1 - \frac{1}{2}(\omega(t - t_k))^2(N - 1) + O((t - t_k)^4) \\ O((t - t_k)^3) \end{pmatrix}. \quad (4.44)$$

In case of linear polarization, the end-point potential multiplied with 2π , i.e. $2\pi\tilde{V}_0(\alpha_0^{lin}, \mathbf{r})$, as shown in Appendix A of Chapter 3, is generated by a uniformly accelerated proton moving along a trajectory $\alpha(t) = \frac{1}{2}\alpha_0^{lin}(\omega t)^2\mathbf{e}_1$. Therefore, as can be seen from Eq.(4.44), for large quiver amplitudes, in the bichromatic case the charge density accumulates around the spikes much the same as the charge density for linear polarization does near its two end points³. In the bichromatic case, the lowest order correction to the end-point potential comes from the motion of the proton perpendicular to the line connecting the spike and the origin of the star, i.e. along \mathbf{e}_2 . In Appendix A it is shown that this correction scales as $(\alpha_0^{bi})^{-1}$ (note that $\tilde{V}_0(\alpha_0^{bi}, \mathbf{r})$ scales as $(\alpha_0^{bi})^{-1/2}$). This implies that for large quiver amplitudes, in case of bichromatic radiation, the dressed potential can be replaced by N end-point potentials \tilde{V}_0 , one placed at a spike of the star, each having their axis directed towards the origin. This allows the reduction of the problem to that of N independent electrons, each placed under the influence of one of these end-point potentials. For large α_0 , the electron clouds around the spikes of the star do not overlap, because their linear extension is $O(\alpha_0^{1/3})$, see Ref.[122], whereas the distance between the spikes is $O(\alpha_0)$.

³The linear polarization case is in fact a special case of Eq.(4.43), obtained by setting $N = 2$.

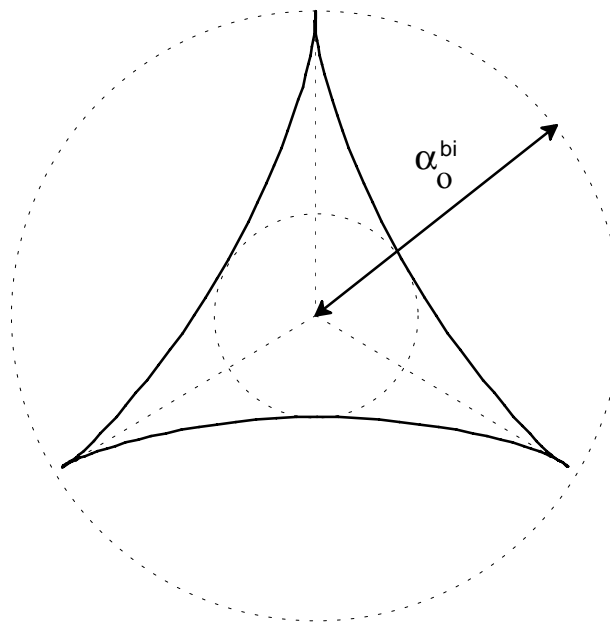


Figure 4.3: Star-like classical electron trajectory (as well as line of charge) for the bichromatic polarized field described by Eq.(4.43) with $N = 3$. The trajectory evolves between two circles of radii $\alpha_0^{bi}/3$ and α_0^{bi} . It is tangent to the radii connecting the spikes to the origin; the motion has zero velocity at the spikes, which are points of accumulation of charge along the "line of charge".

4.3.2 The Appearance Values

Before one can apply the scaling laws of the end-point potential to the case of bichromatic radiation, one has to take into account the N times higher speed the proton passes the end-points with, as can be extracted from Eq.(4.44). Therefore, the scaling laws are to be expressed in terms of α'_0 , which equals $\alpha'_0 = (N - 1) \alpha_0^{bi} = N \alpha_0^{mono}$. As a result, the energy W_{bi} of an electron, bound to a corner of an N -star, scales with α_0^{bi} as $W_{bi}(\alpha_0^{bi}) = -0.56 \times [(N - 1)\alpha_0^{bi}]^{-2/3} = -0.56 \times [N\alpha_0^{mono}]^{-2/3}$; i.e. the binding energy of an electron bound to a spike is the same as that of the hydrogen atom exposed to a field with an N times larger amplitude. Moreover, the distance from the centre of electronic charge to the corner of the star scales as $2.3 \times [(N - 1)\alpha_0^{bi}]^{1/3}$.

In contrast to the monochromatic circular case, around the spikes the potential is so steep (there is a square-root singularity) that the electrons can be treated as fixed at their equilibrium position; i.e. at a distance $2.3 \times [(N - 1)\alpha_0^{bi}]^{1/3}$ away from the corner (this treatment is similar to that of the end-point electrons in the linear case). So, after electron detachment of an N -electron ion, for monochromatic radiation the remaining $N - 1$ electrons are free to move along the circle (they will relax to the corners of an $(N - 1)$ -sided polygon on the circle), whereas in the bichromatic case the $N - 1$ electrons are fixed to their end-points, leaving one spike unoccupied. This reduces the relaxation energy of the transition from N to $N - 1$ electrons for the bichromatic case, thereby decreasing the appearance value. Hence, to dominant order in α_0^{-1} , the total energy $W^{(N)}$ of the N electron system, which is a sum of N times the binding energy W_{bi} and

N	$\alpha_0^{(N)}$ bichromatic	$ W^{(N)}(\alpha_0^{(N)}) $	$137/\alpha_0^{(N)}$
3	1.3×10^1	7.2×10^{-2}	1.0×10^1
4	3.2×10^2	9.4×10^{-3}	4.2×10^{-1}
5	2.7×10^3	2.5×10^{-3}	5.1×10^{-2}
6	6.0×10^3	1.5×10^{-3}	2.2×10^{-2}

Table 4.3: Left column: appearance values of the AMCNI induced by a bichromatic radiation source for various values of N , expressed in terms of α_0^{mono} . Right two columns: lower and upper limit of the validity criterion for the theory applied.

the repulsive energy (for the latter, see Eqs.(4.12) and (4.30), is equal to

$$W^{(N)}(\alpha_0^{bi}) = -N \times 0.56 \times [(N-1)\alpha_0^{bi}]^{-2/3} + \frac{N}{2\sqrt{2}(\alpha_0^{bi} - 2.3[(N-1)\alpha_0^{bi}]^{1/3})} \sum_{k=1}^{N-1} \tilde{V}(\beta_k). \quad (4.45)$$

With this expression for the total energy the appearance values of the AMCNI, induced by a bichromatic laser field, can be calculated using Eq.(4.39). In the bichromatic case, the appearance value $\alpha_0^{(N)}$ is that value of α_0 above which the energy of an AMCNI with N electrons distributed over the N spikes of the line of charge becomes lower than that of the ion with $(N-1)$ electrons distributed over the N spikes⁴. Compared to the monochromatic case, the logarithmic dependence on α_0 of the binding energy, see Eqs.(4.3) and (4.38), is replaced by a power dependence in the bichromatic case, $\alpha_0^{1/3}$. As a result, the repulsive interaction between the N electrons can be compensated by the attractive one with the line of charge at smaller values of α_0 . The appearance values for the bichromatic case, listed in Table 4.3 and expressed for comparison with the monochromatic case in α_0^{mono} , are dramatically smaller for higher N than those found for monochromatic circular polarization⁵.

As for the monochromatic case, the applicability of the theory used can be checked for each N with the validity criterion described by Eq.(4.41), together with the values of the lower limit, i.e. $|W^{(N)}(\alpha_0^{(N)})|$, and the upper limit, $137/\alpha_0^{(N)}$, listed in Table 4.3. However, in the bichromatic case an additional restriction holds: due to the presence of two frequency components, the validity criterion should hold for *both* ω and $(N-1)\omega$. Taking this into account, we see that, H^{2-} and H^{3-} can be induced by a bichromatic field, similar to the monochromatic case. Despite the drastic decrease of the appearance values, the validity criterion applied to the $(N-1)$ -st harmonic prohibits the cases $N = 5$ and higher.

⁴For $N = 2$, this is the procedure used for H^- in a field of linear polarization.

⁵As for the monochromatic case, spontaneous symmetry braking might occur. Application of the scaling laws of the linearly polarized case, i.e. $\Delta E = 0.1 \alpha_0^{-2/3}$ (see Ref.[145]) and $\langle \alpha_0 - r \rangle = 2.3 \alpha_0^{1/3}$ (distance from the spike of the star to the centre of the charge of the electron bound to that spike), yields a polarizability χ which scales as $\alpha_0^{4/3}$. This implies that the polarization in the plane due to the monopole interaction scales as $\alpha_0^{-2/3}$, which can be neglected compared to size of the wave function.

Symmetry braking perpendicular to the plane of the line of charge, i.e. puckering, would occur if $P' = \chi^2/\alpha_0^6 P > P$ (see the footnote for the monochromatic case). For the ground state, $\chi = 52.9 \alpha_0^{4/3}$. So, for $\alpha_0 > 10.8$, i.e. for any AMCNI induced by a bichromatic radiation source (see Table 4.3) puckering does not occur.

	ω (a.u.) (λ)	I (a.u.)	I (W/cm ²)
H^{2-} monochromatic	1.0×10^{-1} (456 nm)	9.3×10^0	3.3×10^{17}
H^{2-} bichromatic	5.0×10^{-1} (91 nm)	2.2×10^1	7.7×10^{17}
H^{3-} monochromatic	1.0×10^{-3} (45.6 μ m)	2.8×10^{-3}	1.0×10^{13}
H^{3-} bichromatic	5.0×10^{-2} (910 nm)	1.3×10^0	4.6×10^{16}

Table 4.4: Laser parameters I and ω required to realize the appearance of H^{2-} resp. H^{3-} in a monochromatic circularly polarized field or a bichromatic field. Under the circumstances created by the intensities and frequencies listed, HFFT is applicable. For $N = 3$, these circumstances for monochromatic fields can be realized by present laser systems, whereas for $N = 4$ the conditions are fulfilled easiest by a bichromatic field. Regarding present day laser developments, the other two cases are within physical reach.

4.4 Realizability and Stability

4.4.1 Experimental Realizability

The experimental realizability of creating bound states of AMCNI for both the monochromatic circularly polarized case and the bichromatic one is perhaps even more challenging than the theoretical prediction. In the monochromatic case, for both H^{2-} and H^{3-} we can extract a frequency, at the appearance value guided by Table 4.2, for which the electrons do not require a relativistic description *and* for which the high-frequency approximation is valid. From the values of $\alpha_0^{(N)}$ and this particular frequency ω we can find the required intensity of the monochromatic field via $I = 2[\alpha_0\omega^2]^2$. We have listed such values for ω and I in Table 4.4. From these values we can conclude that present day laser systems are capable to create circumstances in which experimental evidence for the appearance of H^{2-} in a monochromatic circularly polarized laser field might be realized. Although the conditions required for the appearance of H^{3-} lie beyond current laser capacities, expected developments in optics might bring these conditions within physical reach in the near future.

For the bichromatic case, laser parameters can be obtained in a similar way as for the monochromatic case, using Table 4.3. The values for ω are those of the fundamental. Note that for bichromatic radiation, the parameters required to induce a bound state of H^{3-} lie well within present day laser capacities.

For both monochromatic and bichromatic fields, the major challenge for experimental realization will be to bring together the right number of electrons and nuclei (by collision or dissociation) during the duration of the laser pulse.

4.4.2 Stability of the Ions

We did not calculate the lifetime of the ions explicitly. However, one can estimate the lifetime based on calculations on atomic hydrogen, since the electrons in an AMCNI behave similarly as in atomic hydrogen: for the monochromatic case the electronic wavefunction is toroidally shaped for both the AMCNI and hydrogen, whereas for the bichromatic case the shape of the electronic wavefunction around the end-points of the star is much the same as that for hydrogen in a linearly polarized field. Therefore one can assume that the lifetime of an N -electron AMCNI induced by a monochromatic or

bichromatic field is N times shorter than that of atomic hydrogen in a circularly resp. linearly polarized field.

For a monochromatic circular polarized field, comparison with the calculations for atomic hydrogen [28] then yields a lifetime of H^{2-} , at its appearance with laser parameters listed in Table 4.4, of the order of 10 ps. Although there are no calculations on atomic hydrogen in the regime where H^{3-} is bound, by extrapolation one finds a lifetime of the order of $10\mu s$! For the bichromatic case, applying the laser parameters from Table 4.4, comparison with results from the linear case [146] yields lifetimes of H^{2-} and H^{3-} of the order of 1 fs resp. 0.1 ps at their appearance. Note that for comparison with the linear case, the frequency as listed in Table 4.4 has to be divided by $\sqrt{N-1}$, thereby taking into account the higher velocity the proton passes the spikes with in the bichromatic case.

Moreover, for both the monochromatic and bichromatic case, these calculations show that for α_0 larger than the appearance value, the lifetime of the AMCNI increases; in other words, the AMCNI stabilizes against electron-detachment.

A Bichromatic Radiation and the End-Point Potential

In Chapter 3 it is shown that the end-point potential $\tilde{V}_0(\alpha_0; \mathbf{r})$ can be generated, up to a factor 2π , by a proton moving uniformly accelerated along a line. For bichromatic radiation, the orbit, in the vicinity of a spike of the star, is traced out by the proton much the same as it is in the case of linear polarization, as is reflected in the expression for $\alpha(t)$ in Eq.(4.44). Making a lowest order expansion for $\alpha(t)$, similar as for the linear case, the dressed Coulomb potential around the end-point (in this case spike k of the star) can be written as

$$V_0(\alpha_0^{bi}; \mathbf{r}) = -\frac{\omega}{2\pi} \int_{-\pi/\omega}^{+\pi/\omega} \frac{dt}{|\mathbf{r} + \frac{1}{2}\alpha_0^{bi}(N-1)(\omega t)^2 \mathbf{e}_1 + \frac{1}{3}\alpha_0^{bi}(N-1)(N-2)(\omega t)^3 \mathbf{e}_2 + O(t^4)|} \quad (4.1)$$

where \mathbf{r} is the distance measured from the end-point (for simplicity the moment t_k at which the proton reaches the spike is taken to be zero). Changing to the new variable $u = \omega t \sqrt{\alpha_0^{bi}}$, in the limit for large α_0^{bi} , Eq.(4.1) reads

$$V_0(\alpha_0^{bi}; \mathbf{r}) \cong -\frac{1}{2\pi \sqrt{\alpha_0^{bi}}} \int_{-\infty}^{+\infty} \frac{du}{|\mathbf{r} + \frac{1}{2}(N-1)u^2 \mathbf{e}_1 + \frac{1}{6}(N-1)(N-2)u^3 / \sqrt{\alpha_0^{bi}} \mathbf{e}_2|}. \quad (4.2)$$

From Eq.(4.2) it can be seen that the lowest order correction to the end-point potential in case of bichromatic radiation comes from the motion along \mathbf{e}_2 , i.e. perpendicular to the line connecting the spike of the star and the middle of the star. Moreover, this correction is an order $\sqrt{\alpha_0^{bi}}$ smaller than the dominant term, which conveys the end-point potential. In the limit for large α_0 , the dressed Coulomb potential for the bichromatic case can be written as

$$\begin{aligned} \lim_{\alpha_0 \rightarrow \infty} V_0(\alpha_0^{bi}; \mathbf{r}) &= -\frac{1}{2\pi} \int_{-\infty}^{+\infty} \frac{dt}{|\mathbf{r} + \frac{1}{2}(N-1)\alpha_0^{bi}t^2 \mathbf{e}_1|} + O((\alpha_0^{bi})^{-1}) \\ &= \tilde{V}_0((N-1)\alpha_0^{bi}; \mathbf{r}) + O((\alpha_0^{bi})^{-1}). \end{aligned} \quad (4.3)$$

Note that the end-point potential in the bichromatic case is evaluated at

$$\alpha_0 = (N - 1)\alpha_0^{bi} = N\alpha_0^{mono}, \quad (4.4)$$

to correct for the fact that the proton charge is smeared out over N end-points (i.e. spikes).

5

DRESSAGE OF AMCNI BY LINEARLY POLARIZED LASER FIELDS

5.1 Introduction

It has been shown that a linearly polarized laser field can change the character of a hydrogen atom or ion dramatically. For example, the negative hydrogen ion H^- , which has only one bound state in vacuum, can be distorted by the (linearly polarized) field such that excited states of the ion appear in the field (see for example Dörr *et al*, Ref.[132]). The appearance of these light-induced excited states of H^- in a linearly polarized field is predicted, based on a fully correlated calculation [133]. Even more striking is the appearance of bound states of atomic multiply charged negative ions (AMCNI) of hydrogen in the field. Whereas in vacuum AMCNI do not support bound states (for the proof that AMCNI of hydrogen do not exist in vacuum, see E. Lieb, Ref.[139]), we have shown (see Chapter 3), with a self-consistent field calculation, that a high-frequency radiation field can induce the appearance of a bound state of the simplest AMCNI of hydrogen, H^{2-} . Motivated by the appearance of these light-induced states, in the previous Chapter an analytical treatment of AMCNI induced by a circularly polarized field is presented (for atomic hydrogen in a circularly polarized field, see Pont, Ref.[124]). In the present Chapter we give a similar treatment for the appearance and structure of AMCNI in case of linear polarization, yielding expressions for the total binding energy and wavefunction of the N -electron system.

In analogy with high-frequency Floquet theory¹ for the case of circular polarization, in the high-frequency limit the Schrödinger equation of the N -electron system in the Kramers-Henneberger frame (the rest frame of a free electron quivering in the field) can be written as

$$\sum_{i=1}^N \left\{ \frac{1}{2} \mathbf{p}_i^2 + V_0(\mathbf{r}; \alpha_0) + \sum_{j < i} \frac{1}{|\mathbf{r}_i - \mathbf{r}_j|} \right\} \Psi = W^{(N)}(\alpha_0) \Psi. \quad (5.1)$$

where $\alpha_0 = E_0/\omega^2$ is the amplitude of the quiver motion $\alpha(t) = -\alpha_0 \hat{\mathbf{z}} \cos \omega t$ in a field $E_0 \hat{\mathbf{z}} \cos \omega t$.

In the linear case, the effective attractive potential, the "dressed potential" $V_0(\mathbf{r}; \alpha_0)$, felt by the electrons is the cycle-average of the space-translated Coulomb potential (see

¹For HFFT, see Chapter 1 Section 1.5 in this Thesis or Gavrila in Ref.[116]

Ref.[123]),

$$\begin{aligned} V_0(\mathbf{r}, \alpha_0) &= \frac{\omega}{2\pi} \int_0^{2\pi/\omega} \frac{1}{|\mathbf{r} - \alpha(t)|} dt \\ &= \int_{-\alpha_0}^{+\alpha_0} \sigma(z) \frac{1}{|\mathbf{r} - \hat{\mathbf{z}}z|} dz. \end{aligned} \quad (5.2)$$

where

$$\sigma(z) = \frac{1}{\pi \sqrt{\alpha_0^2 - z^2}}. \quad (5.3)$$

is the cycle-averaged charge density generated by the quivering proton.

We see from Eq.(5.2), that, in contrast to the circular case, the attractive interaction between the electrons and the line of charge now depends on the position along the line of charge (in the circular case the dressed potential is generated by a charge circle with homogeneous charge density $1/2\pi\alpha_0$). The linear problem is still cylindrically symmetric, which allows us to separate off the azimuthal part of the Hamiltonian. In the linear case the azimuthal motion is *around* the line of charge rather than *along* it. Since the charge density $\sigma(z)$ is indeed inhomogeneous, the electronic motion along the line of charge is not determined by the Coulombic interaction between the electrons only, as it is in the circular case, but also by the attractive interaction with the line of charge.

In principle, the binding of a single electron to the dressed potential V_0 thus requires the solution of a two-dimensional Schrödinger equation in the (ρ, z) -plane. In practice the dependence of the potential on z is smooth compared to that on ρ , except at the end-points $z = \pm\alpha_0$. The logarithmic singularity (as a function of ρ) in the potential well near the charge line confines all bound electrons within a narrow cylindrical region around the charge line. Interelectron repulsion will keep the electrons apart, and this means that all electrons except two will remain located far away from the end points. Such electrons will be referred to as *internal* electrons. For all internal electrons we can thus *adiabatically* separate the Schrödinger equation into a ρ - and a z -dependent part: The potential governing the z -motion is derived by solving the ρ -equation for a problem where z is confined to one particular value. For the end-point electrons, this separation is not possible, and they require special treatment.

The main reason that the case of linear polarization can not be solved as straightforwardly as the circular case, is that the energetically most favorable configuration of the electrons along the charge line is not obvious from a symmetry argument, but depends on α_0 and has to be calculated numerically.

Since we are looking for the appearance of the AMCNI, we are interested in the ground-state eigenvalue only. As long as $W^{(N)} > W^{(N-1)}$, one of the electrons of the N -electron ion auto-detaches and, therefore, the AMCNI is unstable. In order to determine the stability of an AMCNI, we define the detachment energy as

$$D^{(N)}(\alpha_0) \equiv W^{(N-1)}(\alpha_0) - W^{(N)}(\alpha_0). \quad (5.4)$$

According Eq.(5.4), the detachment energy $D^{(N)}(\alpha_0)$ is the energy required to detach one of the N electrons from a N -electron AMCNI at a particular value α_0 . Therefore, the requirement for the stability of a N -electron AMCNI reads $D^{(N)}(\alpha_0) \geq 0$. As can be seen from structure equation, Eq.(5.1), for fixed N , in HFFT the stability of the AMCNI depends on α_0 only. The value of α_0 for which $D^{(N)}(\alpha_0) = 0$ is referred to as

the *appearance value* $\alpha_0^{(N)}$. For values of α_0 larger than the appearance value $\alpha_0^{(N)}$, none of the N electrons will auto-detach, and the N -electron AMCNI supports a bound state.

Since the criteria for the applicability of HFFT are independent of the polarization, the criterion the frequency has to obey reads, similar to the case of circular polarization (see Chapter 4 in this Thesis),

$$|W^{(N)}(\alpha_0)| \ll \omega \ll 137/\alpha_0. \quad (5.5)$$

In addition, the force exerted by the light on the electron is large enough to directly pull the electron away from the proton if

$$\alpha_0\omega^2 \gg 1/16. \quad (5.6)$$

In that case, the electron is forced to quiver. Therefore, if the latter condition is fulfilled, HFFT applies to all states². If the appearance value $\alpha_0^{(N)}$, obtained using HFFT, is such that there does not exist a frequency that obeys Eq.(5.5), the prediction of the appearance of a N -electron AMCNI cannot be founded by HFFT. Suppose that at the appearance value, the requirement in Eq.(5.5) can be fulfilled. The range for α_0 in which this requirement remains fulfilled depends on the scaling behavior of $W^{(N)}(\alpha_0)$ as a function of α_0 . If $|W^{(N)}(\alpha_0)|$ decreases less rapidly than $137/\alpha_0$, there exists a critical value α_0^c , obeying $|W^{(N)}(\alpha_0^c)| = 137/\alpha_0^c$, above which HFFT can no longer be applied. Therefore, if Eq.(5.5) can be obeyed at the appearance value, the range for α_0 in which the N -electron AMCNI supports a bound state is defined by

$$\alpha_0^{(N)} \leq \alpha_0 \ll \alpha_0^c(N). \quad (5.7)$$

In Section 5.4 we will discuss the validity criteria for various values of N .

In the next Section we start giving a more detailed description of the internal and end-point electrons, where after the induction of the AMCNI by the laser field is clarified. In Section 5.3, we derive the appearance value and the structure of the AMCNI for two particular cases, that of H^{2-} and H^{3-} . The applicability of the theory is discussed in Section 5.4 and we conclude this Chapter in Section 5.5.

5.2 AMCNI in a Linearly Polarized Laser Field

5.2.1 End-point Electrons and Internal Electrons

In contrast to the circular case the electron configuration of the ground state of the AMCNI does depend on α_0 for linear polarization. Although the exact configuration can not be predicted based on symmetry arguments, calculations on H^- and H^{2-} (see Ref.[133] and Chapter 3 in this Thesis resp.) in linearly polarized laser fields clarify the global structure of the electron configuration: Since the positive charge density of the charge line diverges at the end-points $z = \pm\alpha_0$, the centres of charge of two of the N electrons are located near these end-points. In the following, these two electrons will be referred to as *end-point electrons*. On the other hand, due to the attractive interaction between the remaining $N - 2$ electrons and the line of charge, these $N - 2$ internal electrons, if bound, are located along the charge line between the two end-point electrons. In order to find the exact configuration that minimizes the total energy, we

²If $\alpha_0\omega^2 < 1/16$, some states can still be described by HFFT, but there will be other states as well in which an electron sticks to the proton. For a description of this regime of bistability, see Muller in Ref.[147].

need an expression for the potential generated by the line of charge for both the $N - 2$ internal electrons and the two end-point electrons. With the expressions for the total energy we can solve Eq.(5.4) in order to find the appearance values.

Let us first focus on the *internal electrons*. For the internal electrons, there are no scaling laws available from the one-electron problem, simply because, for large α_0 , the electronic wavefunction of a one-electron system is clustering around the end-points. However, provided the extension of the electronic wavefunction transverse to the line of charge $\langle \rho \rangle$ is small compared to $|\alpha_0 - \langle z \rangle|$, the potential felt by the $N - 2$ internal electrons can be written (in cylindrical coordinates) as

$$W_{b,int}(\alpha_0; z, \rho) = -\frac{2}{\pi\sqrt{\alpha_0^2 - z^2}} \left[\ln \frac{4(\alpha_0^2 - z^2)}{\alpha_0} - \ln \rho \right]. \quad (5.8)$$

In Appendix A it is derived that, for α_0 large, for an internal electron ($\alpha_0 - \langle z \rangle \approx O(\alpha_0/\ln^2 \alpha_0)$). This means that the internal electrons, relative to α_0 , barely approach the end-point electrons as α_0 increases. As can be seen from Eq.(5.8), this implies that in the region where the internal electron moves, the attractive potential is a smooth function of z . Moreover, as α_0 increases, Eq.(5.8) remains valid as an expression for the potential, generated by the line of charge, felt by the internal electrons. Due to the logarithmic singularity of $W_{b,int}$ in the ρ -direction and the smooth behavior of $W_{b,int}$ as a function of z , for an internal electron the energy spacing between the ground state and the first radially excited state is high compared to the spacings corresponding to excitations in the z -direction. As a result, we can adiabatically separate the motion in the ρ -direction from the motion along the line of charge³.

After adiabatic separation, the z -dependent attractive potential, referred to as the logarithmic potential, for an internal electron can be written as

$$W_{b,int}(\alpha_0; z) = -\frac{1}{\pi\sqrt{\alpha_0^2 - z^2}} \left[\ln \frac{32(\alpha_0^2 - z^2)^{3/2}}{\pi\alpha_0^2} - 2E_i \right], \quad (5.9)$$

where E_i is the energy of level i in the ρ -direction. In what follows, we will consider the ground state only, so $i = 0$, for which $E_{i=0} = 0.179935$. We see from Eq.(5.9) that, for α_0 large, the binding energy for the internal electrons scales as $\alpha_0^{-1} \ln \alpha_0$. Whereas the number of end-point electrons remains constant (namely 2), the number of internal electrons increases as N increases. Therefore, increasing the number of electrons from N to $N + 1$ implies that the binding energy of the additional electron, see Eq.(5.9), has to compensate the repulsive e-e interaction between this (internal) electron and the original N electrons. From the scaling behavior of the binding energy of an internal electron as a function of α_0 , one can argue that the appearance value $\alpha_0^{(N)}$ increases rapidly with increasing N , in order to compensate for the repulsive e-e interaction, which scales as α_0^{-1} .

Next we consider one of the *end-point electrons*, in absence of the remaining $N - 1$ electrons. An end-point electron behaves very similar to the electron in atomic hydrogen, a case that has been studied extensively by M. Pont *et al*, see Refs.[123] and [122]. For large α_0 , the potential generated by the dressed potential V_0 can be approximated by the so-called "end-point" potential \tilde{V}_0 , supporting a bound state $\tilde{\Phi}_{ep}$ with an energy that

³For the adiabatic approximation, see for example Messiah, *Quantum Mechanics*, Ref.[105], Chap.XVII, § 13.

scales as $\widetilde{W}_{b,ep}(\alpha_0) = C_b \cdot \alpha_0^{-2/3}$. For the ground state, denoted as $\widetilde{\Phi}_{ep}^0$, $C_b = 0.56$, i.e.

$$\left[\frac{1}{2}\mathbf{p}^2 + \widetilde{V}_0(\alpha_0; \mathbf{r}) \right] \widetilde{\Phi}_{ep}^0(\mathbf{r}) = 0.56 \cdot \alpha_0^{-2/3} \widetilde{\Phi}_{ep}^0(\mathbf{r}). \quad (5.10)$$

Moreover, the centre of charge $\langle \widetilde{\Phi}_{ep}^0 | z | \widetilde{\Phi}_{ep}^0 \rangle \equiv \langle z \rangle_{ep}$ of the end-point electron is slightly polarized away from the end-point, i.e. $(\alpha_0 - \langle z \rangle_{ep}) = C_p \cdot \alpha_0^{1/3}$ (see Ref.[123]), where $C_p = 2.3$. To lowest order in α_0^{-1} , the deviation $\delta \widetilde{V}_0 \equiv V_0 - \widetilde{V}_0$ of the end-point potential from the exact dressed potential is proportional to $\delta \widetilde{V}_0 \sim [2\pi\alpha_0(\alpha_0 - z)]^{-1}$. First order perturbation theory, treating $\delta \widetilde{V}_0$ as a perturbation to the end-point potential, yields an energy correction to $\widetilde{W}_{b,ep}(\alpha_0)$ of order $O(\alpha_0^{-4/3})$. Besides, the perturbation $\delta \widetilde{V}_0$ induces a correction to the polarization of the electron cloud equal to

$$\langle \delta z \rangle_{\delta \widetilde{V}_0} \equiv \langle \widetilde{\Phi}_{ep}^0 | (\alpha_0 - z) G_{ep} \delta \widetilde{V}_0 | \widetilde{\Phi}_{ep}^0 \rangle. \quad (5.11)$$

The direction of this correction is along the polarization axis *away from the end-point*, the correction being of order $O(\alpha_0^{-1/3})$. Here G_{ep} is the Green's function for the Hamiltonian containing the end-point potential \widetilde{V}_0 . Next we will show that, as long as the appearance values of the AMCNI are large, we can apply these scaling laws for the two end-point electrons of an AMCNI of hydrogen as well.

It is intuitively clear that, due to the e-e interaction, the presence of the remaining $N - 1$ electrons will induce a change in the *polarization* of the end-point electron. The presence of the internal electrons induces a polarization of the end-point electron *towards the end-point*. In lowest order perturbation theory, the change in the polarization due to the presence of the internal electrons equals

$$\langle \delta z \rangle_{1/r_{12}} \equiv \langle \widetilde{\Phi}_{ep}^0 | (\alpha_0 - z) G_{ep} \frac{1}{r_{12}} | \widetilde{\Phi}_{ep}^0 \rangle, \quad (5.12)$$

where r_{12} denotes the distance between the end-point electron and an internal electron. Since for an internal electron $(\alpha_0 - \langle z \rangle) = O(\alpha_0 / \ln^2 \alpha_0)$, one can show that, by applying the scaling laws for the end-point potential, the change in polarization $\langle \delta z \rangle_{1/r_{12}}$ scales as $\alpha_0^{-2/3} \ln^2 \alpha_0$ (see Appendix A). The correction to the polarization induced by the end-point potential appears to be significantly smaller than the dominant term in the polarization, i.e. $\langle \delta z \rangle_{\delta \widetilde{V}_0} + \langle \delta z \rangle_{1/r_{12}} \ll 2.3\alpha_0^{1/3}$: in our numerical calculation on H^{2-} ($N = 3$), the total correction is of the order of 1% at the appearance value $\alpha_0^{(N=3)} = 155$. Despite the fact that $\langle \delta z \rangle_{1/r_{12}}$ is of lower order in α_0^{-1} , $\langle \delta z \rangle_{\delta \widetilde{V}_0} < \langle \delta z \rangle_{1/r_{12}}$ for H^{2-} at its appearance value. In other words, the end-point electron cloud is slightly polarized towards the end-points compared with its position in the end-point potential \widetilde{V}_0 at the appearance value. Although the end-point electron cloud polarizes away from the end-point as α_0 increases, within the accuracy of the calculation, the distance to the end-point never exceeds $2.3\alpha_0^{1/3}$. This means that the polarization of the end-point electron in H^{2-} is, despite the interaction with the internal electron, determined by the interaction with the end-point potential. Therefore, applying the scaling laws of the end-point potential, we are likely to overestimate the repulsion energy between the internal electron on one hand and the end-point electron on the other. The results from the calculation on H^{2-} showed that, even in the presence of more electrons, the *binding energy* of an end-point electron, $W_{b,ep}(\alpha_0)$, has, within an accuracy of less than 0.1%, exactly the same scaling behavior as in the case it would be isolated, from the appearance

value on. Since, for $N > 3$, the appearance value $\alpha_0^{(N)}$ increases rapidly, and therefore, according Appendix A, also the interelectronic distance, we conclude that the scaling laws for both binding energy and polarization of the end-point potential are applicable for the end-point electrons of an AMCNI of hydrogen as well.

Based on the scaling laws for the binding energy of both the internal electrons and the end-point electrons, one can qualitatively argue that any N-electron system will become bound as α_0 increases: as α_0 increases the Coulombic repulsion energy between the N electrons, which scales as α_0^{-1} , decreases more rapidly than the binding energy.

As for the circular case, see Chapter 4, we will investigate the dependence of $\alpha_0^{(N)}$ as a function of N . From Eqs.(5.9) and (5.10), we see that the character of the dressed potential V_0 experienced by the end-point electrons is different from that experienced by the internal electrons, which is reflected in the different scaling behavior of their binding energy. With the expressions for the dressed potential for both the end-point electrons and the internal electrons we can, using a harmonic approximation for the potential, solve the Schrödinger equation, Eq.(5.1), in order to obtain the eigenvalues $W^{(N)}(\alpha_0)$, from which the appearance values $\alpha_0^{(N)}$ can be extracted.

5.2.2 The N-electron Hamiltonian

For notational convenience, let us number the N electrons from $z = -\alpha_0$ to $z = +\alpha_0$, where z is the coordinate along the line of charge. We define for z (similar as for φ in the circular case determining the position on the charge circle),

$$z_i \equiv z_i^0 + \Delta z_i, \quad \forall i = 1, \dots, N, \quad (5.13)$$

and

$$\beta_{ij} \equiv |z_i^0 - z_j^0|, \quad (5.14)$$

where $\{z_1^0, \dots, z_N^0\}$ denotes the electron configuration minimizing the logarithmic potential energy, defined in Eq.(5.9). Note that this configuration is a function of both N and α_0 (in contrast to the circular case where it is a function of N only). Therefore $\{z_1^0, \dots, z_N^0\} = \{z_1^0(\alpha_0), \dots, z_N^0(\alpha_0)\}$. Since the gradient of the dressed potential V_0 is much larger at the end-points than in the internal region, the force, pinning the end-point electrons at z_1^0 resp. z_N^0 , is much larger than the forces pinning the internal electrons. Moreover, at large α_0 , the repulsive potential the end-point electrons feel is small compared to the binding potential generated by the dressed potential V_0 (the latter decreases as $\alpha_0^{-1/2}$). Therefore, the shape of the one-electron wavefunction of each of the two end-point electrons is hardly affected by the e-e interaction. For this reason, we treat the end-point electrons *in the e-e interaction* as fixed particles, located at $z_N^0 = \alpha_0 - 2.3 \alpha_0^{1/3} = -z_1^0$. In other words

$$\Delta z_1 = \Delta z_N = 0. \quad (5.15)$$

In order to find the appearance values $\alpha_0^{(N)}$ by solving $D^{(N)}(\alpha_0) = 0$, we have to investigate the N-electron Schrödinger equation,

$$H^{(N)}(1, \dots, N) \Psi^{(N)} = W^{(N)}(\alpha_0) \Psi^{(N)}, \quad (5.16)$$

We decompose the N-electron Hamiltonian for the linear case according,

$$H^{(N)}(1, \dots, N) = H_{ep}^{(N)}(1) + H_{ep}^{(N)}(N) + H_{int}^{(N)}(2, \dots, N-1) + H_{e-e}^{(N)}(1, \dots, N). \quad (5.17)$$

With the end-point electrons fixed, the last term in Eq.(5.17), the e-e interaction, can be written as

$$H_{e-e}^{(N)} = \sum_{i=2}^{N-1} \left\{ \sum_{j=2}^{i-1} \frac{1}{|\mathbf{r}_i - \mathbf{r}_j|} + \frac{1}{|\mathbf{r}_i - z_1^0 \hat{\mathbf{e}}|} + \frac{1}{|\mathbf{r}_i - z_N^0 \hat{\mathbf{e}}|} \right\} + \frac{1}{z_1^0 - z_N^0}. \quad (5.18)$$

Using Eq.(5.9), $H_{int}^{(N)}$, the Hamiltonian for the internal electrons reads

$$\begin{aligned} H_{int}^{(N)} &= \sum_{i=2}^{N-1} \left\{ \frac{1}{2} \mathbf{p}_i^2 - V_0(\mathbf{r}_i; \alpha_0) \right\} \\ &= \sum_{i=2}^{N-1} \left\{ \frac{1}{2} \mathbf{p}_i^2 - \frac{1}{\pi \sqrt{\alpha_0^2 - z_i^2}} \left[\ln \frac{32(\alpha_0^2 - z_i^2)^{3/2}}{\pi \alpha_0^2} - 2 E_0 \right] \right\}. \end{aligned} \quad (5.19)$$

In the following, we denote the one-electron eigenfunction of $H_{ep}^{(N)}(i)$ as $\Phi^\pm(i)$, where the \pm sign denotes whether Φ is centered at $z = \pm \alpha_0$. So we have

$$\begin{aligned} H_{ep}^{(N)}(i) \Phi^\pm(i) &= W_{b,ep}^{(N)} \Phi^\pm(i) \\ &= \{0.56 \cdot \alpha_0^{-2/3} + O(\alpha_0^{-4/3})\} \Phi^\pm(i). \end{aligned} \quad (5.20)$$

From Eqs.(5.17,5.18) it follows that the Hamiltonian is separable into the coordinates of the end-point electrons on one hand and the coordinates of the internal electrons on the other. Therefore, we write the N-electron wavefunction $\Psi^{(N)}$ as the product

$$\Psi^{(N)} = \Phi^-(1) \cdot \Phi^+(N) \times \Xi_{int}(\mathbf{r}_2, \dots, \mathbf{r}_{N-1}), \quad (5.21)$$

where Ξ_{int} is an arbitrary function describing the internal electrons. The extension of the electronic wavefunction of the internal electrons *perpendicular* to the line of charge, determined by the logarithmic potential in Eq.(5.8), scales as $\langle \rho \rangle = O(\alpha_0^{1/2})$; see for example M. Pont [124](b). The interelectronic distance *along* the line of charge is of order α_0 . Therefore, ignoring the extension of Ξ_{int} perpendicular to the line of charge induces a deviation from the exact total repulsive energy of order $O(\alpha_0^{-2})$, which, for α_0 large, can be neglected. Therefore we write Ξ_{int} as a function of z only, $\Xi_{int} = \Xi_{int}(z_2, \dots, z_{N-1})$, and replace \mathbf{r}_i in Eq.(5.18) by z_i .

Since we apply the scaling laws of the end-point potential for the Hamiltonian describing the interaction of the end-point electrons with the line of charge, $H_{ep}^{(N)}(i)$ where $i = 1, N$, the eigenvalue of $H_{ep}^{(N)}(1) + H_{ep}^{(N)}(N)$ is independent of N . Therefore, in determining the appearance value $\alpha_0^{(N)}$, we can neglect this part of the Hamiltonian in Eq.(5.17). However, we have to take its contribution to $W^{(N)}(\alpha_0)$ into account when considering the validity of the theory applied (see Eq.(5.5)). We denote the N-electron Hamiltonian, used to determine $\alpha_0^{(N)}$, as $\widehat{H}^{(N)}$,

$$\widehat{H}^{(N)} = H^{(N)} - H_{ep}^{(N)}(1) - H_{ep}^{(N)}(N), \quad (5.22)$$

which can be written as

$$\begin{aligned}\widehat{H}^{(N)} = & \sum_{i=2}^{N-1} \left\{ \frac{1}{2} \mathbf{p}_i^2 - \frac{1}{\pi \sqrt{\alpha_0^2 - z_i^2}} \left[\ln \frac{32(\alpha_0^2 - z_i^2)^{3/2}}{\pi \alpha_0^2} - 2E_0 \right] \right\} + \\ & \sum_{i=2}^{N-1} \left\{ \sum_{j=2}^{i-1} \frac{1}{|z_i - z_j|} + \frac{1}{|z_i - z_1^0|} + \frac{1}{|z_i - z_N^0|} \right\} + \frac{1}{z_1^0 - z_N^0}. \quad (5.23)\end{aligned}$$

Denoting the eigenvalue of $\widehat{H}^{(N)}$ as $\widehat{W}^{(N)}$, the total energy $W^{(N)}$ reads, using Eqs.(5.16),(5.20),(5.21) and (5.22),

$$W^{(N)}(\alpha_0) = 2W_{b,ep}(\alpha_0) + \widehat{W}^{(N)}(\alpha_0). \quad (5.24)$$

From Eqs.(5.16),(5.20) and (5.22) we see that, in order to calculate the appearance value $\alpha_0^{(N)}$, we have to solve the following Schrödinger equation,

$$\widehat{H}^{(N)} \Xi_{int}(z_2, \dots, z_{N-1}) = \widehat{W}^{(N)}(\alpha_0) \Xi_{int}(z_2, \dots, z_{N-1}). \quad (5.25)$$

From its solution, we can extract $\alpha_0^{(N)}$, which is a solution of

$$D^{(N)}(\alpha_0) = \widehat{W}^{(N-1)}(\alpha_0) - \widehat{W}^{(N)}(\alpha_0) = 0. \quad (5.26)$$

Moreover, from the solution of Eq.(5.25) we not only extract the appearance values, but, from the wavefunction Ξ_{int} , we also obtain information about the structure of the AMCNI.

5.2.3 The Harmonic Approximation

We proceed by looking for the electron configuration $\{z_2^0, \dots, z_{N-1}^0\}$ that minimizes the logarithmic potential energy. The equation to be solved, in order to find $\{z_2^0, \dots, z_{N-1}^0\}$, is transcendental and therefore cannot be solved analytically. However, the configuration $\{z_2^0, \dots, z_{N-1}^0\}$ can be found numerically. Due to the smooth shape of the total potential in Eq.(5.23), the electron configuration $\{z_1^0, \dots, z_N^0\}$ is unique. Moreover, this configuration is symmetric in $z = 0$, i.e. $z_i^0 = z_{N-i+1}^0$. In our search for the appearance values $\alpha_0^{(N)}$ and the structure of the N-electron wavefunction in the case of linear polarization, we apply a similar treatment as we did for the circular case, where the electrons oscillate around their average position along the charge line. By expanding the logarithmic potential to second order in Δz_i , the harmonic approximation of the Hamiltonian in Eq.(5.23) is denoted as

$$\widehat{H}^{(N)}(2, \dots, N-1) = \widehat{H}_0^{(N)}(2, \dots, N-1) + \widehat{H}_2^{(N)}(2, \dots, N-1), \quad (5.27)$$

with eigenvalues $\widehat{W}_0^{(N)}(\alpha_0)$ resp. $\widehat{W}_2^{(N)}(\alpha_0)$ (the subscripts $j = 0, 2$ denote the order of Δz_i). The Hamiltonian $\widehat{H}_j^{(N)}$ reads:

$$\begin{aligned}\widehat{H}_0^{(N)} &= \frac{1}{2} \sum_{i=1, j \neq i}^N \frac{1}{\beta_{ij}} - \sum_{i=2}^{N-1} \left\{ \frac{1}{\pi \sqrt{\alpha_0^2 - (z_i^0)^2}} \left[\ln \frac{32}{\pi \alpha_0^2} [\alpha_0^2 - (z_i^0)^2]^{3/2} - 2 E_0 \right] \right\} \\ &\equiv \widehat{W}_0^{(N)}(\alpha_0),\end{aligned}\quad (5.28)$$

$$\begin{aligned}\widehat{H}_2^{(N)} &= \sum_{i=2}^{N-1} \left[\frac{1}{2} \frac{\partial^2}{\partial \Delta z_i^2} + \frac{1}{2} A_i \Delta z_i^2 \right] + \frac{1}{2} \sum_{i=1, j \neq i}^N \frac{1}{\beta_{ij}^3} (\Delta z_i - \Delta z_j)^2 \\ &\equiv \sum_{i=2}^{N-1} \frac{1}{2} \frac{\partial^2}{\partial \Delta z_i^2} + \frac{1}{2} (\Delta z_2, \dots, \Delta z_{N-1}) \mathbf{V} \begin{pmatrix} \Delta z_2 \\ \vdots \\ \Delta z_{N-1} \end{pmatrix} + O(\Delta z^3),\end{aligned}\quad (5.29)$$

where $A_i^{(N)}$, the second derivative of the logarithmic potential evaluated at z_i^0 , is defined as

$$A_i^{(N)} \equiv \frac{\alpha_0^2 + 2(z_i^0)^2}{\pi[\alpha_0^2 + (z_i^0)^2]^{5/2}} \left(2 E_0 + 3 - \ln \frac{32}{\pi \alpha_0^2} [\alpha_0^2 - (z_i^0)^2]^{3/2} + \frac{3(z_i^0)^2}{\alpha_0^2 + 2(z_i^0)^2} \right). \quad (5.30)$$

Since z_i^0 depends on α_0 only, $\widehat{H}_0^{(N)}$ is a function of α_0 only, whereas $\widehat{H}_2^{(N)}$ is a function of both α_0 and the coordinates Δz_i . The elements of the matrix \mathbf{V} can be written as

$$\begin{aligned}\mathbf{V}_{ii} &= A_i^{(N)} + \sum_{j \neq i}^N \frac{2}{\beta_{ij}^3} \\ \mathbf{V}_{ij} &= -\frac{2}{\beta_{ij}^3} = \mathbf{V}_{ji},\end{aligned}\quad (5.31)$$

where the indices refer to the numbers assigned to the electrons (i.e., for $N = 3$, \mathbf{V} consists of \mathbf{V}_{22} only). Since the N-electron configuration minimizing the total energy is unique and symmetric in $z = 0$, the diagonal elements of \mathbf{V} are restricted to

$$\mathbf{V}_{ii} = \mathbf{V}_{N-i+1, N-i+1}; \quad N \geq 3. \quad (5.32)$$

As for the circular case, the matrix \mathbf{V} is written in a symmetric form, and, since it is real, be diagonalized by a matrix \mathbf{D} . In the following, the basis on which \mathbf{V} is diagonal is denoted as $\{u_2, \dots, u_{N-1}\}$, where u_m is a linear combination of the coordinates Δz_j , i.e. $u_m = \sum_{j=2}^{N-1} \mathbf{D}_{mj} \Delta z_j$. From Eq.(5.29), one can recognize in $\widehat{H}_2^{(N)}$, after diagonalization of \mathbf{V} , the Hamiltonian of a set of uncoupled harmonic oscillators. The diagonal elements contain the force constants $C_m^{(N)}$, as for the circular case. So one can, after diagonalization of \mathbf{V} and with the configuration $\{z_1^0, \dots, z_N^0\}$ obtained numerically, solve the Schrödinger equation Eq.(5.25), using expressions of the harmonic oscillator. Expressed in normal coordinates, the solution of Eq.(5.25) reads

$$\begin{aligned}\widehat{H}^{(N)} \Xi_{int} &= \left[\widehat{W}_0^{(N)}(\alpha_0) + \widehat{W}_2^{(N)}(\alpha_0) \right] \Xi_{int} \\ &= \left[\widehat{W}_0^{(N)}(\alpha_0) + \sum_{m=2}^{N-1} \left(n_m + \frac{1}{2} \right) \sqrt{C_m^{(N)}(\alpha_0)} \right] \Xi_{int}.\end{aligned}\quad (5.33)$$

As can be seen from Eq.(5.33), the energy $\widehat{W}^{(N)}$ is a function of the set of oscillator quantum numbers $\{n_m\}$. Therefore, the appearance value $\alpha_0^{(N)}$ depends on which eigenstate of $\widehat{H}^{(N)}$ we are considering. As for the circular case, we see from Eqs.(5.29,...,5.33), that the contribution to $\widehat{W}^{(N)}$ due to the motion of the internal electrons along the line of charge, i.e. $\widehat{W}_2^{(N)}$, is of order $\widehat{W}_2^{(N)} = O(\alpha_0^{-3/2})$. The eigenfunction Ξ_{int} of $\widehat{H}^{(N)}$ is given by

$$\Xi_{int\{n_m\}} = \prod_{m=2}^{N-1} N_{n_m} \exp\left(-\frac{1}{2} (C_m^{(N)}(\alpha_0))^{1/2} u_m^2\right) \times H_{n_m}\left((C_m^{(N)}(\alpha_0))^{1/4} u_m\right), \quad (5.34)$$

where H_{n_m} is a Hermite polynomial of order n_m and N_{n_m} the normalization constant for the n_m^{th} Hermite polynomial. Since we are interested in the appearance values of the AMCNI, we will consider the ground state in the following, i.e. $n_m = 0 \forall m$. $\Xi_{int\{n_m\}}$ can be written in terms of z_2, \dots, z_{N-1} using the inverse transformation \mathbf{D}^{-1} and Eq.(5.13).

Comparing Eq.(5.29) with its analogue for the circular case, we encounter an important difference. Whereas for the circular case the elements on each diagonal of the matrix \mathbf{V} are the same, i.e. $\mathbf{V}_{ij} = \mathbf{V}_{i+1,j+1} \forall i, j$, for linear polarization they are not. This is due to two effects. Firstly, since for the circular case the binding energy does not depend on the position along the line of charge (in that case the azimuthal angle), the N -electron configuration is invariant under azimuthal rotations over $2\pi/N$. For linear polarization however, we have seen that the binding energy does depend on the position along the line of charge, i.e. z . Therefore, the A_i depend on i , which gives rise to different diagonal elements, see Eq.(5.31) (note that for circular polarization, due to the azimuth-independent binding energy, $A_i = 0 \forall i$). Secondly, due to the z -dependent binding energy in the linear case, neighboring electrons need not be equally spaced, implying that $\beta_{ij} \neq \beta_{i+1,j+1}$ ⁴. Therefore, there is no universal representation for the matrix \mathbf{D} as there is in the circular case, where $\mathbf{D}_{mj}^{circ} = \exp(-imj\frac{2\pi}{N})$, but \mathbf{D} will be different for each N in the linear case.

However, for linear polarization there are two exceptions to for which the $\mathbf{V}_{ij} = \mathbf{V}_{i+1,j+1}$. The first exception is the case of $N = 3$. In this case the matrix \mathbf{V} is a 1×1 matrix. Moreover, due to the symmetry in $z = 0$, see Eq.(5.32), the diagonal terms of \mathbf{V} are the same for $N = 4$ as well, $\mathbf{V}_{22} = \mathbf{V}_{33}$, and there are two off-diagonals consisting of one element. For $N > 4$, the matrix \mathbf{V} has to be diagonalized numerically in order to find the force constants of the $N - 2$ uncoupled harmonic oscillators.

We will end this section with a remark about the different spin states. Since the Hamiltonian is spin-independent, the anti-symmetrized wavefunction can be written as a sum of products of an orbit part times a N -dimensional spin state. Since the overlap of the electronic orbitals in the spatial part of the wavefunction is zero, the exchange energy is zero. Therefore, all spin-states are degenerate.

In the next sections, we will treat the cases $N = 3$ and $N = 4$ explicitly. Finally, based on these results, we will discuss the validity of the theory applied.

⁴There is one exception for which $\beta_{ij} = \beta_{i+1,j+1}$; For N odd, $\beta_{ij} = \beta_{i+1,j+1}$ for $i = (N + 1)/2 - 1$ and $j = i + 1$. This is due to the symmetry of the dressed potential in the plane $z = 0$.

5.3 The Appearance and Structure of AMCNI

5.3.1 N=3, Laser-induced H²⁻

In the case $N = 3$, there is only one internal electron, the case of H^{2-} which has been studied numerically in Chapter 3 of this Thesis. These numerical calculations have shown that the total energy $W^{(N=3)}(\alpha_0)$ is minimized if the internal electron is centered around $z = 0$, i.e. $z_2^0(\alpha_0) = 0$. Note that for $N = 3$ the configuration minimizing the total energy, $z_2^0(\alpha_0)$, is independent of α_0 (for linear polarization, H^{2-} is the only AMCNI for which this is the case). Together with Eqs.(5.27) through (5.30), this implies that the 3-electron Hamiltonian reads

$$\hat{H}^{(N=3)} = \hat{H}_0^{(N=3)} + \hat{H}_2^{(N=3)} \quad (5.35)$$

with

$$\begin{aligned} \hat{H}_0^{(N=3)} &= -\frac{1}{\pi\alpha_0} \left(\ln \frac{32\alpha_0}{\pi} - 2E_0 \right) + \frac{5}{2(\alpha_0 - 2.3\alpha_0^{1/3})} \\ &\equiv \hat{W}_0^{(N=3)}(\alpha_0), \end{aligned} \quad (5.36)$$

$$\hat{H}_2^{(N=3)} = \frac{1}{2} \frac{\partial^2}{\partial \Delta z_2^2} + \frac{1}{2} \mathbf{V}_{22} \Delta z_2^2 + O((\Delta z_2)^3) \quad (5.37)$$

For $N = 3$, the normal coordinate u_2 equals Δz_2 . Applying Eq.(5.31), the only diagonal element in the matrix \mathbf{V} in $\hat{H}_2^{(N=3)}$ can be expressed as follows,

$$\begin{aligned} \mathbf{V}_{22} &= A_2^{(N=3)} + 2/\beta_{12}^3 + 2/\beta_{23}^3 \\ &= \frac{1}{\pi\alpha_0^3} \left(2E_0 + 3 - \ln \frac{32\alpha_0}{\pi} \right) + \frac{4}{(\alpha_0 - 2.3\alpha_0^{1/3})^3} \\ &\equiv C_2^{(N=3)}(\alpha_0). \end{aligned} \quad (5.38)$$

Leaving the superscript ($N = 3$), $C_2(\alpha_0)$ is the force constant of the harmonic potential along the z-axis for the internal electron. For α_0 large enough (i.e. $\alpha_0 > 8.2 \times 10^5$), $C_2(\alpha_0)$ becomes negative, resulting in a potential barrier centered at $z = 0$: i.e. $z = 0$ becomes a point of unstable equilibrium. For these large values of α_0 , the attractive interaction with the line of charge and the repulsive interaction with the end-point electrons together generate a potential for the internal electron that consists of two wells separated by the barrier of finite height at $z = 0$. As α_0 increases, the wells become deeper and wider, resulting in a saddle point in the wavefunction at $z = 0$. Moreover, the centres of the wells become more separated. For large enough α_0 , the barrier is so large that the wavefunction of the internal electron splits into two non-overlapping parts; in other words, the internal electron dichotomizes⁵.

With Eq.(5.38), $\hat{H}_2^{(N=3)}$ reduces to the Hamiltonian of a single harmonic oscillator

$$\hat{H}_2^{(N=3)} = \frac{1}{2} \frac{\partial^2}{\partial \Delta z_2^2} + \frac{1}{2} C_2(\alpha_0) \Delta z_2^2 + O(\Delta z_2^3), \quad (5.39)$$

with eigenvalues

$$\hat{W}_2^{(N=3)}(\alpha_0) = (n_2 + \frac{1}{2}) \sqrt{C_2(\alpha_0)}. \quad (5.40)$$

⁵For a detailed description of the phenomenon dichotomy, see M. Pont, Ref.[122].

The eigenfunction $\Xi_{int}(u_2)$, where $u_2 = \Delta z_2 = z_2$, reads

$$\Xi_{int}(z_2) = N_{n_2=0} \exp\left(-\frac{1}{2} (C_2(\alpha_0))^{1/2} z_2^2\right). \quad (5.41)$$

Now we are able to write down the 3-electron eigenfunction of the ground state of H^{2-} .

$$\Psi_{\{n_2=0\}}^{(N=3)} = N_{n_2=0} \Phi^-(1) \Phi^+(3) \exp\left(-\frac{1}{2} (C_2(\alpha_0))^{1/2} z_2^2\right). \quad (5.42)$$

So, for the ground state, the total energy of H^{2-} is given by

$$\begin{aligned} \widehat{W}^{(N=3)}(\alpha_0) &= \widehat{W}_0^{(N=3)}(\alpha_0) + \widehat{W}_2^{(N=3)}(\alpha_0) \\ &= -\frac{1}{\pi\alpha_0} \left(\ln \frac{32\alpha_0}{\pi} - 2E_0 \right) + \frac{5}{2(\alpha_0 - 2.3\alpha_0^{1/3})} + \frac{1}{2}\sqrt{C_2(\alpha_0)}. \end{aligned} \quad (5.43)$$

In order to calculate the appearance value $\alpha_0^{(N=3)}$, we need an expression for the binding energy of H^- . The scaling laws of the end-point potential are applicable for H^{2-} from its appearance value on. Therefore, since in H^- the correction to the end-point potential due to the internal electrons is not present, the scaling laws of the end-point potential are applicable for H^- as well (this is confirmed by numerical calculations). So the energy $\widehat{W}^{(N=2)}$ of H^- can be expressed as (leaving the contribution from $H_{ep}^{(N)}(1) + H_{ep}^{(N)}(N)$)

$$\widehat{W}^{(N=2)}(\alpha_0) = \frac{1}{2(\alpha_0 - 2.3\alpha_0^{1/3})}. \quad (5.44)$$

The value of $\alpha_0^{(N=3)}$ can now be calculated, using Eqs.(5.43) and (5.44), by solving

$$D^{(N=3)}(\alpha_0) = \widehat{W}^{(N=2)}(\alpha_0) - \widehat{W}^{(N=3)}(\alpha_0) = 0. \quad (5.45)$$

We find an appearance value of $\alpha_0^{(N=3)} = 162$, to be compared to the value $\alpha_0^{(N=3)} = 155$ obtained from a self consistent field calculation⁶, see Chapter 3.

The deviation from the Hartree result can be imputed to the fact that the expression for the binding energy of the internal electron, Eq.(5.8), is accurate only as long as $\langle \rho \rangle \ll |\alpha_0 - z|$. From the Hartree calculation it follows that $\langle \rho \rangle \approx 10$ and that the extension of the internal-electron wavefunction is of the order of 50. However, from Eqs.(5.38) and (5.42) we see that the extension of the internal electron along the z-axis scales as $\alpha_0^{3/4}$. So, as α_0 increases, the wavefunction of the internal electrons relatively contracts towards $z = 0$ as $\alpha_0^{-1/4}$, increasing the accuracy of the expression for the binding energy. Since this holds for all N , we expect that this will not cause considerable loss of accuracy for $N > 3$, since $\alpha_0^{(N)}$ increases rapidly.

Another feature that causes the deviation between the Hartree and the analytical result for $\alpha_0^{(N=3)}$ is the fact that, at α_0 slightly larger than the appearance value, the energy of the first axially excited state of the internal electron is only a factor three lower

⁶Similar as for the circularly polarized case (see Chapter 4), one can construct a bichromatic field by superposing two linearly polarized fields $E^{(1)}$ and $E^{(2)}$, where $E^{(1)} = E_0 \sin \omega t$ and $E^{(2)} = E_0/3 \sin 3\omega t$. In this field, in the K-H-frame the velocity of the proton is zero at $z = \pm\alpha_0$ and $z = 0$. Compared to the monochromatic case, the binding energy of the internal electron increases dramatically due to the higher charge density at $z = 0$ in the bichromatic case. The binding energy of the end-point electrons, however, decreases due to a decreasing charge density at the end-points. As a result, in contrast to the circular case, the appearance value for $N = 3$ does *not decrease* by applying the bichromatic field, but remains roughly the same.

than that for the first radial excited state. This means that the adiabatic separation, on which our final expression for the binding energy Eq.(5.9) for the internal electron is based, might not be very accurate in this case. However, as α_0 increases, the Coulombic interaction with the end-point electrons decreases rapidly. Therefore, the spacings of the levels corresponding to axially excited states decrease, where the spacing scales as $\alpha_0^{-3/2}$, see Eqs.(5.38,5.40). As can be seen from Eq.(5.9), the spacings of the radially excited states only decrease as α_0^{-1} with increasing α_0 , from which we conclude that for larger α_0 , and therefore for larger N , the adiabatic separation is more accurate.

5.3.2 N=4, Laser-induced H³⁻

For $N = 4$, there are two internal electrons. The equation to be solved, Eq.(5.25), in this case reads

$$\widehat{H}^{(N=4)} \Xi_{int\{n_m\}}(z_2, z_3) = \widehat{W}^{(N=4)}(\alpha_0) \Xi_{int\{n_m\}}(z_2, z_3). \quad (5.46)$$

The configuration $\{z_2^0, z_3^0\}$, minimizing the total energy, has to be determined numerically, and is, in contrast to the case $N = 3$, a function of α_0 , i.e. $\{z_2^0, z_3^0\} = \{z_2^0(\alpha_0), z_3^0(\alpha_0)\}$. According Eqs.(5.27) through (5.29), we decompose the Hamiltonian in Eq.(5.46), into

$$\begin{aligned} \widehat{H}_0^{(N=4)}(2,3) &= \frac{1}{2} \sum_{i=1, j \neq i}^4 \frac{1}{\beta_{ij}} - \frac{2}{\pi \sqrt{\alpha_0^2 - \{z_2^0(\alpha_0)\}^2}} \left[\ln \frac{32}{\pi \alpha_0^2} [\alpha_0^2 - \{z_2^0(\alpha_0)\}^2]^{3/2} - 2E_0 \right] \\ &\equiv \widehat{W}_0^{(N=4)}(\alpha_0), \end{aligned} \quad (5.47)$$

$$\begin{aligned} \widehat{H}_2^{(N=4)}(2,3) &= \sum_{i=2}^3 \left[\frac{1}{2} \frac{\partial^2}{\partial \Delta z_i^2} + \frac{1}{2} A_i^{(N=4)} \Delta z_i^2 \right] + \frac{1}{2} \sum_{i=1, j \neq i}^4 \frac{1}{\beta_{ij}^3} (\Delta z_i - \Delta z_j)^2 \\ &\equiv \sum_{i=2}^3 \frac{1}{2} \frac{\partial^2}{\partial \Delta z_i^2} + \frac{1}{2} (\Delta z_2, \Delta z_3) \mathbf{V} \begin{pmatrix} \Delta z_2 \\ \Delta z_3 \end{pmatrix} + O(\Delta z^3). \end{aligned} \quad (5.48)$$

From Eq.(5.31) we derive that \mathbf{V} is given by

$$\mathbf{V} = \begin{pmatrix} A_2^{(N=4)} + \frac{2}{\beta_{21}^3} + \frac{2}{\beta_{23}^3} + \frac{2}{\beta_{24}^3} & -\frac{2}{\beta_{23}^3} \\ -\frac{2}{\beta_{23}^3} & A_3^{(N=4)} + \frac{2}{\beta_{13}^3} + \frac{2}{\beta_{23}^3} + \frac{2}{\beta_{43}^3} \end{pmatrix}. \quad (5.49)$$

Since, for $N = 4$, we have $A_2^{(N=4)} = A_3^{(N=4)}$, $\beta_{12} = \beta_{34}$ and $\beta_{24} = \beta_{13}$, the matrix in Eq.(5.49) obeys $\mathbf{V}_{ij} = \mathbf{V}_{i+1,j+1}$. This implies that, similar to the circular case, \mathbf{V} can be diagonalized introducing normal coordinates u_m . For $N = 4$, we get

$$\begin{aligned} u_2 &= \frac{1}{\sqrt{2}} (\Delta z_2 + \Delta z_3) \\ u_3 &= \frac{1}{\sqrt{2}} (\Delta z_2 - \Delta z_3). \end{aligned} \quad (5.50)$$

On the basis spanned by $\{u_2, u_3\}$, the diagonal elements of \mathbf{V} can be expressed as

$$\begin{aligned}\mathbf{V}_{22} &= A_2^{(N=4)} + \frac{2}{\beta_{12}^3} + \frac{2}{\beta_{24}^3} \\ &\equiv C_2^{(N=4)}(\alpha_0) \\ \mathbf{V}_{33} &= A_2^{(N=4)} + \frac{2}{\beta_{12}^3} + \frac{2}{\beta_{24}^3} + \frac{4}{\beta_{23}^3} \\ &\equiv C_3^{(N=4)}(\alpha_0)\end{aligned}\quad (5.51)$$

In terms of u_2 and u_3 , the Hamiltonian $\hat{H}_2^{(N=4)}$ can be written as the sum of two harmonic oscillators,

$$\hat{H}_2^{(N=4)}(2, 3) = \sum_{m=2}^3 \left\{ \frac{1}{2} \frac{\partial^2}{\partial u_m^2} + \frac{1}{2} C_m(\alpha_0) u_m^2 \right\}, \quad (5.52)$$

with eigenvalues

$$\widehat{W}^{(N=4)}(\alpha_0) = \widehat{W}_0^{(N=4)}(\alpha_0) + \sum_{m=2}^3 \left(n_m + \frac{1}{2} \right) \sqrt{C_m(\alpha_0)}, \quad (5.53)$$

where we have omitted the superscript ($N = 4$) on the force constants. The two normal modes consist of a symmetric oscillation u_2 and an anti-symmetric oscillation u_3 , both along the line of charge. Note that the eigenfrequency of the anti-symmetric oscillation is larger than that of the symmetric oscillation, see Eq.(5.51), $C_3(\alpha_0) > C_2(\alpha_0)$.

The eigenfunction of $\hat{H}^{(N=4)}$ reads

$$\Xi_{int\{n_m\}}(u_2, u_3) = \prod_{m=2}^3 N_{n_m} \exp \left(-\frac{1}{2} (C_m(\alpha_0))^{1/2} u_m^2 \right) \times H_{n_m} \left((C_m(\alpha_0))^{1/4} u_m \right). \quad (5.54)$$

After expressing $\Xi_{int\{n_m\}}$ in terms of $\Delta z_2 = z_2 - z_2^0$ and $\Delta z_3 = z_3 - z_3^0$, the wavefunction for the internal electrons can be expressed as

$$\begin{aligned}\Xi_{int\{n_2=n_3=0\}}(z_2, z_3) &= \prod_{m=2}^3 N_{n_m} \exp \left(-\frac{1}{4} (z_m - z_m^0)^2 \left[\sqrt{C_2} + \sqrt{C_3} \right] \right) \times \\ &\quad \exp \left(-\frac{1}{2} (z_2 - z_2^0)(z_3 - z_3^0) \left[\sqrt{C_2} - \sqrt{C_3} \right] \right).\end{aligned}\quad (5.55)$$

Since $z_2^0 = -z_3^0$, it can be seen that $\Xi_{int\{n_2=n_3=0\}}$ is variant under interchanging electron 2 and 3. The overlap between the electrons, both internal and end-point, can be neglected from the appearance value on, as can be verified by inserting the force constants from Eq.(5.51). Therefore, as for $N = 3$, all spin states are degenerate and the total N -electron wavefunction, including the spin-coordinates, can be written in anti-symmetric form using Eq.(5.55) for the spatial part of the internal electrons. The spatial part of the wavefunction for the ground state for all 4 electrons, see Eq.(5.21), can be expressed as

$$\Psi_{\{n_m=0\}}^{(N=4)} = \Phi^-(1)\Phi^+(4)\Xi_{int\{n_2=n_3=0\}}(z_2, z_3). \quad (5.56)$$

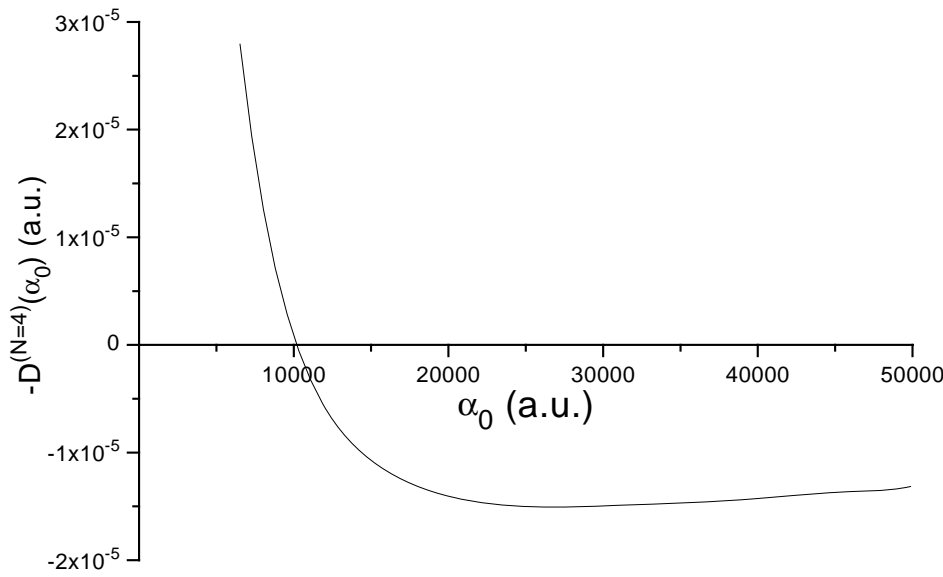


Figure 5.1: The detachment energy of H^{3-} , induced by a linearly polarized laser field, as a function of α_0 . For $\alpha_0 > \alpha_0^{(N=4)} = 1.02 \times 10^4$, H^{3-} becomes bound. As α_0 increases, the detachment energy reaches its maximum at $\alpha_0 = 2.76 \times 10^4$, where $D^{(N=4)}(\alpha_0)$ equals $D^{(N=4)}(2.76 \times 10^4) = 1.5 \times 10^{-5}$ ($= 0.41$ meV). Finally, as α_0 increases further, the detachment energy slowly decreases to zero.

Using Eq.(5.43) for $\widehat{W}^{(N=3)}$, we can calculate the appearance value $\alpha_0^{(N=4)}$ by solving

$$D^{(N=4)}(\alpha_0) = \widehat{W}^{(N=3)}(\alpha_0) - \widehat{W}^{(N=4)}(\alpha_0) = 0. \quad (5.57)$$

The appearance value we extract from Eq.(5.57) is $\alpha_0^{(N=4)} = 1.02 \times 10^4$. In Figure 5.1 the detachment energy is depicted as a function of α_0 . The detachment energy reaches its maximum at $\alpha_0 = 2.76 \times 10^4$ where it equals $D^{(N=4)}(\alpha_0 = 2.76 \times 10^4) = 1.50 \times 10^{-5}$. Subsequently, for larger α_0 , the detachment energy decreases slowly to zero. At the appearance value the configuration $\{z_2^0, z_3^0\}$ is determined by $z_3^0 = -z_2^0 = 4.54 \times 10^3$. Since the extension of the electronic orbitals perpendicular to the line of charge is of order $\alpha_0^{1/2}$, this extension is much smaller than $\alpha_0 - |z_i^0|$ in the regime where H^{3-} is bound. Therefore the requirement for the validity of the expression for the binding energy of the internal electrons, see Eq.(5.9), is fulfilled. For values of α_0 larger than the appearance value, the equilibrium value z_3^0 is plotted as a function of α_0 in Figure 5.2. From this Figure we see that the internal electrons scale linearly with α_0 , as is derived in Appendix A, and therefore relatively do not move towards the end-points as α_0 increases. Similarly as for the case $N = 3$, the extension along the polarization axis of the wavefunction of the internal electrons around the equilibrium configuration $\{z_2^0, z_3^0\}$ relatively decreases as $\alpha_0^{-1/4}$. In Figure 5.3 we show, as a function of Δz_2 and Δz_3 contour plots of the two-electron wavefunction Ξ_{int} for various values of α_0 . Apart from the relative contraction towards $\{z_2^0, z_3^0\}$ as a function of α_0 , it can be seen from Eq.(5.55) that, independent of α_0 , the wavefunction of the two internal electrons is pronounced in the direction $\Delta z_2 = \Delta z_3$. This electron-electron correlation follows implicitly from

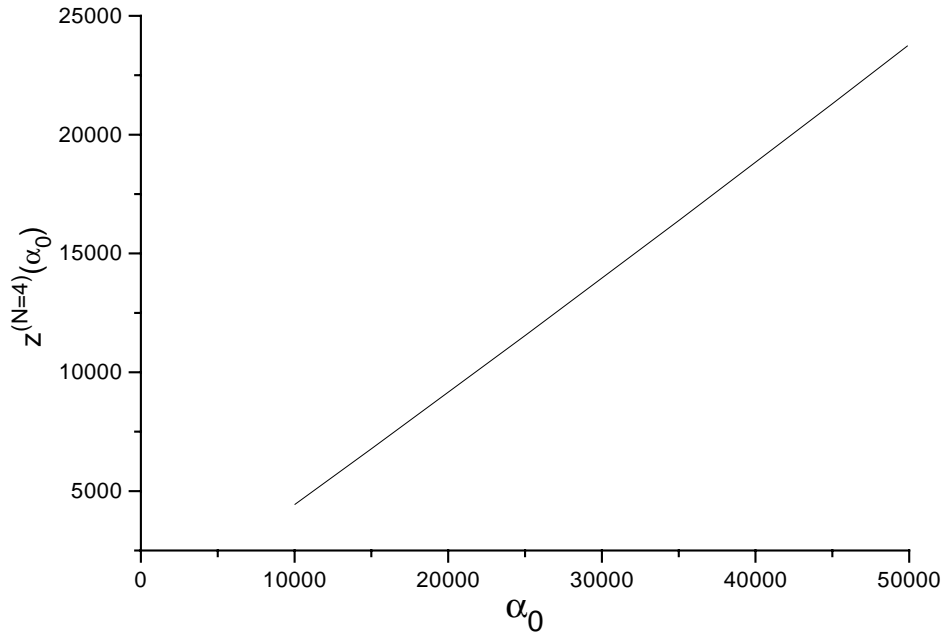


Figure 5.2: The equilibrium value $z_3^0 = -z_2^0$ for $N = 4$ as a function of $\alpha_0 > \alpha_0^{(N=4)}$. If the centre of charge of each of the two intermediate electrons is located at z_2^0 resp. z_3^0 , the total potential is minimized. In a polynomial fit, i.e. $z_3^0 = \sum_{i=0}^{\infty} c_i \alpha_0^i$, the linear coefficient c_1 equals $c_1 = 0.46$, whereas the second order term is of order 10^{-9} , indicating the linear scaling behavior of z_j^0 as a function of α_0 .

the coupling between the harmonic oscillators if expressed in terms of Δz_2 and Δz_3 , see Eq.(5.55).

5.4 Applicability of HFFT

Let us now turn back to the issue of the validity of the theory we applied, see Eqs.(5.5) and (5.7). In order that our calculation is self-consistent, there has to be a frequency obeying Eq.(5.5) at those α_0 for which H^{N-} is stable against auto-detachment, i.e. for values of α_0 that fulfill Eq.(5.7).

For α_0 large, we see from Eq.(5.24) that the dominant term in $W^{(N)}(\alpha_0)$ is determined by the binding energy of the end-point electrons, which scales as $\alpha_0^{-2/3}$. This means that for linear polarization there exists a critical value $\alpha_0^c(N)$ above which the theory is not applicable. In Table 5.1, these values are listed for several N . Since for $\alpha_0 > \alpha_0^{(N+1)}$ the total energy of the $N + 1$ resp. N electron system obeys $|W^{(N+1)}(\alpha_0)| < |W^{(N)}(\alpha_0)|$, the critical value $\alpha_0^c(N)$ decreases as N increases. However, for α_0 large, the total energy $W^{(N)}(\alpha_0)$ is dominated by the energy of the end-point electrons, which is independent of N . Therefore, the difference between the $\alpha_0^c(N)$ becomes negligible for higher N . From Table 5.1 we see that $\alpha_0^c(N = 4)$ and $\alpha_0^c(N = 5)$ differ in the 4-th digit only. For H^{2-} we have $\alpha_0^c(N = 3) = 1.72 \times 10^6$. However, since the force constant $C_2^{(N=3)}(\alpha_0)$ is purely imaginary for $\alpha_0 > 8.2 \times 10^5$, the harmonic approximation of the potential for the internal electron is not useful at $\alpha_0^c(N = 3)$. Therefore, the limitation to the values of

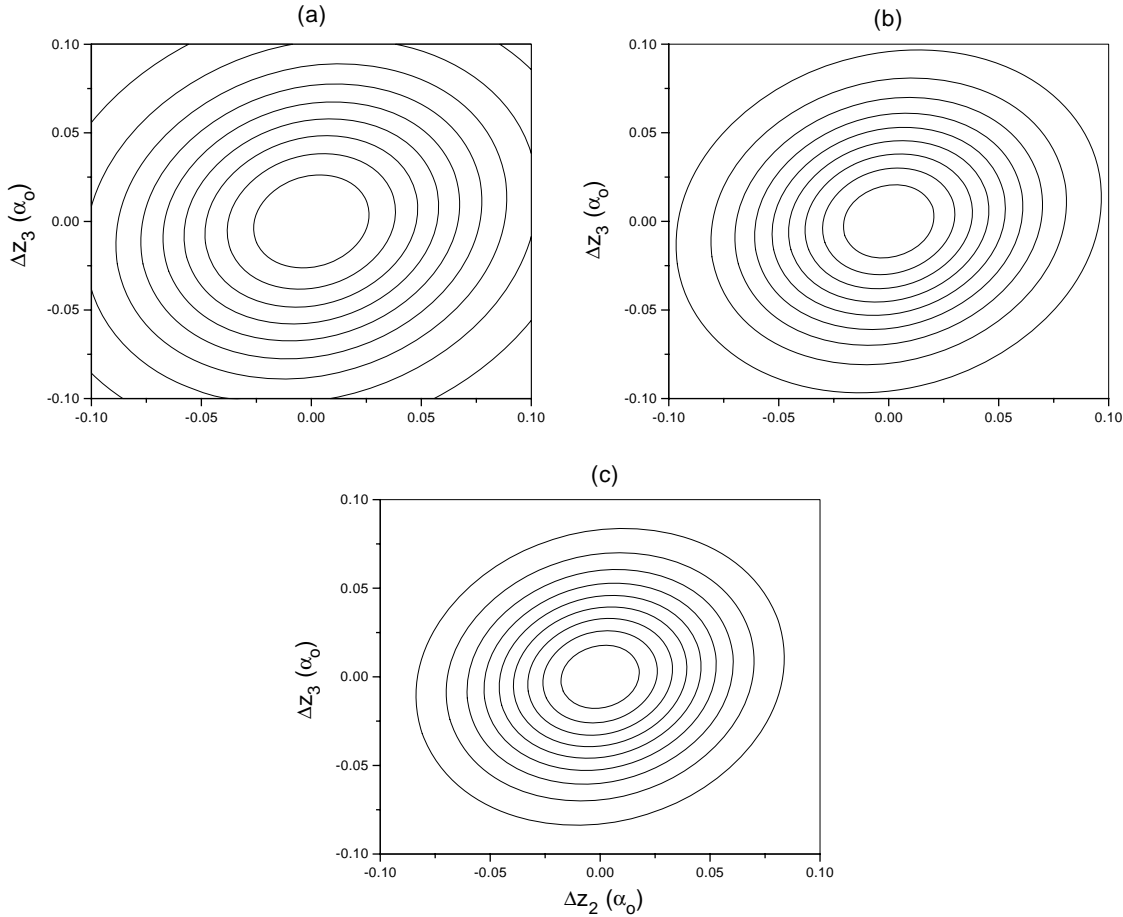


Figure 5.3: Contour plot of the 2-electron wavefunction Ξ as a function of Δz_2 and Δz_3 for various values of α_0 : (a) $\alpha_0 = \alpha_0^{(N=4)}$, appearance value (b) $\alpha_0 = 2.76 \times 10^4$, maximum detachment energy (c) $\alpha_0 = 5.00 \times 10^4$. Note that as α_0 increases the extension of the wavefunction relatively decreases, i.e. the wavefunction contracts into two δ -functions centered at z_2^0 resp. z_3^0 , see text. Independently of α_0 , the wavefunction is pronounced along the line $\Delta z_2 = \Delta z_3$ due to the electron-electron interaction .

N	$\alpha_0^{(N)}$	$\alpha_0^{c(N)}$	$W^{(N)}(\alpha_0^{(N)})$	$137/\alpha_0^{(N)}$
3	1.62×10^2	$> 8.2 \times 10^5$	3.43×10^{-2}	8.46×10^{-1}
4	1.02×10^4	$1.64(3) \times 10^6$	2.48×10^{-3}	1.34×10^{-2}
5	1.53×10^6	$1.64(2) \times 10^6$	8.73×10^{-5}	8.93×10^{-5}

Table 5.1: Relevant parameters determining the applicability of HFFT. For $N=3$ and $N=4$, the conditions required for the applicability of HFFT are fulfilled, whereas for $N=5$ the high-frequency theory is not compatible with the non-relativistic description of the electronic motion in HFFT. The critical values for $N=4$ and $N=5$ differ in the 4-th digit only, as indicated with the numbers in brackets.

α_0 for which the theory can be applied for $N = 3$ is defined by $\alpha_0^{(N=3)} \leq \alpha_0 < 8.2 \times 10^5$. Note that this upper limit for α_0 is smaller than the value at which, based on HFFT, dichotomy sets in, which is $\alpha_0^{dicho} \simeq 2 \times 10^6$. Therefore, dichotomy of the wavefunction of the internal electron can not be predicted based on HFFT.

	ω (a.u.) (λ)	I (a.u.)	I (W/cm ²)
H^{2-}	3.0×10^{-1} (152 nm)	1.8×10^2	6.2×10^{18}
H^{3-}	5.0×10^{-3} (9.12 μ m)	6.5×10^{-2}	2.3×10^{14}

Table 5.2: Laser parameters I and ω required to realize the appearance of H^{2-} resp. H^{3-} in a linearly polarized field. Under the circumstances created by the intensities and frequencies listed, HFFT is applicable.

For $N = 3$ and 4, the appearance values are much smaller than α_0^c , whereas for $N = 5$ the appearance value is only slightly smaller than the critical value. Therefore, based on the condition in Eq.(5.7), the appearance of H^{N-} in a linearly polarized field for $N = 3, 4, 5$ can be predicted by HFFT. The relevant question is whether Eq.(5.5) can be obeyed for these values of α_0 , which we will answer now. Since the difference between the upper and lower limit defining the condition in Eq.(5.5) decreases as α_0 increases, the condition is most easily fulfilled at the appearance value. In Table 5.1 the upper and lower limit for the frequency, evaluated at the appearance value, are listed. We see that, for $N = 3$, at the appearance value, the theory is self-consistent as long as the frequency is defined by

$$0.0343 \ll \omega \ll 0.846. \quad (5.58)$$

For example, if $\omega = 0.3$, relativistic effects can be neglected (the proton speed is roughly 30% of the speed of light only) and, moreover, the high-frequency condition is fulfilled, i.e. HFFT is applicable.

In Table 5.2 we list the intensity and frequency required to induce a bound state of H^{2-} at its appearance value. We see that the laser conditions required to induce a bound state of H^{2-} in a linearly polarized field lie within experimental reach. As α_0 increases to its maximum value 8.2×10^5 , the band in which ω may vary decreases. Because $|W^{(N=3)}(\alpha_0)|$ is a monotonically decaying function, an upper limit for α_0 implies that the frequency has a lower limit $\omega^c = |W^{(N=3)}(\alpha_0 = \alpha_0^c)|$ below which the theory loses self-consistency. Inserting $\alpha_0^c = 8.2 \times 10^5$, we find for $N = 3$ that $\omega^c = 1.31 \times 10^{-4}$.

Let us now concentrate on the validity criterion for $N = 4$. As for $N = 3$, for the theory to be applicable, there has to be a frequency that obeys Eq.(5.5) in the regime where H^{3-} has bound states. At $\alpha_0^{(N=4)}$, the criterion reads

$$2.5 \times 10^{-3} \ll \omega \ll 1.37 \times 10^{-2}. \quad (5.59)$$

For $\omega = 5.0 \times 10^{-3}$, relativistic effects are negligible. Although the high-frequency approximation seems to be disputable, we expect HFFT to be applicable at this frequency, based on one-dimensional model calculations⁷. In Table 5.2, for this particular frequency, the intensity required to induce a bound state of H^{3-} is listed. Note that this intensity is one order of magnitude larger than required to fulfill the condition described in Eq.(5.6). These laser parameters lie within physical reach. Comparing with the case of $N = 3$, it is clear that the frequency regime in which the HFFT is applicable becomes smaller as N increases. This can be understood as follows. The appearance value increases rapidly with N . As N increases, the total energy $W^{(N)}(\alpha_0)$ is more and more dominated by

⁷With a one-dimensional model calculation, it is shown that as long as the frequency exceeds the binding energy, applying HFFT leads to a small deviation from the result obtained from a full Floquet calculation. Moreover, this deviation in the real and imaginary part of the energy decreases rapidly as α_0 increases. See M. Marinescu and M. Gavrila, Ref.[126].

the binding energy of the end-point electrons, $W_{b,ep}$, since it is of lowest order in α_0^{-1} , namely of order $\alpha_0^{-2/3}$. This implies that for any N , the difference between the upper and lower limit, defining the range in which ω may vary, decreases roughly as $\alpha_0^{-2/3}$. Since the appearance value increases with N , this range decreases with N . Similar as for $N = 3$, there exists a lower limit for the frequency ω^c . For $N = 4$, the critical value α_0^c above which the theory is not self-consistent equals $\alpha_0^c = 1.85 \times 10^6$. From this result we can deduce that in order to induce bound states of H^{3-} in linearly polarized fields, the frequency has to obey $\omega > \omega^c = 7.4 \times 10^{-5}$.

For $N = 5$, we see that Eq.(5.5) can not be obeyed. Although the appearance value is smaller than the critical value $\alpha_0^{c(N=5)}$, the range in which ω may vary is too small to fulfill the condition in Eq.(5.5), even at the appearance value. Therefore we conclude that the appearance of bound states of AMCNI with $N = 5$ or more electrons, induced by a linearly polarized field, can not be founded by HFFT. For the prediction of more-highly charged negative ions a relativistic description or low-frequency theory is required.

5.5 Conclusions

We have shown that the appearance of bound states of AMCNI of hydrogen in a monochromatic linearly polarized laser field can be predicted by HFFT. For linear polarization, the electrons are located on a straight line of length $2\alpha_0$ that, while connected with the nucleus, oscillates harmonically with the frequency of the field and amplitude α_0 , each of the N electrons passing the nucleus twice per period. The shape of the AMCNI and the appearance value depend strongly on the polarization of the field. Whereas for circular polarization the electrons move with constant speed $\alpha_0\omega$, in the linear case the end-point electrons have zero velocity at the position of the nucleus. To dominant order in α_0 , the binding energy for circular polarization scales as $\ln \alpha_0/\alpha_0$ and that of the end-point electrons as $\alpha_0^{-2/3}$. Especially in the regime where α_0 is large, i.e. the regime where bound states of AMCNI appear, this leads to a much larger attractive interaction with the nucleus for the linear case. Moreover, in the circular case the electrons pass the proton once per period only. Despite the smaller (average) interelectronic distance for linear polarization compared to the circular case, increasing the total repulsive energy of order $O(\alpha_0^{-1})$, the appearance values $\alpha_0^{(N)}$ are smaller in the linear case due to the larger binding energy. In other words, due to the relative large binding energy of the end-point electrons, which is dominant for large α_0 , for linear polarization the repulsive interaction between the electrons can be compensated at smaller values of α_0 than for circular polarization.

We find that, founded by HFFT, both H^{2-} and H^{3-} can support bound states in a linearly polarized field, with appearance values $\alpha_0^{(N=3)} = 1.62 \times 10^2$ resp. $\alpha_0^{(N=4)} = 1.02 \times 10^4$. As α_0 increases, the detachment energy reaches a maximum where after it decreases slowly to zero. As α_0 increases, the shape of the electronic orbitals contracts into δ -functions, centered at positions $z_i^0(\alpha_0)$ along the line of charge. These positions depend on both N and α_0 and scale linearly with α_0 . The laser parameters required to induce bound states of H^{2-} and H^{3-} in a linearly polarized laser field are within experimental reach.

For more highly-charged negative ions, the size of the ion, as predicted by HFFT, increases rapidly. Since this size is of order $2\alpha_0$, either a low frequency theory or a

relativistic description for frequencies for which the high-frequency approximation is valid is required. Therefore, the prediction of the existence of AMCNI with $N > 4$ can not be founded by HFFT.

A Applicability of Scaling Laws of End-point Potential in AMCNI

For α_0 large, the potential generated by the line of charge can, in the neighborhood of an end-point, be approximated by the end-point potential \tilde{V}_0 . However, the presence of internal electrons might affect the applicability of the scaling laws of the end-point potential for the end-point electrons. Since the electrons in an AMCNI are spatially widely separated such that the electronic wavefunctions have zero overlap, we can treat the electrons as point particles when describing the e-e interaction. In this Appendix, we first derive the conditions under which the scaling laws for the end-point potential are still applicable in the presence of one or more internal electrons. It will be shown, by deriving the scaling behavior of the position along the charge line of the internal electrons, that these conditions are fulfilled.

A.1 Condition for Applicability

The end-point potential \tilde{V}_0 supports bound states $\tilde{\Phi}_{ep}^0$ (the superscript zero denotes we consider the ground state only), for which scaling laws for binding energy $\tilde{W}_{b,ep}^0(\alpha_0)$ and polarization $\langle r \rangle$ are known, where r is the distance to the end-point (see Pont, Ref.[123]): $\tilde{W}_{b,ep}^0(\alpha_0) = 0.56 \alpha_0^{-2/3} + O(\alpha_0^{-4/3})$ and $\langle \tilde{\Phi}_{ep}^0 | r | \tilde{\Phi}_{ep}^0 \rangle \equiv \langle r \rangle_{ep} = 2.3 \alpha_0^{1/3} + O(\alpha_0^{-1/3})$. Using these scaling laws, the polarizability α_{ep} of an electron bound to the end-point potential is of order

$$\alpha_{ep} = \langle \tilde{\Phi}_{ep} | r G_0 r | \tilde{\Phi}_{ep} \rangle = O(\alpha_0^{4/3}), \quad (\text{A.1})$$

where G_0 is the resolvent operator of the Hamiltonian containing the end-point potential \tilde{V}_0 only.

The condition for the scaling laws of the end-point potential to be applicable in the presence of the internal electrons is that the polarization of the end-point electron is determined asymptotically by the interaction with the line of charge. In order to investigate the polarization in the presence of internal electrons, we *assume* that the distance between the internal electron(s) and the end-point, denoted as γ , scales as a power of α_0 , i.e. $\gamma \sim \alpha_0^n$. The scaling law for the polarization of the bare end-point potential \tilde{V}_0 implies that n can never obey $n < 1/3$. Suppose $n = 1/3$: in other words, the internal and end-point electron asymptotically have the same scaling behavior. The repulsive energy would scale as $\alpha_0^{-1/3}$, whereas the binding energy would scale as $\alpha_0^{-2/3}$. Since in this case the repulsive energy would decrease less rapidly than the binding energy, this is an unstable configuration and therefore $n > 1/3$. For $n > 1/3$, for α_0 large, the distance between the end-point electron and the internal electron asymptotically scales as α_0^n . So, the polarization \mathbf{P}_{int} of the end-point electron, induced by the internal electrons, equals

$$\mathbf{P}_{int} = \alpha_{ep} \mathbf{E} \sim \alpha_{ep} \alpha_0^{-2n} = O(\alpha_0^{4/3-2n}). \quad (\text{A.2})$$

Since the polarization of the end-point electron in the end-point potential only, defined as \mathbf{P}_{ep} , scales as $\mathbf{P}_{ep} \sim \alpha_0^{1/3}$, the condition for the applicability of the scaling laws of the end-point potential for the end-point electron in the presence of internal electrons reads

$$\frac{4}{3} - 2n < \frac{1}{3} \iff n > \frac{1}{2}. \quad (\text{A.3})$$

If n is defined by $1/3 \leq n \leq 1/2$, the polarization is determined asymptotically by the e-e interaction. In that case the scaling laws of the end-point potential can not be applied to end-point electrons in AMCNI. However, we will show now that the condition for applicability in Eq.(A.3) is fulfilled.

A.2 The Scaling Parameter n

From the scaling laws of the end-point potential we see that in the absence of internal electrons, an end-point electron relatively shifts towards the end-points as α_0 increases. Due to the repulsive character of the e-e interaction, the end-point electron will shift to the end-point even more in the presence of internal electrons as well. Consequently, since the binding energy of an internal electron increases as $|z|$ increases, see Eq.(5.9), any internal electron will move towards the end-point as well, minimizing its potential energy. This means that $n < 1$. Since $n < 1$, it is, in order to determine the scaling parameter n , sufficient to consider electrons that shift to the right *or* the left end-point only.

Let N_r be the number of internal electrons that shift towards the right end-point, and let us define the distance to the end-point of internal electron i as

$$\gamma_i = \alpha_0 - \langle z_i \rangle \equiv c_i \alpha_0^n \quad (\text{A.4})$$

The total potential for internal electron i , expressed in terms of the parameter γ_i , can be written as

$$\begin{aligned} V(\gamma_i) = & -\frac{1}{\pi \sqrt{2\alpha_0 \gamma_i - \gamma_i^2}} \left[\ln \left\{ \frac{32}{\pi \alpha_0^2} (2\alpha_0 \gamma_i - \gamma_i^2)^{3/2} \right\} - 2E_0 \right] + \\ & \frac{1}{\gamma_i - z_{ep}} + \sum_{j \neq i}^{N_r} \frac{1}{|\gamma_i - \gamma_j|}, \end{aligned} \quad (\text{A.5})$$

where z_{ep} is the equilibrium position of the end-point electron. We assume that the scaling parameter n is the same for all internal electrons. For α_0 asymptotically large, we can, with $n > 1/3$ in mind, simplify Eq.(A.5), using $2\alpha_0 \gamma \gg \gamma^2$ and $\gamma \gg z_{ep}$. In the electron configuration that minimizes the total energy, the γ_i obeys the relation $\partial_{\gamma_i} V(\gamma_i) = 0$. From this relation, we can extract the scaling behavior of the γ_i . In terms of the rescaled parameter $y_i = \sqrt{\gamma_i / 2\alpha_0}$, this relation reads

$$\ln \alpha_0^{1/3} + \ln y_i = C^{(0)} + \frac{2\pi C_i^{(1)}}{3y_i}, \quad (\text{A.6})$$

where the constants $C^{(0)}$ and $C^{(1)}$ are equal to

$$\begin{aligned} C^{(0)} &= \left(3 + 2E_0 - \ln \frac{256}{\pi} \right) / 3 \\ C_i^{(1)} &= 1 + \sum_{j \neq i}^{N_r} \frac{c_i^2}{(c_i - c_j)^2}. \end{aligned} \quad (\text{A.7})$$

We insert the following ansatz for y_i into Eq.(A.6),

$$y_i = \frac{2\pi C_i^{(1)}}{\ln[\alpha_0 f(\alpha_0)]} \quad (\text{A.8})$$

where f is an arbitrary function of α_0 . From Eqs.(A.6) and (A.8) we extract the following equation for f ,

$$f(\alpha_0) = \left(\frac{2\pi C_i^{(1)} e^{C^{(0)}}}{\ln[\alpha_0 f(\alpha_0)]} \right)^3 \equiv \left(\frac{M}{\ln[\alpha_0 f(\alpha_0)]} \right)^3, \quad (\text{A.9})$$

where M is independent of α_0 . For large α_0 , a solution for f can be found iteratively,

$$f(\alpha_0) = \left(\frac{M}{\ln[\alpha_0 M^3]} \right)^3 \times \left(1 + O \left(\frac{\ln \ln \alpha_0}{\ln \alpha_0} \right) \right). \quad (\text{A.10})$$

From Eqs.(A.8,A.10) we get the following expression for the parameter γ_i ,

$$\gamma_i = \frac{2(2\pi C_i^{(1)})^2 \alpha_0}{\ln^2 \left[\frac{\alpha_0 M^3}{\ln^3(\alpha_0 M)} \right]} \times \left(1 + O \left(\frac{\ln \ln \alpha_0}{\ln^2 \alpha_0} \right) \right). \quad (\text{A.11})$$

So, in the limit for $\alpha_0 \rightarrow \infty$, the distance between the end-point and the internal electron i scales as

$$\lim_{\alpha_0 \rightarrow \infty} \gamma_i \sim \frac{\alpha_0}{\ln^2 \alpha_0}. \quad (\text{A.12})$$

It is clear that this distance does not scale as a power of α_0 . However, according to Eq.(A.12), asymptotically γ_i is larger than any power α_0^n with $n < 1$, and smaller than α_0^n with $n \geq 1$. In other words, the scaling behavior for the internal electrons obeys the restriction imposed in Eq.(A.3). Therefore, the scaling laws of the end-point potential, for both polarization and binding energy to the charge line, are applicable for the end-point electrons in AMCNI of hydrogen.

6

CALCULATION OF AC-QUASIENERGY OF H^- USING INTERPARTICLE COORDINATES

6.1 Introduction

Two-electron atomic systems hold a special appeal, in part because they are the simplest systems which are not amenable to an exact theoretical description. Their properties are frequently calculated by expanding the atomic wavefunction on a set of basis functions that are eigenfunctions of the total orbital angular momentum operator, whose eigenvalues, $L(L + 1)$, label the diagonal blocks of the (block-diagonal) matrix that represents the atomic Hamiltonian. To provide an accurate description of the internal motion of the system, the basis must account for electron correlation. A basis that depends directly on the independent-electron coordinates \mathbf{r}_1 and \mathbf{r}_2 , which locate the electrons relative to the nucleus, is usually simple to use, but it suffers from the disadvantage that an individual basis function — an appropriately symmetrized product of a function of \mathbf{r}_1 and a function of \mathbf{r}_2 — does not account for electron correlation at all; consequently, convergence with increasing basis size is slow. Moreover, the coordinates \mathbf{r}_1 and \mathbf{r}_2 are unsuitable for separating the internal and external motions of the system. The internal motion depends on only the three interparticle distances, $r_1 \equiv |\mathbf{r}_1|$, $r_2 \equiv |\mathbf{r}_2|$, and $r_3 \equiv |\mathbf{r}_1 - \mathbf{r}_2|$, while the orientation of the atom can be specified by three Euler angles, α , β , and γ . Recall that the external space is spanned by the rotation matrices $\mathcal{D}_L^{M,K}(\alpha, \beta, \gamma)$, which are simultaneously eigenfunctions of $\hat{\mathbf{L}}^2$ and the projections, \hat{L}_z and \hat{L}'_z , of $\hat{\mathbf{L}}$ along space-fixed and body-fixed axes, with eigenvalues $L(L + 1)$, M and K respectively.

Unfortunately, the algebra involved in implementing a basis that depends on the three interparticle distances can be tedious, particularly if the atom or ion is in a state whose total orbital angular momentum quantum number, L , is large. There are several sources of algebraic difficulty, but two problems are particularly noteworthy: (1) The first problem is that the external and internal motions of the atomic system are coupled since the angular momenta of the individual electrons are coupled to give a total angular momentum $L(L + 1)$. Hence, while the atomic Hamiltonian commutes with $\hat{\mathbf{L}}^2$ and \hat{L}_z , it does not commute with \hat{L}'_z . Consequently, the atomic Hamiltonian couples rotation matrices $\mathcal{D}_L^{M,K}(\alpha, \beta, \gamma)$ with different K -values. In other words, although the rotation matrices constitute an acceptable basis for the external space, they do not yield a representation of the atomic Hamiltonian that is a diagonal matrix (of the differential operators r_1 , r_2 and r_3) acting on the internal space¹. Nor, in general, can a unitary transformation yield a diagonal representation. (2) The second problem is that the

¹If the atomic Hamiltonian were diagonal on this basis, the solution of the three-dimensional problem would be uniquely defined by the three angular quantum numbers L , M and K . However, due to

range of r_3 depends on r_1 and r_2 , and therefore r_3 does not vary entirely independently of r_1 and r_2 ; consequently, integration over each of these three variables cannot be done independently.

Fortunately, both of these problems can be circumvented: (1) It turns out that — through a unitary transformation of the basis $\mathcal{D}_L^{M,K}(\alpha, \beta, \gamma)$ — the atomic Hamiltonian can be represented as a *tri-diagonal* matrix whose non-vanishing elements are relatively simple differential operator expressions; see Eqs. (6.9) through (6.12) in the next section. (2) The intra-dependence of the interparticle coordinates can be removed by transforming to perimetric coordinates u , v , and w , which are linear combinations of r_1 , r_2 , and r_3 :

$$u = r_2 + r_3 - r_1, \quad (6.1)$$

$$v = r_1 + r_3 - r_2, \quad (6.2)$$

$$w = 2(r_1 + r_2 - r_3). \quad (6.3)$$

In contrast to r_1 , r_2 , and r_3 , the perimetric coordinates *vary independently* of each other, over the range 0 to ∞ . These coordinates are particularly useful when the two electrons are strongly correlated; indeed, each of the planes $u = 0$, $v = 0$, and $w = 0$ has the special significance that the electrons lie on a line passing through the nucleus — on the same side of the nucleus if u or v is zero, and on opposite sides if $w = 0$. In the case of the negative hydrogen ion, H^- , the two-electron probability distribution has maxima on each of these planes. In case $u = 0$ or $v = 0$, the electron configuration is referred to as the screening configuration, whereas $w = 0$ corresponds to the so-called anti-screening configuration.

Almost forty years ago, Pekeris [148] initiated a series of pioneering calculations in which the internal motion of helium and helium-like ions was represented on a Sturmian-type basis composed of the functions

$$\phi_{lmn}(r_1, r_2, r_3) = e^{-(k_1 u + k_2 v + k_3 w)} L_l(2k_1 u) L_m(2k_2 v) L_n(2k_3 w), \quad (6.4)$$

where $L_p(x)$ is a Laguerre polynomial of order p , and where k_1 and k_2 are variable parameters, with k_3 chosen to be $(k_1+k_2)/2$ so that the exponent $k_1 u + k_2 v + k_3 w$ is $2(k_2 r_1 + k_1 r_2)$. If k_1 and k_2 are chosen to be equal, this “perimetric-Sturmian” basis has the outstanding merit that each block of the matrix representing the atomic Hamiltonian is *sparse*, provided that the atomic Hamiltonian is tri-diagonalized in the external space (see the next section). The sparseness stems from the property $\int_0^\infty dx e^{-x} x^p L_m(x) L_n(x) = 0$ when $|m - n| > p$. Furthermore, if $k_1 = k_2$, the matrix elements can be calculated in integer arithmetic, and therefore without roundoff error, as long as the largest integer involved does not exceed the register capacity of the computer. The choice $k_1 = k_2$ is certainly appropriate for the ground state, and the advantages just mentioned permitted Pekeris to perform a calculation of ground-state properties of helium and helium-like ions to an accuracy which at the time was unprecedented, and which is rarely matched in contemporary calculations.

In this Chapter, we outline a general formalism for treating a two-electron system, and its interaction with radiation, using a set of basis functions which depend on the interparticle distances (or linear combinations of these distances, e.g. perimetric coordinates). We carry out the angular momentum algebra, and integrate the matrix

the radial dependence of the atomic Hamiltonian, it cannot have a complete set of common eigenvectors with the rotation matrices.

elements over the Euler angles, for all values of L . The matrix representing the atom-field interaction is block-codiagonal; the codiagonal blocks, labelled $L \pm 1$, are sparse on the perimetric-Sturmian basis if k_1 and k_2 are chosen to be equal. We have used the perimetric-Sturmian basis, with $k_1 = k_2$, to calculate the second- and fourth-order AC-shifts and widths of the negative hydrogen ion over a range of frequencies, and we give some benchmark results. These calculations required the inclusion of S ($L = 0$), P ($L = 1$), and D ($L = 2$) states. In addition, by constructing a 3-level effective Hamiltonian (see Chapter 1, Sec. 1.4.4) from the zeroth-, first-, and second-order perturbed wavefunctions, we have obtained estimates of the AC-shifts and widths in the nonperturbative-field regime, where the atom-field interaction is relatively strong. Using this model, we have explored photodecay in the autoionizing resonance region below the two-electron escape threshold, and stabilization against photoionization at frequencies above the threshold for two-electron escape.

While all non-vanishing blocks of the matrices representing the atomic Hamiltonian and atom-field interaction are sparse on the perimetric-Sturmian basis, if $k_1 = k_2$, the sparseness diminishes as L increases, the reason being that each ϕ_{lmn} must be multiplied by a prefactor $r_1^{l_1} r_2^{l_2}$, where $l_1 + l_2 = L$, to take into account the centrifugal barrier² (see the next section). In addition, for the same reason, the algebraic expressions for the non-vanishing matrix elements become more complicated as L increases. (We were unable to calculate these matrix elements entirely in integer arithmetic for $L \geq 2$ since intermediate integers larger than the register capacity were encountered.) These problems are magnified if k_1 and k_2 are chosen to be different; indeed, matrix elements can no longer be calculated in integer arithmetic, even in principle, and the matrices are much less sparse since, after appropriate symmetrization of the basis, the matrix elements contain integrals over u and v that are of the form $\int_0^\infty dx x^p \exp[-(k_1 + k_2)x] L_l(2k_1 x) L_m(2k_2 x)$, integrals that do not possess orthogonality properties if $k_1 \neq k_2$. (However, the integral over w does give rise to some sparseness, even when $k_1 \neq k_2$.)

The disadvantage of taking $k_1 = k_2$ is that the basis has only one length scale, whereas if the atom is in an excited state the two electrons in general experience different length scales. For this reason, in his treatment of excited S-states, and P-states, Pekeris took k_1 and k_2 to be different. However, as indicated in the previous paragraph, the algebra involved in calculating matrix elements for the case $k_1 \neq k_2$ is far more tedious than for the case $k_1 = k_2$, especially if $L \neq 0$. In fact, Pekeris found the algebra too daunting for P states, and he abandoned the Sturmian-type basis, choosing in place of the triple product of Laguerre polynomials simple powers³ of u , v , and w [149]. Our strategy is to exploit the sparseness and simplicity afforded by the choice $k_1 = k_2$ to accommodate a very large number of basis functions, in the hope that the large basis size compensates for the deficiency inherent in a single length scale. In this respect, our strategy is similar to the one adopted by Wintgen and Delande,[150] who recently used the perimetric-Sturmian basis with $k_1 = k_2$ to calculate, to very high accuracy, various properties of doubly-excited P-state resonances of helium, as well as cross sections for double photoexcitation of P states from the ground state of helium.

²If L increases, the maximum power p in $\int_0^\infty dx e^{-x} x^p L_m(x) L_n(x) = 0$ increases. Therefore, for larger L , there are less m and n for which $|m - n| > p$, which reduces the sparseness.

³The basis functions $\exp[-(k_2 r_1 + k_1 r_2)] u^l v^m w^n$ in general involve both even and odd powers of r_3 . However, terms with $l = m$ and $n = 0$ involve only even powers of r_3 . A basis which possesses only even powers of r_3 would offer no advantage over a basis that depends directly on the independent-electron coordinates \mathbf{r}_1 and \mathbf{r}_2 since $r_3^2 = r_1^2 + r_2^2 - 2\mathbf{r}_1 \cdot \mathbf{r}_2$.

In the next Section we present the formalism involving the Euler angles and the interparticle coordinates describing the interaction between a two-electron atom or ion and an AC-field. In Section 6.3 we show our results of calculations in which this formalism is applied to calculate the AC-quasienergie of H^- at various different intensities and frequencies.

6.2 Decomposition in Euler Angles and Interparticle Coordinates

6.2.1 Atomic Hamiltonian

The Hamiltonian of the unperturbed two-electron system is

$$H_a = -\frac{1}{2}\nabla_1^2 - \frac{1}{2}\nabla_2^2 - \frac{Z}{r_1} - \frac{Z}{r_2} + \frac{1}{r_3}. \quad (6.5)$$

Fixing the z -axis to be the polar axis, and defining θ_1 and ϕ_1 to be the polar and azimuthal angles of \mathbf{r}_1 , and θ_2 and ϕ_2 to be the polar and azimuthal angles of \mathbf{r}_2 , we introduce

$$\zeta_1 = \sin(\theta_1)e^{i\phi_1}, \quad (6.6)$$

$$\zeta_2 = \sin(\theta_2)e^{i\phi_2}. \quad (6.7)$$

We assume that the unperturbed system is in an eigenstate of the total orbital angular momentum operator, $\hat{\mathbf{L}}^2$, and its projection, \hat{L}_z along the z -axis, with eigenvalues $L(L+1)$ and M , respectively, and of the inversion operator, with eigenvalue Π . We allow L to be arbitrary, but to keep the formalism relatively simple we restrict M to be zero and the parity Π to be $(-1)^L$. The extension to other values of M and Π can be made using the development explored by Pont and Shakeshaft in Ref. [151]. As shown in Ref. [151], when $M=0$ and $\Pi=(-1)^L$ the wavefunction, $\Psi_L(\mathbf{r}_1, \mathbf{r}_2)$, of the unperturbed atom can be expressed as

$$\Psi_L(\mathbf{r}_1, \mathbf{r}_2) = \frac{1}{\sqrt{(2L!)}} \sum_{l_1+l_2=L} [(\hat{L}_-)^L (r_1 \zeta_1)^{l_1} (r_2 \zeta_2)^{l_2}] f_{l_1, l_2}^L(r_1, r_2, r_3), \quad (6.8)$$

where \hat{L}_- is the angular momentum lowering operator⁴. For fixed L and M there are $L+1$ linearly independent rotation matrices $\mathcal{D}_L^{M, K}(\alpha, \beta, \gamma)$, labelled with K , with parity $(-1)^L$. Consequently, an eigenfunction of $\hat{\mathbf{L}}^2$ and \hat{L}_z can be expressed in terms of a linear combination of these rotation matrices. With the rotation matrices as basis functions, the atomic Hamiltonian possibly is a full $(L+1) \times (L+1)$ matrix. However, by replacing the linear combination of the $L+1$ rotation matrices by a sum over all (i.e. $L+1$) possible products of $\zeta_1^{l_1} \zeta_2^{l_2}$ with $l_1 + l_2 = L$, the sparseness of the atomic Hamiltonian increases (as shown below in Eqs.(6.20) and (6.21), the coordinates ζ_i are coupled to the Euler angles via a unitary transformation). The choice of this angular basis reduces the computational complexity of the determination of the functions $f_{l_1, l_2}^L(r_1, r_2, r_3)$.

⁴The fact that this function is an eigenfunction of $\hat{\mathbf{L}}^2$ and \hat{L}_z can be verified using the relations $\zeta_i = Y_1^1(\Omega_i)$, where $Y_l^m(\Omega)$ is a spherical harmonic, together with the relation $\zeta_i^{l_i} = Y_{l_i}^{l_i}(\Omega_i)$.

Suppressing the arguments r_1 , r_2 , and r_3 of f_{l_1, l_2}^L , for brevity, and noting that H_a commutes with \hat{L}_- , it can be shown that (see Ref.[151])

$$H_a[(\hat{L}_-)^L(r_1\zeta_1)^{l_1}(r_2\zeta_2)^{l_2}]f_{l_1, l_2}^L = \sum_{l'_1 + l'_2 = L} [(\hat{L}_-)^L(r_1\zeta_1)^{l_1}(r_2\zeta_2)^{l_2}]h_a(l'_1, l'_2 | l_1, l_2)f_{l_1, l_2}^L, \quad (6.9)$$

where $h_a(l'_1, l'_2 | l_1, l_2)$ is an element of a *tridiagonal* $(L+1) \times (L+1)$ matrix \underline{h}_a of differential operators, defined by

$$\begin{aligned} h_a(l_1, l_2 | l_1, l_2) &\equiv -\frac{1}{2} \left[\frac{\partial^2}{\partial r_1^2} + \frac{2}{r_1} \frac{\partial}{\partial r_1} + \frac{\partial^2}{\partial r_2^2} + \frac{2}{r_2} \frac{\partial}{\partial r_2} + 2 \frac{\partial^2}{\partial r_3^2} + \frac{4}{r_3} \frac{\partial}{\partial r_3} \right. \\ &\quad \left. + \left(\frac{r_1^2 - r_2^2 + r_3^2}{r_1 r_3} \right) \frac{\partial^2}{\partial r_1 \partial r_3} + \left(\frac{r_2^2 - r_1^2 + r_3^2}{r_2 r_3} \right) \frac{\partial^2}{\partial r_2 \partial r_3} \right] \\ &\quad - \frac{Z}{r_1} - \frac{Z}{r_2} + \frac{1}{r_3} - \frac{l_1}{r_1} \frac{\partial}{\partial r_1} - \frac{l_2}{r_2} \frac{\partial}{\partial r_2} - \frac{(l_1 + l_2)}{r_3} \frac{\partial}{\partial r_3}, \end{aligned} \quad (6.10)$$

$$h_a(l_1 - 1, l_2 + 1 | l_1, l_2) \equiv \frac{l_1}{r_3} \frac{\partial}{\partial r_3}, \quad (6.11)$$

$$h_a(l_1 + 1, l_2 - 1 | l_1, l_2) \equiv \frac{l_2}{r_3} \frac{\partial}{\partial r_3}, \quad (6.12)$$

with $h_a(l'_1, l'_2 | l_1, l_2) \equiv 0$ unless $l'_1 = l_1$ and $l'_2 = l_2$, or unless $l'_1 = l_1 \pm 1$ and $l'_2 = l_2 \mp 1$. We transform the energy eigenvalue problem to a standard matrix eigenvalue problem by representing H_a on the set of basis functions

$$\Phi_{lmn}^{Ll_1l_2}(\mathbf{r}_1, \mathbf{r}_2; \pm) = \Phi_{lmn}^{Ll_1l_2}(\mathbf{r}_1, \mathbf{r}_2) \pm \Phi_{lmn}^{Ll_1l_2}(\mathbf{r}_2, \mathbf{r}_1), \quad (6.13)$$

where $l_1 + l_2 = L$ and

$$\Phi_{lmn}^{Ll_1l_2}(\mathbf{r}_1, \mathbf{r}_2) = \frac{1}{\sqrt{(2L)!}} [(\hat{L}_-)^L(r_1\zeta_1)^{l_1}(r_2\zeta_2)^{l_2}] \phi_{lmn}(r_1, r_2, r_3). \quad (6.14)$$

In conformity with each term in the sum on the right-hand side of Eq. (6.8), each basis function has parity $(-1)^L$ and is an eigenfunction of $\hat{\mathbf{L}}^2$ and \hat{L}_z , with eigenvalues $L(L+1)$ and 0, respectively. The basis functions are appropriately symmetrized; the choice of sign, on the right-hand side of Eq. (6.13), is + for singlet states and - for triplet states. In this section, we need not specify the functions $\phi_{lmn}(r_1, r_2, r_3)$ — we do not assume they are the perimetric-Sturmian functions defined by Eq. (6.4) — but if they are chosen to satisfy the condition $\phi_{lmn}(r_1, r_2, r_3) = \phi_{mln}(r_2, r_1, r_3)$, a condition satisfied by the perimetric-Sturmian functions when $k_1 = k_2$, we must impose the restrictions $l_1 < l_2$ if $l_1 \neq l_2$ and $l \leq m$ if $l_1 = l_2$, to avoid linear dependence between $\Phi_{lmn}^{Ll_1l_2}(\mathbf{r}_1, \mathbf{r}_2; \pm)$ and $\Phi_{mln}^{Ll_2l_1}(\mathbf{r}_1, \mathbf{r}_2; \pm)$. To form the matrix representation of H_a we must evaluate the matrix elements (suppressing, hereafter, the arguments of $\Phi_{lmn}^{Ll_1l_2}$ and ϕ_{lmn})

$$M_{l'm'n'lmn}^{ll'l''l_1l_2} = \int d\tau (\Phi_{l'm'n'}^{ll'l''l_1l_2})^* H_a \Phi_{lmn}^{Ll_1l_2}, \quad (6.15)$$

where $d\tau$ is the 6-dimensional volume element, which can be expressed as

$$d\tau = d\alpha \sin\beta d\beta d\gamma r_1 r_2 r_3 dr_1 dr_2 dr_3, \quad (6.16)$$

where α , β , and γ are the standard Euler angles (see e.g. [152]). Using Eq. (6.9), noting that $\hat{L}_-^\dagger = \hat{L}_+$, and that $(\hat{L}_+)^L(\hat{L}_-)^L = 2L!$ when acting on an eigenfunction of $\hat{\mathbf{L}}^2$, we

can rewrite Eq. (6.15) as

$$\begin{aligned} M_{l'm'n'lmn}^{l''_1 l''_2 l_1 l_2} &= \sum_{l'_1 + l'_2 = L} \int d\tau (r_1 \zeta_1^*)^{l''_1} (r_2 \zeta_2^*)^{l''_2} \phi_{l'm'n'} (r_1 \zeta_1)^{l'_1} (r_2 \zeta_2)^{l'_2} h_a(l'_1, l'_2 | l_1, l_2) \phi_{lmn} \quad (6.17) \\ &= \int_0^\infty dr_1 \int_0^\infty dr_2 \int_{|r_1 - r_2|}^{r_1 + r_2} dr_3 r_1 r_2 r_3 \phi_{l'm'n'} (\underline{m} \cdot \underline{h}_a)_{(l'_1, l'_2), (l_1, l_2)} \phi_{lmn}, \quad (6.18) \end{aligned}$$

where \underline{m} is a $(L+1) \times (L+1)$ matrix whose elements are the operators

$$\underline{m}_{(l''_1, l''_2), (l'_1, l'_2)} = r_1^{l''_1 + l'_1} r_2^{l''_2 + l'_2} \int_0^{2\pi} d\alpha \int_0^\pi \sin \beta d\beta \int_0^{2\pi} d\gamma (\zeta_1^{l''_1} \zeta_2^{l''_2})^* \zeta_1^{l'_1} \zeta_2^{l'_2}, \quad (6.19)$$

with the rows and columns of the matrix labelled by the pairs of indices (l''_1, l''_2) and (l'_1, l'_2) , respectively, subject to $l''_1 + l''_2 = L$ and $l'_1 + l'_2 = L$, and where \underline{h}_a is the $(L+1) \times (L+1)$ matrix whose elements are $h_a(l'_1, l'_2 | l_1, l_2)$ with rows and columns labelled similarly. The matrix \underline{m} couples the internal and external motions of the atomic system; it accounts for the coupling of the angular momenta of the individual electrons to give a total angular momentum of $L(L+1)$. Note that we have not complex conjugated $\phi_{l'm'n'}$ in Eqs. (6.17) and (6.18) since $\phi_{l'm'n'}$ is real if the parameter k is real. However, to satisfy outgoing-wave boundary conditions, appropriate to the photodecay of the system, we need to choose k to be in the lower right quadrant of the complex plane. We can analytically continue the right-hand side of Eq. (6.18) from real to complex k since the expression on the right-hand side is analytic in k (it would not be analytic, were we to complex conjugate $\phi_{l'm'n'}$).

We now evaluate the matrix elements of \underline{m} . We temporarily express ζ_1 and ζ_2 in terms of the three Euler angles and the angle θ_{12} between \mathbf{r}_1 and \mathbf{r}_2 . We have [151]

$$\zeta_1 = e^{i\alpha} [\cos \beta \cos(\gamma - \frac{1}{2}\theta_{12}) + i \sin(\gamma - \frac{1}{2}\theta_{12})], \quad (6.20)$$

$$\zeta_2 = e^{i\alpha} [\cos \beta \cos(\gamma + \frac{1}{2}\theta_{12}) + i \sin(\gamma + \frac{1}{2}\theta_{12})]. \quad (6.21)$$

Evidently, the triple integral on the right-hand side of Eq. (6.19) is a function of θ_{12} only, it is periodic in θ_{12} with period 2π (since ζ_1 and ζ_2 are invariant under the change $\theta_{12} \rightarrow \theta_{12} + 2\pi$), and it is even in θ_{12} (since ζ_1 and ζ_2 are invariant under the simultaneous changes $\beta \rightarrow \pi - \beta$, $\gamma \rightarrow \pi - \gamma$, and $\theta_{12} \rightarrow -\theta_{12}$). Hence it should be possible to express this integral as a rapidly convergent sum of powers of $\cos \theta_{12}$. We write the integral as a sum of Legendre polynomials:

$$\underline{m}_{(l'_1, l'_2), (l_1, l_2)} = r_1^{l'_1 + l_1} r_2^{l'_2 + l_2} \sum_{s=0}^{\infty} a_s P_s(\cos \theta_{12}), \quad (6.22)$$

where the coefficients a_s are given as

$$\begin{aligned} a_s &= \frac{2s+1}{2} \int_0^\pi \sin \theta_{12} d\theta_{12} \int_0^{2\pi} d\alpha \int_0^\pi \sin \beta d\beta \int_0^{2\pi} d\gamma \\ &\quad \left[(\zeta_1^*)^{l'_1} (\zeta_2^*)^{l'_2} \zeta_1^{l_1} \zeta_2^{l_2} P_s(\cos \theta_{12}) \right]. \quad (6.23) \end{aligned}$$

Switching integration variables from $(\theta_{12}, \alpha, \beta, \gamma)$ to $(\theta_1, \phi_1, \theta_2, \phi_2)$ we have

$$a_s = \frac{2s+1}{C_{l'_1} C_{l'_2} C_{l_1} C_{l_2}} \int d\Omega_1 \int d\Omega_2 [Y_{l'_1}^{l'_1}(\Omega_1) Y_{l'_2}^{l'_2}(\Omega_2)]^* P_s(\cos \theta_{12}) Y_{l_1}^{l_1}(\Omega_1) Y_{l_2}^{l_2}(\Omega_2), \quad (6.24)$$

where $d\Omega_1$ and $d\Omega_2$ are the solid angles enclosing \mathbf{r}_1 and \mathbf{r}_2 , respectively, and where⁵

$$C_l = (-1)^l \sqrt{\frac{(2l+1)!}{2^{2l+2}\pi(l!)^2}}. \quad (6.25)$$

If we now use the addition theorem to write $P_s(\cos \theta_{12})$ as a sum of terms in $Y_s^m(\Omega_1) [Y_s^m(\Omega_2)]^*$, the integrals over Ω_1 and Ω_2 factorize into an integral over Ω_1 , whose integrand is a product of three spherical harmonics, and an integral over Ω_2 , whose integrand is also a product of three spherical harmonics. These integrals are standard, and can be written in terms of Clebsch-Gordan coefficients, which in the present case take on a relatively simple form. We find that $a_s = 0$ if any one of the following inequalities holds:

$$\begin{aligned} s &< |l'_1 - l_1|, \quad s < |l'_2 - l_2|, \\ s &> l'_1 + l_1, \quad s > l'_2 + l_2, \\ (-1)^s &\neq (-1)^{l'_1+l_1}, \quad (-1)^s \neq (-1)^{l'_2+l_2}. \end{aligned}$$

Therefore, the infinite sum on the right-hand side of Eq. (6.22) truncates to a finite sum. For those values of s for which none of the preceding inequalities holds, we find that

$$\begin{aligned} a_s &= 2^{2L+1}\pi^2(2s+1) \frac{(l'_1)!(l'_2)!! l_1! l_2! (l_2 + s - l'_2)!! (l_1 + s - l'_1)!!}{(l'_1 + l_1 + s + 1)!! (l'_2 + l_2 + s + 1)!!} \\ &\times \frac{[(l'_1 + l_1 + s)/2]!!}{[(l_1 - l'_1 + s)/2]!! [(l'_1 - l_1 + s)/2]!! [(l'_1 + l_1 - s)/2]!!} \\ &\times \frac{[(l'_2 + l_2 + s)/2]!!}{[(l_2 - l'_2 + s)/2]!! [(l'_2 - l_2 + s)/2]!! [(l'_2 + l_2 - s)/2]!!}. \end{aligned} \quad (6.26)$$

Note that

$$\cos \theta_{12} = (r_1^2 + r_2^2 - r_3^2)/(2r_1 r_2), \quad (6.27)$$

but since the largest power of $\cos \theta_{12}$ appearing with $a_s \neq 0$, on the right-hand side of Eq. (6.22), is $l'_1 + l_1$ or $l'_2 + l_2$, negative powers of r_1 and r_2 introduced through $P_s(\cos \theta_{12})$ are offset by the prefactor $r_1^{l'_1+l_1} r_2^{l'_2+l_2}$ before the sum. Hence the matrix elements of \underline{m} are finite sums of nonnegative powers of r_1 , r_2 , and r_3 , and the sum of the powers is $2L$.

To evaluate the triple integral over r_1 , r_2 , and r_3 on the right-hand side of Eq. (6.18), it is expedient to transform to perimetric coordinates, so that the integration variables have independent ranges. Hence we write

$$\int_0^\infty dr_1 \int_0^\infty dr_2 \int_{|r_1-r_2|}^{r_1+r_2} dr_3 r_1 r_2 r_3 \dots = \frac{1}{256} \int dU (u+v)(2u+w)(2v+w) \dots, \quad (6.28)$$

where $\int dU \equiv \int_0^\infty du \int_0^\infty dv \int_0^\infty dw$. If the $\phi_{lmn}(r_1, r_2, r_3)$ are chosen to be the perimetric-Sturmian functions, the integrand of the triple integral is a finite sum of products of polynomials in u , v , and w , multiplied by simple exponential factors in u , v , and w , and this triple integral can be evaluated exactly; if $k_1 = k_2$ the integral can be expressed as

⁵Note that $\zeta^l = \sin^l \theta e^{il\varphi}$ and that $Y_l^l(\Omega) = (-1)^l \left[\frac{(2l+1)!}{2^{2l+2}\pi(l!)^2} \right] \sin^l \theta e^{il\varphi}$.

a rational number, which is zero if either $|l' - l|$, $|m' - m|$, or $|n' - n|$ is larger than some finite number.

6.2.2 Interaction with Radiation

We consider the interaction of the bare system with the radiation field in both the length and velocity gauges. This interaction couples only those states whose total orbital angular momentum quantum numbers, L and L' , differ by unity, so the matrix representing the interaction is block-codiagonal.

In the *length gauge* the interaction is proportional to $z_1 + z_2$, which we rewrite as $r_1 \cos \theta_1 + r_2 \cos \theta_2$. To represent the interaction on our basis, we must evaluate the matrix elements

$$\int d\tau (\Phi_{l'm'n'}^{L'l'_1l'_2})^* (r_1 \cos \theta_1 + r_2 \cos \theta_2) \Phi_{lmn}^{Ll_1l_2},$$

where $L' = L \pm 1$. Actually, we need only consider $L' = L + 1$; the matrix elements for the cases $L' = L - 1$ and $L' = L + 1$ are related by symmetry. If T_1^M is a tensor of first rank, we have the commutation relation⁶

$$[(\hat{L}_+)^K, T_1^0] = \sqrt{2} K T_1^1 (\hat{L}_+)^{K-1}. \quad (6.29)$$

Using Eq. (6.29) we have

$$\begin{aligned} & (\hat{L}_+)^{L+1} (r_1 \cos \theta_1 + r_2 \cos \theta_2) (\hat{L}_-)^L [(r_1 \zeta_1)^{l_1} (r_2 \zeta_2)^{l_2}] \phi_{lmn} \\ &= -(L+1)(r_1 \zeta_1 + r_2 \zeta_2) (\hat{L}_+)^L (\hat{L}_-)^L [(r_1 \zeta_1)^{l_1} (r_2 \zeta_2)^{l_2}] \phi_{lmn} \\ &= -(L+1)(2L!) (r_1 \zeta_1 + r_2 \zeta_2) (r_1 \zeta_1)^{l_1} (r_2 \zeta_2)^{l_2} \phi_{lmn}. \end{aligned} \quad (6.30)$$

It follows from Eqs. (6.14) and (6.30) that, with $L' = L + 1$,

$$\begin{aligned} & \int d\tau (\Phi_{l'm'n'}^{L'l'_1l'_2})^* (r_1 \cos \theta_1 + r_2 \cos \theta_2) \Phi_{lmn}^{Ll_1l_2} \\ &= -\sqrt{\frac{L+1}{2(2L+1)}} \int d\tau (r_1 \zeta_1^*)^{l'_1} (r_2 \zeta_2^*)^{l'_2} \phi_{l'm'n'} (r_1 \zeta_1 + r_2 \zeta_2) (r_1 \zeta_1)^{l_1} (r_2 \zeta_2)^{l_2} \phi_{lmn} \\ &= \int dr_1 \int dr_2 \int dr_3 r_1 r_2 r_3 \phi_{l'm'n'} (\underline{m} \cdot \underline{d})_{(l'_1, l'_2), (l_1, l_2)} \phi_{lmn}, \end{aligned} \quad (6.31)$$

where \underline{d} is a $(L' + 1) \times (L + 1)$ matrix whose elements are

$$\underline{d}_{(l'_1, l'_2), (l_1, l_2)} = -\sqrt{\frac{L+1}{2(2L+1)}} (\delta_{l'_1, l_1+1} \delta_{l'_2, l_2} + \delta_{l'_1, l_1} \delta_{l'_2, l_2+1}). \quad (6.32)$$

In the *velocity gauge* the interaction is proportional to

$$\frac{\partial}{\partial z_1} + \frac{\partial}{\partial z_2},$$

and we must evaluate the matrix elements

$$\int d\tau (\Phi_{l'm'n'}^{L'l'_1l'_2})^* \left(\frac{\partial}{\partial z_1} + \frac{\partial}{\partial z_2} \right) \Phi_{lmn}^{Ll_1l_2},$$

⁶This can be proven by induction, using the commutation relation for a tensor of first rank: $[\hat{L}_\pm, T_L^M] = \sqrt{L(L+1) - M(M \pm 1)} T_L^{M \pm 1}$.

where $L' = L \pm 1$. Again, we need only consider $L' = L + 1$; the matrix elements for the cases $L' = L - 1$ and $L' = L + 1$ are related by antisymmetry ($\partial_z^\dagger = -\partial_z$). We first observe that

$$\begin{aligned} & (\hat{L}_+)^{L+1} \left(\frac{\partial}{\partial z_1} + \frac{\partial}{\partial z_2} \right) (\hat{L}_-)^L [(r_1 \zeta_1)^{l_1} (r_2 \zeta_2)^{l_2}] \phi_{lmn} \\ &= -(L+1) \left(\frac{\partial}{\partial x_1} + i \frac{\partial}{\partial y_1} + \frac{\partial}{\partial x_2} + i \frac{\partial}{\partial y_2} \right) (\hat{L}_+)^L (\hat{L}_-)^L [(r_1 \zeta_1)^{l_1} (r_2 \zeta_2)^{l_2}] \phi_{lmn} \\ &= -(L+1)(2L!) \left(\frac{\partial}{\partial x_1} + i \frac{\partial}{\partial y_1} + \frac{\partial}{\partial x_2} + i \frac{\partial}{\partial y_2} \right) (r_1 \zeta_1)^{l_1} (r_2 \zeta_2)^{l_2} \phi_{lmn}. \end{aligned} \quad (6.33)$$

Writing $r_1 \zeta_1 = x_1 + iy_1$, we see that when $(\partial/\partial x_1) + i(\partial/\partial y_1)$ acts on any function of $r_1 \zeta_1$, it yields zero. A similar remark applies if particles 1 and 2 are interchanged. Hence we can move the factor $(r_1 \zeta_1)^{l_1} (r_2 \zeta_2)^{l_2}$ past the derivatives on the right-hand side of Eq. (6.33). Using this result, and also the relation

$$\begin{aligned} \left(\frac{\partial}{\partial x_1} + i \frac{\partial}{\partial y_1} + \frac{\partial}{\partial x_2} + i \frac{\partial}{\partial y_2} \right) f_{l_1, l_2}^L &= \left(\frac{x_1}{r_1} \frac{\partial}{\partial r_1} + i \frac{y_1}{r_1} \frac{\partial}{\partial r_1} + \frac{x_2}{r_2} \frac{\partial}{\partial r_2} + i \frac{y_2}{r_2} \frac{\partial}{\partial r_2} \right) \phi_{lmn} \\ &= \left(\zeta_1 \frac{\partial}{\partial r_1} + \zeta_2 \frac{\partial}{\partial r_2} \right) \phi_{lmn}, \end{aligned} \quad (6.34)$$

yields

$$\begin{aligned} & \int d\tau (\Phi_{l'm'n'}^{L'l'_1l'_2})^* \left(\frac{\partial}{\partial z_1} + \frac{\partial}{\partial z_2} \right) \Phi_{lmn}^{Ll_1l_2} \\ &= -\sqrt{\frac{L+1}{2(2L+1)}} \int d\tau (r_1 \zeta_1^*)^{l'_1} (r_2 \zeta_2^*)^{l'_2} \phi_{l'm'n'} \left(\zeta_1 \frac{\partial}{\partial r_1} + \zeta_2 \frac{\partial}{\partial r_2} \right) (r_1 \zeta_1)^{l_1} (r_2 \zeta_2)^{l_2} \phi_{lmn} \\ &= \int dr_1 \int dr_2 \int dr_3 r_1 r_2 r_3 \phi_{l'm'n'} (\underline{m} \cdot \underline{v})_{(l'_1, l'_2), (l_1, l_2)} \phi_{lmn}, \end{aligned} \quad (6.35)$$

where \underline{v} is a $(L'+1) \times (L+1)$ matrix whose elements are

$$\underline{v}_{(l''_1, l''_2), (l_1, l_2)} = -\sqrt{\frac{L+1}{2(2L+1)}} \left(\delta_{l''_1, l_1+1} \delta_{l''_2, l_2} \frac{1}{r_1} \frac{\partial}{\partial r_1} + \delta_{l''_1, l_1} \delta_{l''_2, l_2+1} \frac{1}{r_2} \frac{\partial}{\partial r_2} \right). \quad (6.36)$$

6.3 AC Shifts and Widths of H⁻

In this Section we present accurate estimates of second- and fourth-order AC-shifts and widths of the negative hydrogen ion, over a range of frequencies, for light that is linearly polarized. We also resum the perturbation series implicitly by constructing an effective Hamiltonian using just the first three terms of the perturbative expansion of the Floquet wavefunction, and we present rates for decay in the nonperturbative-field regime. All of our calculations were done using the perimetric-Sturmian basis specified by Eqs. (6.4), (6.13), and (6.14), with $k_1 = k_2 \equiv k$. The nonnegative indices l , m , and n of the Laguerre polynomials, on the right-hand side of Eq. (6.4), took on maximum values N_l , N_m , and N_n , respectively, which were restricted by the condition $N_l + N_m + N_n = N_{\max}$ where typically $N_{\max} = 25$. The nonlinear parameter k was chosen to lie in the lower right quadrant of the complex plane so that the basis can accommodate both closed (bound-state) channels and open (outgoing-wave) channels. Typically, k was chosen so

ω	Re E_2 (l)	Re E_2 (v)	Im E_2 (l)	Im E_2 (v)
0.18705	7.33257946	7.33257984	-6.43545251	-6.43545237
0.18975	7.18171648	7.18171685	-6.22458289	-6.22458272
0.19205	7.05609946	7.05609981	-6.05253504	-6.05253491
0.19950	6.66691123	6.66691158	-5.53909251	-5.53909238
0.20000	6.64173224	6.64173255	-5.50686473	-5.50686460
0.20050	6.61666864	6.61666895	-5.47490139	-5.47490126
0.22840	5.38474954	5.38477127	-4.03946797	-4.03947348
0.23000	5.32306202	5.32306224	-3.97422138	-3.97422128
0.23100	5.28493415	5.28493436	-3.93421039	-3.93421029
0.23180	5.25467191	5.25467213	-3.90261899	-3.90261889

Table 6.1: Real and imaginary parts of the coefficient E_2 of the F^2 -term in the Rayleigh-Schrödinger expansion of the AC-quasienergy for H^- , in the length (l) and velocity (v) gauges, for various values of the frequency ω in the region of the lowest ${}^1S^e$ and ${}^1D^e$ resonances below the $H(n = 2)$ and $H(n = 3)$ excitation thresholds. These resonances have no effect on E_2 .

ω	Re E_4 (l)	Re E_4 (v)	Im E_4 (l)	Im E_4 (v)
0.192050	987.986	987.919	-11.4588	-11.4975
0.189750	797.106	797.103	-2756.63	-2756.64
0.187050	38.0371	37.9533	400.733	400.702
0.199500	-1030.56	-1030.60	1906.34	1906.42
0.200000	-420.027	-419.617	-6909.91	-6910.77
0.200500	1022.65	1023.39	-869.213	-868.846
0.228400	157.683	158.740	65.9388	65.9284
0.230000	112.250	112.241	25.1247	25.1177
0.231000	231.100	231.091	125.545	125.566
0.231800	114.068	114.041	121.235	121.223

Table 6.2: Real and imaginary parts of the coefficient E_4 of the F^4 -term in the Rayleigh-Schrödinger expansion of the AC-quasienergy for H^- , in the length (l) and velocity (v) gauges, for various values of the frequency ω .

that $|k| = 0.5$ and $\arg(k) = -30^\circ$. We made no attempt to select the value of k which gives the best ground-state energy (indeed, the optimal k for that purpose would be real). Using the parameters just given, we calculated the ground-state binding energy of H^- to be 0.52775102 a.u., which is correct to the eight figures given. Subtracting 0.5 a.u., the electron affinity is 0.02775102 a.u.

6.3.1 Perturbation Expansion of the AC-Quasienergy

Consider an atomic system dressed by an oscillating monochromatic electric field, whose amplitude and frequency are F and ω , respectively. Making the Floquet ansatz (see Chapter 1, Sec.1.3.1), the state vector, $|\Psi(t)\rangle$, has the harmonic expansion

$$|\Psi(t)\rangle = e^{-iE(F)t/\hbar} \sum_{N=-\infty}^{\infty} e^{-iN\omega t} |\mathcal{F}_N\rangle, \quad (6.37)$$

where $E(F)$ is the quasienergy of the perturbed initial bound state, and where the $|\mathcal{F}_N\rangle$ are the harmonic components of the state vector. The quasienergy can be expressed as $E(F) = E^{(0)} + \Delta(F) - i\Gamma(F)/2$, where $E^{(0)}$ is the energy of the initially unperturbed bound state, and where $\Delta(F)$ and $\Gamma(F)$ are the shift and width induced by the electric field, whose amplitude is F . For sufficiently weak fields the atom-field interaction can be treated as a perturbation. The Rayleigh-Schrödinger perturbation expansion of the quasienergy is a power series in F^2 :

$$E(F) = \sum_{m=0}^{\infty} E^{(2m)} F^{2m}. \quad (6.38)$$

To determine the F -independent coefficient $E^{(2m)}$, we must solve the equations satisfied by the n -th order subcomponents, $|\psi_N^{(n)}\rangle$, of the N -th harmonic component for $|N| \leq n \leq m$. Before writing down these equations, we need to introduce more notation. Writing the atom-field interaction as

$$V(t) = FV_+e^{-i\omega t} + FV_-e^{i\omega t}, \quad (6.39)$$

we introduce the Floquet Hamiltonian matrix, $\mathbf{H}(F)$, which is a tridiagonal matrix whose elements are operators $\mathbf{H}_{MN}(F)$, which are matrices with

$$\mathbf{H}_{MN}(F) = (H_a - M\hbar\omega)\delta_{MN} + FV_+\delta_{M,N+1} + FV_-\delta_{M,N-1}. \quad (6.40)$$

Collecting the harmonic components $|\mathcal{F}_N\rangle$ into the column vector $|\mathcal{F}\rangle\rangle$, we have the eigenvalue problem

$$\mathbf{H}(F)|\mathcal{F}\rangle\rangle = E(F)|\mathcal{F}\rangle\rangle. \quad (6.41)$$

The Rayleigh-Schrödinger series is generated by expanding $|\mathcal{F}\rangle\rangle$ in the power series

$$|\mathcal{F}\rangle\rangle = \sum_{n=0}^{\infty} F^n |\psi^{(n)}\rangle\rangle, \quad (6.42)$$

where $|\psi^{(n)}\rangle\rangle$ is a F -independent column vector whose elements $|\psi_N^{(n)}\rangle$ are null vectors for $|N| > n$. Substituting the right-hand side of Eq. (6.42) into Eq. (6.41), using Eq. (6.38), and collecting equal powers of F , noting that $\mathbf{H}_{MN}(F)$ is linear in F , we arrive at the following set of coupled equations (cf Pan *et al*, Ref.[4]) for the $|\psi_N^{(n)}\rangle$, with $n \geq |N| \geq 0$ (cf Eq.(1.32) in Chapter 1):

$$(H_a - N\hbar\omega)|\psi_N^{(n)}\rangle + V_+|\psi_{N-1}^{(n-1)}\rangle + V_-|\psi_{N+1}^{(n-1)}\rangle = \sum_{m=0}^{n/2} E^{(2m)}|\psi_N^{(n-2m)}\rangle. \quad (6.43)$$

In the case of the hydrogen atom, the coefficients $E^{(2m)}$ can be calculated to very high order, with high accuracy, and without great computational effort (see e.g. Refs. [4] and [82]). However, in the case of a two-electron system, the calculation of these coefficients is much more challenging. For the purpose of providing a benchmark, we give, in Tables 1-4, estimates of $E^{(2)}$ and $E^{(4)}$ for H⁻, obtained in the length and velocity gauges, for selected frequencies. It is reasonable to suppose that these estimates are accurate to the number of figures — typically seven for $E^{(2)}$ and four for $E^{(4)}$ — that are insensitive to whether the length or velocity gauge is used⁷.

⁷For gauge invariance, see Chapter 1, Sec.1.4.2.

ω	Re E ₂ (l)	Re E ₂ (v)	Im E ₂ (l)	Im E ₂ (v)
0.627751	1.33220820	1.33220821	-0.524953187	-0.524953052
0.727751	1.01989280	1.01989279	-0.309690568	-0.309690481
0.827751	0.796452214	0.796452205	-0.193247293	-0.193247233
0.927751	0.635275152	0.635275143	-0.126309920	-0.1263098762
1.02775	0.516699564	0.516699556	-8.57989863[-2]	-8.57989531[-2]
1.12775	0.427563497	0.427563491	-6.01945136[-2]	-6.01944874[-2]
1.22775	0.359164884	0.359164879	-4.34049732[-2]	-4.34049516[-2]
1.32775	0.305685085	0.305685080	-3.20434724[-2]	-3.20434544[-2]
1.42775	0.263160480	0.263160476	-2.41431941[-2]	-2.41431788[-2]
1.52775	0.228835566	0.228835562	-1.85179768[-2]	-1.85179636[-2]
1.62775	0.200755973	0.200755969	-1.44284255[-2]	-1.44284142[-2]

Table 6.3: Same as Table 6.1 but for values of ω above the two-electron escape threshold.

ω	Re E ₂ (l)	Re E ₂ (v)	Im E ₂ (l)	Im E ₂ (v)
0.627751	0.697603	0.697730	-0.489991	-0.490010
0.727751	0.295628	0.295679	-9.58287[-2]	-9.58342[-2]
0.827751	0.129228	0.129252	-1.09303[-2]	-1.09326[-2]
0.927751	5.95241[-2]	5.95369[-2]	5.84499[-3]	5.84327[-3]
1.02775	2.89153[-2]	2.89231[-2]	7.29659[-3]	7.29489[-3]
1.12775	1.47513[-2]	1.47569[-2]	5.76058[-3]	5.75924[-3]
1.22775	7.86236[-3]	7.86658[-3]	4.08347[-3]	4.08308[-3]
1.32775	4.35693[-3]	4.35957[-3]	2.80101[-3]	2.80128[-3]
1.42775	2.49904[-3]	2.50049[-3]	1.90902[-3]	1.90912[-3]
1.52775	1.47747[-3]	1.47854[-3]	1.30694[-3]	1.30671[-3]
1.62775	8.97219[-4]	8.98260[-4]	9.02795[-4]	9.02672[-4]

Table 6.4: Same as Table 6.2 but for values of ω above the two-electron escape threshold.

6.3.2 Decay Rate

The total rate of decay of the atomic system is the AC-width, $\Gamma(F)$, which has the Rayleigh-Schrödinger expansion

$$\Gamma(F) = \sum_{m=1}^{\infty} \Gamma^{(2m)} F^{2m}, \quad (6.44)$$

where $\Gamma^{(2m)} \equiv -2\text{Im}E^{(2m)}$. For a given order of perturbation, say $2m$, there can be more than one ionization processes that contribute to the partial decay rate $\Gamma^{(2m)}$. In particular, we write the partial rate of decay by absorption of m photons in lowest (i.e. $2m$ -th) order in F as $\Gamma_{2m}F^{2m}$. If N_0 is the minimum number of photons which the system must absorb to decay, we have $\Gamma^{(2N)} = 0$ for $N < N_0$, and $\Gamma^{(2N_0)} = \Gamma_{2N_0}$. However, $\Gamma^{(2N)} \neq \Gamma_{2N}$ when $N > N_0$; rather, $\Gamma^{(2N)}$ includes contributions from the interference of the amplitude for absorption of N photons and concomitant emission of $N - M$ photons with the amplitude for absorption of M photons, where $N_0 \leq M < N$. These additional contributions are corrections, which are of order $2N$ in F and may be negative, to the partial rate of decay due to *net* absorption of M photons. While $\Gamma(F)$

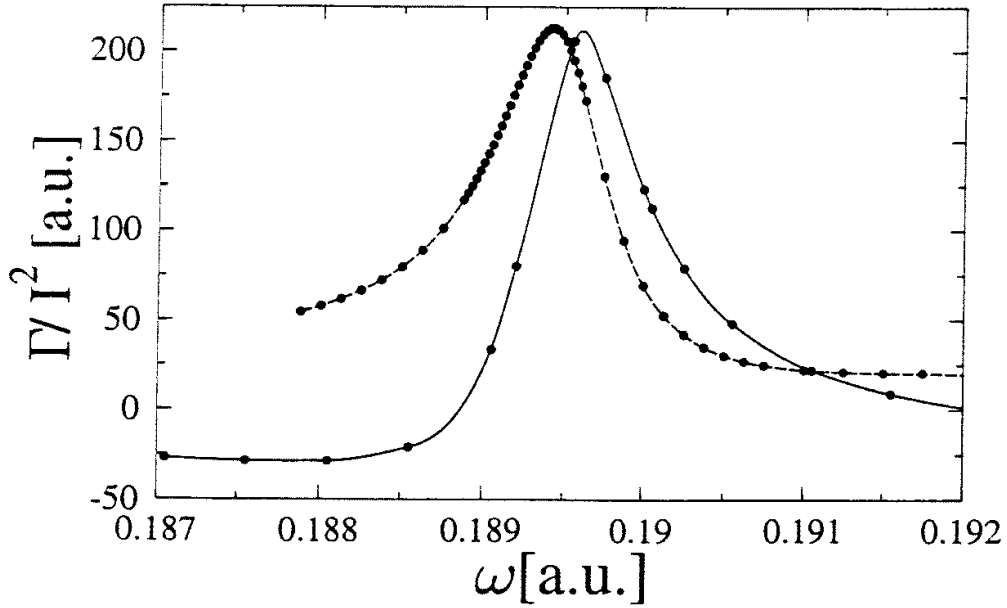


Figure 6.1: I^2 -contributions to rate of decay when H⁻ is illuminated by linearly polarized light of frequency ω and intensity $I = cF^2/(8\pi)$ in the vicinity of the lowest ${}^1S^e$ resonance below the H($n = 2$) excitation threshold. Dashed and solid lines are $\Gamma_4(F^2/I)^2$ and $\Gamma^{(4)}(F^2/I)^2$, respectively, where $\Gamma_4 F^4$ is the rate of decay due to two-photon absorption, in order I^2 , and $\Gamma^{(4)} F^4$ is the rate of decay due to all processes of second order in I (see text). The solid circles are the calculated points; we have interpolated through these points. The position and width of the resonance of the unperturbed H⁻ ion are -0.1487763 and 1.733×10^{-3} a.u., respectively.

is necessarily positive, since it is the total rate of decay, there is no restriction on the sign of $\Gamma^{(2N)}$ for $N > N_0$.

In Figures 6.1 through 6.3 we show the F -independent quantities $\Gamma^{(4)}(F^2/I)^2$ and $\Gamma_4(F^2/I)^2$, where $I \equiv cF^2/(8\pi)$ is the intensity of the light, *vs* frequency ω in the vicinities of four resonances of H⁻, the lowest ${}^1S^e$ and ${}^1D^e$ resonances below the H($n = 2$) and H($n = 3$) excitation thresholds. Note that $N_0 = 1$ over the frequency ranges shown, but that these resonances are reached (in the final channel) by 2-photon absorption. The values of Γ_4 were taken from the calculations of Proulx *et al*, Ref.[153], which are in good agreement with more recent calculations by Sanchez *et al* [154]. The difference in the profile-shapes of Γ_4 and $\Gamma^{(4)}$, seen in these figures, is due primarily to the correction of second order in I (contained in $\Gamma^{(4)} F^4$) to the partial rate of decay due to net absorption of one photon. This difference is especially pronounced in the case of the resonances below the H($n = 3$) excitation thresholds, where we see (in Figure 6.3) that Γ_4 and $\Gamma^{(4)}$ are of opposite sign, and evidently the I^2 -correction to the net-one-photon detachment rate is relatively large and negative. Of course, the photodetachment rate calculated *through* second order in I , namely $\Gamma^{(2)} F^2 + \Gamma^{(4)} F^4$, is positive over all frequencies and intensities for which perturbation theory is applicable. The profile-shape of Γ_4 in Figure 6.2 is in good agreement with the profile-shape of the electron yield measured by Stintz *et al* [155] in the region of the lowest ${}^1D^e$ resonance below the H($n = 2$) excitation threshold, but the measured electron yield peaks at a photon energy slightly lower, by about 2.5 meV, than the energy at which the theoretical estimate Γ_4 peaks. This energy

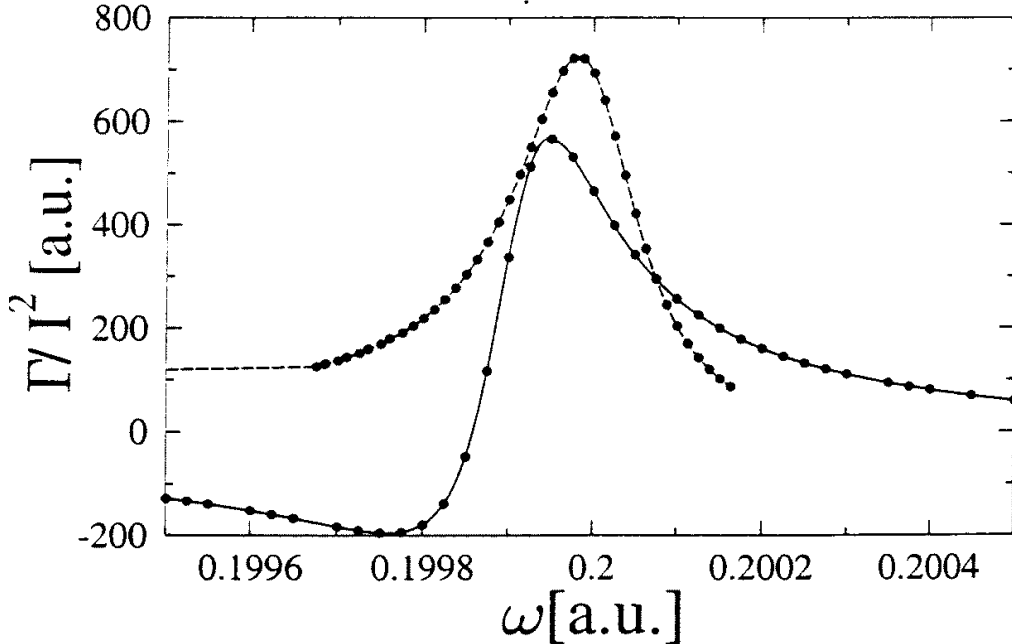


Figure 6.2: Same as Figure 6.1 but in the vicinity of the lowest $^1D^e$ resonance below the $H(n = 2)$ excitation threshold. The position and width of the resonance are -0.1279368 and 3.176×10^{-3} a.u., respectively.

difference is almost precisely the difference in the positions of the peaks of the profiles of Γ_4 and the more accurately calculated $\Gamma^{(4)}$. Since experimentally photoelectron spectra can be obtained with very high accuracy, the difference is most probably caused by the calculation of Γ_4 . In the calculation of Γ_4 by Proulx *et al.*, the basis functions for the two-electron system consist of products of one-electron basis functions. Therefore, in contrast to the calculations of $\Gamma^{(4)}$, only even powers of the interelectronic coordinate r_3 are included in the calculation of Γ_4 . As a result, correlation effects, playing an important role in the ionization process of H^- , are included to a higher extent in the calculation of $\Gamma^{(4)}$, yielding more accurate results. The difference between the positions of the peaks of Γ_4 and $\Gamma^{(4)}$ in Figure 6.2 could be a result of including insufficient electron-electron correlation in the calculation of Γ_4 . To our knowledge, there are no measurements of $\Gamma^{(4)}$. We have calculated the positions and widths of the resonances of the unperturbed H^- ion, and we give our estimates in the figure captions; these estimates are in agreement with (more accurate) values given by others (see for example Bhatia and Ho, Ref.[156]).

6.3.3 Beyond Perturbation Theory

Perturbation theory is useful only for field strengths smaller than the radius of convergence of the perturbation series⁸. At larger field strengths a nonperturbative approach is required. During the last few years, sophisticated calculations of rates for multiphoton detachment of H^- by a nonperturbative laser field have been carried out using the

⁸The singularities of $E(F)$ are branch points, corresponding to either a resonance or a channel closing, and the radius of convergence of the perturbation series is determined by the branch point that is nearest to the origin in the complex F -plane. See e.g. Manakov and Fainshtein, Ref.[12] and Pont and Shakeshaft, Ref.[7].

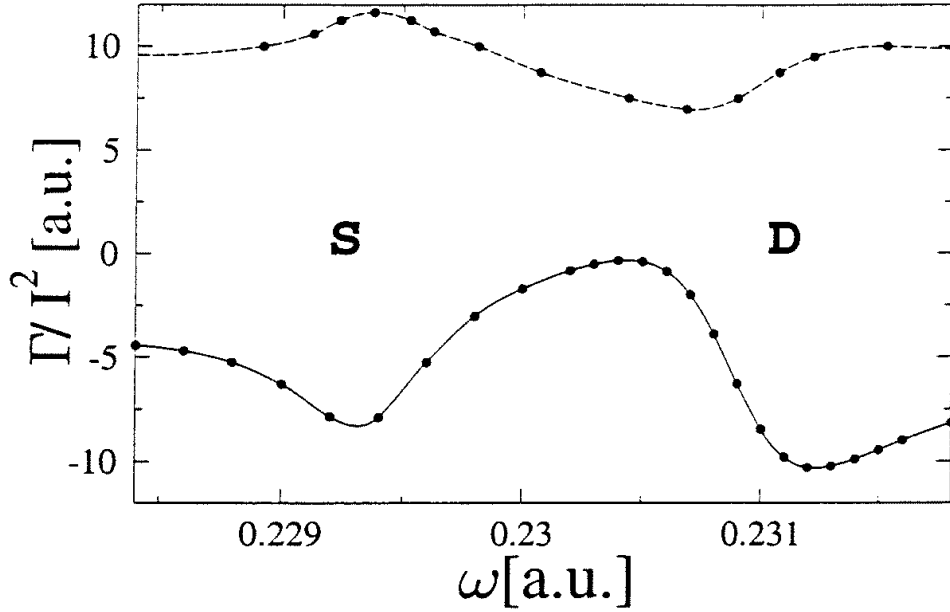


Figure 6.3: Same as Figure 6.1 but in the vicinity of the lowest ${}^1\text{S}^{\text{e}}$ and ${}^1\text{D}^{\text{e}}$ resonances below the $\text{H}(n=3)$ excitation threshold. The position and width of the ${}^1\text{D}^{\text{e}}$ resonance are -0.06595327 and 1.658×10^{-3} a.u., respectively, and the position and width of the ${}^1\text{S}^{\text{e}}$ resonance are -0.06900580 and 1.419×10^{-3} a.u., respectively.

R-Matrix-Floquet method (see Refs.[157],[158],[159],[160]). Here we consider a less comprehensive approach [114]. It is based on constructing an effective Hamiltonian that is the representation of the true Hamiltonian on a finite set of basis vectors that are successive terms in the Rayleigh-Schrödinger expansion of the Floquet state vector of the dressed atom. Thus, rather than generate the Rayleigh-Schrödinger series, we expand $|\mathcal{F}\rangle\rangle$ on a finite basis spanned by the F -independent vectors $\{|\psi^{(n)}\rangle\rangle, n = 0, \dots, n_{\max}\}$:

$$|\mathcal{F}\rangle\rangle = \sum_{n=0}^{n_{\max}} a_n(F) |\psi^{(n)}\rangle\rangle. \quad (6.45)$$

Substituting the latter expansion into Eq. (6.41) we obtain the following equations for the coefficients $a_n(F)$:

$$\sum_{n=0}^{n_{\max}} H_{mn}(F) a_n(F) = E(F) \sum_{n=0}^{n_{\max}} S_{mn} a_n(F), \quad (6.46)$$

where the elements $H_{mn}(F)$ represent the Floquet Hamiltonian on our basis, i.e.

$$H_{mn}(F) = \langle\langle \psi^{(m)} | \mathbf{H}(F) | \psi^{(n)} \rangle\rangle \quad (6.47)$$

$$= \sum_{M=-m}^m \sum_{N=-n}^n \langle\langle \psi_M^{(m)} | \mathbf{H}_{MN}(F) | \psi_N^{(n)} \rangle\rangle, \quad (6.48)$$

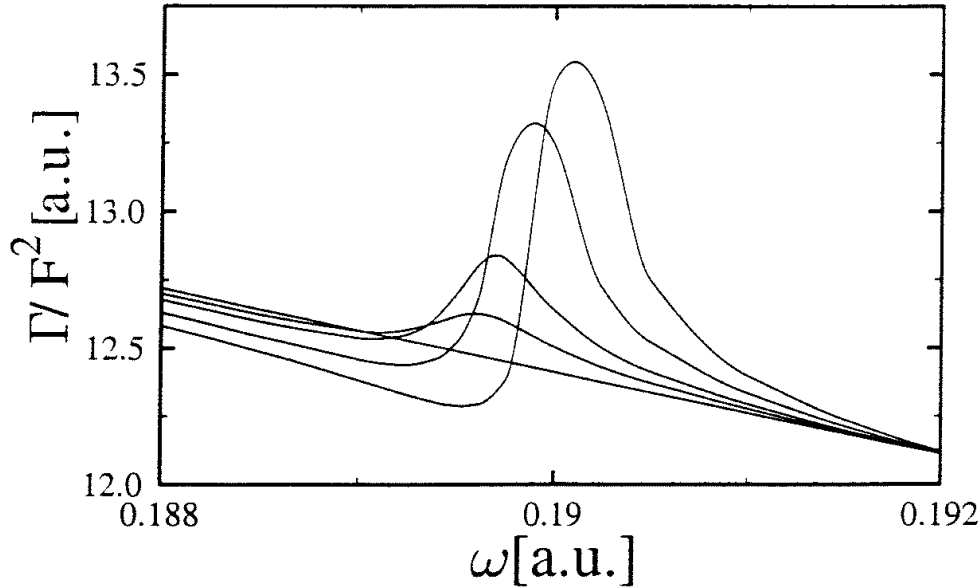


Figure 6.4: Total rate of decay, Γ , divided by intensity I , em vs frequency ω in the vicinity of the lowest ${}^1\text{S}^e$ resonance of H^- below the $\text{H}(n = 2)$ excitation threshold, for 5 different intensities. In order of increasing maxima of Γ/I , the intensities are 1.0×10^{10} , 7.5×10^{11} , 1.5×10^{12} , 3.0×10^{12} , and 5.0×10^{12} W/cm².

and where S_{mn} are the elements of the overlap matrix, i.e.

$$S_{mn} = \langle\langle \psi^{(m)} | \psi^{(n)} \rangle\rangle \quad (6.49)$$

$$= \sum_{N=-l}^l \langle \psi_N^{(m)} | \psi_N^{(n)} \rangle, \quad (6.50)$$

where l is the smaller of m and n . Therefore we arrive at the generalized eigenvalue problem

$$\underline{H}(F)\underline{\mathbf{a}}(F) = E(F)\underline{S}\underline{\mathbf{a}}(F), \quad (6.51)$$

where $\underline{H}(F)$ and \underline{S} are the $(n_{\max} + 1) \times (n_{\max} + 1)$ matrices whose elements are $H_{mn}(F)$ and S_{mn} , respectively, and where $\underline{\mathbf{a}}(F)$ is the vector of length $n_{\max} + 1$ whose elements are $a_n(F)$. Note that the bra $\langle \psi_M^{(m)} |$ in the scalar product used above is defined so that only the angular part, and not the radial part, is complex conjugated.

While the model Hamiltonian approach is, generally speaking, no match for the R-Matrix-Floquet method, it has the merit that the largest part of the computation, namely, the determination of the basis vectors $\{|\psi^{(n)}\rangle\}$, $n = 0, \dots, n_{\max}\}$, is independent of F , and once this task has been performed, $E(F)$ can be readily estimated for many values of F ; one has to solve only a $(n_{\max} + 1) \times (n_{\max} + 1)$ matrix eigenvalue problem. Furthermore, in the weak-field limit, the perturbation expansion is reproduced through order $2n_{\max}$ in F . However, the intensity range over which this approach is useful is rather limited in the vicinity of resonances (see Baik *et al*, Ref.[114]).

Nevertheless, we have used the 3-level model Hamiltonian, constructed from the zeroth-, first-, and second-order perturbed wavefunctions, to explore the way in which

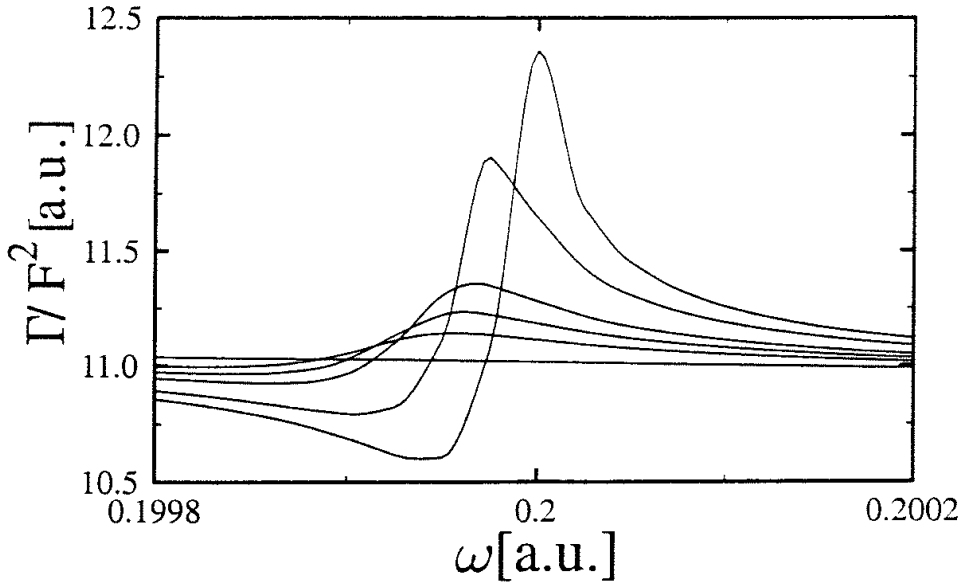


Figure 6.5: Same as Figure 6.4, but for the lowest ${}^1\text{D}^{\text{e}}$ resonance below the $\text{H}(n=2)$ excitation threshold, and for the 6 different intensities (in order of increasing maxima of Γ/I): 1.0×10^{10} , 2.0×10^{11} , 3.0×10^{11} , 4.0×10^{11} , 6.0×10^{11} , and $7.5 \times 10^{11} \text{ W/cm}^2$.

the absorption profiles at the lowest ${}^1\text{S}^{\text{e}}$ and ${}^1\text{D}^{\text{e}}$ resonances below the $\text{H}(n=2)$ threshold change as the intensity varies beyond the perturbative regime. Denoting by $\Gamma(F)$ the total decay rate estimated using the three-level model Hamiltonian, we give, in Figures 6.4 and 6.5, some results for $\Gamma(F)/F^2$ vs ω for several different intensities. At low intensities only one-photon absorption is significant, $\Gamma(F)$ is linear in I , and the contribution from the two-photon resonances is negligible, so that $\Gamma(F)$ does not show any significant change as ω varies in the vicinity of a resonance. However, as the intensity increases two-photon processes become very important, and $\Gamma(F)$ exhibits a pronounced variation as ω varies in the vicinity of a resonance⁹. We see that the resonance profiles begin changing at fairly small intensities, a feature found earlier by Fearnside [160]. In a recent study of resonant photodetachment of H⁻ into the 2-photon channel, Fearnside used the R-Matrix-Floquet method to calculate nonperturbative partial rates for photodetachment into the two-photon channel, and found the resonance profiles to be insensitive to I only up to rather small intensities (the profiles become intensity-dependent when perturbation theory breaks down, i.e., where the Rabi frequency of oscillation between the excited resonance and the ground state is equal to the characteristic width of the resonance)¹⁰. Note that each resonance profile of the total rate $\Gamma(F)$ becomes narrower

⁹In Figures 6.4 and 6.5 we see that the contribution to the total rate from the two-photon processes changes sign while crossing the resonance. On the contrary, the contribution from the one-photon ionization (which is linear in F^2) does not show this behavior, which can be understood considering the following: At the frequencies we used, the sign of the resolvent operator corresponding to a two-photon process, $G(E^{(0)} + 2\omega - H_{at})$, changes sign as $E^{(0)} + 2\omega$ crosses the resonance energy. Since at the frequencies we used the resonance can be reached from the ground state by two-photons only, the resolvent operator for the one-photon ionization process $G(E^{(0)} + \omega - H_{at})$ does not change sign as ω varies.

¹⁰For a two-level system, the branch point determining the radius of convergence of the perturbation series is located at $F = (E^{(0)} - E_R)/2V_{g,R}$ (cf Eq.(1.48) in Chapter 1). Here $V_{g,R}$ is the matrix element

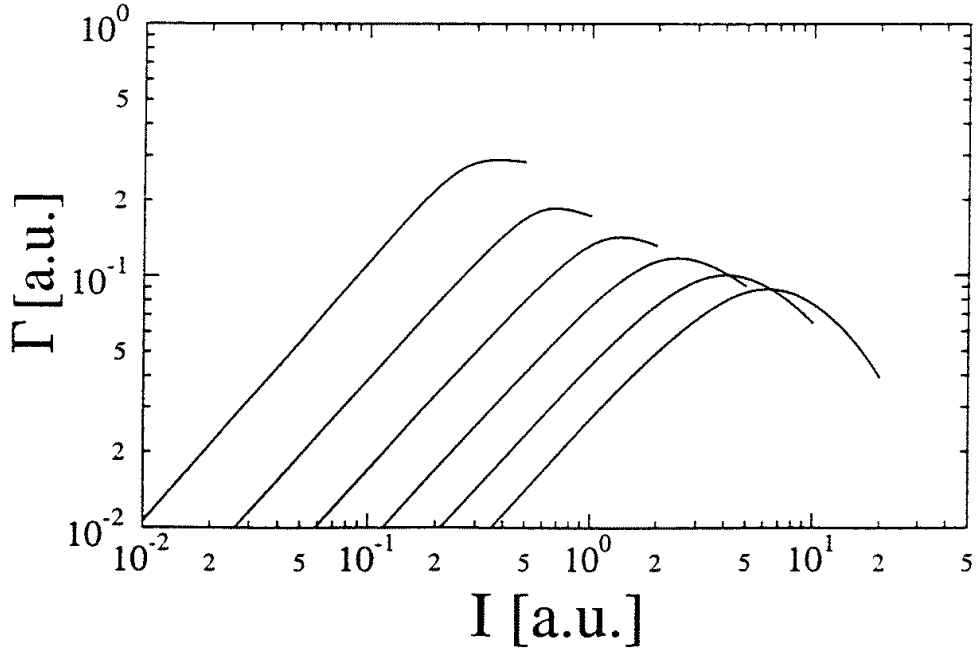


Figure 6.6: Total rate of decay, Γ , of H^- em vs intensity I for various frequencies. In order of decreasing maxima, the frequencies are in excess of the two-electron escape threshold by 0.1, 0.3, 0.5, 0.7, 0.9, 1.1, a.u.

with increasing intensity, and that its maximum height increases. Both of these features are in agreement with the results of Fearnside. As shown by Kim and Lambropoulos, see Ref.[161], the narrowing of the profiles can be explained by destructive interference between the field-independent auto-detaching pathway and the field-induced pathway. Field-independent auto-detachment is induced by configuration interaction. There exists a field-induced pathway that can interfere with the field-independent pathway: Detachment by stimulated absorption and subsequent emission (or vice versa) of a photon from the auto-detaching state to the continuum. At low intensities, the auto-detachment is dominated by the field-independent pathway. As the intensity increases, however, the field-dependent pathway can not be neglected and interference with the field-independent pathway sets in. In our case, the two pathways appear to interfere destructively, and therefore the rate of auto-detachment decreases as is represented by the smaller width. Note also that the resonances shift upwards relative to the ground state as I increases (cf the ponderomotive shift; see Chapter 1, Sec.1.1.2); this feature is expected, since quasibound states are much less compact than the ground state, and are more easily polarized by low-frequency light.

6.3.4 High Frequencies and Stabilization

In high-frequency fields the rate of ionization is dominated by the ionization process involving the minimum number of photons required to couple the initial state with the

of the coupling between the ground state and the resonance and E_R is the complex energy of the resonance, $E_R = W_R - i\Gamma/2$ with Γ the characteristic width of the resonance. In the dressed state picture, using the rotating wave approximation with ω on resonance, the nominator is proportional to the characteristic width of the resonance and $FV_{0,R}$ is equal to the Rabi frequency.

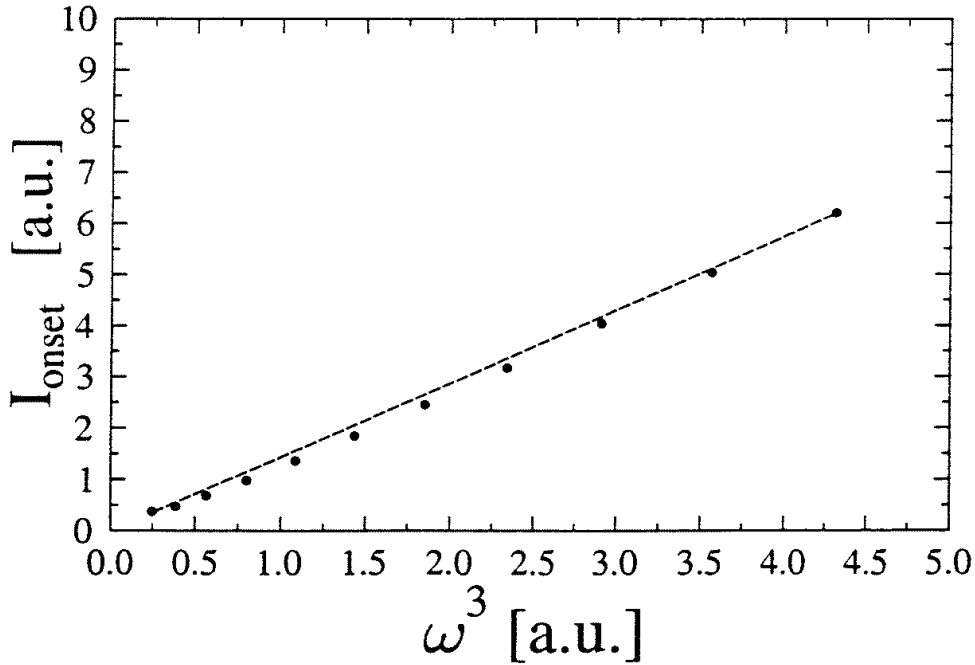


Figure 6.7: Onset intensity, I_{onset} , for stabilization of H⁻ against decay em vs the cube of the frequency ω .

continuum (for atomic hydrogen see e.g. Pont, PhD Thesis, Ref.[162]). In other words, in the photoelectron spectrum the height of the ATI peaks is very small compared to the height of the lowest order peak, which, in high-frequency fields, corresponds to the one-photon ionization process. This can be understood with the following hand-waving argument: At increasing frequencies, the speed the electron leaves the core with after absorption of a photon increases. Since the electron can absorb photons only when it is close to the core, in high-frequency fields it has little time to absorb an excess photon. Consequently, we expect that the angular part of the electronic wavefunction is dominated by low- L character. Moreover, since there are no resonances of H⁻ above the threshold for two-electron escape, the model Hamiltonian approach is ideal at frequencies above this threshold. In Figure 6.6 we show the total rate for decay of H⁻ versus intensity I , calculated using the 3-level model Hamiltonian (including S , P and D states) for various frequencies above the two-electron escape threshold. At weak fields one-photon decay is dominant, and we see that the rate rises linearly with increasing I until an intensity is reached beyond which *multiphoton* processes become important and perturbation theory breaks down. As I increases further, the rate reaches a maximum and then begins decreasing, indicating the onset of stabilization of the ion against ionization. There is an extensive literature on stabilization, see for example several articles in Ref.[163], but our focus here is on the intensity I_{onset} for the onset of stabilization. As shown by Pont and Shakeshaft in Ref.[69], the intensity I_{onset} is approximately that intensity for which the ponderomotive energy $F^2/(4\omega^2)$ (the “quiver” energy of a free electron) is equal to the photon energy ω . This condition, which is purely kinematical in origin, implies that I_{onset} increases with increasing ω as ω^3 . In Figure 6.7 we show I_{onset} vs ω^3 for H⁻; as expected, the curve is a straight line. Since our computer code was written to include only the values 0, 1, and 2 for the angular momentum quantum number, L ,

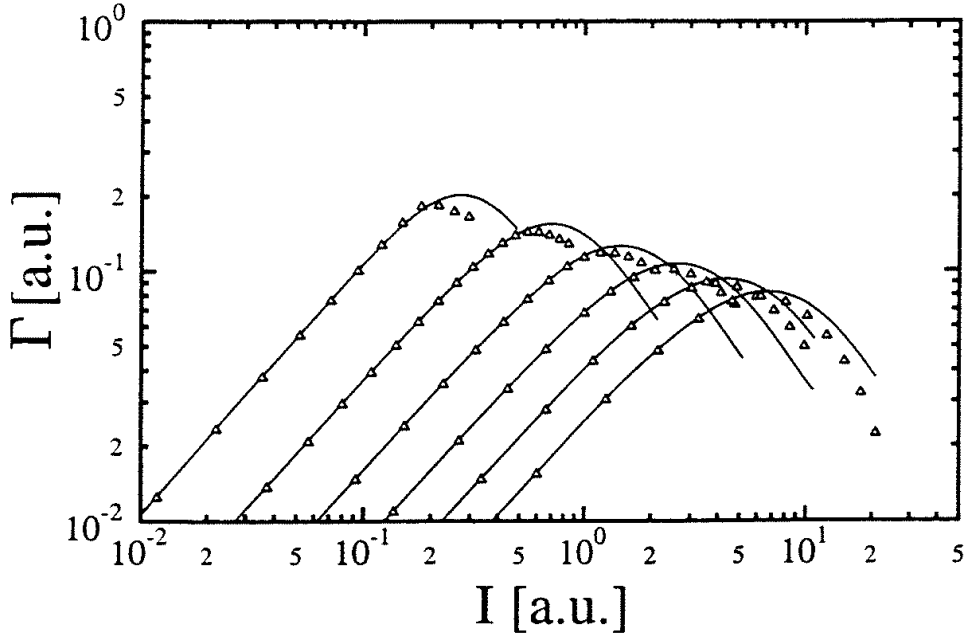


Figure 6.8: Total rate of ionization, Γ , of H em vs intensity I for various frequencies, based on a model Hamiltonian whose size is 3×3 (open triangles) or 21×21 (solid lines). In order of decreasing maxima, the frequencies are in excess of the ionization threshold by 0.1, 0.3, 0.5, 0.7, 0.9, 1.1, a.u.

we were unable to test the convergence of our results with respect to n_{\max} by increasing the size ($n_{\max} + 1$) of the model Hamiltonian matrix beyond $n_{\max} = 2$. Naturally, the reader may wonder whether the results shown in Figures 6.6 and 6.7, computed with $n_{\max} = 2$, are even approximately correct at the higher intensities considered. However, due to the absence of resonances, we expect our results would converge rapidly were we to increase n_{\max} . Our confidence that the results shown in Figures 6.6 and 6.7 are at least qualitatively correct is supported by results for H, shown in Figure 6.8, where we see that ionization rates obtained with $n_{\max} = 2$ do not differ substantially from the fully converged results; the positions and heights of the maxima of the rates are given rather accurately using $n_{\max} = 2$, especially so at higher frequencies.

Note the close similarity between the rates for H and H^- , indicating that at frequencies above the two-electron escape threshold the correlation between the electrons has little influence on decay rates even at nonperturbative intensities. This similarity can be understood considering the electron configurations in H^- . In both the screening and anti-screening configuration in H^- , the probability density of one electron is concentrated close to the nucleus whereas the other electron is relatively far away from the nucleus. Therefore, in contrast to the outer electron, the inner electron can undergo a hard collision with the nucleus and absorb a photon, with the outer electron as a spectator. Although the presence of the outer electron significantly perturbs the probability density of the inner electron in the region relatively far away from the nucleus, it only

mildly perturbs the probability density in the region close to the nucleus. We therefore expect the rates of photodecay for H and H⁻ to be similar¹¹.

6.4 Remarks about Method

We have presented an application of the perimetric-Sturmian basis to the calculation of AC-shifts and widths of H⁻. The system H⁻ is the most suitable candidate, among the helium-like ions, to which this basis can be applied. As the atomic number Z increases, electron correlation in a helium-like ion becomes less significant. In the large- Z limit, when the dynamical interaction between the electrons can be neglected, the atomic wavefunction has only a *geometric* dependence on r_3 , through the matrix \underline{m} which depends on even powers of r_3 up to the power $2L$; see Eqs. (6.18), (6.22), and (6.27). However, the perimetric coordinates put the relative motions of all three particles (the two electrons and the nucleus) on the same footing, and each perimetric Sturmian function $\phi_{lmn}(r_1, r_2, r_3)$ depends on r_3 , so that individual basis functions $\Phi_{lmn}^{Ll_1l_2}(\mathbf{r}_1, \mathbf{r}_2; \pm)$ depend on r_3 , even apart from the geometric dependence; independence from r_3 can only be achieved through substantial cancellation among basis functions, leading to roundoff error. We suspect that significant roundoff error is already present in estimates of D-state energy eigenvalues of He when a large perimetric-Sturmian basis is employed. Perhaps of greater importance is that the decreasing sensitivity of the dynamical part of the wavefunction to r_3 , as Z increases, implies that the inclusion of high powers of r_3 in $\phi_{lmn}(r_1, r_2, r_3)$ is wasteful. For $Z = 2$ and larger, it is probably more efficient to employ the more traditional basis (see e.g. Refs. [164] and [165]) consisting of terms of the form $\exp[-(k_1 r_1 + k_2 r_2)] r_1^l r_2^m r_3^n$, where the maximum values of l and m can be large, but where powers of r_3 are restricted by keeping the maximum value of n to be small.

¹¹The calculations show a slightly larger rate for H⁻ than for H. This could be induced by the screening configuration in which the outer electron pushes the inner towards the nucleus, increasing the probability for the inner electron to scatter with the nucleus.

7

DETACHMENT RATES OF H^{2-} IN AN INTENSE LINEARLY POLARIZED LASER FIELD

In the presence of intense high-frequency laser fields the character of atomic systems can change dramatically. Both the stability of the system and the shape of the wavefunction describing the atomic states are affected by the interaction with the radiation field. In intense radiation fields, the structure of the system can be deformed so strongly that new atomic states appear in the field which do not exist in absence of the field. Even systems that do not support any stable state in absence of the field can support stable "light-induced states" in the field (see Chapter 1, Secs.1.3.3 and 1.6.1).

A typical example of a system without stable configurations in vacuum is an atomic multiply charged negative hydrogen ion. In Chapters 3 and 5 we have shown that bound states of H^{2-} can exist in high-frequency linearly polarized laser fields. The appearance

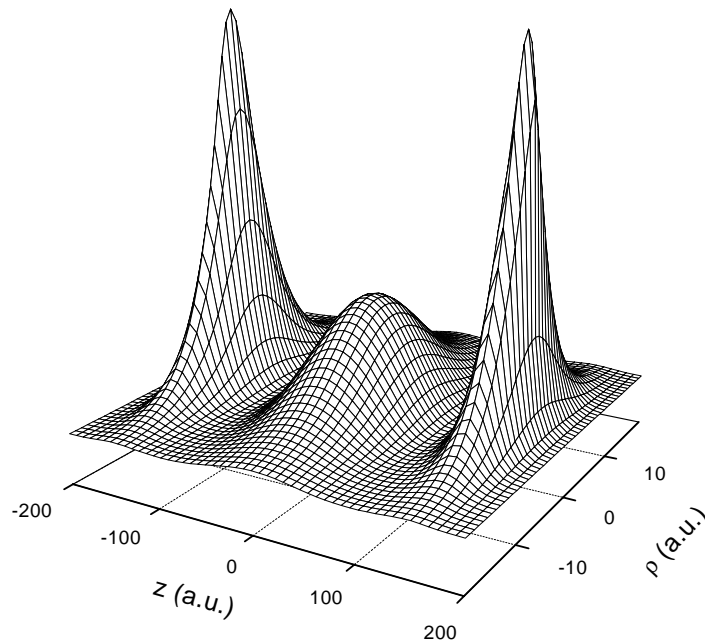


Figure 7.1: The three-electron wavefunction of H^{2-} in a linearly polarized (along z -axis) laser field at $\alpha_0 = 155$. Note there is no spatial overlap between the one-electron orbitals. The orbital of the electron centered around $z = 0$ is more diffuse in the z -direction than the orbitals at $z \pm \alpha_0$. Despite the repulsive interaction with the electron around $z = 0$, the wavefunctions of the electrons at $z \pm \alpha_0$ are slightly polarized towards $|z| < \alpha_0$ due to the attraction those electrons feel with the positive line charge.

of these bound states has to be considered as a highly non-perturbative phenomenon in the sense that the electron distribution required for the stability of these bound states of H^{2-} can be imposed by intense radiation fields only.

The bound states obtained in Chapter 3 are eigenstates of the *time-independent* dressed-potential Hamiltonian H_0 (see Chapter 1, Sec.1.5). In high-frequency Floquet theory (HFFT) H_0 is the Hamiltonian one obtains in the limit $\omega \rightarrow \infty$, which depends on the intensity I and frequency ω of the field through the parameter $\alpha_0 = I^{1/2}/\omega^2$ only. In the present Chapter, we go beyond the high-frequency approximation and consider the behavior of H^{2-} in a radiation field with finite, but still large, frequencies. As shown in the next Section (see also Chapter 1, Sec.1.5), beyond the high-frequency limit the energy of H^{2-} becomes complex; in other words, electron detachment sets in by the interaction with the field.

For the H^{2-} ion there are, provided the frequency is high enough, three electrons that can detach by absorption of one or more photons from the field. From Chapter 3 we know that in the high-frequency limit, the wavefunction of the three electrons is concentrated along a straight line segment extending from $z = -\alpha_0$ to $z = +\alpha_0$, where the z -axis is chosen to be parallel to the polarization axis. As shown in Figure 7.1, two of the three electrons are located around the end-points of the line of charge at $z = \pm\alpha_0$. They are referred to as the end-point electrons, whereas the third electron, which is located around $z = 0$, is referred to as the internal electron.

In this Chapter we will focus on the internal electron, and in particular on its rate of detachment in laser fields with finite frequencies. We present calculations on the detachment rates of the internal electron for various different frequencies and intensities.

7.1 The Complex Quasienergy Beyond the High-Frequency Limit

7.1.1 The Floquet Ansatz

We treat the interaction between the ion and the radiation field within the Floquet framework, applicable for monochromatic fields with time-independent amplitude (for details on Floquet theory, see Chapter 1, Sec.1.3). Following the Floquet ansatz we write the wavefunction of the H^{2-} ion as $\Psi(\mathbf{R}; t) = \exp(-iEt) \sum_n \exp(-in\omega t) \phi_n(\mathbf{R})$, where \mathbf{R} is an abbreviation for the three electronic coordinates. Inserting this expression for the wavefunction into the time-dependent Schrödinger equation for the ion exposed to a radiation field in the Kramers-Henneberger frame¹, one obtains an infinite set of *time-independent* coupled differential equations for the Floquet components $\phi_n(\mathbf{R})$,

$$\left(E_n - \sum_{i=1}^3 \left\{ H_{0,i} + \sum_{j < i} \frac{1}{r_{ij}} \right\} \right) \phi_n(\mathbf{R}) = \sum_{m \neq n} \left(\sum_{i=1}^3 V_{n-m}(\mathbf{r}_i) \right) \phi_m(\mathbf{R}). \quad (7.1)$$

Here $E_n \equiv E + n\omega$ and $H_{0,i} \equiv \frac{1}{2}\mathbf{p}_i^2 + V_0(\mathbf{r}_i; \alpha_0)$ is the dressed-potential Hamiltonian for electron i (see also Chapter 1, Sec.1.5.1).

In order to define the solution of Eq.(7.1) uniquely, boundary conditions have to be imposed for the Floquet components ϕ_n . For this purpose it is important to note that the index n of the Floquet components ϕ_n determines the net number of photons exchanged with the field. Let us define N_0 as the smallest integer for which $\text{Re}(E_{N_0}) > 0$. Therefore,

¹For details on the Kramers-Henneberger frame, see Chapter 1, Sec.1.5.1.

for $n \geq N_0$, the detachment channel n is open, whereas for $n < N_0$ the detachment channel is closed. As a result, for $n \geq N_0$ asymptotically the Floquet component is represented by an outgoing wave with momentum $k_n = \sqrt{2E_n}$, whereas for $n < N_0$ the ϕ_n decreases exponentially at large distances. For both cases, this asymptotic behavior can be described with the boundary condition

$$\phi_n(\mathbf{R}) \rightarrow \frac{1}{r} \prod_{j=1}^3 f_n(\hat{\mathbf{r}}_j) \exp[i(k_{n,j} r_j - \nu_n \ln 2k_{n,j} r_j)] \text{ for } r_j \rightarrow \infty, \quad (7.2)$$

where $r_j \equiv |\mathbf{r}_j|$. For complex k_n , this boundary condition is known as the Siegert boundary condition [94]. The factor $\nu_n = Ze^2\mu/\hbar^2 k_n$ provides for the logarithmic distortion of the phase in case the potential has a Coulombic tail due to a remaining charge Z (for short range potentials, $Z = 0$). The angular asymptotic behavior is described by the ionization amplitude $f_n(\hat{\mathbf{r}})$. The fact that the asymptotic momentum k_n is complex is the reason that, in the Floquet framework, the quasienergy $E = \frac{1}{2}k_n^2 - n\omega$ has an imaginary part.

7.1.2 The High-Frequency Regime

In Chapter 1 (Sec.1.5.2) we described a method to solve Eq.(7.1) for high-frequency radiation fields. Here we will apply this method to the three-electron case of H^{2-} . For this purpose, we will for notational convenience use the following abbreviations, $H_0^{ion} \equiv \sum_{i=1}^3 \left\{ H_{0,i} + \sum_{j < i} \frac{1}{r_{ij}} \right\}$ and $V_{n-m}^{ion}(\mathbf{R}) \equiv \sum_{i=1}^3 V_{n-m}(\mathbf{r}_i)$. In terms of H_0^{ion} and $V_{n-m}^{ion}(\mathbf{R})$ the solution of Eq.(7.1) can be expressed as

$$\phi_n(\mathbf{R}) = \phi_0(\mathbf{R}) \delta_{n0} + (1 - \delta_{n0}) G^{(+)}(E_n) \sum_{m \neq n} V_{n-m}^{ion}(\mathbf{R}) \phi_m(\mathbf{R}), \quad (7.3)$$

where $G^{(+)}(E_n)$ is the Greens' function of the Hamiltonian H_0^{ion} , which in operator notation reads $G^{(+)}(E_n) = (E_n - H_0^{ion})^{-1}$.

For high frequencies, i.e. frequencies large compared to the level spacing of the eigenstates of the Hamiltonian H_0^{ion} , the operator $G^{(+)}(E_n)$ scales as ω^{-1} . Consequently, in the high-frequency limit, defined as the limit $\omega \rightarrow \infty$, the resolvent operator goes to zero, $\lim_{\omega \rightarrow \infty} G^{(+)}(E_n) \rightarrow 0$. We will define limits of the Floquet components in the high-frequency limit as $\lim_{\omega \rightarrow \infty} \phi_n \equiv \Phi_n$. From Eq.(7.3) it follows that in the high-frequency limit all Φ_n are zero except the $n = 0$ term. The latter is defined as² $\Phi_0(\mathbf{R}) = \Phi_{0,A}(\mathbf{r}_1) \Phi_{0,B}(\mathbf{r}_2) \Phi_{0,C}(\mathbf{r}_3)$, where the $\Phi_{0,X}(\mathbf{r}_i)$ are L^2 one-electron orbitals. $\Phi_0(\mathbf{R})$ is an eigenfunction of H_0^{ion} with eigenvalue $W^{H^{2-}}$. Since $H_{0,i}$ is Hermitian, so is H_0^{ion} , and therefore $W^{H^{2-}}$ is real, illustrating the stability of H^{2-} against photodetachment in the high-frequency limit.

Here we will go beyond the high-frequency limit and consider *finite frequencies*. In contrast to the high-frequency limit, for finite frequencies, terms of order ω^{-1} and higher obtained after iterating Eq.(7.3) have to be taken into account. Consequently, beyond the high-frequency limit the Floquet components $\phi_{n \neq 0}(\mathbf{R})$ are non-zero and

²As shown in Chapter 3, in the Kramers-Henneberger frame the one-electron orbitals of the ground state of the dressed-potential Hamiltonian have zero overlap. Since the three electrons are widely separated, correlation effects can be neglected. Therefore, the three-electron wavefunction of H^{2-} can be written as a product of one-electron orbitals, treating the electron-electron interaction with a Hartree-Hamiltonian. In addition, since the Hamiltonian is spin-independent, all spin-states are degenerate.

can be expressed in terms of the zeroth order Floquet component $\phi_0(\mathbf{R})$ by iteration. Solving the Schrödinger equation by using such an iteration procedure is useful for numerical calculations if it converges rapidly. In the high-frequency regime the iteration procedure converges as ω^{-1} , which has been tested in one-dimensional model calculations by Bardsley and Comella [59] and by Bhatt *et al* [121]. The amplitude of the Floquet components in the channels $n \neq 0$ at finite frequencies are equal to

$$\phi_{n \neq 0}(\mathbf{R}) = G_n^{(+)} \sum_{m \neq n} V_{n-m}^{ion}(\mathbf{R}) \phi_m(\mathbf{R}), \quad (7.4)$$

where $G_n^{(+)} \equiv G^{(+)}(E_n)$. In addition to this equation for the $\phi_{n \neq 0}$, we see from Eq.(7.1) that for finite frequencies ϕ_0 obeys the following equation

$$(E - H_0^{ion}) \phi_0(\mathbf{R}) = \sum_{m \neq 0} V_{-m}^{ion}(\mathbf{R}) \phi_m(\mathbf{R}). \quad (7.5)$$

Eqs.(7.4) and (7.5) are the central equations for solving the Schrödinger equation for an atom or ion in a high-frequency monochromatic radiation field by iteration. In the following, we will write the Floquet components as a sum over the contributions obtained after each iteration, $\phi_n = \sum_{\lambda=0}^{\infty} \phi_n^{(\lambda)}$. We see from Eq.(7.4) that after each iteration the number of resolvent operators in the expression for $\phi_{n \neq 0}$ increases by one. In other words, for high frequencies, each term $\phi_{n \neq 0}^{(\lambda)}$ in the series for $\phi_{n \neq 0}$ is smaller than $\phi_{n \neq 0}^{(\lambda-1)}$ by approximately a factor ω . Consequently, since ϕ_n appears on the right-hand side of Eq.(7.5), $\phi_0^{(\lambda)}$ decreases as ω^{-1} as λ increases: this implies that the iteration procedure generates a perturbation series for the Floquet components and the quasienergy in ω^{-1} . We solve Eqs.(7.4) and (7.5) by iteration, collecting terms of equal order in ω^{-1} , with the initial condition $\phi_0^{(0)} = \Phi_0$ and $\phi_n^{(0)} = 0$.

Since our purpose is to gain insight in the stability of H^{2-} in an intense high-frequency laser field, we are particularly interested in the energy correction to $W^{H^{2-}}$ for fields with finite frequencies. Therefore we expand the quasienergy E in a series of increasing iteration number, $E = W^{H^{2-}} + \sum_{\lambda=1}^{\infty} \Delta E^{(\lambda)}$. To lowest order in ω^{-1} , the expression for the energy correction is equal to $\Delta E^{(1)}$ and reads

$$\begin{aligned} \Delta E^{(1)} &= \sum_{n \neq 0} \langle \Phi_0 | V_{-n}^{ion} | \phi_n^{(1)} \rangle \\ &= \sum_{n \neq 0} \langle \Phi_0 | V_{-n}^{ion} G_n^{(+)} V_n^{ion} | \Phi_0 \rangle, \end{aligned} \quad (7.6)$$

Since the resolvent operator has an imaginary part, the quasienergy after one iteration is complex, in contrast to the energy $W^{H^{2-}}$ obtained after zero iterations. This means that in a field with finite frequency there is a finite probability that one or more electrons of the ion will photodetach. In principle, for finite frequencies, the iteration procedure is not converged after one iteration. However, for finite but large frequencies the corrections to both Φ_0 and its eigenvalue $W^{H^{2-}}$ are dominated by the term obtained after one iteration. In the next Section we will discuss a method we developed to calculate the detachment rate for H^{2-} obtained from the imaginary part of $\Delta E^{(1)}$.

7.2 Calculation of the Detachment Rate

7.2.1 One-Electron Detachment

To calculate the detachment rate of H^{2-} in a high-frequency radiation field, we proceed from Eq.(7.6),

$$\Delta E^{(1)} = \sum_{m \neq 0} \langle \Phi_0 | V_{-m}^{ion} | \phi_m^{(1)} \rangle. \quad (7.7)$$

To evaluate this matrix element we need an expression for the Floquet component $\phi_m^{(1)}$ obtained after one iteration, which is given by (cf Eq.(7.4)),

$$\phi_m^{(1)}(\mathbf{R}) = G^{(+)} \left(W_m^{H^{2-}} \right) V_m^{ion}(\mathbf{R}) \Phi_0(\mathbf{R}), \quad (7.8)$$

or

$$\left(W_m^{H^{2-}} - H_0^{ion} \right) \phi_m^{(1)}(\mathbf{R}) = V_m^{ion}(\mathbf{R}) \Phi_0(\mathbf{R}). \quad (7.9)$$

The right-hand side of this equation consists of a sum of three terms, consisting of the one-electron operator $V_m(\mathbf{r}_i)$ times $\Phi_0(\mathbf{R})$. Since Eq.(7.9) is a linear equation for $\phi_m^{(1)}(\mathbf{R})$, the latter can be expressed as a linear combination of the solutions of

$$\left(W_m^{H^{2-}} - H_0^{ion} \right) \Xi_l(\mathbf{R}) = V_m(\mathbf{r}_l) \Phi_0(\mathbf{R}), \quad (7.10)$$

where each Ξ_l describes the contribution to detachment arising from the interaction of the laser with electron l . Let us use the following ansatz for the three-electron function,

$$\Xi_l(\mathbf{R}) = \sum_{\tilde{A}, \tilde{C}} \phi_{\tilde{B}; \tilde{A}\tilde{C}}(\mathbf{r}_i) \phi_{\tilde{A}\tilde{C}}(\mathbf{r}_j, \mathbf{r}_k), \quad (7.11)$$

where i, j, k is a permutation of 1, 2, 3 and $\phi_{\tilde{A}\tilde{C}}(\mathbf{r}_j, \mathbf{r}_k)$ is an eigenfunction of the dressed-potential Hamiltonian for H^- with eigenvalue $W_{\tilde{A}\tilde{C}}^{H^-}$. In this ansatz electron i is assumed to detach. Therefore, in case $l = i$, we see from Eq.(7.10) that we are dealing with detachment of electron i through interaction between the field and electron i , referred to as direct detachment. Note that it is also possible that $l \neq i$, when electron i detaches through e-e-interaction with another electron that interacts with the field. This process we refer to as indirect detachment.

The expression for the three-electron wavefunction Ξ_l in Eq.(7.11) is still exact and includes electron-electron correlation. If we assume that after one-electron detachment the remaining H^- ion is left behind in an energetically low-lying state, we can neglect correlation effects in the eigenstates of the remaining H^- ion, and therefore we will write $\phi_{\tilde{A}\tilde{C}}(\mathbf{r}_j, \mathbf{r}_k)$ as the product $\phi_{\tilde{A}}(\mathbf{r}_j) \phi_{\tilde{C}}(\mathbf{r}_k)$.

Inserting $\Xi_l(\mathbf{R})$ into Eq.(7.10), we get the following equation in case of direct detachment,

$$\sum_{\tilde{A}, \tilde{C}} \left(W_m^{H^{2-}} - W_{\tilde{A}\tilde{C}}^{H^-} - H_{0,i} - \frac{1}{r_{ij}} - \frac{1}{r_{ik}} \right) \phi_{\tilde{B}; \tilde{A}\tilde{C}}(\mathbf{r}_i) \phi_{\tilde{A}}(\mathbf{r}_j) \phi_{\tilde{C}}(\mathbf{r}_k) = V_m(\mathbf{r}_i) \Phi_0(\mathbf{R}). \quad (7.12)$$

Suppose that $\phi_{\tilde{A}_0} \phi_{\tilde{C}_0}$ is the final state of the H^- -ion we are interested in. We premultiply both sides of Eq.(7.12) with the bra $\langle \phi_{\tilde{A}_0}(\mathbf{r}_j) \phi_{\tilde{C}_0}(\mathbf{r}_k) |$. Next, we integrate over the

coordinates \mathbf{r}_j and \mathbf{r}_k , yielding an equation for the function $\phi_{\tilde{B};\tilde{A}\tilde{C}}(\mathbf{r}_i)$ which reads,

$$\left(W_m^{H^{2-}} - W_{\tilde{A}_0\tilde{C}_0}^{H^-} - H_{0,i} \right) \phi_{\tilde{B};\tilde{A}_0\tilde{C}_0}(\mathbf{r}_i) - \sum_{\tilde{A},\tilde{C}} H_{i,\tilde{A},\tilde{C}}^{e-e} \phi_{\tilde{B};\tilde{A}\tilde{C}}(\mathbf{r}_i) = \langle \phi_{\tilde{C}_0}(\mathbf{r}_k) | \Phi_{0,X_k}(\mathbf{r}_k) \rangle V_m(\mathbf{r}_i) \Phi_{0,X_i}(\mathbf{r}_i) \langle \phi_{\tilde{A}_0}(\mathbf{r}_j) | \Phi_{0,X_j}(\mathbf{r}_j) \rangle, \quad (7.13)$$

with $X_1 = A$, $X_2 = B$ and $X_3 = C$, and where $H_{i,\tilde{A},\tilde{C}}^{e-e}$ is given by

$$H_{i,\tilde{A},\tilde{C}}^{e-e} = \langle \phi_{\tilde{A}_0}(\mathbf{r}_j) \phi_{\tilde{C}_0}(\mathbf{r}_k) | \frac{1}{r_{ij}} + \frac{1}{r_{ik}} | \phi_{\tilde{A}}(\mathbf{r}_j) \phi_{\tilde{C}}(\mathbf{r}_k) \rangle. \quad (7.14)$$

Since in our case the interelectronic distance is of the order of $\alpha_0 > 155$, the electrons can be treated as uncorrelated and therefore $H_{i,\tilde{A},\tilde{C}}^{e-e}$ can be approximated by its Hartree-expression $H_{i,\tilde{A}_0,\tilde{C}_0}^{e-e}$, where

$$H_{i,\tilde{A}_0,\tilde{C}_0}^{e-e} = \sum_{m \neq i} \int \frac{\rho(\mathbf{r}_m)}{r_{im}} d\mathbf{r}_m, \quad (7.15)$$

with $\rho(\mathbf{r}_j) = \langle \phi_{\tilde{A}_0}(\mathbf{r}_j) | \phi_{\tilde{A}_0}(\mathbf{r}_j) \rangle$ and $\rho(\mathbf{r}_j) = \langle \phi_{\tilde{C}_0}(\mathbf{r}_k) | \phi_{\tilde{C}_0}(\mathbf{r}_k) \rangle$. Consequently, $\phi_{\tilde{B};\tilde{A}\tilde{C}}$ in the left-hand side of Eq.(7.13) reduces to $\phi_{\tilde{B};\tilde{A}_0\tilde{C}_0}(\mathbf{r}_i)$. In Eq.(7.13), $\phi_{\tilde{B};\tilde{A}_0\tilde{C}_0}(\mathbf{r}_i)$ determines the amplitude of electron-detachment of electron i in the channel in which the remaining H^- ion is left in the state labelled by $\tilde{A}_0\tilde{C}_0$.

In case of indirect detachment of electron i through interaction of electron j with the field, Eq.(7.13) has to be rewritten as

$$\left(W_m^{H^{2-}} - W_{\tilde{A}_0\tilde{C}_0}^{H^-} - H_{0,i} \right) \phi_{\tilde{B};\tilde{A}_0\tilde{C}_0}(\mathbf{r}_i) - \sum_{\tilde{A},\tilde{C}} H_{i,\tilde{A},\tilde{C}}^{e-e} \phi_{\tilde{B};\tilde{A}\tilde{C}}(\mathbf{r}_i) = \Phi_{0,B}(\mathbf{r}_i) \langle \phi_{\tilde{C}_0}(\mathbf{r}_k) | \Phi_{0,X_k}(\mathbf{r}_k) \rangle \langle \phi_{\tilde{A}_0}(\mathbf{r}_j) | V_m(\mathbf{r}_j) | \Phi_{0,X_j}(\mathbf{r}_j) \rangle. \quad (7.16)$$

In case the right-hand side of Eq.(7.13) or Eq.(7.16) is zero, $\phi_{\tilde{B};\tilde{A}_0\tilde{C}_0}(\mathbf{r}_i)$ is a continuum wavefunction. Therefore it does not obey the required (Siegert) boundary condition for a detaching electron and so it can not be considered as a solution of our equation.

Suppose an electron detaches indirectly. As can be seen from Eq.(7.16), only in those channels \tilde{A}_0 for which $\langle \phi_{\tilde{A}_0} | V_m | \Phi_{0,X_j} \rangle$ is non-zero, indirect detachment takes place. Since V_m is a local operator, this matrix element differs from zero considerably only if $\phi_{\tilde{A}_0}$ does not differ too much from Φ_{0,X_j} . Therefore $H_{0,i} + H_i^{e-e}$ does not differ much from the Hamiltonian for $\Phi_{0,B}(\mathbf{r}_i)$. Since the right-hand side of Eq.(7.16) is a multiple of $\Phi_{0,B}(\mathbf{r}_i)$, this means that $\phi_{\tilde{B};\tilde{A}_0\tilde{C}_0}(\mathbf{r}_i)$ can be approximated by a multiple of $\Phi_{0,B}(\mathbf{r}_i)$. From this we conclude that the indirect detachment process can be neglected compared to the direct process, which will be discussed next.

Let us consider the case in which an *end-point electron* detaches directly, i.e. $i = 1$, $j = 2$ and $k = 3$ in the equations above (due to the symmetry in the plane $z = 0$, we can treat both end-point electrons on the same footing.). Based on the shape of the ground state of H^{2-} , we see that the right-hand side of Eq.(7.13) for direct detachment is unequal to zero as long as $\phi_{\tilde{C}_0}(\mathbf{r}_3)$ is concentrated at the end-point $z = +\alpha_0$ and $\phi_{\tilde{A}_0}(\mathbf{r}_2)$ is pronounced around $z = 0$. Since in the ground state of H^- the wavefunction

has zero amplitude at $z = 0$, this implies that if an end-point electron detaches directly, it leaves the H^- ion in a superposition of excited states³ $\phi_{\tilde{C}_0}(\mathbf{r}_3) \sum_{\tilde{A}_0} \phi_{\tilde{A}_0}(\mathbf{r}_2)$.

In case the *internal electron* detaches directly, we have $i = 2$, $j = 1$ and $k = 3$. For this case it is important to note that the one-electron orbitals of the end-point electrons in H^{2-} and in the ground state of the H^- ion, both calculated in the high-frequency limit, are approximately the same. Inserting the expression for $\Phi_0(\mathbf{R})$ into Eq.(7.13), we see that electron-detachment takes place in basically one channel $\tilde{A}_0 \tilde{C}_0$, namely the channel in which the H^- ion is left in its ground state. In the following we denote the ground-state energy of the H^- ion as W^{H^-} . In the approximation that the one-electron orbitals of the end-point electrons in the ground state of both H^{2-} and H^- are the same, i.e. $\langle \phi_{\tilde{A}_0}(\mathbf{r}_1) | \Phi_{0,A}(\mathbf{r}_1) \rangle = \langle \phi_{\tilde{C}_0}(\mathbf{r}_3) | \Phi_{0,C}(\mathbf{r}_3) \rangle$, we obtain from Eq.(7.13) the following equation for the wavefunction of the directly detaching internal electron,

$$\left(W_m^{H^{2-}} - W^{H^-} - H_{0,2} - H_{2,\tilde{A}_0 \tilde{C}_0}^{e-e} \right) \phi_{\tilde{B};\tilde{A}_0 \tilde{C}_0}(\mathbf{r}_2) = V_m(\mathbf{r}_2) \Phi_{0,B}(\mathbf{r}_2). \quad (7.17)$$

In the remaining part of this Chapter, we will concentrate on the direct detachment rate for the internal electron, i.e. $\phi_m^{(1)}(\mathbf{R}) = \Xi_{m=2}(\mathbf{R})$. In case we assume that the wavefunctions of the end-point electron in the ground state of H^- and H^{2-} are equal, one can write the solution of Eq.(7.9) as

$$\phi_{m \neq 0}^{(1)}(\mathbf{R}) \simeq \Phi_{0,A}(\mathbf{r}_1) \phi_{\tilde{B};AC}(\mathbf{r}_2) \Phi_{0,C}(\mathbf{r}_3). \quad (7.18)$$

Note that the Fourier components V_m of the space-translated Coulomb potential in Eq.(7.17) have parity $(-1)^m$. Since $\Phi_{0,B}(\mathbf{r}_2)$ has even parity, we see from Eq.(7.17) that the symmetry of the Floquet components $\phi_{\tilde{B};AC}(\mathbf{r}_2)$ should be $(-1)^m$, and therefore depends on the channel number m . With the expression for $\phi_{m,\tilde{B};AC}(\mathbf{r}_2)$, labelled with m and obtained after solving Eq.(7.17), we calculate the correction $\Delta E^{(1)}$ to $W^{H^{2-}}$ by inserting this expression into Eq.(7.7).

In order to ensure that the energy correction obtained after one iteration is a reliable representation for the correction to W , we will consider frequencies that are much larger than the largest level spacing in the ion⁴. Since the detachment energy $D^{int} = W^{H^{2-}} - W^{H^-}$ of the internal electron is smaller than the level spacings, at the frequencies we consider all channels with positive m are open, i.e. $N_0 = 1$. So the amplitude of the Floquet components in all channels $m \geq 1$ does contribute to the detachment rate. The detachment rate $\Gamma^{(int)}$ of the internal electron can be extracted from the imaginary part of $\Delta E^{(1)}$, and can be expressed as

$$\begin{aligned} \Gamma^{(int)} &= -2 \operatorname{Im} \sum_{m \geq 1} \left\langle \Phi_{0,B}(\mathbf{r}_2) | V_m(\mathbf{r}_2) | \phi_{m,\tilde{B};AC}(\mathbf{r}_2) \right\rangle \\ &\equiv \sum_{m \geq 1} \Gamma_m^{(int)}. \end{aligned} \quad (7.19)$$

³Although not calculated, it is unlikely that the projection of $\Phi_{0,B}(\mathbf{r}_2)$ on eigenstates $\phi_{\tilde{B}_0}(\mathbf{r}_2)$ of H^- will have a contribution from continuum states. As a result, there will be no shake-up of the internal electron into the continuum by configuration interaction. Therefore, as anticipated, only the end-point electron will detach.

⁴The largest level spacing of the ion, determining the applicability of the theory we apply, is given by the spectrum of the end-point electrons (see below).

In other words, the total rate of detachment can be expressed as a sum of partial detachment rates $\Gamma_m^{(int)}$ in the open channels m . For notational convenience, we will write $\phi_{m,\tilde{B};AC}(\mathbf{r}_2)$ as $\phi_m(\mathbf{r}_2)$.

In order to evaluate the matrix elements for the partial rates in Eq.(7.19), we have to extract an expression for $\phi_m(\mathbf{r}_2)$ from the inhomogeneous equation Eq.(7.17). The method we applied for this purpose will be discussed in the next paragraph.

7.2.2 Basis Set Method

Our method of solving Eq.(7.17) consists of finding a *basis set representation* for the Floquet component $\phi_m(\mathbf{r}_2)$. This method is explained in detail in Chapter 2, Sec.2.2, and we will recall here the basics.

In case of linear polarization, the dressed-potential Hamiltonian is axially symmetric around the polarization axis (i.e. the z -axis). The line of charge, extending from $z = -\alpha_0$ to $z = +\alpha_0$, is parallel to the polarization axis. The axial symmetry reduces solving Eq.(7.17) to a 2-dimensional problem. As for molecular hydrogen (see e.g. Kolos and Roothaan, Ref.[142]), prolate spheroidal coordinates⁵ (ξ, η) , centered at the end-points of the line of charge at $z = \pm\alpha_0$, are appropriate coordinates for $\alpha_0 \gg 1$.

Let us define the expression between brackets on the left-hand side of Eq.(7.17) as $D_m^{int} - H_{0,2} - H_2^{e-e} \equiv D_m^{int} - H^{int}$. Following the procedure described in Chapter 2, we find an expression for the Floquet component ϕ_m in terms of basis functions by minimizing the square of the norm of a function Θ , where Θ is defined as the difference between the left- and right-hand side of Eq.(7.17). Let us re-express Eq.(7.17) as

$$(D_m^{int} - H^{int}) \phi_m^{(1)}(\xi_2, \eta_2) = V_m \Phi_{0,B}(\xi_2, \eta_2). \quad (7.20)$$

Since $\Phi_{0,B}$ is a square-integrable function which peaks at the line of charge in the vicinity of $z = \eta = 0$, $V_m \Phi_{0,B}$ vanishes exponentially at large distances. Therefore, since $D_m^{int} > 0$ for positive m , at large distances ϕ_m is an eigenfunction of the Hamiltonian H^{int} with eigenvalue D_m^{int} . However, approaching the line of charge from infinity, i.e. towards the region where $V_m \Phi_{0,B}$ is non-zero, the character of ϕ_m should change from a continuum wavefunction to a solution of the inhomogeneous equation Eq.(7.20). In order to represent this spatial behavior of ϕ_m , we use three types of basis functions. To illustrate the role of the different type of basis functions, let us define the region where $V_m \Phi_{0,B}$ is non-zero as region I, and the region where it is negligible small as region II.

The first type consists of L^2 functions that are designed to represent ϕ_m in region I. They are of the following form,

$$\chi_m^{N,M,\gamma}(\xi, \eta) = (\xi - 1)^N e^{-\gamma(\xi-1)} (1 - \eta^2)^M \times \begin{cases} \eta & \text{for } m \text{ odd} \\ 1 & \text{for } m \text{ even} \end{cases}. \quad (7.21)$$

where N and M are positive integers and γ a positive real parameter. Since ϕ_m describes a detached electron that moves away from the position of the zeroth order function $\Phi_{0,B}(\xi_2, \eta_2)$, it should be pronounced around $\eta = 0$. The η -dependence of the basis function is constructed such that it is possible to locate the Floquet component ϕ_m around $\eta = 0$ with relatively few basis functions, increasing the speed of the convergence.

⁵See e.g. Abramowitz and Stegun, Ref.[137]. If r_+ and r_- are defined as $r_{\pm} \equiv |\mathbf{r} \pm \alpha_0 \hat{\mathbf{z}}|$, the coordinates ξ and η are given by $\xi = (r_+ + r_-)/2\alpha_0$ and $\eta = (r_+ - r_-)/2\alpha_0$. From these definitions it follows that $\xi \in [1, \infty)$ and $\eta \in [-1, +1]$. On the line of charge we have $\xi = 1$ and ξ increases as \mathbf{r} increases; η varies from -1 to $+1$ as z increases from $-\alpha_0$ to $+\alpha_0$.

In addition, since the inversion operator transforms (ξ, η) to $(\xi, -\eta)$, the additional factor η for the odd channels insures the right parity for the basis function $\chi_m^{N,M,\gamma}$.

The second type of basis function is constructed for region II, which is given by

$$\chi_c^{M,k_m}(\xi, \eta) = \frac{1}{\xi} e^{i\beta(\xi)} (1 - \eta^2)^M \times \begin{cases} \eta & \text{for } m \text{ odd} \\ 1 & \text{for } m \text{ even} \end{cases}, \quad (7.22)$$

where $\beta(\xi) = k_m \alpha_0 \xi - \frac{1}{k_m} \ln \xi$ is the asymptotic phase of the Floquet component in channel m . The logarithmic tail reflects the effect on the phase of the long range potential generated by the remaining H^- ion. This basis function obeys the following relation

$$[D_m^{int} - H^{int}] \chi_c^{M,k_m}(\xi, \eta) = 0 + O\left(\frac{1}{\xi^3}\right). \quad (7.23)$$

The error of order ξ^{-3} comes from the kinetic energy of this basis function in the η -direction.

Finally, the third type of basis function we used is a mixture of the first and second type,

$$\chi_m^{N,M,\gamma,k_m}(\xi, \eta) = (\xi - 1)^N e^{-\gamma(\xi-1)} e^{i\beta(\xi)} (1 - \eta^2)^M \times \begin{cases} \eta & \text{for } m \text{ odd} \\ 1 & \text{for } m \text{ even} \end{cases}. \quad (7.24)$$

This is an L^2 function with the same oscillatory behavior as the basis function designed for region II. As for the functions for region I, N, M and γ are real and positive. Compared to the first type of basis functions, the exponential factor γ in basis functions of the third type is chosen to be much smaller. As a result, it has a larger spatial extent. The third type of basis function appears to be essential for coupling the behavior of $\phi_m^{(1)}$ in region I and region II.

The calculations of the detachment rates are performed at large values of α_0 , typically of the order of $\alpha_0 = 200$ and larger, simply because the dressed-potential Hamiltonian supports bound states for $\alpha_0 = 155$ and larger (see Chapter 3). Since for increasing α_0 the wavefunctions of the end-point electrons relatively contract on the end-points⁶, in the calculation of $\phi_m^{(1)}$ we approximated the end-point electrons by point charges located at the end-points. This approximation for the e-e repulsion induces an error in the detachment rates that is negligible compared to the accuracy of the calculation.

7.2.3 Evaluation of Matrix Elements

Once the representation for $\phi_m^{(1)}$ in terms of basis function is known, the matrix element

$$\Gamma_m^{(int)} = -2 \operatorname{Im} \langle \Phi_{0,B}(\xi, \eta) | V_{-m}(\xi, \eta) | \phi_m^{(1)}(\xi, \eta) \rangle \quad (7.25)$$

has to be evaluated in order to obtain the detachment rate for the internal electron in channel m . Although the evaluation can be performed analytically for the basis functions of the first type, basis functions involving the phase factor $\beta(\xi)$ require a numerical approach⁷. However, if the functions $\Phi_{0,B}(\xi, \eta)$, $V_{-m}(\xi, \eta)$ and $\phi_m^{(1)}(\xi, \eta)$ are known throughout space, accurate quadrature formulas can be applied for the integration to calculate the partial rates. The Fourier components V_{-m} of the space-translated Coulomb potential can be calculated for any ξ and η , except on the line of charge

⁶The distance between the end-point and the center of charge of an end-point electron scales as $2.3\alpha_0^{1/3}$, see e.g. Ref.[122].

⁷See Chapter 2, Sec.2.2.3.

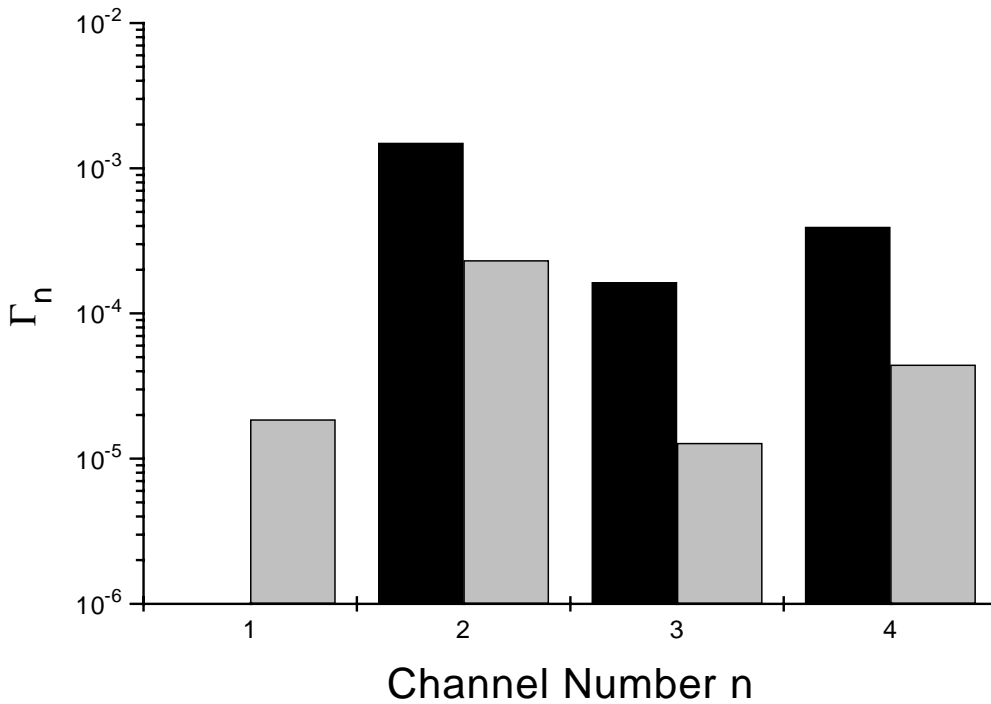


Figure 7.2: Rate of detachment Γ_n of the internal electron via the direct detachment process (see text), evaluated at $\omega = 3 \times 10^{-3}$. The values indicated by the black bars correspond to $\alpha_0 = 200$, and those by the gray bars to $\alpha_0 = 400$. The partial rates at $\alpha_0 = 400$ are smaller than at $\alpha_0 = 200$, indicating that the internal electron stabilizes against photodetachment as the intensity increases.

($\xi = 1$) where V_{-m} diverges logarithmically⁸. Moreover, $\Phi_{0,B}(\xi, \eta)$ and $\phi_m^{(1)}(\xi, \eta)$ are smooth functions, which are known in terms of linear combinations of basis functions, and therefore they can be evaluated at any point throughout space.

For the numerical evaluation of the matrix element in Eq.(7.25), we have used Simpson's integration method. However, due to the logarithmic singularity of the Fourier components V_{-m} , the region close to the line of charge requires a special treatment in the integration, see Appendix A of this Chapter.

7.3 Stabilization and Angular Dependence of the Electron Detachment

7.3.1 Detachment Rates of Internal Electron

We present results of calculations of partial detachment rates $\Gamma_n^{(int)}$ of the internal electron under various different conditions of the laser field. In particular, we are interested in the dependence of the detachment rate on the intensity and the frequency. In order to study the former, we performed calculations at various different values of α_0 at fixed frequency. In addition, we present calculations at different values of ω at fixed α_0 . The results of the calculations are given in Figures 7.2 and 7.3.

Comparing the results of the rate of detachment for fixed frequency and $\alpha_0 = 200$ and 400 respectively, we see that the rate of detachment of the internal electron decreases

⁸On the end-points, i.e. where $\xi^2 - \eta^2 = 0$, V_{-m} has a square-root singularity.

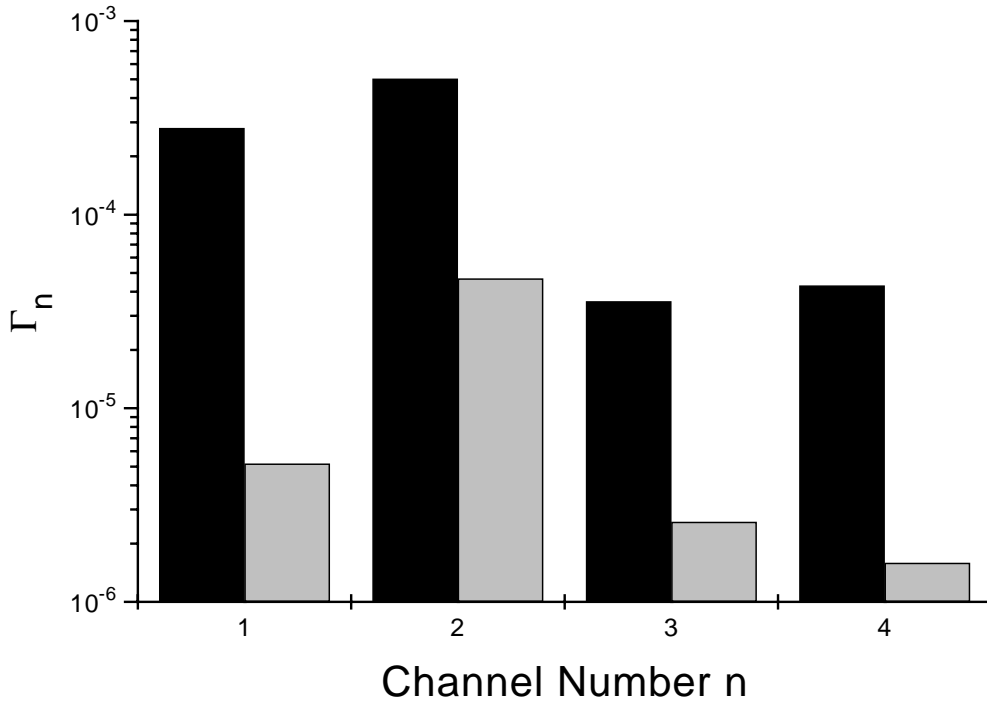


Figure 7.3: Same as Figure 7.2, but now for $\omega = 6 \times 10^{-3}$. Comparison with Figure 7.2 shows that the detachment rate decreases as the frequency increases, illustrating the convergence to the high-frequency limit.

as α_0 increases from 200 to 400. In terms of the intensity this means that the stability of the internal electron against photodetachment increases as the intensity increases. This counterintuitive phenomenon, referred to in literature as *stabilization*, has been shown for the first time by Pont and Gavrila in atomic hydrogen exposed to an intense high-frequency field, see Ref.[28]. We see that stabilization sets in irrespective of the frequency we consider, i.e. 3×10^{-3} or 6×10^{-3} .

In order to illustrate the stabilization of the internal electron in terms of total detachment rates we calculated the total rate for the internal electron over a wider range of values of α_0 . The frequency at which these calculations are performed equals $\omega = 5 \times 10^{-3}$, at which the high-frequency approximation for the internal electron is applicable (see below, Sec.7.4.2). The results are depicted in Figure 7.4. From this Figure we see that at fixed frequency the total detachment rate decreases as α_0 increases, implying the stabilization against photodetachment of the internal electron. The detachment rate obtained with this numerical calculation shows a decreasing exponential scaling behavior, for which we have no explanation in terms of analytical expressions.

If the frequency increases while keeping α_0 fixed, we see that the detachment rate decreases. This is consistent with the fact that at increasing frequency the Floquet components $\phi_n^{(1)}$ will vanish, see Eq.(7.4). Consequently, according Eq.(7.7), to lowest order in ω^{-1} , the energy correction $\Delta E^{(1)}$ to the quasienergy decreases and finally will vanish in the limit $\omega \rightarrow \infty$. So, if the frequency increases, the detachment rate converges to its value in the high-frequency limit which equals zero.

In Figure 7.2 we see that in channel 1 the detachment rate equals zero for $\alpha_0 = 200$, whereas it is non-zero for $\alpha_0 = 400$ at the same frequency and for $\alpha_0 = 200$ at $\omega =$

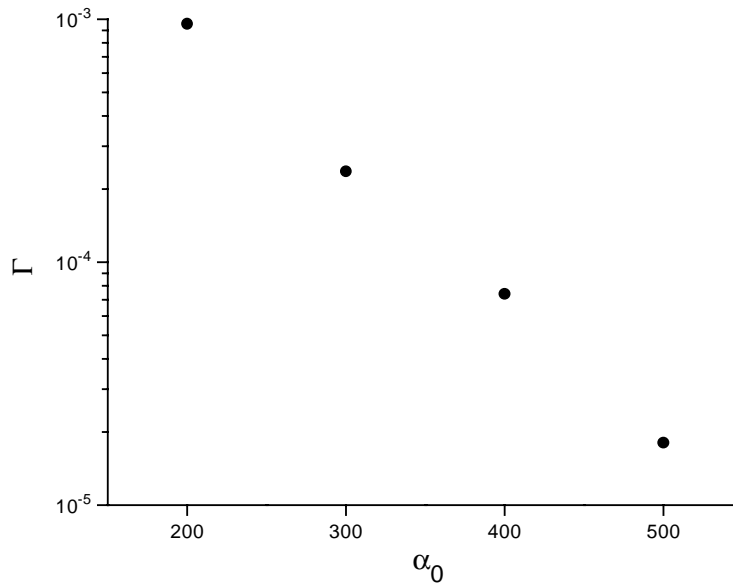


Figure 7.4: Total detachment rate of the internal electron for various different values of α_0 at fixed frequency equal to $\omega = 5 \times 10^{-3}$. The rate of detachment decreases as α_0 increases implying the internal electron stabilizes against photodetachment.

6×10^{-3} , see Figure 7.3. In other words, both stabilization and convergence to the high-frequency limit seem to be contradicted by this particular channel. This contradiction, however, is paradoxical and can be explained considering the shape of the potential felt by the internal electron. As shown in Chapter 3, in order to detach, the internal electron has to pass a potential barrier perpendicular to the polarization axis. Since at $\alpha_0 = 200$ a photon energy $\omega = 3 \times 10^{-3}$ is not sufficient to bridge the energy gap between the ground state and the height of this barrier (cf Figure 3.1), the detachment rate by absorption of one single photon is strongly suppressed. Our calculation yields a detachment rate that is vanishingly small compared to the accuracy of the calculation.

Comparing the partial rates for a certain fixed frequency and quiver amplitude α_0 , we see that the detachment rate does not decrease monotonically with the channel number. From Figures 7.2 and 7.3 we see that the rates in both the even and the odd channels decrease, but that those in the even channels are larger in the sense that $\Gamma_{2n} > \Gamma_{2n-1}$ for integer n . The total detachment rate is dominated by the rates in the channels with n even. This effect reflects the fact that the internal electron effectively sees twice the frequency of the laser field because the proton passes the internal electron twice per period.

7.3.2 Detachment Rates of H^{2-}

Once the detachment rates for the internal electron are known, the natural question arises what the rate of the total ion H^{2-} is. In order to answer this question, let us consider the following. Since the binding energy of the end-point electrons in the high-frequency limit is much larger than that of the internal electron, the applicability of the high-frequency approximation is determined by the end-point electrons (for details, see below). In case the high-frequency approximation is applicable, this approximation holds better for the internal electron, since the latter has smaller level spacings. Therefore, for a

fixed frequency, the wavefunction of the internal electron will resemble its high-frequency counterpart $\Phi_{0,B}$ more than the wavefunctions of the end-point electrons resemble their high-frequency limits $\Phi_{0,A}$ and $\Phi_{0,C}$. Based on this observation, one would expect that the internal electron is more stable against photodetachment than the two end-point electrons. This in turn would imply that, for finite high frequencies, the total detachment rate is determined by the detachment rate of the end-point electrons.

To find an estimate for the detachment rate of the end-point electrons in H^{2-} , let us consider the singly charged negative hydrogen ion, H^- . In H^- at large α_0 , each of the two electrons are concentrated at one of the two end-points. In the regime where the electrons of H^- are widely separated and have negligible overlap, the two-electron wavefunction can be approximated by a product of two one-electron orbitals. In the ground state of H^- , these one-electron orbitals hardly differ from those of the end-point electrons in the ground state of⁹ H^{2-} . It has been shown by Gavrila and Schertzer [125] that the detachment rate of H^- roughly equals twice the ionization rate of atomic hydrogen, i.e. $\Gamma^{(H^-)} \simeq 2\Gamma^{(H)}$. Due to the similarity of the orbitals of the end-point electrons of H^{2-} and H^- , the detachment rate of each of the end-point electrons in H^{2-} is expected to be of the order of $\Gamma^{(H)}$ as well.

Comparison of the rate of detachment of the internal electron and the rate of the end-point electrons, based on results of atomic hydrogen obtained by Pont, shows that the internal electron is much more stable against photodetachment than the end-point electrons. At $\alpha_0 = 200$ and for $\omega = 0.125$, the detachment rate of H^- equals $\Gamma^{(H^-)} = 7.18 \times 10^{-4}$. By extrapolating the results of our calculations on the detachment rate of the internal electron in H^{2-} to the same laser conditions, one gets $\Gamma^{(int)} \simeq 5 \times 10^{-6}$. This illustrates the fact due to the smaller level spacings of the internal electron, for a fixed high frequency the internal electron resembles its high-frequency counterpart more than the end-point electrons.

7.3.3 Angular Distribution of the Photoelectron

In the following we will briefly comment on the angular distribution of the Floquet components ϕ_n of the photodetaching internal electron. Since the electron escapes from the H^{2-} ion, its wavefunction asymptotically is an outgoing wave. For $\alpha_0 = 200$ we depict in Figure 7.5 the imaginary part of the Floquet component ϕ_2 , which is an eigen function of H^{int} with eigen value $W_{n=2}^{H^{2-}} - W^{H^-}$. Here the z -axis is chosen to be parallel to the polarization axis and the ρ -axis is perpendicular to the polarization axis. From this Figure we see that the amplitude of this Floquet component is pronounced in the direction perpendicular to the polarization axis, which is a typical feature found for all other Floquet components and at other different values of α_0 as well. Since in the initial state the internal electron is sandwiched by the two end-point electrons, the repulsive electron-electron interaction prevents the internal electron to escape in the direction parallel to the polarization axis.

In Figure 7.6 we show the angular distribution of the Floquet components for various different channels at $\alpha_0 = 200$. The ϕ_n are plotted as a function of η at $\xi = 6$, i.e. at a distance of roughly 1000 atomic units away from the initial position of the internal

⁹In the ground state, the end-point electrons in H^- are located *between* the end-points and close to $z = \pm\alpha_0$. Due to the e-e repulsion with the internal electron in H^{2-} , the end-point electrons in H^{2-} are polarized slightly towards the end-points $z = \pm\alpha_0$ compared to their position in H^- .

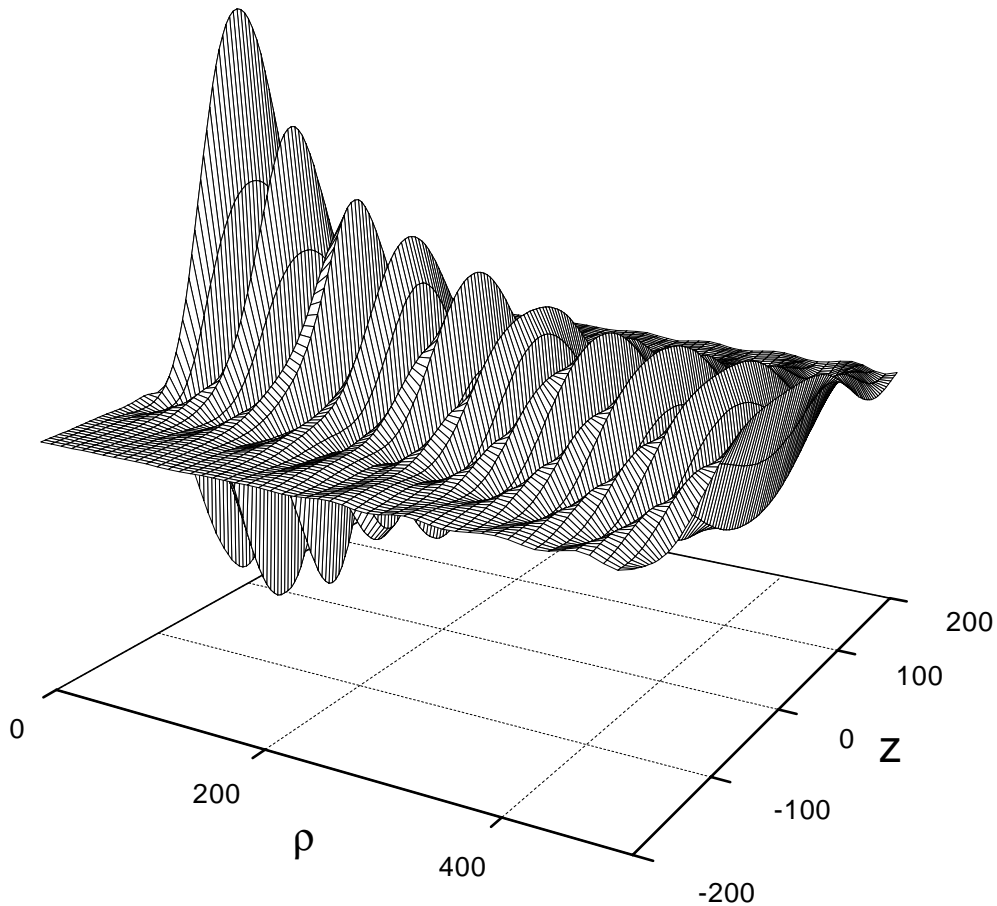


Figure 7.5: Imaginary part of the Floquet component $\phi_{n=2}$ at $\alpha_0 = 200$ as a function of ρ and z , calculated at $\omega = 5 \times 10^{-3}$. The amplitude of this Floquet component is non-zero at large distances illustrating the non-zero detachment rate in channel 2 at this particular value of α_0 .

electron. Asymptotically η is equal to $\cos \theta$, where θ is the angle with the polarization axis. We see that, in contrast to the case of atomic hydrogen, the angular distribution does not vary rapidly. Since at large α_0 the one-electron wavefunction of atomic hydrogen is dichotomized¹⁰, the rapid oscillations in that case are caused by interference of amplitudes of the electronic wavefunction escaping from both end-points. In case of the internal electron of H^{2-} however, the repulsive interaction with the end-point electrons prevents the internal electron to dichotomize at these values of α_0 . As a final remark on the angular distribution we mention that the fact that the partial rate of detachment in the even channels is larger than the rate in the odd channels is reflected in the amplitude of the Floquet components at large distances, as can be seen from Figure 7.6.

¹⁰See Chapter 1 for details on dichotomy.

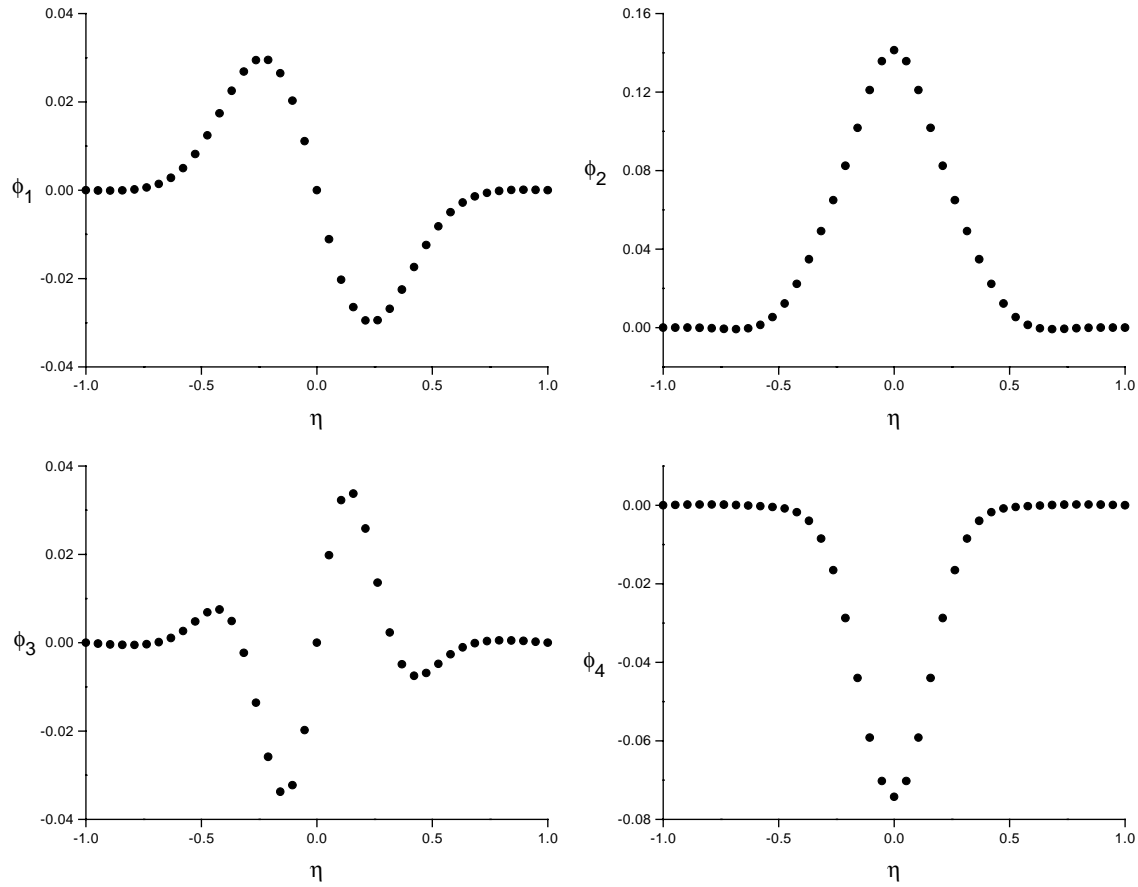


Figure 7.6: Angular distribution of the Floquet components ϕ_n for channel 1 through 4. For both odd and even channels the maximum amplitude decreases as the channel number increases. The maximum amplitude in the channels with even channel number $2n$ is larger than the channels with odd channel number $2n - 1$, in correspondence with the rates of detachment extracted from these Floquet components, cf Figures 7.2 and 7.3.

7.4 Applicability of the Calculation

7.4.1 Discretization of the Inner Product

The Floquet component $\phi_m^{(1)}$ obeying Eq.(7.20), which is used for the calculation of the partial rate $\Gamma_m^{(1)}$, is found by minimizing the function Θ ,

$$|\Theta\rangle = |(D_m^{int} - H^{int}) \phi_m^{(1)} - V_m \Phi_{0,B}\rangle. \quad (7.26)$$

The minimization procedure is constructed such that it iteratively adds one basis function to the representation of $\phi_m^{(1)}$. With the basis set representation of $\phi_m^{(1)}$, $|\Theta|^2$ typically is four orders of magnitude smaller than $|V_m \Phi_{0,B}|^2$. For details concerning the construction of $\phi_m^{(1)}$ we refer the reader back to Chapter 2, Sec.2.2.

Since we are not able to evaluate matrix elements involving the square of the Hamiltonian H^{int} analytically, the square of the norm of Θ is calculated by numerical integration, thereby discretizing the inner product. We define the square of the norm as ε , i.e. $\varepsilon \equiv <\Theta|\Theta>$. As long as the supports in the numerical integration procedure are chosen appropriately (see below), the discretization of the inner product does not affect

	$\omega_{exc}^{e.p.}$	ω_{exc}^{int}
axial excitation	$3.83 \cdot 10^{-3}$	$6.19 \cdot 10^{-4}$
radial excitation	$8.25 \cdot 10^{-3}$	$3.39 \cdot 10^{-3}$

Table 7.1: Energy spacings between the ground state and the first excited state of H^{2-} at $\alpha_0 = 200$. In the right column the energy required to excite the internal electron, ω_{exc}^{int} , to the lowest radially resp. axially excited state (see text) is listed. The middle column contains the corresponding excitation energies for the end-point electrons, $\omega_{exc}^{e.p.}$.

the result of ε . In order to ensure the invariance of the inner product, restrictions on the positions of the supports are imposed by both the Hamiltonian and the basis functions.

The inner product is invariant under the discretization by the numerical integration as long as Θ is a smooth function on the length scale determined by the spatial separation between the supports. Moreover, outside the region where the supports are located, Θ is supposed to be zero. Since Θ is constructed by $D_m^{int} - H^{int}$ acting on a linear combination of basis functions χ , these restrictions for the positions of the supports are imposed by the variation of the basis functions. In order to find an accurate representation of ϕ_m in terms a basis functions, the variation of the basis functions is large. Consequently, the supports are required to lie dense in the ξ, η -plane.

Changing to the discretized inner product involving the numerical integration potentially leads to a different spectrum of the Hamiltonian H^{int} . Moreover, an inappropriate choice of the distribution of the supports might affect the Hermiticity of the Hamiltonian H^{int} defined on the discretized inner product. The spectrum of the Hamiltonian, defined on the discretized inner product, is invariant as long as the variation of both the potential and the kinetic energy of the basis functions is small over the interval separating the supports. The same requirement holds for the conservation of the Hermiticity of the Hamiltonian.

We checked both the spectrum and the Hermiticity of the Hamiltonian by calculating eigenvalues of the bound states of the dressed-potential Hamiltonian, evaluating the matrix elements with the discretized inner product. From these calculations we conclude that the supports need to be distributed homogeneously in the η -direction, whereas in the ξ -direction the spacing between the supports has to decrease exponentially as one approaches the logarithmic singularity at $\xi = 1$. The supports are located at 39 different values for η and 54 different values for ξ , giving a total of 2106 supports.

7.4.2 High-Frequency Regime

For the applicability of the calculation in the high-frequency regime, the frequency ω should be larger than the largest level spacing in the spectrum of the ion. In order to determine this lower limit for the frequency, we calculated the excitation energies of both the end-point electrons and the internal electron by calculating the spectrum of the dressed-potential Hamiltonian.

To identity the excited states, let us consider the corresponding wavefunctions. In Figure 7.7 the wavefunctions of both the internal and end-point electrons of various different excited states at $\alpha_0 = 200$ are depicted. From this Figure we see that there are two types of excited states. Firstly, the electronic wavefunction can be axially excited. With this we mean that the corresponding wavefunction has at least one nodal plane

on the line of charge, i.e. it is excited in the η -direction, see Figures 7.7 (a) and (b). Secondly, there are also excited states with nodal planes in the ξ -direction and those are referred to as radially excited states, see Figures 7.7 (c) and (d). In contrast to the Hartree-Hamiltonian for the end-point electrons, for the internal electron, at large values of α_0 , the Hartree-Hamiltonian is almost separable in ξ and η . Therefore, the motion of the internal electron in the ξ - and η -direction is practically decoupled, which is reflected by the shape of the radially and axially excited state for the internal electron. For the end-point electrons, however, the shape of the radially excited state reflects the coupling between the motion in the ξ - and η -direction by the slight oscillation along the polarization axis, see Figure 7.7 (c).

For $\alpha_0 = 200$ the excitation energies for the lowest axially and radially excited states listed in Table 7.1. The excitation energy at this particular value of α_0 determines a lower limit for the frequency for higher values of α_0 as well since the excitation energies decrease at increasing α_0 . From Table 7.1 it follows that the axially excited states energetically lie far below the radially excited states. In addition, from these values we see that the excitation energies of the end-point electrons is larger than that for the internal electron and therefore the former determines the lower limit for the frequency in the calculation of the *total rate* of H^{2-} . Since we concentrate on the detachment rates of the internal electron only, the lower limit for the frequency for our calculation is determined by the excitation energy to the radially excited state of the internal electron, i.e. $\omega > 3.39 \times 10^{-3}$.

In axially excited states, the interelectronic distance, which scales as α_0 , is smaller compared to that in the ground state. Therefore, due to the repulsive e-e interaction, α_0 is an important parameter determining the excitation energy of the axially excited states. In contrast to the axially excited states, the e-e interaction hardly influences the excitation energy of the radially excited states. According the scaling laws of the "end-point potential"¹¹, the latter scales as $\alpha_0^{-2/3}$ for the end-point electrons, whereas it scales roughly as $\ln(\alpha_0)/\alpha_0$ for the internal electron. Consequently, as α_0 increases, the energy curves of the axially and radially excited states of the end-point electrons are expected to cross, whereas those of the internal electron are not. Due to the coupling, although very weak, between the radially and axially excited states, these crossing should be avoided crossings. For α_0 just above the value where H^{2-} becomes stable (i.e. the so-called "appearance value" $\alpha_0 = 155$, see Chapter 3), for both the internal and the end-point electrons the 3-rd excited state is the first radially excited state. As anticipated above, at $\alpha_0 = 1000$, the first radially excited state for the internal electron is still the 3-rd excited state. For the end-point electrons however, at $\alpha_0 = 1000$ the lowest lying radially excited state corresponds the 4-th excited state, and therefore it has crossed once an axially excited state¹².

In order to detach, the internal electron has to pass a potential barrier generated by the attractive interaction with the line of charge and the repulsive e-e interaction with the end-point electrons. In principle, the height of this barrier gives a classical lower limit for the frequency required to couple the initial state of the internal electron with the continuum. However, the height of this barrier is smaller than the excitation energy of the end-point electrons and therefore the presence of the potential barrier does not

¹¹See the Appendix of Chapter 3 for details on the end-point potential.

¹²In case of H^- the situation is similar; see Muller and Gavrila, Ref.[133].

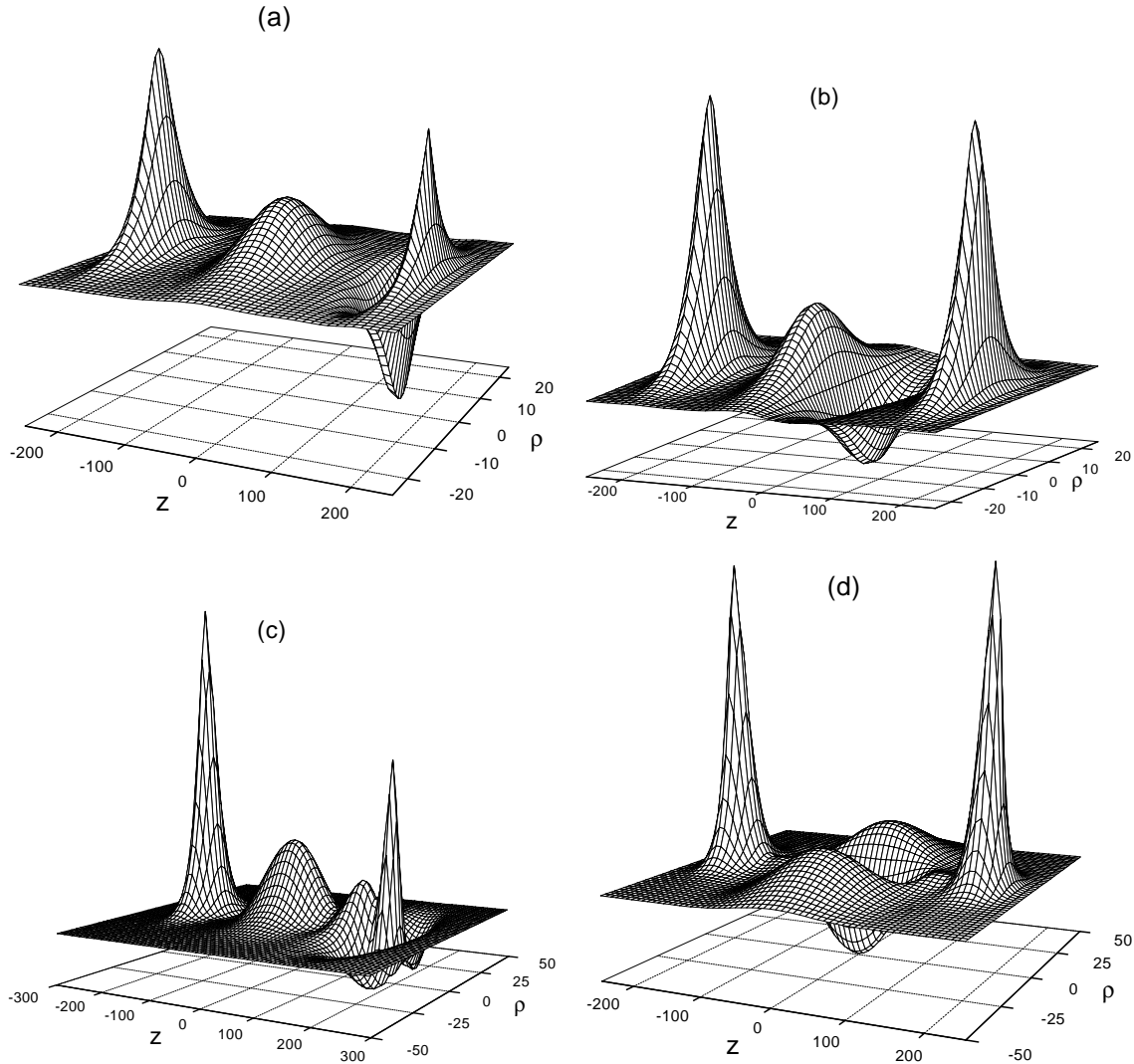


Figure 7.7: Three-electron wavefunction of H^{2-} at $\alpha_0 = 200$. In Figures (a) and (b) an end-point electron resp. internal electron is in its first axially excited state. Figures (c) and (d) illustrate the first radially excited states of an end-point resp. internal electron. The energy spacing between the ground state and the radially excited state is larger than that for the corresponding axially excited states, see Table 7.1. In addition, for both the radially and axially excited states, the excitation energy for the internal electron is much smaller than that for the end-point electron. The states in which the internal electron is excited correspond to shape-resonances (for details, see Chapter 3, Sec.3.4.2).

impose a more restrictive condition on the frequency as imposed by the excitation energy of the end-point electrons.

Apart from the fact that on general theoretical grounds there is only a lower limit for the frequency in the calculation, the finite memory size available in computers yields an upper limit for the frequency. If the frequency increases, the number of oscillations per unit length of the Floquet components ϕ_n gets so large that the number of δ -functions required to sample the basis functions becomes too large for the computer to handle. Moreover, if the frequency would not be restricted from above by a finite memory size,

k	x_k	w_k
1	0.2031878699799799	0.6275004874579875
2	1.0000000000000000	0.3724995125420125
Error	0.0650727316766768	0.0468121300200201

Table 7.2: Weights and abscissas for numerical integration of both polynomials with maximum degree $i_{max} = 1$ and the product of the logarithm and polynomials with maximum degree $j_{max} = 0$, see Eq.(A.1). The weights and abscissas as listed are defined for the integration interval $[0,1]$. One degree of freedom, the position of $x_{i_{max}}$, is chosen to be 1. The last row in this Table indicates the error in the numerical integration of a polynomial of degree $i_{max} + 1$ or this polynomial multiplied with a logarithm resp., evaluated with the weights and abscissas listed.

k	x_k	w_k
1	0.0531397303717936	0.1853819489988701
2	0.4849119985451659	0.6299296370140333
3	1.0000000000000000	0.1846884139870967
Error	0.0065420916088756	0.0023662717386089

Table 7.3: Same as Table 7.2, but now for $i_{max} = 2$ and $j_{max} = 1$.

strong oscillations of the basis functions at high frequencies would induce errors in the calculation by cancellation during the integration.

A Quadrature Formulas for a Logarithmic Singularity

To deal with the logarithmic singularity in the Fourier components V_n , we calculated weights and abscissas for the numerical integration in the ξ -direction. The abscissas x_k and weight factors w_k are determined such that the integral of both $F(\xi) = (\xi - 1)^i$ and $G(\xi) = (\xi - 1)^j \ln(\xi - 1)$ are evaluated exactly on the interval $(\xi - 1) \in [0, 1]$ for various different values of i and j . We calculated x_k and w_k for two cases. Firstly, for the case in which j_{max} is smaller than i_{max} by one. In this case, the remaining degree of freedom is used to fix the position of one of the $i_{max} + 1$ abscissas, which is chosen to lie on the boundary of the integration interval, i.e. $x_{i_{max}} = 1$. Secondly, for the case in which the maximum value of i , i_{max} , equals the maximum value of j , j_{max} . In both cases we have

$$\int_0^1 [c_F F(x+1) + c_G G(x+1)] dx = c_F \sum_{k=0}^{i_{max}} F(x_k + 1) w_k + c_G \sum_{k=0}^{i_{max}} G(x_k + 1) w_k, \quad (\text{A.1})$$

with c_F and c_G arbitrary constants.

For the case $x_{i_{max}} = 1$, the values for the positions of the abscissas and their corresponding weights for $i_{max} \in [1, 3]$ are listed in Tables 7.2 through 7.4. In our calculation we used the 4-point quadrature formula with weights and abscissas listed in Table 7.4. For the case $i_{max} = j_{max}$, the values for x_k and w_k are listed in Tables 7.5 through 7.7 for $i_{max} \in [0, 2]$.

j	x_j	w_j
1	0.018993541581	0.068995204710
2	0.215368312425	0.343750223561
3	0.659864016307	0.478038044659
4	1	0.109216527070
Error	0.0005878155013050	0.0001267159156358

Table 7.4: Same as Table 7.2, but now for $i_{max} = 3$ and $j_{max} = 2$.

k	x_k	w_k
1	0.3678794411714423	1
Error	-0.1321205588285577	-0.1178794411714423

Table 7.5: Weights and abscissas for numerical integration of both polynomials with maximum degree $i_{max} = 0$ and the product of the logarithm and polynomials with maximum degree $j_{max} = 0$, see Eq.(A.1). The weights and abscissas as listed are defined for the integration interval $[0,1]$. The last row in this Table indicates the error in the numerical integration of a polynomial of degree $i_{max} + 1$ or this polynomial multiplied with a logarithm resp., evaluated with the weights and abscissas listed.

k	x_k	w_k
1	0.0882968651376532	0.2984998937055252
2	0.6751864909098874	0.7015001062944748
Error	-0.0112085058401987	-0.0201428773701384

Table 7.6: Same as Table 7.5, but now with $i_{max} = 1$ and $j_{max} = 1$.

k	x_k	w_k
1	0.0288116625310452	0.1033307079651954
2	0.3040637296125011	0.4546365259701731
3	0.8116692253442406	0.4420327660646314
Error	-0.0008470796726348	-0.0020459953074560

Table 7.7: Same as Table 7.5, but now with $i_{max} = 2$ and $j_{max} = 2$.

SAMENVATTING VOOR IEDEREEN

Op deze pagina aangekomen zal de niet-natuurkundige zich wellicht afvragen wat het geen beschreven in de hieraan voorafgaande hoofdstukken allemaal te betekenen heeft. Ik kan me dit levendig voorstellen en maak dan ook graag van de gelegenheid gebruik me in deze samenvatting in het bijzonder te richten tot diegenen die niet vertrouwd zijn met het lezen van natuurkundige artikelen of proefschriften.

Vanwege de enorme verscheidenheid aan onderzoeksgebieden binnen de natuurkunde is het voor de overzichtelijkheid van belang de inhoud van dit proefschrift een plaats te geven alvorens er over uit te weiden. Kort gezegd valt dit onderzoek onder de noemer atoomfysica. De atoomfysica omvat de studie van de structuur van atomen, die bestaan uit een elektrisch positief geladen kern en één of meerdere negatief geladen elektronen. De atoomfysica is op zich weer een zeer uitgebreid onderzoeksterrein, en de plaats van dit proefschrift vereist derhalve nadere specificatie. Een van de onderzoeksgebieden binnen de atoomfysica omvat de studie naar de interactie tussen licht en materie. Onder licht verstaan atoomfysici in het algemeen laserlicht¹³, terwijl voor materie atomen en/of ionen (elektrisch geladen deeltjes) gelezen moet worden. Derhalve wordt dit onderzoeksgebied vaak aangeduid met laser-atoom fysica. Zoals de titel van dit proefschrift reeds aangeeft, richt het hier beschreven onderzoek zich in het bijzonder op de interactie tussen *intens* laserlicht en ionen. Mede dankzij ontwikkelingen in de lasertechnologie heeft dit onderzoek zich in het afgelopen decennium sterk kunnen ontwikkelen en vertakken en wordt het inmiddels als apart onderzoeksgebied beschouwd. Het in dit proefschrift beschreven onderzoek maakt deel uit van deze zogenaamde super-intense laser-atoom fysica.

Uit het dagelijks leven weten wij dat licht interactie heeft met vele vormen van materie. De veruit bekendste lichtbron is de door velen aanbeden zon. In zonlicht wordt onze huid bruin en warm (en ons humeur optimaal). Voor bomen, planten en onszelf is de interactie met zonlicht zelfs onontbeerlijk om te overleven. Het voor de mens, en voor vele andere wezens, veruit belangrijkste orgaan gebaseerd op de interactie tussen licht en materie is het oog.

Om te begrijpen waarom ik in de context van laser-atoom fysica het menselijk oog aanroer is het van belang te weten dat licht een vorm van energie is. De energie van licht wordt door twee factoren bepaald, de intensiteit en de kleur van het licht. De verschillende invloed die deze twee factoren hebben op de energie van het licht komt voort uit het feit dat licht bestaat uit zogenaamde fotonen, die we voor het gemak als deeltjes zullen beschouwen. Een foton kan beschouwd worden als een energiepakketje en de *hoeveelheid* energie die het bevat bepaalt de *kleur* die ons oog er aan toekent. Zo draagt bijvoorbeeld een foton in een groene lichtbundel meer energie dan een foton in een rode lichtbundel. De *intensiteit* van de lichtbundel neemt toe naarmate het *aantal*

¹³Een laser zendt in één richting licht uit dat bestaat uit slechts één kleur. Hiermee onderscheidt laserlicht zich van licht afkomstig van een gloeilamp in de zin dat een gloeilamp in alle richtingen licht uitzendt dat alle kleuren van de regenboog bevat. Al die kleuren tezamen worden door ons oog als wit licht geïnterpreteerd.

fotonen in deze lichtbundel toeneemt. Dit betekent dat een intense lichtbundel meer energie bevat dan een zwakke. Het feit dat licht opgebouwd is uit fotonen impliceert dat de energie van een lichtbundel niet elke willekeurige waarde kan hebben, maar dat deze een veelvoud is van de energie van één foton. Met andere woorden, de energie van licht is “gekwantiseerd”.

De interactie tussen licht en het menselijk oog enerzijds en tussen licht en een atoom of ion anderzijds is vergelijkbaar in de zin dat de reactie van het atoom op het licht, net zoals die van het oog, afhangt van de kleur en intensiteit van het licht: Het atoom “ziet” als het ware het licht. Hoe het atoom licht “ziet” kan verklaard worden met het gegeven dat een atoom slechts in bepaalde toestanden kan verkeren. Deze verschillende toestanden worden gekenmerkt door de beweging van de elektronen in het atoom. Aan gezien beweging een vorm van energie is houdt dit in dat atomaire toestanden in energie van elkaar verschillen: in een laag-energetische toestand bewegen de elektronen langzamer dan in een energetische hoger gelegen toestand¹⁴. Om van een laag-energetische toestand naar een hoog-energetische toestand over te gaan heeft het atoom energie nodig, en wel precies die hoeveelheid energie die die twee toestanden scheidt. In geval het atoom meer energie wordt aangeboden dan nodig voor de overgang neemt het atoom het benodigde deel daarvan niet op (een atoom kan zijn bord niet deels leeg eten). Mits beschenen met een lichtbundel met fotonen die de juiste hoeveelheid energie dragen is het voor het atoom mogelijk de overgang naar een hoger-energetische toestand te maken door één foton te absorberen. In geval de totale energie van een aantal fotonen gelijk is aan het energieverlies tussen de twee toestanden van het atoom, kan het atoom de overgang maken door absorptie van dat aantal fotonen. De kans dat het atoom één of meer fotonen absorbeert neemt toe naarmate het aantal fotonen in de lichtbundel, i.e. de intensiteit, toeneemt.

Gezien het voorafgaande gaat de overeenkomst tussen het menselijk oog en het atoom nog een stapje verder. Stel dat het atoom een overgang van een laag-energetische naar een hoog-energetische toestand kan maken door absorptie van een groen foton, en niet door absorptie van een aantal rode fotonen. Met rood licht beschenen zal het atoom in de laag-energetische toestand blijven, terwijl het met groen licht beschenen in de hoog-energetische toestand kan geraken. Afhankelijk van de kleur van het licht dat het atoom “ziet” wordt het in staat gesteld actie te ondernemen in de vorm van het absorberen van een foton waardoor de elektronen in het atoom sneller gaan bewegen. Het is alsof het atoom voor het stoplicht staat en, alsof het een oog is, selektief reageert op de kleur die het ziet, wel of niet energie opneemt om vervolgens wel of niet zijn elektronen in beweging te zetten.

Uit onze belevingswereld weten we dat we een kracht op een voorwerp moeten uitoefenen als we dat voorwerp willen laten bewegen. Zo moet ook op elektronen een kracht worden uitgeoefend om ze in beweging te zetten. Het feit dat het licht een atomaire overgang kan veroorzaken, d.w.z. elektronen kan laten bewegen, betekent dus niets anders dan dat het licht een kracht uitoefent op de elektronen. Deze kracht neemt toe naarmate de intensiteit van het licht toeneemt. Als een atoom beschenen wordt met licht werken er drie krachten op de elektronen van dit atoom. In de eerste plaats de aantrekkende elektrostatische kracht tussen de positief geladen kern van het atoom en de negatief geladen elektronen. In de tweede plaats de afstotende elektrostatische kracht

¹⁴De energetisch laagste toestand wordt de “grond-toestand” genoemd en de energetisch hoger gelegen toestanden worden aangeduid met de term “aangeslagen toestanden”.

tussen de elektronen. Tot slot, de kracht van het licht werkend op de elektronen. De kracht ten gevolge van lichtbronnen die wij in het dagelijks leven tegen komen (zon, gloeilamp etc.) is verwaarloosbaar klein ten opzichte van de elektrostatische krachten in een atoom. Voor een adequate natuurkundige beschrijving van een atoom beschermen met dit soort licht kan de invloed van het licht op het atoom als een kleine verstoring worden beschouwd.

De situatie verandert drastisch zodra een atoom beschermen wordt met een laser die een zodanige lichtintensiteit genereert dat de kracht die het licht uitoefent op het atoom van dezelfde orde van grootte of zelfs groter is dan de elektrostatische krachten in het atoom. In het laatste geval worden de elektronen als het ware gedresseerd door het laserlicht en spelen de elektrostatische krachten niet meer de dominante rol van voorheen. Een gevolg van deze dressuur is dat de atomaire toestanden sterk worden vervormd. In een waterstofatoom, bestaande uit één proton (de kern) en één elektron, wordt de ruimte waar het elektron zich kan bevinden door het veld volledig in tweeën gescheurd. Door het laserlicht langzaam te dimmen smelt deze ruimte weer tot één geheel samen, resulterend in een *stabiele* atomaire toestand waarin de beweging van het elektron bepaald wordt door de elektrostatische krachten. De krachten ten gevolge van intens laserlicht zijn echter ook in staat elektronen in een bepaalde configuratie te laten bestaan die niet in een stabiele atomaire toestand overgaat als het licht wordt gedimd; Een atoom waarin de electronen in zo'n configuratie bewegen zal gedurende het dimmen van het licht uit elkaar vallen. Dit betekent dat de interactie met het licht leidt tot nieuwe *stabiele* atomaire toestanden, zogenaamde licht-geïnduceerde toestanden.

Het zijn deze licht-geïnduceerde toestanden die een centrale rol spelen in dit proefschrift. Het gegeven dat het beschijnen van een atoom met intens laserlicht kan leiden tot stabiele atomaire toestanden die niet gerelateerd zijn aan stabiele toestanden van het onbeschermen atoom geeft aanleiding tot de volgende vraag: Kan de interactie met intens laserlicht leiden tot stabiele toestanden van een atomair systeem dat geen stabiele toestanden kent in afwezigheid van dit laserlicht? Een voorbeeld van laatstgenoemd systeem is een negatief geladen waterstofion, bestaande uit één proton en meer dan twee elektronen. Een dergelijk ion wordt ook wel een meervoudig negatief geladen waterstofion genoemd omdat de totale lading van zo'n ion meer dan één en negatief is. Vanwege het feit dat de afstotende krachten tussen de elektronen onderling in zo'n ion niet kan worden gecompenseerd door de aantrekende kracht tussen elk elektron en het proton valt zo'n ion vanzelf uit elkaar. Met andere woorden, een meervoudig negatief geladen waterstofion heeft geen stabiele toestanden. In dit proefschrift wordt een theoretische studie gepresenteerd naar de mogelijkheid met intens laserlicht stabiele toestanden van deze ionen te maken.

In het algemeen kan theoretisch natuurkundig onderzoek op twee manieren worden uitgevoerd. Enerzijds kan met behulp van pen en papier een kwalitatieve studie worden verricht aan een natuurkundig proces waarbij het rekenen aan desbetreffend proces van secundair belang is. Een hieruit voortvloeiende *analytische* beschrijving wordt meestal gegeven in termen van voor een buitenstaander ingewikkeld aandoende formules. Anderzijds kan een computer uitkomst bieden aan berekeningen die zo groot van omvang zijn dat het onmogelijk is deze uit te voeren met pen en papier. De aanpak van complexe natuurkundige vraagstukken met behulp van deze zogenaamde *numerieke* berekeningen

heeft de laatste jaren aan populariteit gewonnen door de sterke toename van de beschikbare computercapaciteit. Bij het onderzoek beschreven in dit proefschrift is van beide methoden gebruik gemaakt. In de hoofdstukken 3, 6 en 7 worden numerieke berekeningen gepresenteerd en in de hoofdstukken 4 en 5 wordt een analytische presentatie gegeven over meervoudig negatief geladen waterstofionen in intens laserlicht.

Zoals eerder aangegeven zijn we geïnteresseerd in de mogelijkheid een stabiele toestand van een meervoudig negatief geladen waterstofion te maken, gebruik makende van de interactie tussen dit type ion en intens laserlicht. In hoofdstuk 3 concentreren wij ons op de simpelste in zijn soort, het H^{2-} -ion, bestaande uit één proton en drie elektronen. Omdat de afstotende kracht tussen elektronen onderling en de aantrekkende kracht tussen het proton en de elektronen afneemt naarmate de afstand tussen deze deeltjes afneemt, is het voor het creëren van een stabiele toestand voor H^{2-} van belang dat de elektronen niet te dicht bij elkaar in de buurt komen en dat tegelijkertijd de elektronen zo nu en dan wel het proton van dichtbij zien. Om dit gedaan te krijgen biedt, zoals aangewezen met behulp van een numerieke berekening in hoofdstuk 3, de interactie met intens laserlicht een helpende hand. Het laserlicht oefent namelijk een zodanige kracht uit op de elektronen dat deze heen en weer gaan bewegen¹⁵. De essentie is dat het licht de elektronen zodanig kan laten bewegen dat ze één voor één gedurende een korte periode dichtbij het proton zijn terwijl de afstand tussen de elektronen onderling groot blijft; Het licht dresseert als het ware de elektronen. Bij deze dressuur is het van belang dat de elektronen zo snel langs het proton bewegen dat deze niet aan het proton kunnen blijven “plakken”. Mocht een elektron aan het proton blijven plakken, neutraliseert het elektron de lading van het proton en zullen daardoor de andere elektronen zich niet meer aangetrokken voelen tot het proton. Om dit plakken te voorkomen moet de *kleur* van het laserlicht violet zijn. Naarmate de *intensiteit* van het laserlicht toeneemt wordt de gemiddelde afstand tussen de elektronen onderling en tussen de elektronen en het proton groter. Cruciaal voor het ontstaan van stabiele toestanden van H^{2-} is het feit dat naarmate deze afstanden toenemen de afstotende kracht tussen de elektronen onderling sneller afneemt dan de aantrekkende kracht tussen de elektronen en het proton. Bij toenemende intensiteit zal er derhalve een moment zijn waarop de aantrekkende krachten in het ion het winnen van de afstotende krachten waardoor er een stabiele toestand ontstaat van het H^{2-} -ion. Het ontstaan van deze stabiele toestand is aangewezen met de numerieke berekeningen gepresenteerd in hoofdstuk 3.

In de hoofdstukken 4 en 5 slaan we een ander pad in en geven we een analytische beschrijving van de stabiele toestanden van meervoudig negatief geladen waterstofionen. We beperken ons daarbij niet alleen tot het H^{2-} -ion, maar kijken ook naar de mogelijkheid stabiele toestanden van waterstofionen met meer dan 3 elektronen te creëren. Dit doen we voor twee soorten licht: Ten eerste voor zogenaamd *circulair gepolariseerd* laserlicht, een term die illustreert dat elektronen door dit licht, mits het licht intens genoeg is, gedwongen worden langs een cirkel te bewegen. Ten tweede voor *lineair gepolariseerd* laserlicht, licht dat bij hoge intensiteit de elektronen forceert langs een rechte lijn te bewegen. Met behulp van zowel circulair als lineair gepolariseerd laserlicht blijkt het mogelijk te zijn, zoals beschreven in hoofdstuk 4 respectievelijk 5, stabiele toestanden van negatief geladen waterstofionen met 3 of 4 elektronen te maken. Door de afstotende

¹⁵Het licht oefent op het proton dezelfde kracht uit, maar is niet in staat dit te laten bewegen omdat het proton veel zwaarder is dan de elektronen.

kracht tussen de elektronen onderling neemt de minimale afmeting van de cirkel, repectievelijk rechte lijn, waarlangs de elektronen van desbetreffende waterstofionen in een stabiele toestand kunnen bewegen (zie omslag van dit proefschrift) toe naarmate het aantal elektronen in het ion toeneemt.

In de hoofdstukken 6 en 7 gaan we weer op de numerieke toer. We richten ons in deze hoofdstukken op de stabiliteit van negatief geladen waterstofionen beschenen met laserlicht. Het blijkt dat de interactie met dit laserlicht nogal tweeslachtig is. Ondanks het feit dat stabiele toestanden van bovengenoemde waterstofionen door toedoen van de krachten die het laserlicht uitoefent op de elektronen bestaan, is het niet uit te sluiten dat één van de elektronen een foton absorbeert. Het gevolg hiervan kan zijn dat het desbetreffende elektron de energie van het foton zal gebruiken om het ion te verlaten. Kortom, voor meervoudig negatief geladen waterstofionen werkt de aanwezigheid van laserlicht zowel stabiliserend als destabiliserend.

In hoofdstuk 6 wordt een methode gepresenteerd die zeer geschikt is om de stabiliteit uit te rekenen voor ionen waarvoor de mogelijkheid bestaat dat twee elektronen het ion verlaten. Als voorbeeld is het *enkelvoudig* negatief geladen waterstofion H^- gekozen, bestaande uit één proton en twee elektronen. Processen waarin twee elektronen ontsnappen zijn in het algemeen zeer complex omdat de ontsnappende elektronen elkaar beïnvloeden tijdens de ontsnapping. Het wederzijds beïnvloeden van elektronen wordt *elektron-elektron correlatie* genoemd. Details van processen waarbij deze vorm van correlatie een belangrijke rol speelt zijn in het algemeen moeilijk te berekenen.

Tot slot wordt in hoofdstuk 7 de stabiliteit van het meervoudig negatief geladen waterstofion H^{2-} bestudeerd. Hierbij is de aandacht gericht op H^{2-} in lineair gepolariseerd laserlicht. In dit licht liggen de drie elektronen op één rechte lijn. Door de kracht die het licht op de drie elektronen uitoefent trillen ze langs deze rechte lijn. Gedurende elke trilling passeren ze allen het proton, maar de twee buitenste elektronen staan in vergelijking met het middelste elektron relatief lang stil bij het proton. De buitenste elektronen plakken als het ware beter. Nu is het belangrijk te weten dat het om te ontsnappen voor het elektron belangrijk is in de buurt van het proton te zijn op het moment dat het elektron het foton absorbeert. Het ligt dus in de lijn der verwachtingen dat het middenelektron van H^{2-} minder makkelijk zal ontsnappen dan de twee buitenste elektronen. De numerieke berekeningen die in hoofdstuk 7 staan gepresenteerd bevestigen deze verwachting. Een opmerkelijk resultaat van deze berekeningen is dat de mate waarin elektronen ontsnappen afneemt naarmate de intensiteit van het laserlicht toeneemt. De verklaring hiervoor moet worden gezocht in het plakken van elektronen als de intensiteit toeneemt. Zoals eerder vermeld neemt bij toenemende intensiteit de afmeting van het ion, d.w.z. de afstand waarover de elektronen trillen, toe. De tijd die de elektronen in de nabijheid van het proton zijn neemt derhalve af bij hogere intensiteiten. Dit op zijn beurt impliceert dat bij toenemende intensiteit de elektronen minder de gelegenheid krijgen aan het proton te plakken. Ze zullen derhalve minder makkelijk een foton kunnen absorberen om vervolgens te ontsnappen.